


# Railway Trackbed Deterioration

By

Ji Yu, MSc

*Thesis submitted to the University of Nottingham*

*for the degree of Doctor of Philosophy*

*October 2016*

# Abstract

In this thesis, the main objective is to identify the resilient deformation behaviour of rail trackbed especially in ballast and calculate the stress distribution. A purpose-designed three dimensional Finite Element railway trackbed model is presented in which linear elastic behaviour is assumed in all parts of the model. The study has also evaluated the effects of different variables including moving load magnitude, loading speed and stiffness of materials on stress conditions and deflections based.

A comprehensive literature review on a wide background of railway trackbed has been carried out. Railway ballast specifications, deformation mechanisms, resilient and permanent deformation behaviour of granular material, introduction of fouling material and its influence on ballast behaviour are explained to provide the basis for trackbed analysis.

Results show that a higher vertical displacement underneath the sleeper may occur when the loading speed is higher than 120km/h. Also, higher speed and Young's modulus of ballast can result in higher damaging stresses. A stiffer subgrade can result in less rotation of sleeper. A significant effect of subgrade stiffness on stress paths and rotation of sleeper can only be found when Young's modulus of subgrade is in a low level. Stiffer rail pad can lead ballast element get cracked more easily. Softer pad results in less damaging stresses. In addition, there is no obvious change of either the stress ratio or sleeper rotation as stiffness of the ballast increased.

# Acknowledgements

First, I would like to thank Dr. Nick Thom for his great guidance, massive support and supervision throughout this project. Moreover, I am grateful that he spent hours proof-reading my thesis patiently and gave me many comments.

I would also like to thank my friends: Dr. Liu Shu, Dr. Lu Yang, Dr. Wang Juan, Dr. Yuan Ran for the selfless helps and splendid discussions on my research.

Finally, greatest respect to my parents for their constant encouragement and support and forever love.

# Contents

Abstract ..... I

Acknowledgements ..... II

List of Figures ..... VII

List of Tables ..... XIV

List of Notations ..... XV

1 Introduction ..... 1

1.1 Background ..... 1

1.2 Aim and Objectives ..... 4

1.3 Thesis Outline ..... 5

2 Literature Review ..... 7

2.1 Track Components ..... 7

2.1.1 Description of Components and Functions ..... 8

2.1.2 Track Forces ..... 11

2.2 Ballast ..... 14

2.2.1 Ballast Specifications ..... 14

2.2.2 Ballast Deformation Modes ..... 16

2.2.3 Resilient Behaviour of Granular Material ..... 17

2.2.4 Permanent Deformation Behaviour of Granular Material ..... 20

2.2.5 Fouling Material and its Influence on Trackbed Behaviour ..... 25

2.3 Finite Element Method ..... 28

2.3.1 Two-dimensional Problems ..... 31

2.3.2 Three-dimensional problems ..... 33

2.3.3 Higher order quadratic elements ..... 34

2.4 Dynamic Ballasted Railway Trackbed Modelling .....35
2.5 ABAQUS.....44
2.5.1 Elements .....45
2.5.2 Material damping.....47
2.5.3 Boundary Condition.....49
2.6 Summary .....51
3 Preliminary Study – 2D Simulations..... 53
3.1 Two-dimensional Simulation Practice.....53
3.1.1 Longitudinal Section .....55
3.1.2 Transversal Cross section.....69
3.2 Summary .....77
4 3D Trackbed Model Design ..... 78
4.1 3D Model .....78
4.1.1 Dimension .....78
4.1.2 Material Properties .....81
4.1.3 Load .....82
4.1.4 Step.....84
4.1.5 Boundary Condition.....84
4.1.6 Mesh.....85
4.2 Boundary Condition .....86
4.3 Subgrade Depth.....89
4.3.1 Theoretical Depth .....89
4.3.2 Subgrade Depth Design .....91
4.4 Mesh Density.....95
4.5 Loading.....97

4.6 Frequency Response ..... 105
4.7 Summary ..... 109
5 Detailed Dynamic Loading Case Study ..... 111
5.1 Model Description ..... 111
5.1.1 Step ..... 111
5.1.2 Load ..... 112
5.1.3 Mesh ..... 112
5.1.4 Boundary Conditions ..... 116
5.2 Reference Model ..... 117
5.2.1 Stress ..... 117
5.2.2 Sleeper Rotation ..... 125
5.2.3 Initial Stresses ..... 128
5.2.4 Principal Stress Rotation ..... 131
5.3 Summary ..... 141
6 Parametric Analysis of Trackbed Properties ..... 143
6.1 Solution controls ..... 143
6.2 Load speeds ..... 145
6.3 Loading magnitudes ..... 152
6.4 Material properties ..... 154
6.4.1 Young's modulus of ballast ..... 154
6.4.2 Young's modulus of rail pad ..... 159
6.4.3 Young's modulus of subgrade ..... 164
6.5 Summary ..... 170
7 Conclusions and Recommendations ..... 172
7.1 Conclusions ..... 172

7.2 Recommendations.....176

Reference……....178

Appendix A..... 190

Appendix B..... 193

Appendix C..... 196

Appendix D……...201

# List of Figures

Figure 1.1 Simulation project flowchart ..... 3

Figure 2.1 Structure overview of railway trackbed, (a) longitudinal view, and (b) cross section view (Selig and Waters, 1994) ..... 8

Figure 2.2 Rail deflection and load distribution into trackbed (Selig and Waters, 1994) .....13

Figure 2.3 Strains in granular materials during one cycle of load application (Wright, 1983) .....17

Figure 2.4 Ballast behaviour in the cyclic triaxial test (Selig and Waters, 1994).....18

Figure 2.5 Relationship between resilient modulus and bulk stress (Alva-Hurtado, 1980) .....20

Figure 2.6 Permanent strain affected by stress ratio (Knutson, 1976) .....21

Figure 2.7 Effect of difference in sequence of loading on permanent strain (Selig and Waters, 1994).....22

Figure 2.8 Contribution of number of cyclic loads on settlement (Shenton, 1975) ....23

Figure 2.9 Stresses on pavement elements: (a) Stress beneath rolling wheel load; (b) principal stresses and planes (Brown, 1996).....24

Figure 2.10 Influence of loading frequency on permanent strain (Shenton, 1975) ....25

Figure 2.11 Sources of ballast fouling (Selig and Waters, 1994).....26

Figure 2.12 Effect of various degrees and types of the fouling materials on ballast settlement (Han and Selig, 1997) .....27

Figure 2.13 Effect of water content on ballast settlement with different degree and type of fouling materials (Han and Selig, 1997).....28

Figure 2.14 Summary of the derivation of FEM formulation .....31

Figure 2.15 2D plane stress and plane strain problems .....32

Figure 2.16 Three dimensional continuum element of (a) 4-node tetrahedron element (b) 8-node hexahedron element (c) 6-node wedge element.....33

Figure 2.17 High order quadratic elements .....35

Figure 2.18 Overview of (a) 2D ballasted trackbed (Yang *et al.* 2009) and (b) 3D ballasted trackbed (Nguyen 2012) .....36

Figure 2.19 3D vehicle of (a) lateral view (b) front view and (c) top view .....37

Figure 2.20 Creation of ballast aggregates FE model (Aikawa, 2015) .....38

Figure 2.21 Impact load on aggregate model and Von Mises stress distribution (Aikawa, 2015) .....38

Figure 2.22 Comparison of wheel track contact force under single wheelset and multiple wheelsets moving load (Blanco-Lorenzo *et al.* 2011).....39

Figure 2.23 (a) Stresses (b) horizontal (U1) and vertical (U2) displacements on natural ground at different train speed (Yang *et al.* 2009) .....41

Figure 2.24 Stress path of soil element on natural ground at a speed of (a) $0.5V_c$ (b) $V_c$ and (c) $1.25V_c$ (Yang *et al.* 2009) .....42

Figure 2.25 Schematic of the FE dynamic model (Bian *et al.* 2016).....43

Figure 2.26 Contour plot of vertical displacement induced at ground surface in XY and YZ planes at a speed of (a) 50m/s (b) 120m/s and (c) 200m/s (Bian *et al.* 2016) .....44

Figure 2.27 Influence of (a) alpha damping (b) beta damping on deflection (Lu, 2010) .....49

Figure 2.28 Viscous Damping Boundary (Ross, 2004).....50

Figure 3.1 The sketches of idealised and simplified track deflections under a wheel load .....56

Figure 3.2 Vertical displacement with distance .....58

Figure 3.3 Dimensions of the longitudinal section model in 2D .....59

Figure 3.4 Sketch of Case 1 meshed model .....61

Figure 3.5 Measuring nodes in the longitudinal model .....62

Figure 3.6 Comparison of vertical stresses vary with mesh sizes .....63

Figure 3.7 Comparison of vertical displacements vary with mesh sizes.....63

Figure 3.8 Vertical stresses change with different mesh sizes compared to Case 1 .64

Figure 3.9 Vertical displacements change with different mesh sizes compared to Case 1 .....64

Figure 3.10 Comparison of vertical stresses with different mesh sizes .....65

Figure 3.11 Contour plot of vertical stress distribution (a) for the entire model (b) detail under the load .....66

Figure 3.12 (a) Sketch of partial ballast in 2D model (b) Vertical stress distribution at different depths .....67

Figure 3.13 Contour plot of vertical displacement distribution .....68

Figure 3.14 Trends of vertical rail displacement .....69

Figure 3.15 Dimensions of the transversal cross section model in 2D .....70

Figure 3.16 Sketch of Case 1 meshed model .....71

Figure 3.17 Measuring nodes distribution .....72

Figure 3.18 Contour plot of vertical displacement distribution for the entire model ...72

Figure 3.19 Contour plot of vertical stress distribution.....73

Figure 3.20 Comparison of vertical displacements with different mesh sizes.....74

Figure 3.21 Vertical stresses vary with mesh sizes at (a) nodes 3-6 (b) node 1 (c) node 2 .....75

Figure 3.22 Comparison of the results from same position in two different models ..76

Figure 4.1 Dimensions of the simplified rail UIC60 in m (Esveld, 2001) .....79

Figure 4.2 (a) Sketch of sleeper and railpad (b) Dimensions of model (c) Overview of 3D model .....80

Figure 4.3 Load pressure located on the surface of rail .....83

Figure 4.4 The user subroutine moving load control .....84

Figure 4.5 The mesh of the 3D model for optimising design .....86

Figure 4.6 Meshed damped boundary for alpha value test .....87

Figure 4.7 Influence of the alpha damping coefficient on vertical displacement.....88

Figure 4.8 Vertical displacement comparisons on different subgrade depths .....92

Figure 4.9 Comparison of peak vertical displacement from 8m and 155m depth subgrade models.....93

Figure 4.10 Coarse meshed 3D model sketch .....94

Figure 4.11 Maximum vertical displacements on different nodes.....95

Figure 4.12 Maximum vertical displacement comparisons on different mesh quantities.....97

Figure 4.13 The user subroutine for two moving loads.....98

Figure 4.14 Points underneath moving load path.....99

Figure 4.15 Vertical stresses on ballast surface under single load and double loads with a speed of (a) 60km/h (b) 120km/h (c) 200km/h and (d) 300km/h .....100

Figure 4.16 Vertical stresses 150mm beneath ballast surface under single load and double loads with a speed of (a) 60km/h (b) 120km/h (c) 200km/h and (d) 300km/h .....102

Figure 4.17 Maximum vertical displacement comparisons with single and double wheel loads .....103

Figure 4.18 Power spectrum analysis obtained from vertical sleeper velocity data of (a) 3D simulation and (b) geophone attached to the sleeper.....107

Figure 4.19 Power spectrum analysis for horizontal sleeper velocity data obtained from (a) 3D simulation and (b) geophone attached to the sleeper .....108

Figure 5.1 An overview of the fine meshed rail trackbed model .....113

Figure 5.2 Mesh for ballast.....114

Figure 5.3 (a) Mesh on Surface 2 & 3 (b) Mesh on Surface 1 .....115

Figure 5.4 A meshed damping layer serves as an absorbing boundary.....116

Figure 5.5 Paths at (a) the bottom corner of the sleeper (b) the centre line of the sleeper .....117

Figure 5.6 Contour plot of vertical stress in ballast.....118

Figure 5.7 Stresses varying with depth at path 367 .....119

Figure 5.8 Vertical stress contour plot of YZ plane underneath bottom sleeper .....120

Figure 5.9 Locations at the interface underneath moving load .....120

Figure 5.10 Variation in stress at path 23756 (middle of sleeper) .....121

Figure 5.11 Element penetration occurs at the interface between subballast and subgrade .....122

Figure 5.12 (a) Lateral stress (b) Vertical stress (c) Horizontal stress versus time at different nodes .....124

Figure 5.13 Shear stresses changes against time at different nodes .....125

Figure 5.14 Sketch of sleeper rotation under the moving train (Bogacz et al., 2014) .....126

Figure 5.15 Rotation of the sleeper during the train passage .....128

Figure 5.16 Sketch of crib ballast .....129

Figure 5.17 Sketch of the simplified structure .....130

Figure 5.18 Permanent deformation under repeated loading (Inam et al., 2012) ....131

Figure 5.19 Effect of Young's modulus on principal stress rotation at (a) surface of natural ground (b) 0.49S below the natural ground surface at the centreline of two rails (Powrie *et al.* 2007).....133

Figure 5.20 Effect of Poisson's ratio on principal stress rotation at (a) surface of natural ground (b) 0.49S below the natural ground surface at the centreline of two rails (Powrie *et al.* 2007).....134

Figure 5.21 Calculation points for principal stress rotation .....135

Figure 5.22 Principal stress rotations at the points under middle sleeper .....136

Figure 5.23 Principal stress rotations at different points under the bottom corner of the sleeper .....137

Figure 5.24 Vertical and shear stress at different points under the moving load .....139

Figure 5.25 Axial and shear stresses at different points under a moving load (Shi, 2009) .....140

Figure 6.1 Maximum in-plane (a) Vertical stress (b) Horizontal stress (c) Shear stress with different speeds .....147

Figure 6.2 Maximum vertical displacement on the bottom corner of the sleeper (4355 in Figure 5.9) at different speeds.....147

Figure 6.3 Rotations of sleeper at different speeds.....148

Figure 6.4 Effect of load speed on principal stress rotation at (a) A (b) D (see Figure 5.21).....149

Figure 6.5 Stress path for ballast at sleeper bottom corner at different speeds: (a) 60km/h (b) 120km/h (c) 200km/h (d) 300km/h .....151

Figure 6.6 Maximum in-plane (a) Vertical stress (b) Horizontal stress (c) Shear stress with different loading magnitudes.....153

Figure 6.7 Rotations of sleeper at different loading magnitudes .....154

Figure 6.8 Maximum in-plane (a) Vertical stress (b) Horizontal stress (c) Shear stress with different $E_{ballast}$.....155

Figure 6.9 Rotations of sleeper at different $E_{ballast}$ .....156

Figure 6.10 Effect of $E_{ballast}$ on principal stress rotation at (a) A (b) D (see Figure 5.21) .....157

Figure 6.11 Stress path in ballast at sleeper bottom corner at different $E_{ballast}$: (a) 100MPa (b) 140MPa (c) 200MPa (d) 280MPa .....158

Figure 6.12 Stress path under single and duel load in ballast at sleeper bottom corner at different $E_{ballast}$: (a) 100MPa (b) 140MPa (c) 200MPa (d) 280MPa .....159

Figure 6.13 Maximum in-plane (a) Vertical stress (b) Horizontal stress (c) Shear stress with different $E_{pad}$.....161

Figure 6.14 Rotations of sleeper at different $E_{pad}$ .....162

Figure 6.15 Effect of $E_{pad}$ on principal stress rotation at (a) A (b) D (see Figure 5.21) .....163

Figure 6.16 Stress path for ballast at sleeper bottom corner at different $E_{pad}$: (a) 6.9MPa (b) 20MPa (c) 60MPa.....164

Figure 6.17 Maximum in-plane (a) Vertical stress (b) Horizontal stress (c) Shear stress with different $E_{subgrade}$ .....166

Figure 6.18 Rotations of sleeper at different $E_{subgrade}$ .....166

Figure 6.19 Effect of $E_{subgrade}$ on principal stress rotation at (a) A (b) D (see Figure 5.21).....168

Figure 6.20 Stress path in ballast at sleeper bottom corner at different $E_{subgrade}$: (a) 35MPa (b) 75MPa (c) 100MPa (d) 150MPa.....169

Figure B1 Stress path under model with and without damping at nodes (a) 4355 and (b) 23756……..……...195

Figure C1 Contour plot of (a) x axis (b) z axis normal stress……...197

Figure C2 Contour plot of shear stress on (a) XY (b) XZ (c) YZ plane……..199

Figure C3 Contour plot of longitudinal displacement towards (a) X (b) Y (c) Z axis……200

Figure D1 (a)Lateral (b) Vertical (c) Longitudinal stress paths at middle bottom of the sleeper……..202

Figure D2 Shear stress paths at middle bottom of the sleeper……...203

Figure D3 (a) Lateral (b) Vertical (c) Longitudinal stress paths at bottom corner of the sleeper……..204

Figure D4 Shear stress paths at bottom corner of the sleeper……205

# List of Tables

Table 2.1 The specification for ballast particle size distributions in the UK (RT/CE/S/006 Issue 3, 2000) .....16

Table 3.1 Material Properties .....60

Table 3.2 Consistent units in ABAQUS .....60

Table 3.3 Typical rail-wheel contact areas for different wheel diameters .....61

Table 4.1 Material Properties .....82

Table 4.2 Characteristic for wave velocity calculation .....90

Table 4.3 Mesh quantities for three models .....96

Table 4.4 Maximum vertical stress differences .....104

Table 4.5 Material Properties for the track monitoring site in South Africa .....105

Table 4.6 Freight wagon parameters (Priest *et al.,* 2010) .....106

Table 5.1 Boundary conditions for all surfaces as illustrated in Figure 5.1 .....116

Table 6.1 Variable parameters used in simulations .....143

Table A1 Longitudinal Section……..191

Table A2 Cross Section……192

# List of Notations

| | |
|---|---|
| E | Young's modulus |
| $M_r$ | Resilient modulus |
| n | The number of wheels |
| I | Moment of inertia of the rail with respect to vertical bending |
| k | Track modulus |
| P | The vertical wheel load applied on the rail |
| p' | Mean effective stress |
| q | Transient deviator stress |
| $Q_{tot}$ | Total vertical wheel load on the rail |
| $Q_{stat}$ | Static wheel load = half the static axle load, measured on straight horizontal track |
| $Q_{centr}$ | Increase in wheel load on the outer rail in curves in connection with non-compensated centrifugal force |
| $Q_{wind}$ | Force induced from cross winds, |
| $Q_{dyn}$ | Dynamic wheel load components |
| $S_{tot}$ | The entire cross section area of the superstructure |
| $T_{wave}$ | The total time for a wave return from the bottom subgrade |
| $T_{max}$ | The time for a moving load to pass by a 22m long model at a speed of 60km/h |
| V | Volume |
| $V_p$ | The velocity for the primary wave |
| $V_s$ | The velocity for the secondary wave |
| W | Vehicle weight |

$\varepsilon_{1,r}$ Resilient axial strain after unloading

$\theta$ Bulk stress

$\sigma$ Stress

$\delta_A$, $\delta_O$ Vertical displacement at points A, O

$v$ The Poisson's ratio

$\rho$ The density of the propagation medium

[M] The mass matrix of the model

[K] The stiffness matrix of the mode

# 1 Introduction

## 1.1 Background

In the UK and many other countries, the railway track system plays a significant role in transportation infrastructure. In the UK, Office of Rail and Road reported that over 1.65 billion passengers travel by train in 2014/2015 (ORR, 2015). 255 million more passenger journeys are expected to increase per year especially in between 2013 and 2018 in England and Wales (Network Rail, 2013). Moreover, 110.1 million tonnes of freight were transported in 2014/2015 (ORR, 2015). In order to guarantee a safe, comfortable and reliable rail journey as well as an efficient rail network, the whole railway track system which includes both superstructure and substructure should be maintained at a satisfactory level at all times. For this reason, the company has to spend large amounts of money on railway maintenance. Network Rail invested £1.9 billion on renewing the railway network, including 600km of track replacement, in the year 2014/2015 (Network Rail, 2015). In addition, since traditional ballasted rail track remains the mainstay of most new and upgraded railways, maintenance costs are unlikely to reduce sharply.

To ensure the safety and an acceptable ride quality and comfort level, railway tracks require a specific standard of alignment. In ballasted rail trackbed, the mechanical characteristics of the granular material substructure, which in general consists of a ballast layer, a subballast layer and the subgrade, are the principal factors controlling the level and alignment of the track structure (Suiker et al., 2005). When track

irregularities exceed permissible limits, either traffic speed restrictions or maintenance have to be applied (Selig and Waters, 1994).

Although ballast usually offers a strong and hard layer in the railway substructure and consists of hard angular particles, gradual but continuing degradation occurs under long term repeated traffic loading. As a result, railway track settlement and differential settlement increases steadily. Furthermore, particle degradation can also accelerate ballast fouling. The fine particles are either from subgrade clay pumping or ballast degradation. The fine particles can also fill the void between large ballast aggregates so that the drainage characteristics of ballast will be reduced. Fouling of ballast usually causes the rate of settlement to increase and what is more, differential track settlement might occur. In serious cases, fouled ballast needs to be replaced or cleaned in order to achieve the desired stiffness, bearing capacity, track alignment, passenger comfort and safety.

Vertical settlement is the main issue especially when it occurs non-uniformly over a short length of track (Selig and Waters, 1994). Prediction of differential settlement is therefore meaningful and valuable in order to improve rail track understanding. But the key point is the current relatively poor understanding about ballasted trackbed behaviour and lack of a realistic constitutive railway system model that includes plastic strain under long term dynamic loading. The development of a proper scientific understanding of the effect of dynamic loading, i.e. the deformation response, stress distribution and granular material interaction properties, would allow the optimisation of the performance of the railway system, extend rail trackbed life and reduce the maintenance costs related to the substructure.

This research will concentrate chiefly on deflection and stress within ballast under the load. The flowchart shown in Figure 1.1 describes the progress of the research and the path taken to meet the final aim. The finite element package ABAQUS/Standard version 6.10-2 will be the principal computational tool used throughout this project.

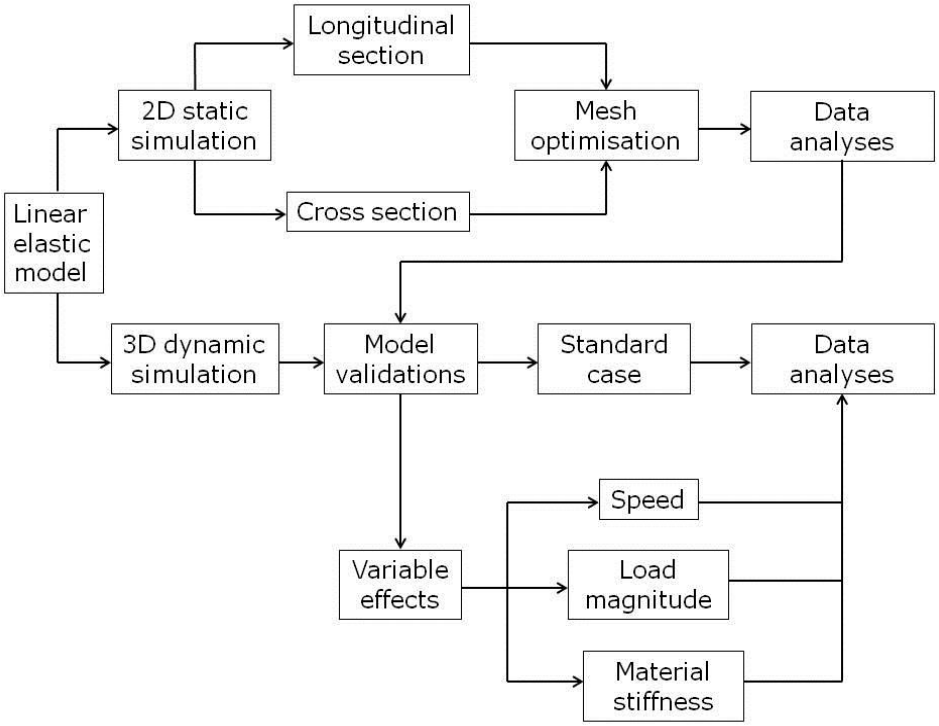



Figure 1.1 Simulation project flowchart

## 1.2 Aim and Objectives

The aim of this research was to develop an understanding of the performance of railway trackbed under realistic traffic loading through a simulation model using the Finite Element Method (FEM). The goal of the research was to investigate the stress and displacement characteristics within ballast which may be further used for predicting the long term behaviour of the railway trackbed system so as to minimise maintenance costs due to ballast settlement and particle degradation and in improving the long term performance of a railway trackbed system. The specific objectives of this project are listed below:

- To develop 2D and 3D finite element models of the entire trackbed system. This includes optimisation of mesh type and density in order to reduce calculation time effectively, as well as to make the results more accurate in simulating engineering reality.
- To identify the stress and deformation behaviour of rail trackbed, especially in the ballast, in a three-dimensional simulation model under dynamic moving load.
- To evaluate the effects of different variables including moving load magnitude, loading speed and stiffness of materials on stress and deflections within ballast based on the 3D railway trackbed model through a comprehensive parametric analysis.
- To identify the impact of the analyses during the research on the prediction of the long-term performance of railway track.

## 1.3 Thesis Outline

This thesis is divided into seven chapters. A summary of the chapter contents is given below.

The first chapter briefly introduces the background and states the aim and objectives of the research.

Chapter 2 presents a literature review on the various track components' functions and maintenance. Granular material performance, which includes railway ballast specifications and deformation mechanisms, is very important for rail trackbed. Resilient and permanent deformation behaviour of granular material, introduction of fouling material and its influence on ballast behaviour are explained in the same section. The Finite Element Method (FEM) and a basic comparison for FEM and DEM are reviewed. Finally, previous research in modelling of ballasted track has also been outlined.

In Chapter 3, the commercial finite element analysis package ABAQUS/Standard Version 6.10-2 is used. Simulation work including model creation and data analysis is presented. To gain a better understanding of mesh size and to optimise the length for a 3D model, two-dimensional models in two different sections are described in which all parts of the model are simulated using linear elastic behaviour. Graphs of stress and displacement distribution under static load are presented. Comparison of vertical displacement between simulated and simplified theoretical analysis results is also described.

In order to obtain a better and more detailed understanding of stress states as well as displacements underneath sleepers in different planes, a 3D rail trackbed model has been developed and is presented in Chapter 4. Several factors including dimensions, boundary conditions and mesh details have been carefully taken into account. A series of confirmation tests and analyses have been carried out and are described in this chapter. Furthermore, an assessment of the difference in response between single and double wheel loads has also been considered.

In order to simulate and determine quantities such as stress and displacement in the out-of-plane direction of a railway system, the purpose-designed 3D dynamic finite element railway track model developed in Chapter 4 has been utilised. The details of a standard case study are illustrated in Chapter 5.

In Chapter 6, a set of analyses comparing the effects of different variables including moving load magnitude, loading speed and stiffness of materials on stress and deflections within ballast are reported.

The key results and the main findings from the simulations are summarised in Chapter 7. The limitations of this research are also identified. Lastly, final conclusions and several recommendations for further study are given.

# 2 Literature Review

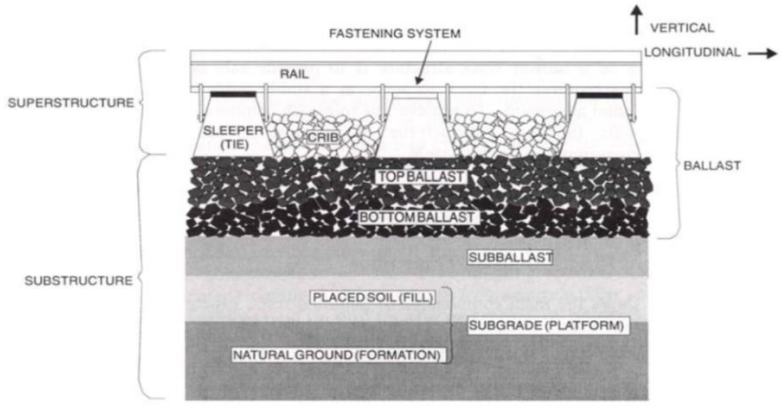
For a conventional railway track, both ballast and subballast layer are important components. One of their main roles is to prevent the transmission of damaging stress changes to the underlying natural ground or subgrade (Yang *et al*., 2009). However, due to lack of understanding about ballast behaviour under dynamic loading, especially regarding ballast degradation and plastic deformation, frequent remedial actions and expensive maintenance are required. In this chapter, current research concerning railway ballast behaviour is reviewed. This literature review also aims to illustrate all the background information required for Finite Element method (FEM) analysis and railway trackbed modelling in this research. Three main sections are included: track components, granular materials and finite element analysis.

## 2.1 Track Components

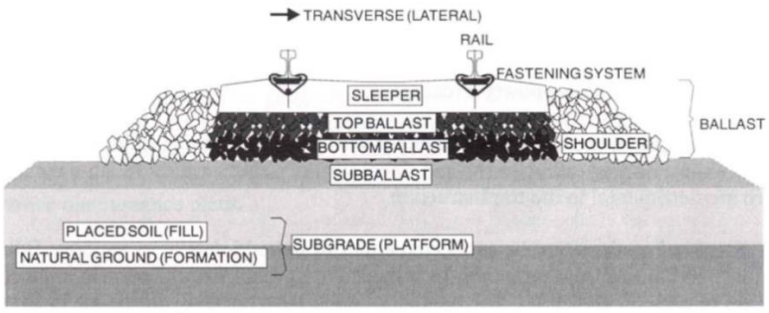
A rail track structure is designed to provide a safe and economical train transportation system for both passenger and heavy haul traffic. This requires a stable track with high quality vertical and horizontal alignment. To achieve this standard all the components of the system must satisfy their own specific functions. This section will describe the components of a conventional ballasted railway system as well as their functions. Loading characteristics and loading speed will be discussed afterwards.

### 2.1.1 Description of Components and Functions

A traditional ballasted railway trackbed includes two parts: superstructure and substructure, which can be seen in Figure 2.1. The superstructure consists of rail, fastening system, rail pads and sleepers (ties). The substructure includes ballast, subballast and subgrade. The wheel loads will be transmitted from the superstructure to the substructure via the sleeper-ballast interface when a train passes over the rails.




(a)




(b)

Figure 2.1 Structure overview of railway trackbed, (a) longitudinal view, and (b) cross section view (Selig and Waters, 1994)

The rail form an important part of the track system. They are longitudinal steel members that directly guide and support the train evenly and continuously. They must have sufficient stiffness to serve as a rigid beam so that they can transfer the concentrated wheel loads to the spaced sleeper supports with relatively little deflection. The profile of the rail surface must be coupled well with the profile of wheels since it influences the guidance of vehicles when they move fast. Any defect on either rails or wheel surface might be detrimental to the railway track structure. Two rail connection methods are adopted currently; one is bolted joints and the other is by welding. Joint and welds have been one of the major locations of maintenance problems, especially for bolted joints.

The fastening system provides the connection to fix rails onto sleepers. Many variations are utilised which depend on the different types of sleeper and the geometries of the rail. The function of the fastening system is to resist the movement of the rail in relation to the sleepers. With more and more rail lines adopting concrete sleepers, rail pads are set at the interface between sleepers and rails. They can effectively absorb some of the energy generated by the vehicle movement.

Nowadays, sleepers are most commonly made of reinforced concrete or timber and they have several functions. One is to restrain rail movement and maintain track gauge by anchoring the superstructure into the substructure. Another role is to provide an even, flat foundation for the rails and to support the fastening system. Finally, sleepers receive the load and distribute it to the wider ballast layer, decreasing the stress to an appropriate ballast pressure level.

Railway ballast comprises coarse granular material and is placed at the top of the substructure into which the sleepers are embedded. Conventionally, good ballast materials are composed of angular, crushed, hard rock, uniformly graded, free of dust, and dirt, and not prone to cementing action (Selig and Waters, 1994). There is no universal standard concerning the specification for ballast index characteristics such as particle size, shape, gradation, surface roughness and material density etc. Ballast is a material with high bearing capacity so that the railway foundation can support the superstructure reliably. In reality, ballast performs many functions. One of the most important is to spread the loads of passing vehicle axles to underlying layers. It can absorb energy and it provides a certain amount of resilience for the railway track. Furthermore, ballast can resist vertical, lateral and longitudinal forces applied to sleepers and retain railway trackbed components in their required position. Material sources of ballast vary with different area in substructure. Further study of ballast materials will be discussed in section 2.2.

Subballast is located between ballast and subgrade. Generally, subballast is a well-graded crushed natural aggregate or slag, or processed sand and gravel mixture. This layer reduces and continues distributing traffic induced stress from the bottom of the ballast. In addition, it plays the role of a barrier to prevent fine material migrating from the subgrade into the ballast and also attrition of the subgrade by the ballast. Because of these important functions, the absence of a subballast layer can cause high maintenance costs unless these functions can be fulfilled in some other manner.

The subgrade is the lowermost construction platform and ideally forms a stable foundation for the ballast and subballast layers. The influence of vehicle induced stresses extends downwards as much as five meters below the bottom of the sleepers (Selig and Waters, 1994). Nevertheless the subgrade can become a further source of rail differential settlement. Often subgrade is divided into two parts: placed soil and natural ground underneath. Existing ground will not be removed wherever possible, unless either the soil formation is not adequate or the trackbed is to be constructed in cut.

### 2.1.2 Track Forces

It is necessary to have a thorough understanding of the type and magnitude of forces that are imposed on a railway system during its operation so that the designed railway trackbed structure is adequate for its purpose. Normally these forces are transmitted by sleepers onto the substructure through wheel-rail-sleeper interactions. Forces are exerted in the vertical, lateral and longitudinal directions and the vertical load, which includes both static load and dynamic load, is the largest. The static vertical load is generated by the vehicle mass plus the dead weight of the railway trackbed components, while the dynamic vertical load is a function of rail vehicle movement, track characteristics and environmental conditions. Dynamic effects, for example ‘bounce’ or wheel forces induced by rail corrugations and joints, can produce large vibrations and impacts. Equation 2.1 (Esveld, 2001) describes the different traffic forces present:

$$Q_{tot} = Q_{quasi\text{-}static} + Q_{dyn} \qquad \text{Equation 2.1(a)}$$

$$Q_{quasi\text{-}static} = Q_{stat} + Q_{centr} + Q_{wind} \qquad \text{Equation 2.1(b)}$$

where:

$Q_{tot}$ : total vertical wheel load on the rail

$Q_{stat}$ : static wheel load = half the static axle load, measured on straight horizontal track,

$Q_{centr}$: increase in wheel load on the outer rail in curves in connection with non-compensated centrifugal force,

$Q_{wind}$: force induced from cross winds,

$Q_{dyn}$ : dynamic wheel load components.

According to Selig and Waters (1994), the vertical wheel force can be considered as follows:

$$F = W/n + k \qquad \text{Equation 2.2}$$

in which,

W: vehicle weight,

n : the number of wheels,

k : dynamic variation ranging from 53kN for light rail to 174kN for heavy haul trains.

The dynamic component is clearly the most complicated and uncertain component of the total wheel load. In detail, the speed of the train, vehicle unsprung mass, static load, wheel diameter, vehicle and track condition and track construction are all major factors that can affect the magnitude of dynamic load (Jeffs and Tew, 1991).

As Figure 2.2 shows, the vertical downward force at the wheel contact point causes the rail to be lifted up at a certain distance away from the wheel. Subsequently the lifted sleeper will be forced down by the advancing wheel which will cause a pumping action. Consequently, this movement causes differential deflections of the track structure and deterioration of the trackbed, and ballast settlement will occur.

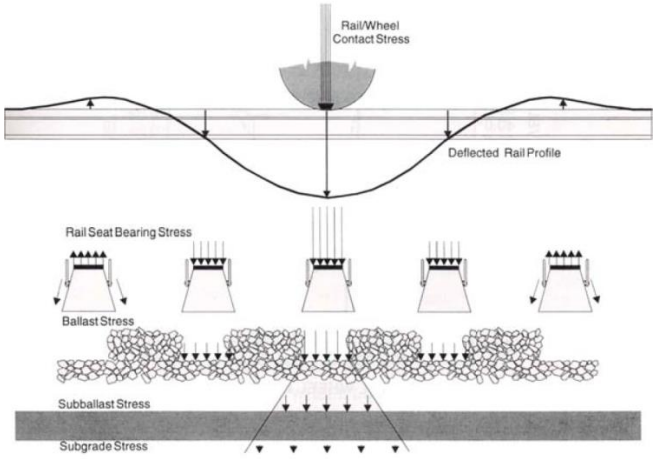



Figure 2.2 Rail deflection and load distribution into trackbed (Selig and Waters, 1994)

Besides the vertical wheel load, as mentioned at the beginning of this section, lateral and longitudinal forces also occur. These are more difficult to predict and measure than the vertical forces. Lateral forces are those forces from lateral wheel motion and buckling reaction and are parallel to the long axis of the railway trackbed cross-section. Longitudinal forces are those forces which are parallel to the rails. They are from: locomotive traction force, braking force, thermal expansion and contraction of rails and rail wave action (Selig and Waters, 1994).

Tamping during maintenance work inducing stresses onto ballast stones is another source of ballast stress. High impact and compression forces cause significant

deterioration to the ballast. Despite this, it is still a commonly used maintenance technique around the world at present.

## 2.2 Ballast

Trackbed deformation, especially non-uniform settlement in the ballast layer, is seen as a significant issue when it occurs over a short distance. Typically over a half of total deformation in a railway trackbed is generated from the ballast layer (Gaskin and Raymond, 1976). Ballast for railway foundations is a granular material which is mainly produced by crushing rock and it has many functions. The most important are to retain track geometry, absorb the sleeper bearing pressure to protect underlying materials, provide drainage for liquid falling onto the superstructure, allow repositioning of the track structure during maintenance work, and store ballast fouling materials (Lim, 2004). Hence ballast is required to be hard, durable, angular, and have large voids between stones. Six aspects of ballast will be discussed individually: ballast specifications, ballast deformation mode, resilient behaviour of granular material, permanent deformation behaviour of granular material, fouling material and its influence on trackbed behaviour.

### 2.2.1 Ballast Specifications

In the UK, selection of ballast materials is based on Railtrack Line Specification (RT/CE/S/006 Issue 3, 2000). Grading, properties, shape of ballast particles are specified in this specification that should ideally satisfy high stiffness, high strength, chemical resistance, and be free from dust and dirt. Ballast with high stiffness can

reduce stress to underlying components, resist track deflection during train passage as well as decrease the bending stress in the rails. High strength will reduce the cumulative deformation under repeated dynamic vehicle loads. It can also impart stability to the track. In addition, ideal ballast should not be impacted by dust, dirt, frost, rain or other mechanical contaminations.

The particle strength is one of the most important factors which can govern ballast degradation, settlement and lateral deformation of the railway trackbed (Salim, 2004). Shi (2009) indicates that the ballast assembly will re-orientate after an individual particle fractures due to over stress and this process will not stop until the breakage is complete.

The mechanical behaviour of ballast stones is influenced by the particle sizes. The peak angle of friction reduces when the confining pressure increases which is less than 300kPa; however, the effect of grain size on friction angle can be ignored when the stress is higher than 400kPa (Indraratna *et al.*, 1998). The ideal particle size range is recommended at around 10-50mm, with only a few stones outside this range (Selig, 1984). Use of a mixture of particle sizes can not only stabilise the railway track structure but also reduce the interactions between stones. Following the European specification (BS EN 13450, 2002), new particle size distributions have been adopted by Network Rail since April, 2005 (see Table 2.1). It can be seen that the size distribution of ballast particles are mainly between 32mm to 50mm.

Table 2.1 The specification for ballast particle size distributions in the UK (RT/CE/S/006 Issue 3, 2000)

| Square Mesh Sieve (mm) | Cumulative % by weight passing BS sieve |
|---|---|
| 22.4 | 0-3 |
| 31.5 | 0-25 |
| 40 | 30-65 |
| 50 | 70-100 |
| 32-50 | 50-100 |
| 63 | 100 |

### 2.2.2 Ballast Deformation Modes

Frictional slip and particle breakage are proposed as two significant modes that cause granular material to be deformed (Selig and Waters, 1994). Either of these deformation modes can happen anywhere in the ballast layer during train passage. They are closely related to each other so that the internal formation of the ballast is continuously changing. Slip is defined as the relative movement between particles in contact under dynamic wheel loads (Liao *et al*., 1995). The main type of damage that accompanies long term slip is ballast abrasion, which means that small fragments are broken off from the stone surface. If the slip is not too great, then the particle may return to its original place after unloading; otherwise the particle may never find its way back and hence, deformation has occurred.

When abrasion occurs heavily in a ballast layer, irreversible deformation caused by vehicle loads will happen (Thom, 2009). Breakage may be avoided if the stress is

relatively low compared to the ballast particle strength. Generally, particle breakage will become more heavily combine with an increasing applied microscopic stress, aggregate size and reduction in numbers of contact with neighbouring particles (McDowell *et al*., 1996). Nevertheless, the deformation mechanism of aggregates in a ballast layer in reality is not fully understood and there would be still a need to study further in the future.

### 2.2.3 Resilient Behaviour of Granular Material

Types of deformation in railway tracked under repeated cyclic loads include both permanent deformation and recoverable resilient deformation, which will be discussed in this section and the next separately. As illustrated in Figure 2.3, when peak stress is exerted on a rail trackbed the maximum strain is obtained and, after unloading, the part which is recoverable is termed ‘resilient’ strain.

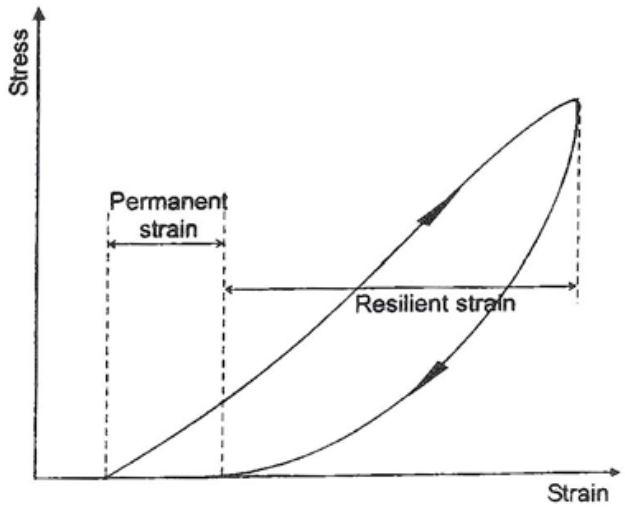



Figure 2.3 Strains in granular materials during one cycle of load application (Wright, 1983)

According to Seed *et al*. (1962), the resilient modulus of a material can be calculated as the repeated deviator stress divided by the recoverable axial strain during unloading in the triaxial test, as in equation 2.3. Resilient behaviour of the railway trackbed is important in that the resilient behaviour of the subgrade can affect the degradation and rate of settlement of the ballast (Raymond and Bathurst, 1987).

$$M_r = q/\varepsilon_{1,r} \qquad \text{Equation 2.3}$$

where,

Mr: resilient modulus,

q: transient deviator stress = $\sigma'1 - \sigma'3$,

$\varepsilon$1,r : resilient axial strain after unloading.

The resilient modulus initially increases gradually resilient strain reduces with the number of repeated loads. The change of the resilient modulus under repeated cyclic load applications in the triaxial test is illustrated in Figure 2.4.

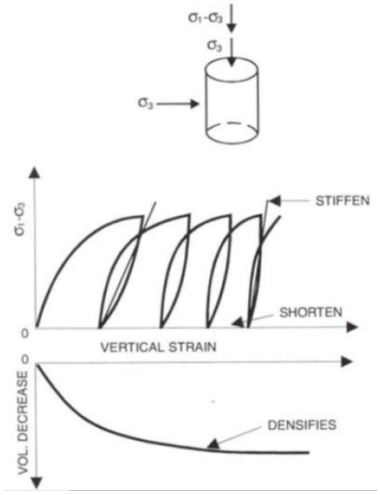



Figure 2.4 Ballast behaviour in the cyclic triaxial test (Selig and Waters, 1994)

There are many factors that can affect the resilient modulus, including: stress state, density, moisture content, grading, stress history, loading cycle numbers and sequence, aggregate type and particle geometry. However, the effect of moisture is negligible when the degree of saturation is low. In contrast, resilient modulus will decrease significantly for high degrees of saturation (Lekarp *et al*., 2000a). The effect of stress, including stress state, sequence history and numbers of cyclic loads, on the resilient modulus is seen as the major factor. The predominant factor affecting resilient modulus is the bulk stress which is included in the widely used K-$\theta$ model as shown in equation 2.4 (Hicks and Monismith, 1971). Figure 2.5 illustrates repeated load triaxial test results on crushed granite ballast which can be interpreted by equation 2.4.

$$M_r = k_1\theta^{k2} \qquad \text{Equation 2.4}$$

where,

$\theta$: bulk stress

$k_1$,$k_2$: constants

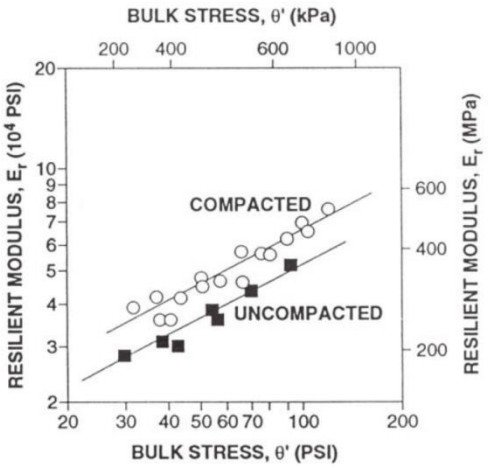



Figure 2.5 Relationship between resilient modulus and bulk stress (Alva-Hurtado, 1980)

Besides the influences discussed above, the type of aggregate can also significantly affect the resilient response. A cyclic loading test with six different materials including three limestones, a sandstone, a granite and a rhyolite showed the resilient modulus for the various materials differing by 20-50% (Zaman *et al*., 1994). Commonly, a ballast layer that consists of crushed aggregate combining both angular and subangular shaped particles can provide a better resilient behaviour and load spreading properties than a material with subrounded on rounded stones (Thom and Brown, 1988).

### 2.2.4 Permanent Deformation Behaviour of Granular Material

As defined in Figure 2.3, permanent strain of granular material is induced by repeated loading and is the irrecoverable strain after unloading. This may be affected by several factors: stress level, sequence of loading, number of repeated load applications, initial density, principal stress rotation and loading frequency.

Stress level plays an important role in affecting the permanent strain. The permanent strain of ballast is a function of both the confining pressure and the deviator stress (Selig and Waters, 1994). Permanent strain accumulated after a certain number of repeated loads has been shown to be directly related to the deviator stress q to confining stress $\sigma_3$ ratio (Knutson, 1976). However, the conventional ratio used is $\frac{q}{p'}$, where p' is the mean effective stress. The permanent strain after a certain number of traffic loads increases with increasing stress ratio, as shown in Figure 2.6. The results in this figure are from triaxial tests on limestone ballast (Knutson, 1976). It is clear that the effect of the cyclic deviator stress and confining pressure on permanent strain is quite significant. A higher deviator stress (while the confining stress is held constant) leads to a higher plastic strain (i.e. 30/5 and 20/5); with decreasing confining pressure, the permanent strain also increases (i.e. 30/5 and 30/15).

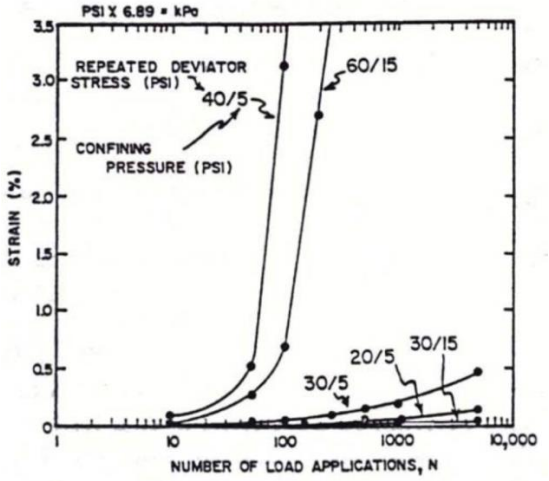



Figure 2.6 Permanent strain affected by stress ratio (Knutson, 1976)

According to Selig and Waters (1994), permanent strain accumulation is not a function of the sequence of loading. A typical result of permanent strain accumulation tests showing the effect of different loading sequences is illustrated in Figure 2.7. During these tests, the deviator stress was varied after every 1000 load applications and clearly, the final permanent vertical strains are approximately equal irrespective of the different loading sequences changes.

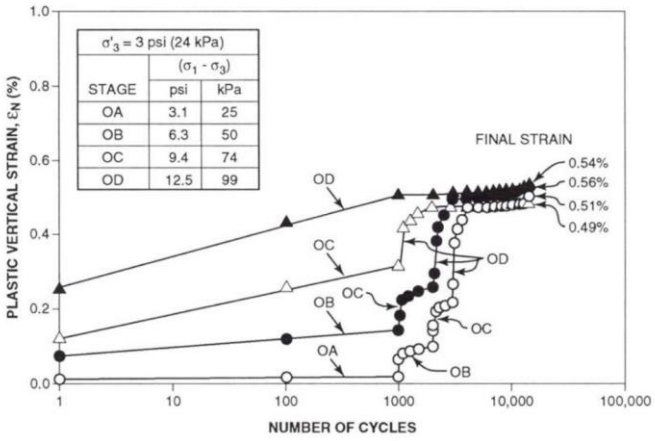



Figure 2.7 Effect of difference in sequence of loading on permanent strain (Selig and Waters, 1994)

It is universally accepted that permanent deformation in granular material under repeated vehicle loading is related to the number of repeated load applications, and the degree of permanent deformation caused by a given number of cyclic loads needs to be taken into account. Generally the permanent deformation of a railway trackbed can be assigned into two stages: the first stage is the initial compression where the grains are compacted to a high density and immediate settlement occurs as a consequence; during the second stage, the deformation is slower and the relationship between number of load applications and settlement tends to be linear (Ionescu *et al*., 1998). As illustrated in Figure 2.8, the track settlement increases

immediately with an increasing number of load applications (Shenton, 1975). After a certain number of load applications, the deformation increase rate tends to be zero and the permanent vertical strain will no longer increase. Nevertheless, this behaviour can only occur when the stresses are relatively low (Lekarp and Dawson, 1998). In other words, permanent strain will continue increasing if higher stresses are applied.

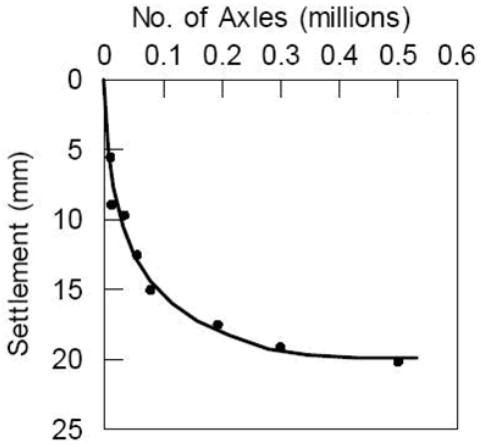



Figure 2.8 Contribution of number of cyclic loads on settlement (Shenton, 1975)

The initial density is defined by the degree of aggregate compaction and many researchers find that it has a significant effect on the accumulation of plastic strain. The lowest density might lead to the highest permanent strain after a certain number of cyclic loads (Knutson, 1976). A small decrease in initial density will increase the permanent strain accumulated significantly; what is more, the effect with angular aggregates is more serious than with rounded aggregates (Lekarp *et al.*, 2000b).

As indicated in Figure 2.9, principal stress rotation occurs in granular materials when a moving load passes over a pavement or railway element in the longitudinal plane

as well as in the transverse plane (Powrie, 2007). Principal stress is rotated during a vehicle passage and it causes the accumulation of permanent strain (Lekarp *et al*., 2000b). However, there is little principal stress rotation for ballast near the sleepers because load within this area is transferred as a concentrated load, and the principal stress will increase rapidly when the wheel load approaches and reduce sharply as the vehicle moves away (Lim, 2004). According to Lim (2004), it is often assumed that approximately half of the load is transferred to the sleeper directly beneath an axle and around 25% of a given wheel load is transferred to each of the adjacent sleepers. The extent of the substructure which experiences principal stress rotation is mainly a function of the stiffness of the ballast and its lower layer. A stiff ballast layer can experience stress spreading at a closer level to the sleeper-ballast interface and those with relatively low stiffness will only be subjected to principal stress rotation effects in the subgrade.

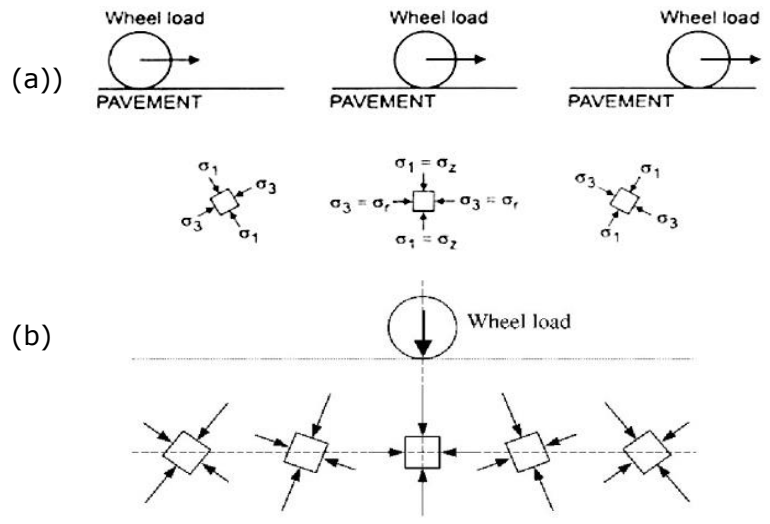



Figure 2.9 Stresses on pavement elements: (a) Stress beneath rolling wheel load; (b) principal stresses and planes (Brown, 1996)

Commonly, the loading frequency does not significantly influence the accumulation of permanent deformation (Shenton, 1975). Figure 2.10 shows the result of a series of cyclic loading tests with different loading frequencies from 0.1 to 30Hz, while maintaining other characteristics (deviator and confining stress) constant. It is clear that there is no significant effect on permanent strain when changing the loading frequency. Nevertheless, the settlement can still be significantly affected by high train speed due to the dynamic forces (Eisenmann *et al*., 1994). The in-situ measurement of dynamic forces in the railway trackbed has a positive relationship with train speed (Kempfert and Hu, 1999).

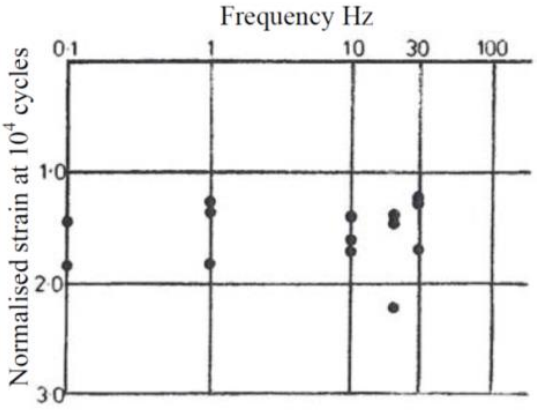



Figure 2.10 Influence of loading frequency on permanent strain (Shenton, 1975)

### 2.2.5 Fouling Material and its Influence on Trackbed Behaviour

A study by the University of Massachusetts for identification of sources of fouling materials shows that ballast breakdown is the main source of fouling material, as shown in Figure 2.11 (Selig and Waters, 1994). The ballast for a new train line has to some extent broken down already because of the transportation and compaction. During its service life, grain breakdown will continue due to repeated traffic load,

maintenance work and weathering effects. One investigation found that around 2-4 kg of fines (diameter less than 14mm) were generated per tamp for one sleeper (Wright, 1983). The tamping tines compress the ballast into the void underneath the repositioned sleeper and an immediate effect on ballast breakage will occur. Furthermore, the influence of tamping will last for some time since the ballast will be loosened and the grains have to be rearranged. Thus, the new contact points can then be fractured under cyclic vehicle loads (Lim, 2004).

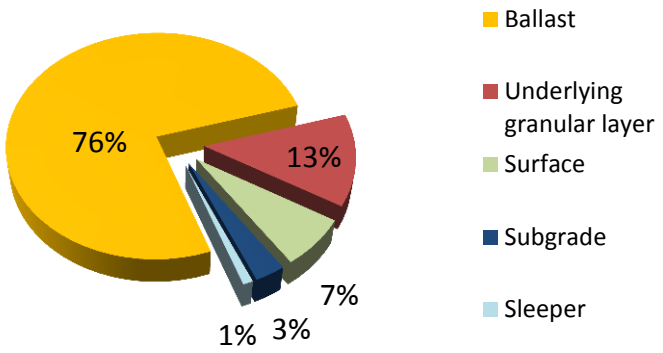



Figure 2.11 Sources of ballast fouling (Selig and Waters, 1994)

Ballast fouling from underlying layers will tend to increase in the presence of water because of the pumping action of traffic. Water can pump the clay slurry which forms at the top of the subgrade up into the ballast. Permeability of ballast will then reduce due to the increase of fouling material. According to Lim (2004), the main source of surface infiltration is wagon spillage and sleeper wear when using either wood or concrete as the material for sleepers.

Different types and degrees of fouling materials have different influences on ballast behaviour. The results from a box test conducted to investigate the effect of various

fouling materials on trackbed settlement are shown in Figure 2.12. It can be seen that the settlement of fouled ballast samples increased with increasing degree of fouling (Han and Selig, 1997).

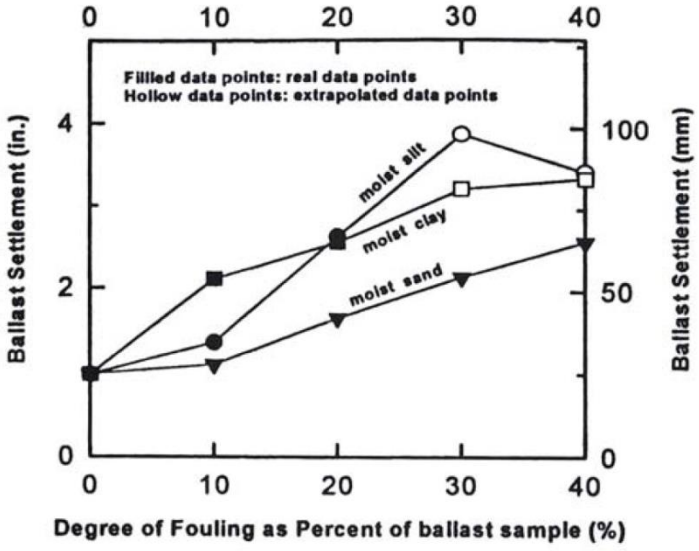



Figure 2.12 Effect of various degrees and types of the fouling materials on ballast settlement (Han and Selig, 1997)

The results of further tests conducted to analyse the effect of water content on ballast settlement are displayed in Figure 2.13. The dry clay in these tests shows the least settlement because of its relatively high strength and stiffness. After saturating with water, the settlement increases with increasing degree of fouling. The same explanation is also suited to wet silt in these tests in which settlement becomes higher at over 30% (Han and Selig, 1997). It is noteworthy that there is relatively small change in ballast settlement no matter what type of fouling material or water content in tests where the fouling degree is less than 20%. Han and Selig (1997) propose that this may be because within this fouling degree, most of the load from traffic is carried by the ballast stones as ballast particles still form the structural

skeleton. It can be inferred that drainage behaviour and ballast cleaning work are significant for the stress distribution and stability of the trackbed structure.

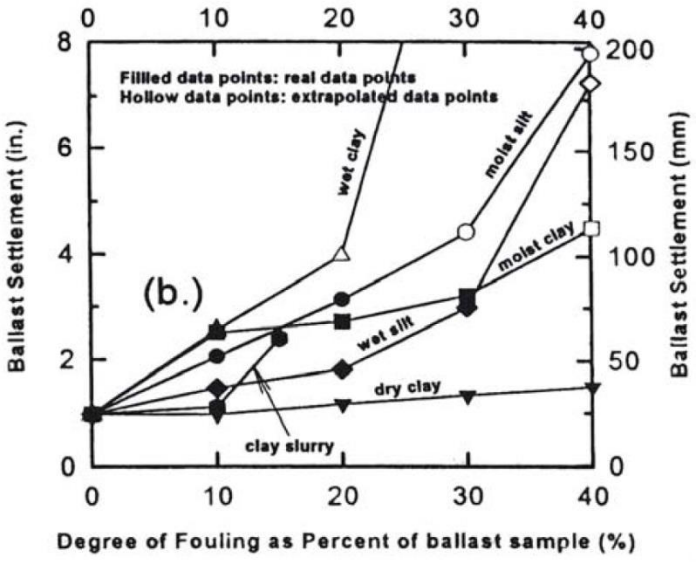



Figure 2.13 Effect of water content on ballast settlement with different degree and type of fouling materials (Han and Selig, 1997)

## 2.3 Finite Element Method

The Finite element method (FEM) and discrete element method (DEM) are two commonly applied methods used in engineering simulation work. The ballast layer in railway trackbed consists of large quantities of distinct particles and interaction will happen between every two contacting stones. This sort of complex behaviour is not satisfactorily understood yet. However, DEM can be used to simulate a wide variety of granular flow and stone mechanics situations. Also, it allows a more detailed study of the micro-dynamics of granular flow and such information is hard to achieve from experimental work or FEM simulation. Many researchers (e.g. Cheng *et al.* 2004; Lim and McDowell 2005) have been focusing on the study of particle breakage using

DEM. Due to the limitations of circular particle shape, Hossain *et al.* (2007) stated a further step that highly angular fresh ballast particles normally cause an increase in settlement and track degradation. This lead to a DEM approach on researching the influence of angular ballast breakage on ballast based trackbed. Huang and Chrismer (2013) employed a DEM approach to simulate the ballast deterioration under cyclic load. Due to the limitation of computing time, only a partial trackbed with the dimension of 1.5x1x0.5m under three adjacent sleepers was applied.

Although DEM can offer a more detailed simulation analysis especially for multiple interacting bodies undergoing large dynamic movements, the duration of the simulation work is limited by computational power. In general, the flow behaviour and micro mechanics between particles are computed depending on numerous individual stone contacts in a virtual simulation. In other words, it is much more time consuming than FEM analysis.

FEM analysis is very suited to practical engineering to solve problems including solid and fluid mechanics, heat transfer and vibrations. In a FEM simulated model, a finite quantity of small elements will be generated within the system being modelled and the behaviour of each element is related to the behaviour of nodes at every element. For example, in a solid mechanics problem, the displacement of one specific element depends on the nodal displacements, which connect two adjacent elements. Meanwhile, the nodal displacement is directly related to the stress and strain in the elements. Once the equations of equilibrium between stresses and loads applied are solved, then the stresses and strains can be known in all the elements.

Although there are many benefits of using FEM simulation, there are also some risks and disadvantages. In FEM analysis, data input is critical; incorrect data input can directly lead to a meaningless result since the procedures are in sequence and every step is closely related to the next. In particular, most researchers (e.g. Lundqvist and Dahlberg, 2005; Wang *et al.*, 2005; Yang *et al.,* 2009) nowadays simulate actual railway engineering problems using FEM based on a linear elastic assumption. Under this condition, each layer of the railway trackbed is characterised by Young's modulus, Poisson's ratio and density. Moreover, an appropriate quantity of elements with acceptable shape as well as proper boundary conditions is essential for meaningful FEM analysis. Bad element shapes or too few elements might cause data inaccuracy and errors in translating real-life boundary conditions into FEM analysis will generally lead to incorrect results.

Considering that the main purposes of this project are exploring the effect of different variables on the stress and displacement distribution in the ballast layer as well as the sleeper rotation, since the DEM is somehow focusing on the analysis of multi interaction properties, consequently, a FEM model is more relevant to be applied in this project.

Three dimensional (3D) models are commonly developed based on several two dimensional (2D) models (Shi, 2009). Although 3D analysis has been widely used by many researchers (e.g. Wang *et al.,* 2005; Banimahd and Woodward, 2007; Powrie et al., 2007) and it can accurately consider realistic geometry, loading and boundary condition, it is more time-consuming and more complicated compared with two dimensional analysis. Hence, before undertaking a three dimensional analysis, good

experience regarding choice of element shape, how to mesh in an appropriate manner and the degrees of freedom required is necessary.

A summary of the derivation of FEM formulation used for continuum elements is presented in Figure 2.14.

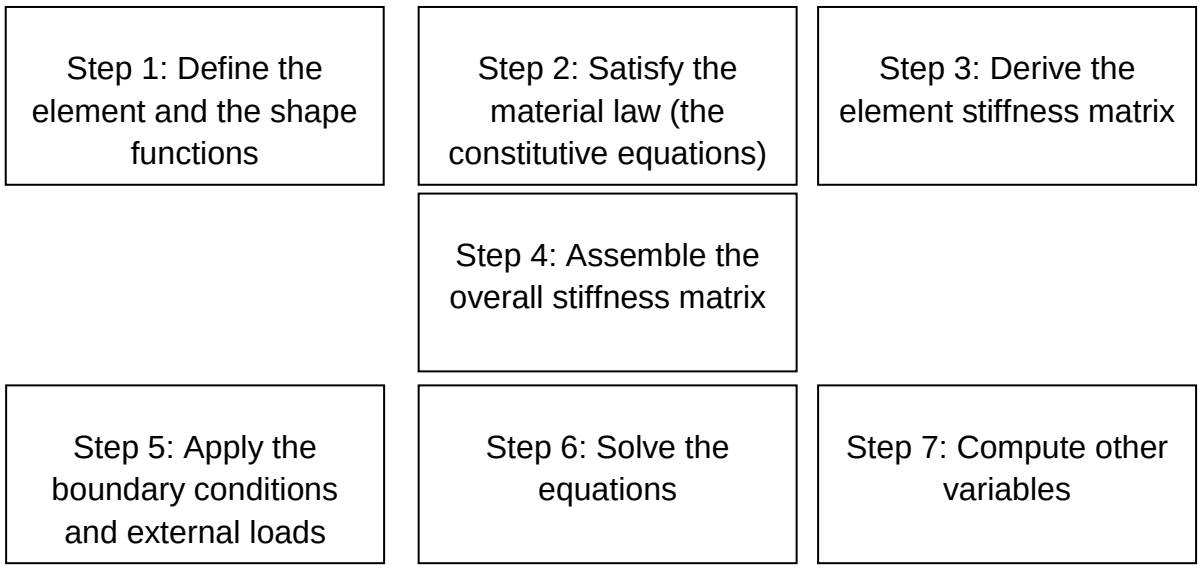


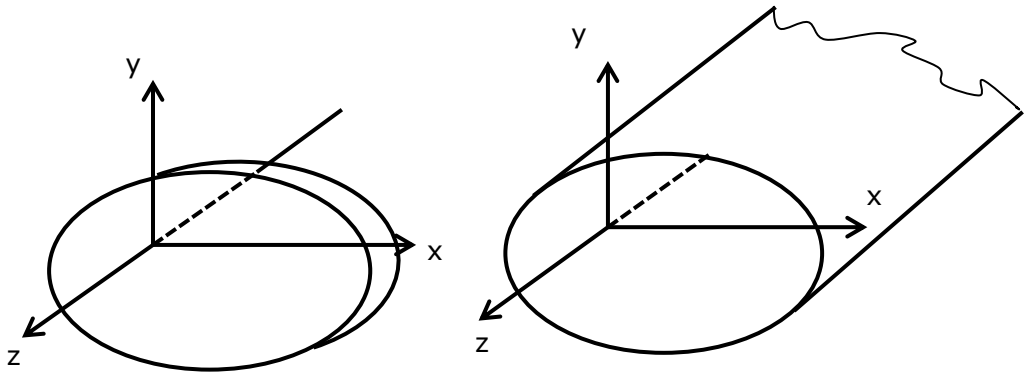

Figure 2.14 Summary of the derivation of FEM formulation

### 2.3.1 Two-dimensional Problems

In many applications it is possible to approximate a 3D problem to a simpler 2D application in which only the x-y plane is modelled. However, it should be emphasised from the outset that there is no such problem as a truly 2D one; all 2D solutions are approximations of 3D solutions, and the z-direction should not be ignored. Two alternative assumptions about the stress and thickness in the z-direction can be made, as follows:

(a) Plane stress is used to define 'thin' geometries in the z-direction where stress across the thickness is neglected (i.e. $\sigma_{zz}=0$), as shown in Figure 2.15(a).

(b) Plane strain is used to define very 'thick' geometries in the z-direction where the strain across the thickness is neglected. However, the stress in that direction is non-zero (i.e. $\varepsilon_{zz}=0$ but $\sigma_{zz}\neq 0$). In other words, the x-y section is remote from the ends where $z=\pm\infty$, as shown in Figure 2.15(b).




(a) Plane stress ($\sigma_{zz}=0$, $\varepsilon_{zz}\neq 0$)

(b) Plane strain ($\sigma_{zz}\neq 0$, $\varepsilon_{zz}=0$)

Figure 2.15 2D plane stress and plane strain problems

Before deriving the FEM formulation, the variables used in 2D formulations should be defined. In 2D continuum problems, these are displacements [u], strains [ε] and stress [σ], defined as follows:

$$[u]=\begin{bmatrix} u_x \\ u_y \end{bmatrix};[\varepsilon]=\begin{bmatrix} \varepsilon_{xx} \\ \varepsilon_{yy} \\ \varepsilon_{xy} \end{bmatrix};[\sigma]=\begin{bmatrix} \sigma_{xx} \\ \sigma_{yy} \\ \sigma_{xy} \end{bmatrix} \qquad \text{Equation 2.5}$$

### 2.3.2 Three-dimensional problems

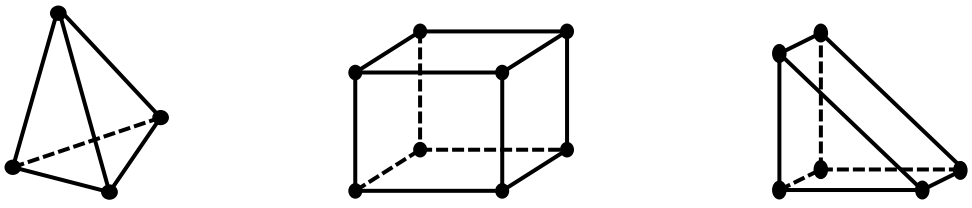
Three dimensional continuum elements can be used to model all practical engineering problems since no dimensional approximation is assumed in displaying the geometry and loads. Nevertheless, the computational cost for 3D problems is higher than that that used in 2D problems. For example, for a 2D problem with 100 nodes and 2 degrees of freedom per node, 200 equations will be generated. For a similar spread of nodes in a 3D problem (10 X 10 X 10 nodes) 3000 equations will be generated.

Typical 3D continuum elements are shown in Figure 2.16. The simplest 3D element is a 4-node constant-strain tetrahedron with a linear variation of displacement as follows:

$$u_x(x,y,z) = C_1+C_2x+C_3y+C_4z$$

$$u_y(x,y,z) = C_5+C_6x+C_7y+C_8z \qquad \text{Equation 2.21}$$

$$u_z(x,y,z) = C_9+C_{10}x+C_{11}y+C_{12}z$$



(a) (b) (c)

Figure 2.16 Three dimensional continuum element of (a) 4-node tetrahedron element (b) 8-node hexahedron element (c) 6-node wedge element

Deviation of the 3D formulation has the same steps as for other elements, with the same matrix notation, except that the 3D matrices are larger than the corresponding 2D matrices. The material law for 3D problems can be rearranged such that the stresses are on the left hand side, resulting in Hooke's law for 3D stresses as follows:

$$\begin{bmatrix} \sigma_{xx} \\ \sigma_{yy} \\ \sigma_{zz} \\ \sigma_{xy} \\ \sigma_{xz} \\ \sigma_{yz} \end{bmatrix} = \frac{E}{(1-2\upsilon)(1+\upsilon)} \begin{bmatrix} 1-\upsilon & \upsilon & \upsilon & 0 & 0 & 0 \\ \upsilon & 1-\upsilon & \upsilon & 0 & 0 & 0 \\ \upsilon & \upsilon & 1-\upsilon & 0 & 0 & 0 \\ 0 & 0 & 0 & \frac{(1-2\upsilon)}{2} & 0 & 0 \\ 0 & 0 & 0 & 0 & \frac{(1-2\upsilon)}{2} & 0 \\ 0 & 0 & 0 & 0 & 0 & \frac{(1-2\upsilon)}{2} \end{bmatrix} \begin{bmatrix} \varepsilon_{xx} \\ \varepsilon_{yy} \\ \varepsilon_{zz} \\ \varepsilon_{xy} \\ \varepsilon_{xz} \\ \varepsilon_{yz} \end{bmatrix} \quad \text{Equation 2.22}$$

### 2.3.3 Higher order quadratic elements

The continuum elements discussed above assume a linear approximation of the displacements over each element. As a result, each element has a constant strain and stress. In order to achieve accuracy in problems where the variables change rapidly (e.g. stress concentration at the bottom corner of a sleeper), a fine mesh with a large number of linear elements has to be utilised. To improve the approximation within each element and use a lower number of elements, higher order quadratic elements can be used. Some samples of high order quadratic elements are shown in Figure 2.17.



(a) A 20-node 3D quadratic element (b) A 8-node 2D quadratic element

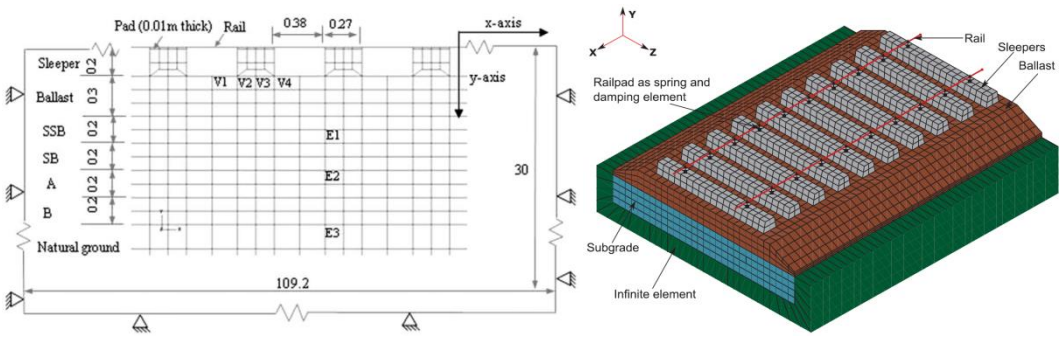
Figure 2.17 High order quadratic elements

## 2.4 Dynamic Ballasted Railway Trackbed Modelling

Ballasted trackbed is still being widely used in many high speed lines nowadays. However, due to the increasing maintenance work caused by trackbed deterioration, it is necessary to have a better understanding of ballast trackbed deterioration mechanisms and prediction of substructure deformation. Several empirical expressions (e.g. Bordin 2001; Ishida *et al.* 2002; Sato 1995; Shenton 1984) exist for predicting track permanent deformation as a function of time, speed, load, and number of cyclic loads. Furthermore, many research projects have been aiming to develop an adequate and efficient dynamic FEM model in either 2D or 3D for calculation of dynamic effects of traffic loadings on railway track settlement and stress state. The research concerns mainly consist of interaction properties between wheel and rail, ground vibration and sleeper types, etc.

As the train speed becomes much higher and reaches 300km/h or more, the accuracy of vehicle rail contact analysis has become one of the most important factors for dynamic simulations. Nguyen *et al.* (2012) stated that railway trackbed dynamic behaviour is generally induced by not only the interaction between the wheel and rail, but also by the train dynamic configuration. Some 2D FEM interaction

models with one or more bogies were carried out, these models were based on rigid bodies and connected by discrete supports (e.g. Knothe and Grassie 1993; Zhai and Cai 1997; Lei and Noda 2002; Yang 2009). Furthermore, to investigate both vertical and lateral dynamic responses of the wheel-rail system and to reach a more realistic situation, other detailed simulations have used a 3D FEM model (e.g. Popp *et al.* 2003; Sun *et al.* 2003; Zhai *et al.* 2009). Typical 2D and 3D layered ballasted trackbed finite element models are illustrated in Figure 2.18. Meanwhile, because of the contact nonlinearities between different layers in the trackbed system, calculation difficulties and additional computing time should be expected.




(a) (b)

Figure 2.18 Overview of (a) 2D ballasted trackbed (Yang *et al.* 2009) and (b) 3D ballasted trackbed (Nguyen 2012)

In general, the rail is modelled based on either Euler or Timoshenko beam formulation on a linear elastic foundation including fastening system, discrete supported sleepers, ballast, subballast and natural ground. To achieve an accurate result of interaction analysis, modelling of vehicles was figured out. In finite element analysis, car bodies, bogies and wheelsets are considered as rigid bodies and linear spring dashpot elements are used to connect with the car body and two bogies,

bogies and wheelsets separately which have been shown in Figure 2.19 (Nguyen *et al.* 2012).

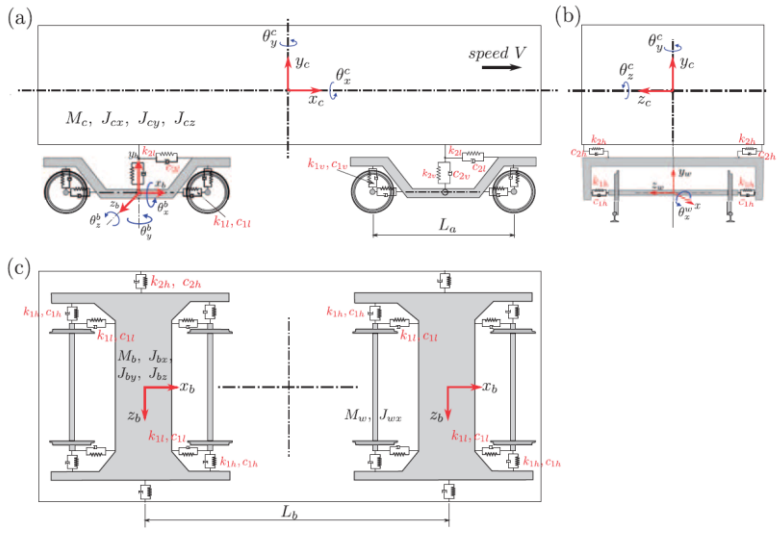



Figure 2.19 3D vehicle of (a) lateral view (b) front view and (c) top view

A comparison of 2D and 3D dynamic model results including contact forces and forces transmitted from train to infrastructure under passing wheel load was made. It has been clearly shown that the dynamic response differences cannot be avoided, and the lateral dynamic response of a cross section has to be neglected under a 2D simulation (Nguyen *et al.* 2012).

A combination of both FE and DE was utilised and a finite element modelling of ballast aggregate was presented by Aikawa (2015) to investigate the ballast behaviour under an impact load and illustrate the ballast layer stress distribution. As shown in Figure 2.20, about 4000 grains were firstly measured and digitised based on the measured numerical data, and then converted into finite element meshes.

1cm size of mesh was adopted and this was assumed to be sufficient to produce stress distribution sufficiently correctly.

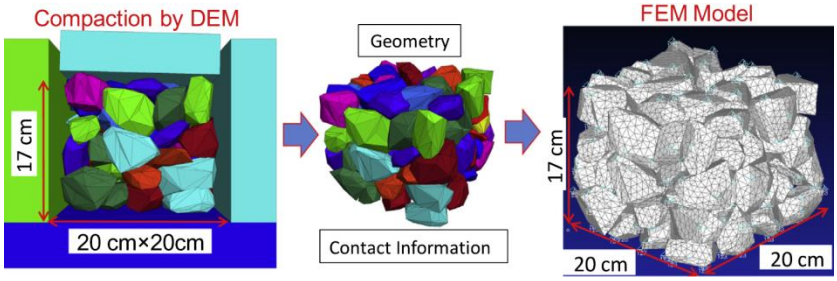



Figure 2.20 Creation of ballast aggregates FE model (Aikawa, 2015)

The impact load and the Von Mises stress distribution are illustrated in Figure 2.21. Apparently, this can give a clear understanding of the internal stress distribution and impact load transmission in the ballast layer. However, because of the complicated modelling process, the FE model size has to be strictly limited and accordingly massive computing time will be required.

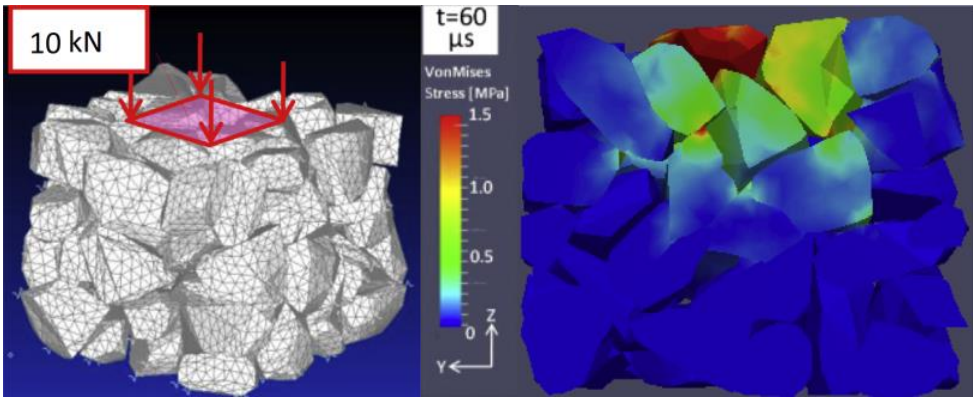



Figure 2.21 Impact load on aggregate model and Von Mises stress distribution (Aikawa, 2015)

A comparison of wheel rail contact forces obtained with single and multiple wheelset moving loads on a slab track was made by Blanco-Lorenzo *et al.* (2011). As

presented in Figure 2.22, the difference in terms of amplitude and the frequency of wheel track contact force is moderate in the time domain. Although the trackbed systems in this study and in Blanco-Lorenzo *et al.2011* are different (i.e. Blanco-Lorenzo *et al*. *2011* focused on a floating slab track whereas this study investigated the behaviour of ballasted railway systems), both studies used a single wheel set in the simulations, which was proved to provide accurate results under pure vertical dynamics (Blanco-Lorenzo *et al.2011*). Therefore, it is evident that the single wheel set is suitable for the simulations in this study. Nevertheless a further investigation of the comparative effects of single and dual loads will be carried out in Chapter 4.

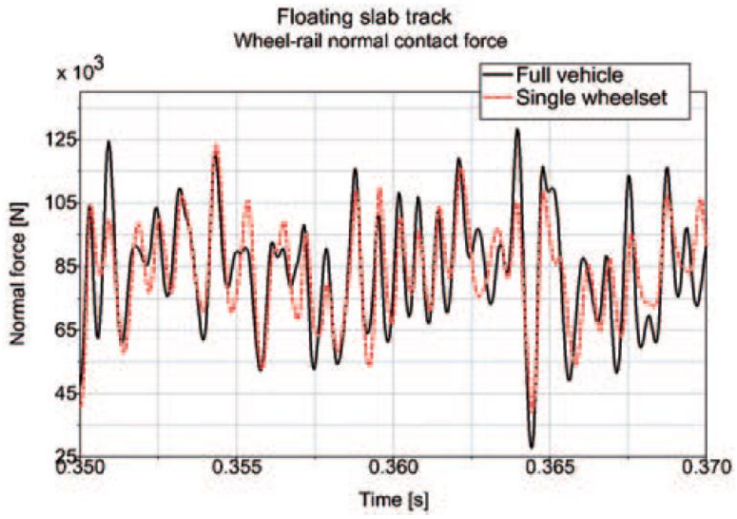



Figure 2.22 Comparison of wheel track contact force under single wheelset and multiple wheelsets moving load (Blanco-Lorenzo *et al.* 2011)

In recent decades, subgrade behaviour and the dynamic effects including train speed, acceleration/braking and geometry variation on its stability have also been widely researched. This is likely to depend on the stress history and the stress paths induced by the moving load (Yang 2009). Powrie *et al.* (2007) carried out laboratory tests to approximate the various patterns of stress change induced by passing trains.

Grabe (2002) and Grabe and Clayton (2009) indicated that when the moving train speed is slower than 240km/h on a firm subgrade, the dynamic effects could be ignored. However, when the train speed reaches the Rayleigh wave velocity of the soil ($V_c$), excessive ground movements may occur (Krylov 1995).

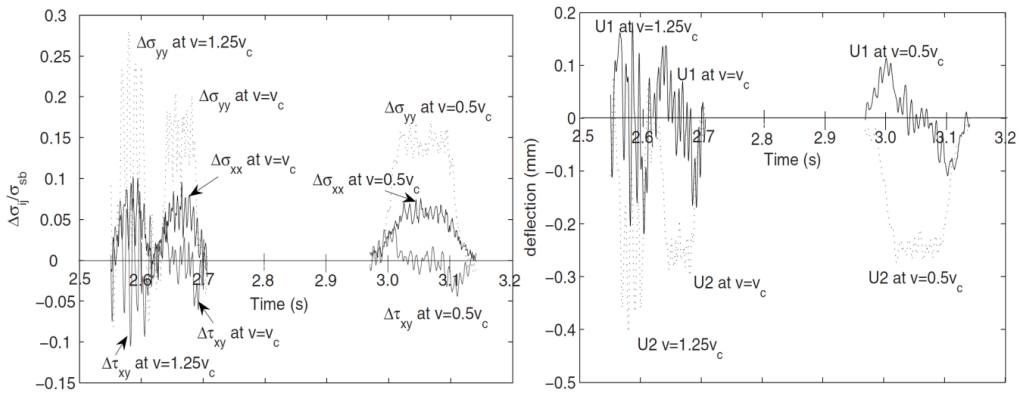
$$V_c = CV_s \qquad \text{Equation 2.23}$$

where ,

C: a constant that ranges between 0.911–0.955 (Prakash 1981)

Vs: shear wave velocity = $\sqrt{(\frac{E}{2(1+\nu)})/\rho}$

As presented in Figure 2.23, a comparison of the effect of train speed on calculated deflections and corresponding stress changes at the middle of the ground surface was made using a 2D finite element railway trackbed model with a three-wagon moving freight train by Yang *et al.* (2009). Eventually, there is a gradual increase in both maximum displacements and stresses as the train speed increases. The analysis indicated that dynamic effects increase the stresses where the shear stress is 80% larger and vertical stress is 20% larger than calculated in the static analysis by Powrie *et al.* (2007) at a train speed of $V_c$ (Yang *et al.* 2009).




(a) (b)

Figure 2.23 (a) Stresses (b) horizontal (U1) and vertical (U2) displacements on natural ground at different train speed (Yang *et al.* 2009)

A Mohr-Coulomb failure line where t=s'sinΦ with an effective frictional angle of 31° is presented in Figure 2.24 to show the stress path changes with increasing train speed (Grabe 2002). Due to the entirely linear elastic model, the line was only for illustrative purposes to make a comparison of effect of train speed on stress path. In this case, the results might not actually meet the failure criterion even if the path crossed over the line. It can clearly be seen that the stress state moved closer to the failure line with increasing train speed. This is also potentially an adverse implication in terms of soil failure (Yang *et al.* 2009).

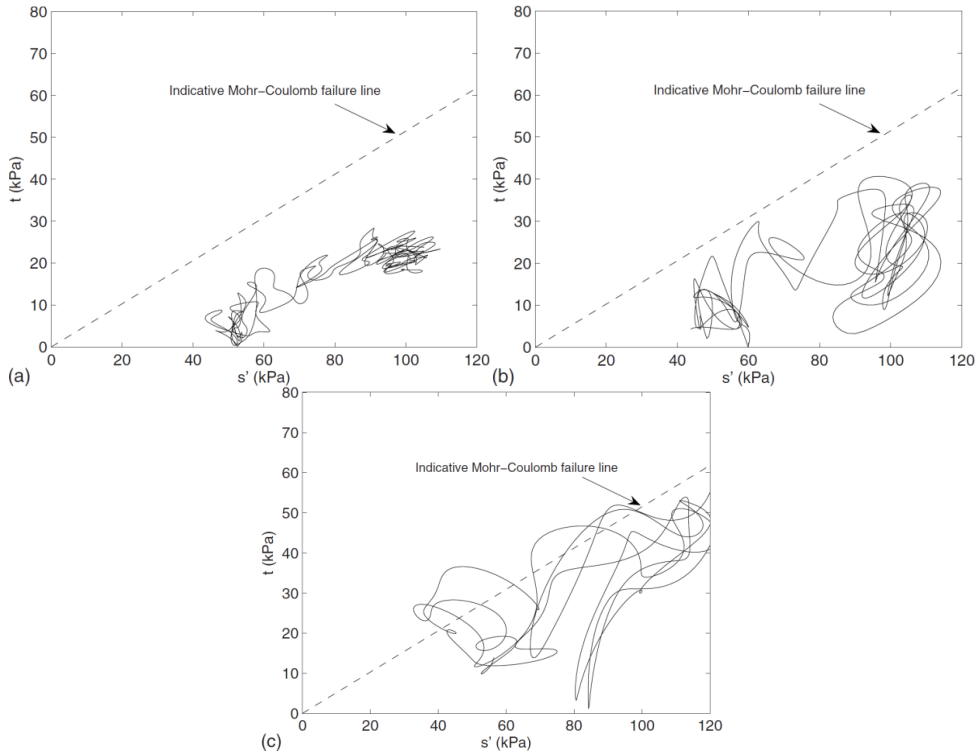



Figure 2.24 Stress path of soil element on natural ground at a speed of (a) $0.5V_c$ (b) $V_c$ and (c) $1.25V_c$ (Yang *et al.* 2009)

Similar projects on the analysis of the dynamic effect of train speed have been done by many researchers (e.g. Fryba 1999; Eason 1965; Krylov 1995). A 3D finite element dynamic model under different moving constant load speeds concerning railway trackbed ground vibrations was analysed by Bian *et al.* (2016). The overview of the finite element model is shown in Figure 2.25.

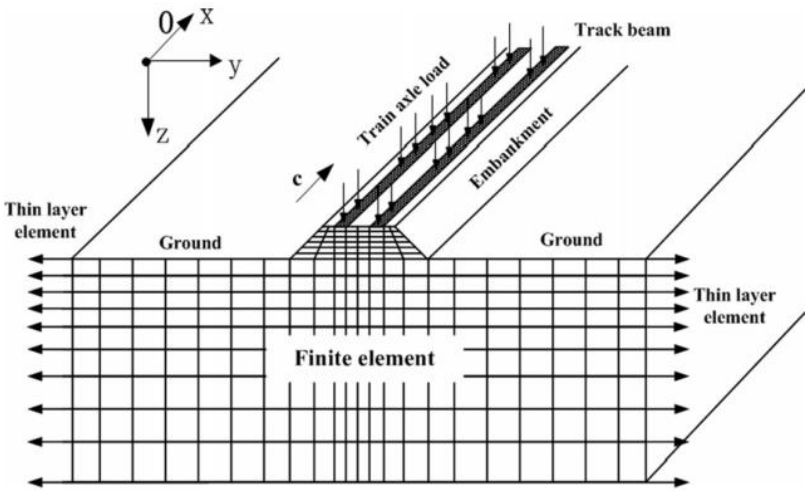



Figure 2.25 Schematic of the FE dynamic model (Bian *et al.* 2016)

Figure 2.26 presents the vertical displacements in both XY and YZ planes induced by the constant moving load. It is clearly proved that at the lower speed, vibration is mainly generated around the axle area, whereas track response does not always increase with train speed, a speed range is expected to exist. The track vibrations should remain small when outside the range (Bian *et al.* 2016).

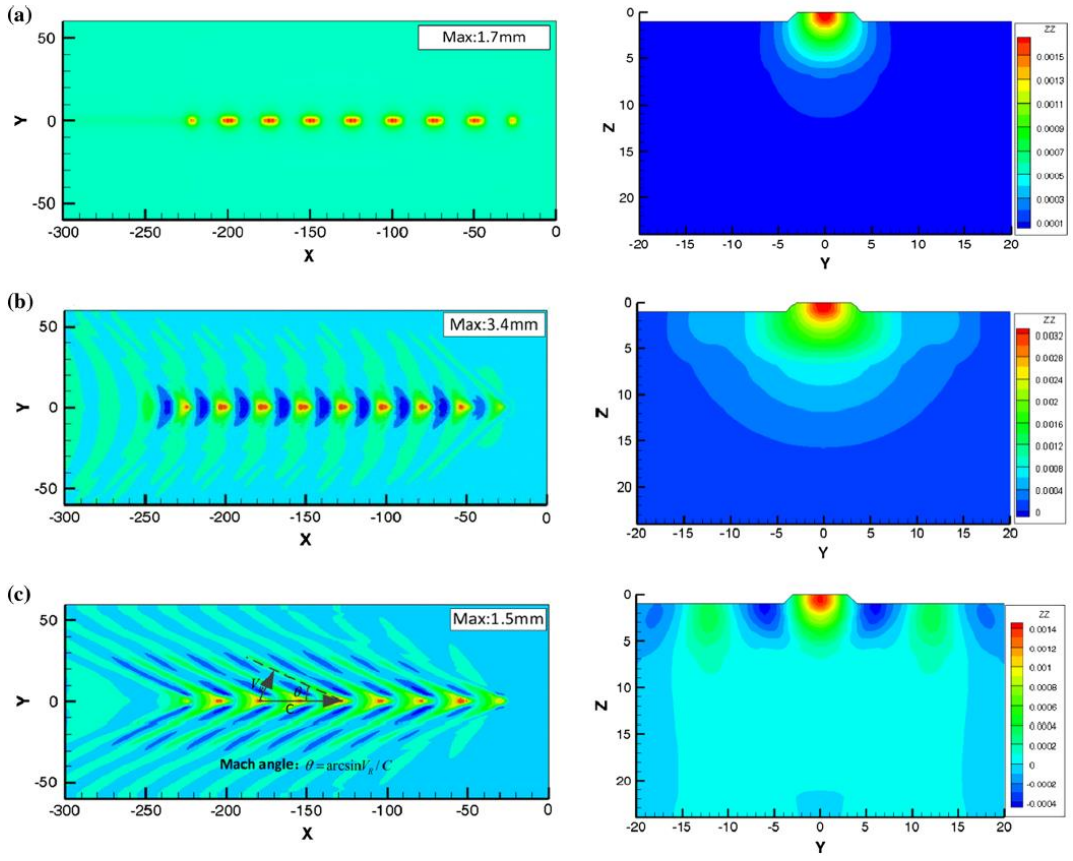



Figure 2.26 Contour plot of vertical displacement induced at ground surface in XY and YZ planes at a speed of (a) 50m/s (b) 120m/s and (c) 200m/s (Bian *et al.* 2016)

## 2.5 ABAQUS

The FE software ABAQUS was used in this research; it generally includes (ABAQUS Analysis User's Manual 6.10):

- ABAQUS/Standard, a general purpose finite element program

- ABAQUS/Explicit, an explicit dynamics finite element program

- ABAQUS/CAE, an interactive environment used to create finite element models, submit ABAQUS analyses, monitor and diagnose jobs, and evaluate results

- ABAQUS/CFD, a general-purpose computational fluid dynamics program

- ABAQUS/Viewer, a subset of ABAQUS/CAE that contains only the postprocessing capabilities of the Visualization module

All of the above except ABAQUS/CFD are utilised in this research.

In order to control the dynamic loading simulations, an ABAQUS/Explicit user subroutine VDload is involved. It can be used to define the variation of magnitude of distribution load as well as the moving load velocity, a function of position, time etc..

### 2.5.1 Elements

To provide a set of tools for solving many problems by FEM, an extensive stress/displacement element library is included in ABAQUS which are (ABAQUS Analysis User's Manual 6.10):

- Continuum elements, e.g. solid elements and infinite elements

- Structural elements, e.g. membrane elements and shell elements

- Rigid elements, e.g. point masses

- Connector elements, e.g. springs and dashpots

- Special-purpose elements, e.g. elastic-plastic joints and surface elements

- Contact elements, e.g. rigid surface contact elements and gap contact elements

It is worth mentioning that only continuum elements (solid elements) are used in this research to model the entire railway trackbed as well as the boundary condition.

**Continuum elements (solid elements)**

Solid elements are the standard volume elements of ABAQUS, they can be used for both linear and nonlinear analysis involving contact, plasticity and large deformations. ABAQUS/Standard and ABAQUS/Explicit both contain first-order (linear) interpolation elements and second-order (quadratic) interpolation elements. The model with second-order elements can achieve more accurate results in ABAQUS/Standard whereas it costs more computing time. As presented in section 2.3.4, a “smoother” result is expected as more nodes are inserted in a second-order element.

Some elements can allow either full or reduced integration. Reduced integration elements can efficiently reduce running time in 3D simulations. Consequently, second-order reduced-integration elements in Abaqus/Standard generally yield more accurate results than the corresponding fully integrated elements (ABAQUS Analysis User’s Manual 6.10). However, as this research is mainly done by ABAQUS/Explicit

where the hex second-order reduced-integration element is not applicable, a first-order reduced-integration element was ultimately chosen.

### 2.5.2 Material damping

Generally, four variables are included in ABAQUS to set up a damping matrix which are as follows:

- alpha, the factor to create mass proportional damping
- beta, the factor to create stiffness proportional damping
- composite, a value for fraction of critical damping
- structural, the factor to create imaginary stiffness proportional damping

Because alpha and beta factors are not relevant to vibration frequencies, only Rayleigh damping which consists of alpha and beta is applied in this research to absorb wave reflection at a boundary. In FE analysis, Rayleigh damping is a matrix that combines mass proportional damping alpha and stiffness proportional damping beta factors as follows:

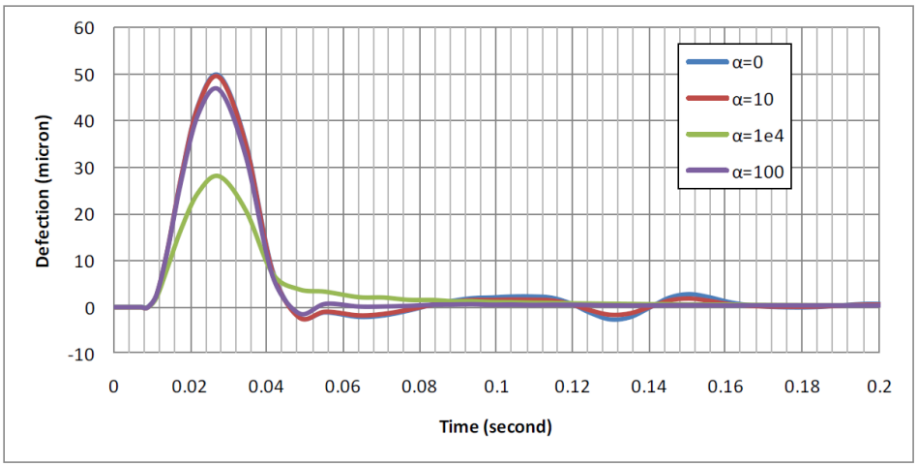
$$[C] = \alpha[M] + \beta[K] \qquad \text{Equation 2.23}$$

Where: [M] is the mass matrix of the model,

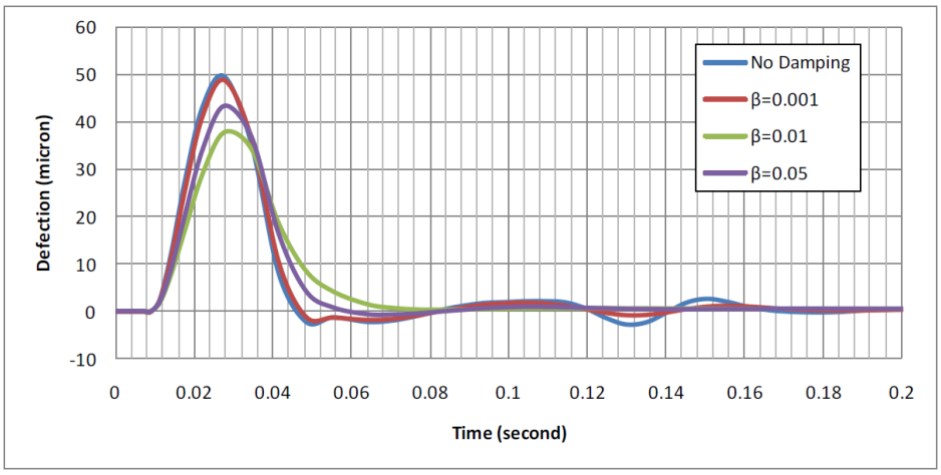
[K] is the stiffness matrix of the model, and

α and β are factors that need to be defined.

Figure 2.27 shows a comparison of deflection histories from an axisymmetric model with α and β factors varied separately which was constructed by Lu (2010). Figure 2.27(a) shows the influence of different alpha factors on deflections. It is clear that there was little influence on deflection when the alpha value was varied between 0 and 100. However, deflection sharply decreased when alpha=$10^4$. The maximum reduced from about 50micron when alpha=0 to 28micron when alpha=$10^4$. Similarly, the influence of beta values on deflection is presented in Figure 2.27(b). The maximum deflection reduced along with increasing beta damping. It is worth noting that phase lags occur when testing with different beta values. Only alpha damping will be chosen for the damped boundary for all the 3D simulations presented in Chapters 4-6.




(a)




(b)

Figure 2.27 Influence of (a) alpha damping (b) beta damping on deflection (Lu, 2010)

### 2.5.3 Boundary Condition

Basically, there are three approaches that can be used to simulate the infinite boundary conditions in ABAQUS: far boundary, infinite element and Viscous Damping Boundary (VDB). For simulation work, any boundaries of the model must allow the energy waves to pass through and never reflect.

In such cases, a very traditional method, which is called far boundary, is to build a model with sufficiently large dimensions. However, it demands large quantities of elements which may lead to extremely long calculation time.

An infinite element is a type of special-purpose element with a specially formulated shape function for the side of an infinite boundary. However, Ross (2004) indicated that a model using infinite elements as its boundary can only represent an object fully enclosed in an infinite medium, e.g. a submarine in the sea.

A more effective approach is that using a viscous damping boundary (VDB). The VDB can also be seen as a set of viscous dampers/dashpots on the boundary. This allows the radiating wave energy to be absorbed by the dashpots (Jiang & Zhang, 2004; Lei & Wei, 2005). The concept of a Viscous Damping Boundary (VDB) is illustrated in Figure 2.28. Both incident primary waves and secondary waves act on the boundary which has an angle Θ from the z – axis. Dashpots elements, which are classified as special purpose elements, can effectively absorb the energy. In ABAQUS, DASHPOT1 and DASHPOT2 elements can be used to connect a node to either the ground or two degrees of freedom. However, because this method can only be used in ABAQUS/Standard whereas the dynamic loading simulations in this research are in ABAQUS/Explicit, a purpose-designed damping layer was constructed which will be fully described in Chapter4.

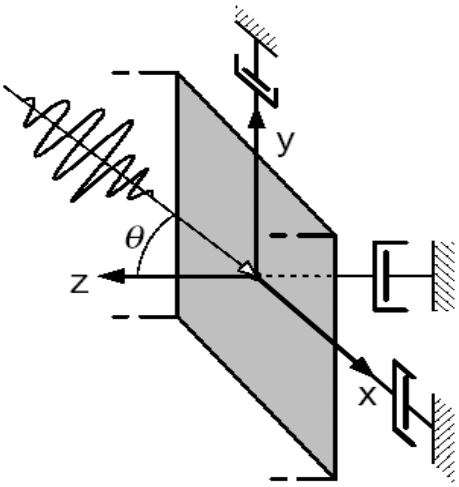



Figure 2.28 Viscous Damping Boundary (Ross, 2004)

## 2.6 Summary

The background to the behaviour of ballasted railway trackbed systems, FEM analysis and previous railway simulations have been presented in this chapter, including a justification for using FEM.

The motivations and novelties of the current study are formed on the basis of the gaps identified in the literature concerning the ballasted railway trackbed systems. The following will organise the summary of the literature into various aspects from which each of the gaps will be identified and the corresponding novelty presented.

Firstly, although extensive research into different trackbed systems, various types of vehicle loadings (e.g. Nguyen *et al.* (2012) set up a 3D model with full car body, bogies and wheelsets to simulate the real wheel load; Blanco-Lorenzo *et al.* (2011) studied the effects of single and multiple wheelsets moving load on a slab track), and the interaction between wheel and rail (e.g. Knothe and Grassie (1993) figured out the effects of high frequencies on wheel/rail interaction behaviours; Lei and Noda (2002) presented an study of dynamic response of wheel/rail system with irregularity of rail vertical profile) have been carried out to evaluate the dynamic response of railway systems, less effort has been made on the dynamic response of ballast under the sleepers. In addition, few research studies were focused on sleeper rotation which will be shown in chapter 5. However, the rotation of the sleeper along its longitudinal axis has not yet been studied. Therefore, the issues regarding the dynamic ballast behaviour and the sleeper rotation will be addressed in this study.

Secondly, some of the previous research has explored granular material behaviour in depth (e.g. Aikawa (2015) presented a study of ballast behaviour under a 3D FEM ballast aggregate model). Nevertheless, a partial ballast model with very limited size cannot achieve a full understanding of the stress states, including principal stress rotation, in the entire railway trackbed. In this context, this research will focus on a full scale modelling of the trackbed system, aiming to gain a more comprehensive understanding of the dynamic response of the ballast under moving train loads.

Thirdly, effects of train speed on the stress and displacement states in natural ground have been computed utilising linear elastic railway trackbed models (e.g. Yang *et al.* (2009) presented a study on stress history and stress paths in subgrade using a 2D railway model; Bian *et al.* (2016) analysed the effects of dynamic loading speeds on natural soil surface vibrations). All the studies stated earlier were devoted to elastodynamics of natural ground, and, therefore, there is a lack of understanding of the behaviour of ballast underneath the track. In addition, there is also a lack of a comprehensive parametric study on the ballasted railway track system using different variables. A study of the effects of loading speed and stiffness of ballast, rail pad and subgrade has been carried out in this thesis.

Although a single wheel load set is adopted in this study, which may be thought as being unrealistic, it was demonstrated by Blanco-Lorenzo *et al.* 2001 that using such a single load was accurate for estimating the main response of a trackbed system. Nevertheless a further investigation of the comparative effects of single and dual loads will be carried out in Chapter 4.

# 3 Preliminary Study – 2D Simulations

In this chapter, the commercial finite element analysis package ABAQUS/Standard Version 6.10-2 has been used. ABAQUS is a powerful engineering simulation software. It is based on the finite element method and it can deal with many problems which range from simple linear analysis to complicated nonlinear models. ABAQUS/Standard 6.10 contains an extensive library of elements that can model virtually any geometry. What's more, an extensive list of material models are included that can simulate most typical engineering material behaviour including reinforced concrete, metals, rubber and geotechnical materials, for example, soil and rock.

In this chapter, simulation work including model creation and data analysis are presented. To have a better understanding of mesh size and to optimise the length for a 3D model, two-dimensional models in two different directions are described in which all parts of the model are simulated using linear elastic behaviour where the computing time can be effectively saved. Graphs of stress and displacement distribution under static load will be presented. Comparison of vertical displacement between simulated and computational result is also described.

## 3.1 Two-dimensional Simulation Practice

The initial analyses were developed with two dimensions in preparation for carrying out a full three dimensional analysis. A key reason is that a two dimensional model requires less computational time and memory. It is suitable for identifying the mesh

size and level of discretization required (Powrie, 2007). Basically, model creation can be divided into eight steps when using ABAQUS/Standard. The sequence is as follows: Part creation – Material properties – Parts assembly – Step – Interaction properties – Load and boundary condition application – Mesh – Job submission and result visualisation.

- The ‘Part creation’ module is used to define and edit a model using tools to generate part geometry and dimensions.
- After each part has been created, ‘Material properties’ and sections should be defined. When a section has been created within a part, then that section can be endowed with the properties of a defined material so that the part can possess all the various properties it should have.
- ‘Part assembly’ is the stage in which all the parts in the model are assembled together to provide a specific geometry.
- In the ‘Step’ module, the whole simulation analysis is divided into either one or several steps; the user can also specify output requests here.
- It is obvious that each part will have surfaces and when they are assembled together, some of them will be adjacent to each other. In reality, interaction will happen and ‘Interaction properties’ are defined in this module. In this study, all adjacent parts of the model were tied to ensure the same degree of freedom at the interfaces.
- ‘The load and boundary condition application’ module defines boundary conditions and load types, magnitudes and direction. Since the prescribed conditions in ABAQUS/Standard are step-dependent objects, all the loads and

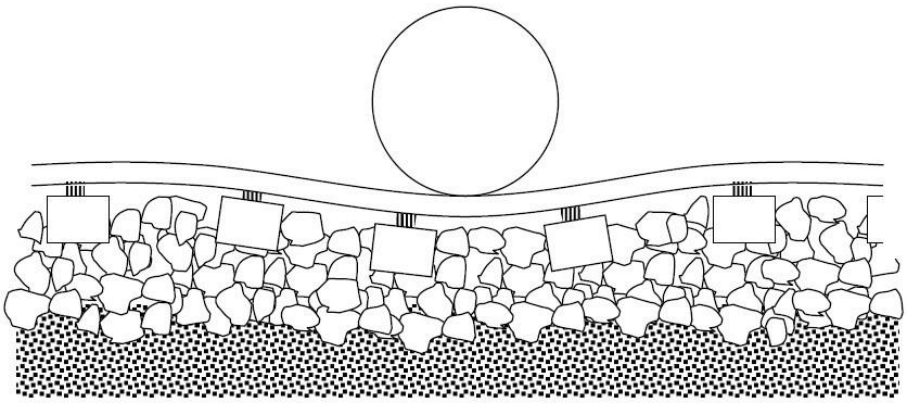
boundary conditions that are predefined have to be specified at the steps in which they are active.

- 'The mesh' module is one of the most important in model creation, in which the entire model is divided into a certain quantity of elements with defined type, size, shape etc. Different types and densities of element could result in significantly different final results
- When the model is done, 'Job submission and result visualisation' can output all the stress and displacement distributions etc. in contour plots.

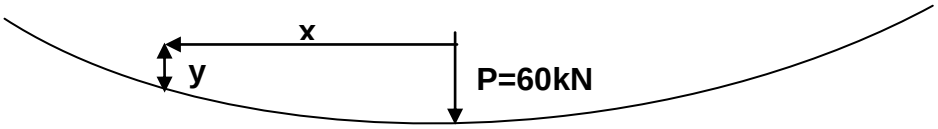
### 3.1.1 Longitudinal Section

#### 3.1.1.1 Model Description

At the start of the research project, a two-dimensional railway trackbed model in longitudinal section was created. In order to decide the initial size of the model to ensure effective boundary conditions, a simple prediction with regard to the vertical deflection of the rail was carried out initially. A load of 25.4 tonnes is the maximum axle load normally permitted on the UK rail network, corresponding to a static wheel load of 125kN (Powrie, 2007). Furthermore, a static wheel load of a passenger coach is generally 60kN (Esveld, 2001). In this model, 60kN was chosen as the magnitude of a wheel static load. The model assumes the rail to be an infinite Euler-Bernoulli beam; an idealised track deflection sketch is displayed in Figure 3.1(a) and the 'Beam on Elastic Foundation' solution to track deflection analysis is presented in Figure 3.1(b).



(a)




(b)

Figure 3.1 The sketches of idealised and simplified track deflections under a wheel load

The vertical displacement of the rail can be predicted using the following equation:

$$y = (P\lambda/2k)\, e^{-\lambda x} [\sin(\lambda x)+\cos(\lambda x)] \qquad \text{Equation 3.1(a)}$$

$$\lambda = \left(\frac{k}{4EI}\right)^{0.25} \qquad \text{Equation 3.1(b)}$$

where,

E: Young's modulus of elasticity for rail steel in Pa,

I: moment of inertia of the rail with respect to vertical bending in $m^4$,

x: longitudinal coordinate with its origin at the point where the design load is applied in m,

k: track modulus which can be interpreted as the foundation resistance force per mm when the rail is deflected 1mm. Esveld (1989) indicates that a track modulus of 9N/$\mathrm{mm}^2$ is a poor one, while 90N/$\mathrm{mm}^2$ is a good track modulus. As the properties of the railway trackbed are to be those of a well-constructed railway system in reality, 90N/$\mathrm{mm}^2$ has been used in calculation.

P: the vertical wheel load applied on the rail in kN.

The values of parameter $I_r$ and E can be found in Table 3.1. After inserting all the parameters,

$$\lambda = \left[90 \times \frac{10^6}{4 \times 210000 \times 10^6 \times 3.055 \times 10^{-5}}\right]^{0.25} = 1.37\mathrm{m}^{-1}$$

Hence, from Equation 3.1:

$$y = \left[60 \times 10^3 \times \frac{1.37}{2 \times 90 \times 10^6}\right] e^{-1.18x}(\sin 1.37x + \cos 1.37x)$$

$$= 4.567 \times 10^{-4} e^{-1.37x}(\sin 1.37x + \cos 1.37x)$$

Figure 3.2 presents the trend of vertical displacement along the longitudinal rail direction. It can be seen that the vertical displacement reduces from under the load with increasing distance along the rail and the superstructure is then lifted slightly after around 2m from the load. With further increasing distance from the load, the deflection returns ever closer to the horizontal.




Figure 3.2 Vertical displacement with distance

When

$x = 1$, $y = -1.37 \times 10^{-1}$mm

$x = 3$, $y = 1.0464 \times 10^{-2}$mm

$x = 5$, $y = -6.711 \times 10^{-4}$mm is extremely small.

Thus, to cover all significant deflections, 5.5m was chosen as the initial rail model length.

A sketch of the model structure with dimensions is illustrated in Figure 3.3. This model consists of six parts: a single rail, seven and a half sleepers with rail pads, ballast, subballast and subgrade. Because the railway trackbed structure is fully symmetrical, in order to save simulation time, a half model was adopted. Following the International Union of Railways (UIC) Code719R (1994), 300mm of ballast and 150mm of subballast were applied in the analysis. In particular, an extended substructure with 10m length was set up. This was intended to be sufficient to eliminate any boundary effects. Although the crib ballast can retain the railway

trackbed and hold the sleepers in a stable position, however, its function is not as significant as the main layer of ballast below. Consequently, this part was simplified and the sleepers were assumed to be placed directly over the ballast layer.

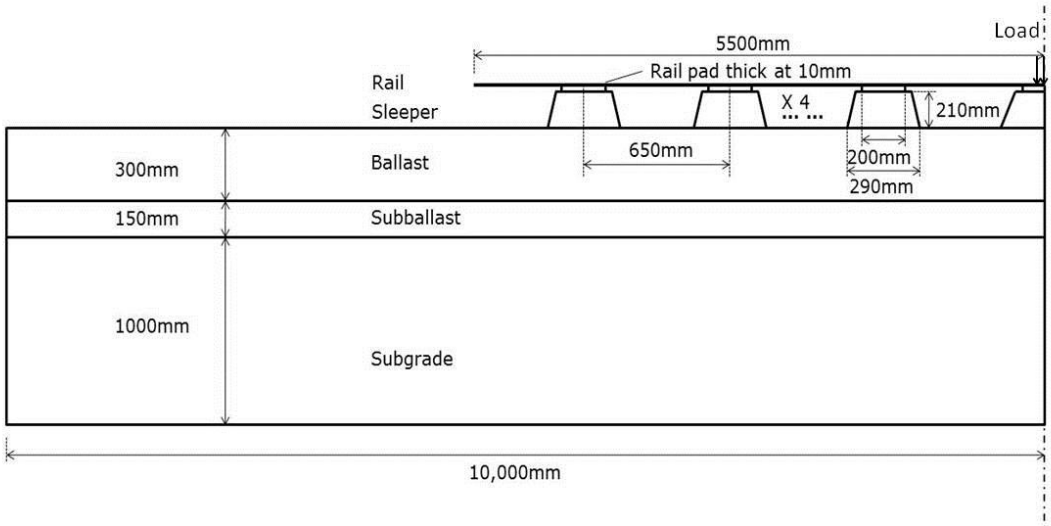



Figure 3.3 Dimensions of the longitudinal section model in 2D

As commonly used on UK rail lines, the G44 sleeper which is made of reinforced concrete was chosen as the sleeper type within this model (Pen, 2008). The rail was simulated as a beam element of appropriate bending stiffness to model a UIC60 rail. Furthermore, all the rail trackbed components were simulated as two-dimensional plane strain shell elements. Use of plane strain elements is a method which means there is no strain occurs at the direction normal to the simulated plane.

The properties of all the materials used in this model which represent a normal railway trackebd are listed in Table 3.1 (Yang *et al*., 2009). Since this model was linear elastic, only Young's modulus and Poisson's ratio are taken into account.

Table 3.1 Material Properties

| Component description | Young's Modulus E (MPa) | Poisson Ratio v | Others |
|---|---|---|---|
| Rail | 210000 | 0.3 | Flexural inertia Ir ($\mathrm{m}^4$): $3.055\text{x}10^{-5}$ |
| Pad | 6.9357 | 0.49 | Natural rubber |
| Sleeper | 30000 | 0.2 | Reinforced concrete |
| Ballast | 140 | 0.4 | |
| Sub-ballast | 140 | 0.4 | |
| Subgrade | 75 | 0.35 | |

In ABAQUS/Standard, the parameters inserted have no specific units. Hence users have to select a constant standard themselves. Two common sets of consistent units are listed in Table 3.2 and the upper one was used in this project.

Table 3.2 Consistent units in ABAQUS

| Length | Force | Mass | Time | Stress | Energy | Density | Acceleration |
|---|---|---|---|---|---|---|---|
| m | N | kg | s | Pa | J | kg/$\mathrm{m}^3$ | m/$s^2$ |
| mm | N | tonne | s | MPa(=N/$\mathrm{mm}^2$) | J | tonne/$\mathrm{mm}^3$ | mm/$s^2$ |

Typically, a real wheel-rail contact area is elliptical and it is around 15mm in the longitudinal direction along the rail under a static wheel load of 60kN (Esveld, 2001). Table 3.3 gives the rail-wheel contact areas for different wheel diameters (Skoglund, 2002). In UK, a diameter of 1.016m of the train wheel is commonly used hence the contact area is $1.548\text{x}10^{-4}\mathrm{m}^2$. Since the rail is simulated as a beam and the trackbed

is simulated by a two-dimensional model, consequently a line load was utilised at the axis of symmetry with a magnitude is 4kN/mm.

Table 3.3 Typical rail-wheel contact areas for different wheel diameters

| Wheel diameter/m | 0.711 | 0.838 | 0.914 | 0.965 | 1.016 | 1.067 |
|---|---|---|---|---|---|---|
| Contact area/$10^{-3}m^2$ | 1.032 | 1.226 | 1.355 | 1.484 | 1.548 | 1.613 |

It is worth mentioning that the displacement in the x and z directions is constrained at both ends of the rail and the two edges of the ballast and subgrade; the bottom of subgrade is set as a rigid boundary; all other surfaces in this model are set as free surfaces.

In order to optimize the mesh density, five average mesh sizes were investigated, of approximately 0.1, 0.08, 0.06, 0.04 and 0.02m, comprising 897, 1185, 1741, 2999 and 9210 elements. These cases were termed as Cases 1 to 5 respectively. The model with CPE8R elements (8-node biquadratic plane strain quadrilateral, reduced integration) is illustrated in Figure 3.4.

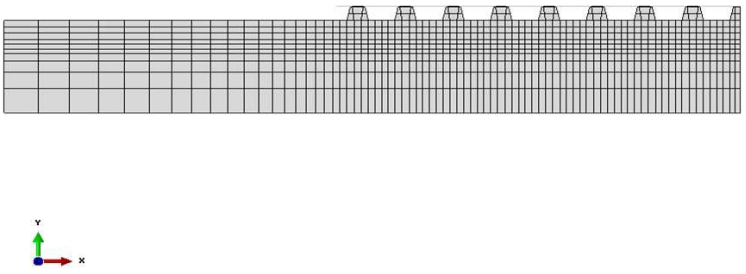


Figure 3.4 Sketch of Case 1 meshed model

In addition, to collect data on vertical stresses and displacements during the simulation work, six measuring nodes were specified as shown in Figure 3.5.

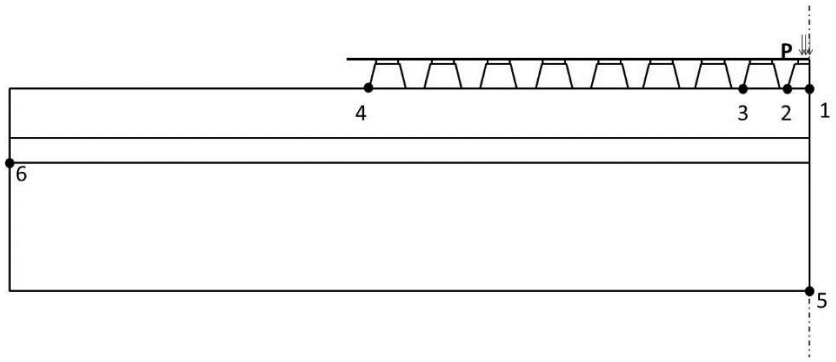



Figure 3.5 Measuring nodes in the longitudinal model

### 3.1.1.2 Data analysis

An optimised mesh size should be determined initially to achieve reliable data. Several typical nodes were chosen as test points. Figure 3.6 and 3.7 presents the vertical stresses and displacements at different measuring points varying with mesh sizes respectively. All the numerical data which was collected during the study is shown in Appendix A. It is obvious that most of the results for both displacement and stress change smoothly. For Node 6, the displacements and stresses were close to zero during the study, from which it can be deduced that the length of the model was large enough. However, for Node 5, which is located on the bottom of subgrade, the vertical stress is nearly 30kPa. In this case, the depth of the subgrade is definitely insufficient as the stress at the boundary is still relatively large.

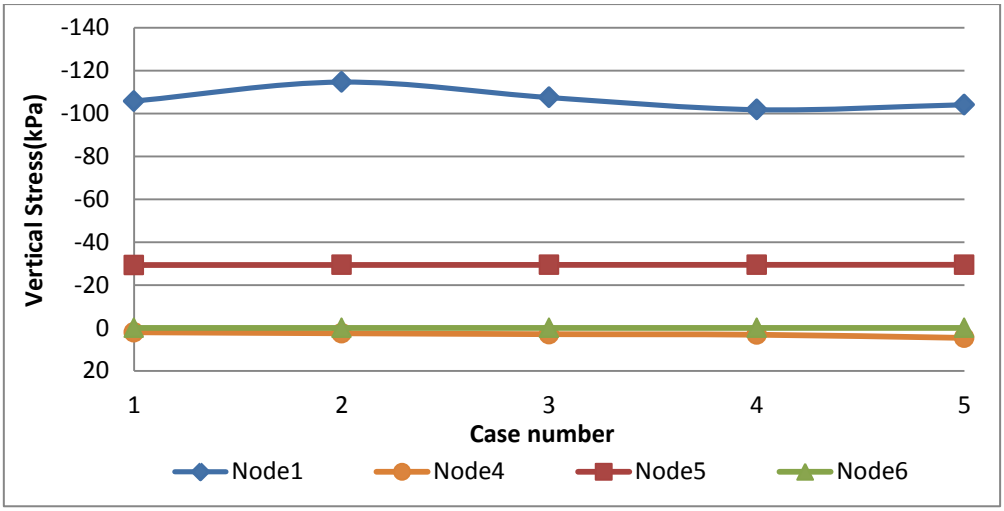



Figure 3.6 Comparison of vertical stresses vary with mesh sizes

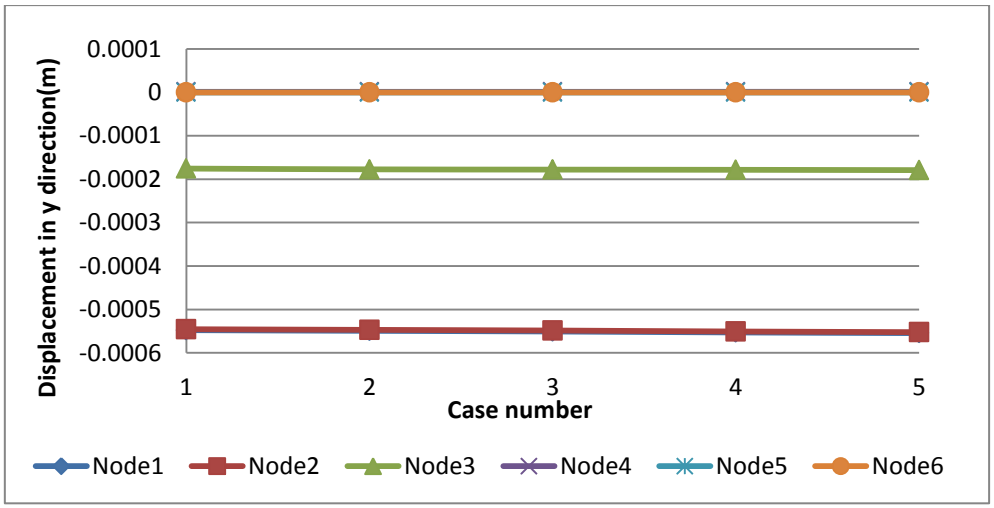



Figure 3.7 Comparison of vertical displacements vary with mesh sizes

Figure 3.8 presents the differences of vertical stresses at different measuring points for different mesh sizes compared to Case 1. There is little change at all nodes except Node 4. The stress at Node 4 for Case 5 is 228% greater than for case 1. However, as shown in Figure 3.6, its absolute value is always very low for all cases.

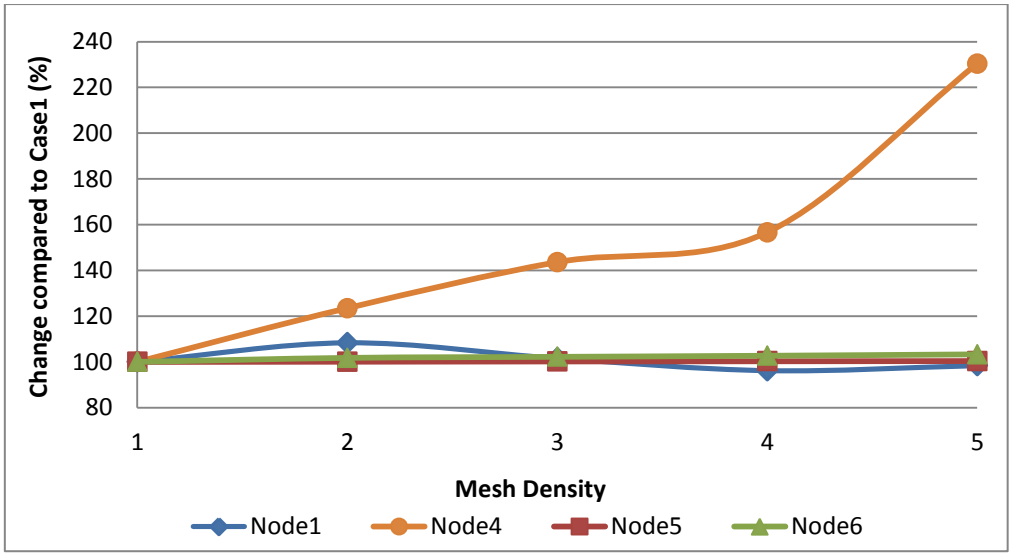



Figure 3.8 Vertical stresses change with different mesh sizes compared to Case 1

With regard to the change of vertical displacement compared to Case 1 as shown in Figure 3.9, all the nodes except Node 5 have a slight increase. However, there is only about 3% for the maximum change among six nodes which is negligible.

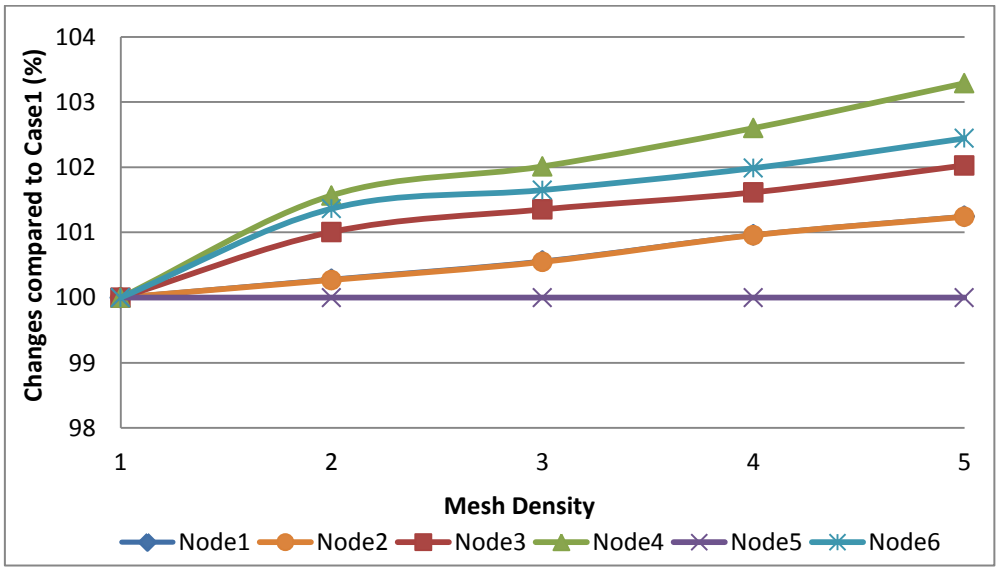



Figure 3.9 Vertical displacements change with different mesh sizes compared to Case 1

It is worth noting that the stress changes sharply after Case 3 at Node 2 as presented in Figure 3.10. The vertical stress for Case 5 is approximately 1.64 times more than Case 3. Similarly, a continuous increase occurs at Node 3. The vertical stress for Case 5 is about 2.25 times more than case 1. After examining the data variation shown in the figure, it was concluded that the results should be appropriate when the model is meshed with 1741 elements, i.e. Case 3.

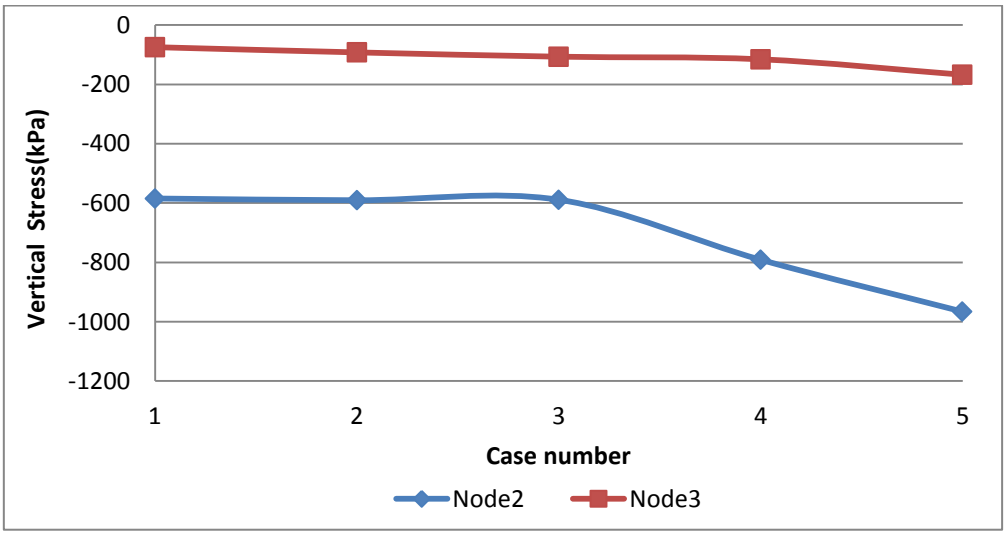
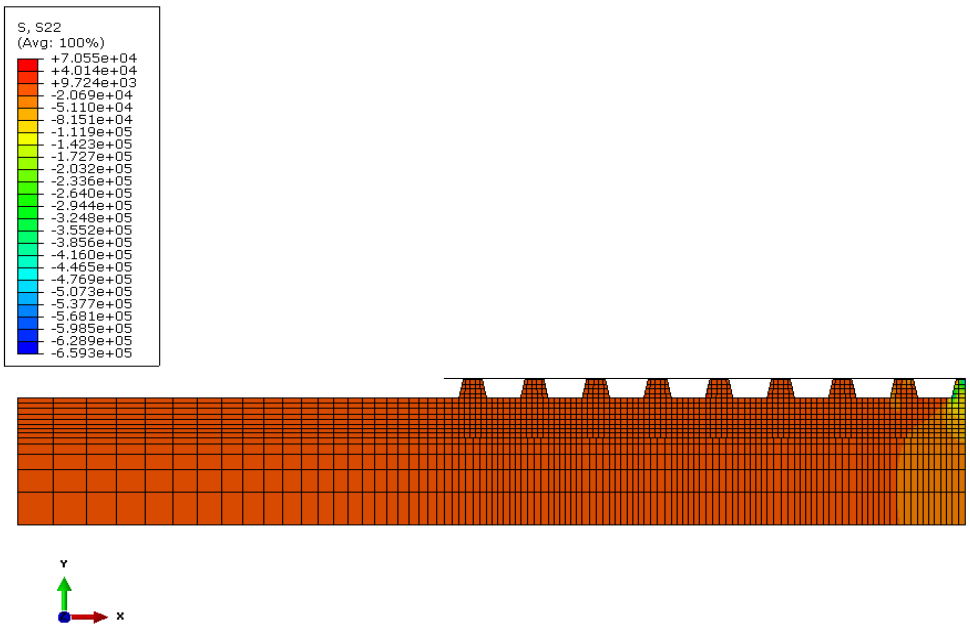
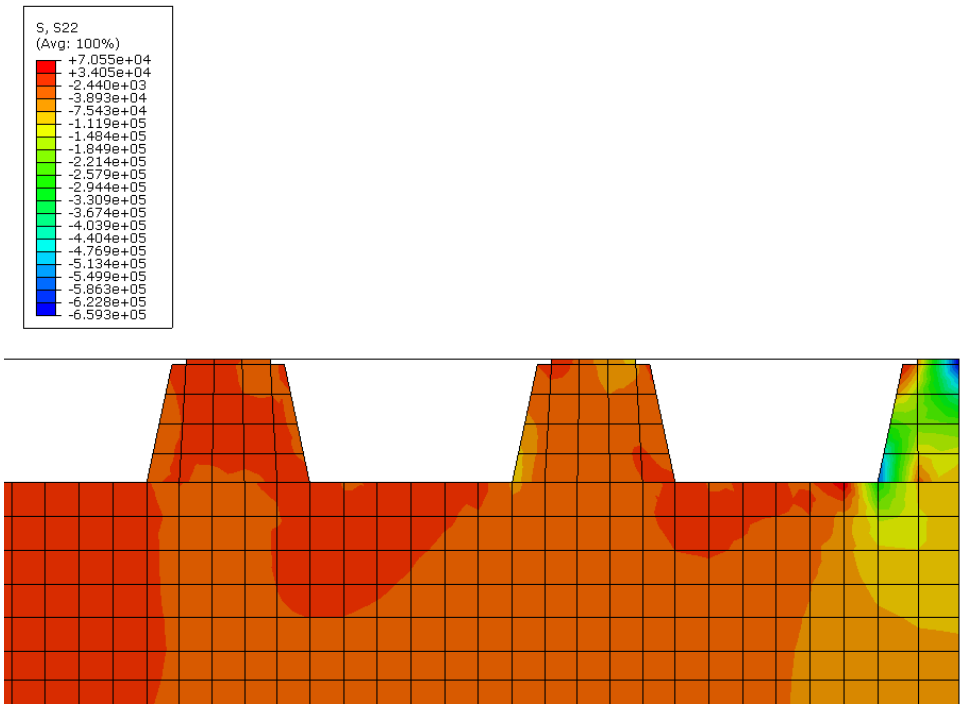



Figure 3.10 Comparison of vertical stresses with different mesh sizes

Figure 3.11 shows a contour plot of vertical stress distribution with a characteristic mesh size of 0.06m (Case 3). It can be clearly noted from Figure 3.11(b) that the stress changes gradually within the railway trackbed and both centre and bottom corner of the loaded sleeper have the largest stress. In other words, calculation difficulties of ABAQUS could potentially occur in these areas because of stress concentrations so that the results might not be accurate enough.



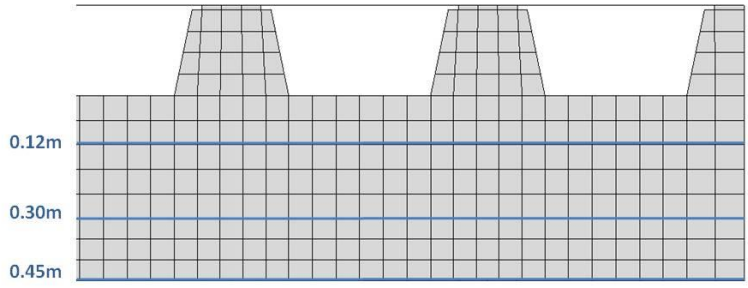

(a)



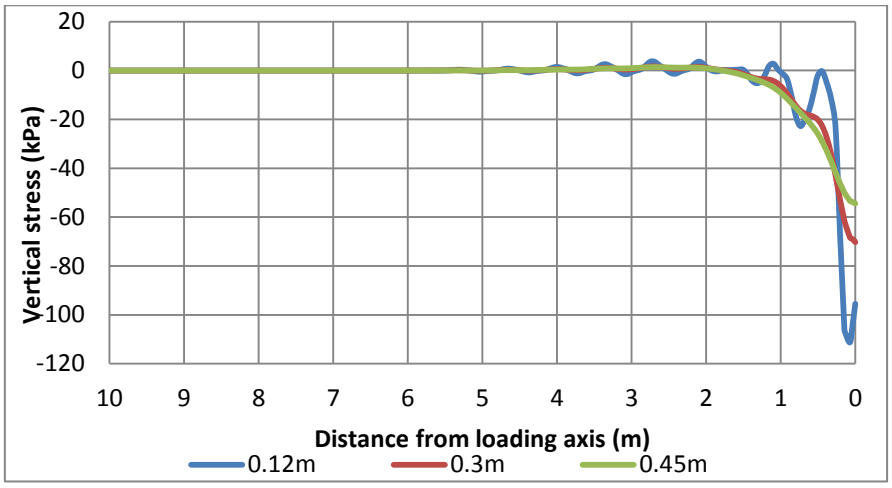

(b)

Figure 3.11 Contour plot of vertical stress distribution (a) for the entire model (b) detail under the load

Figure 3.12(b) illustrates the stress change along the longitudinal direction of the model at different depths in ballast layer. As shown in Figure 3.12(a), three depths are shown, which are 0.12m, 0.3m and 0.45m below the bottom of the sleepers respectively. From the data comparison, stress reduces when the depth increases. Trend lines for both 0.3m and 0.45m reduce relatively smoothly and tend to zero when the distance is approximately 4m from the loading. However, the stress change at 0.12m shows marked oscillation against distance. This is because the stress concentrations occur at every bottom corner of the sleepers and 0.12m is close to the sleepers. Consequently, the trend line shows high stress when it is located beneath the sleeper corners.




(a)




(b)

Figure 3.12 (a) Sketch of partial ballast in 2D model (b) Vertical stress distribution at different depths

A contour plot of vertical displacement distribution is shown in Figure 3.13. The displacement reduces gradually from the centre of the rightmost sleeper both downwards and to the left. The superstructure then is displayed upwards after the third sleeper from the right. With increasing distance from the loading point, the uplift returns to the horizontal again.

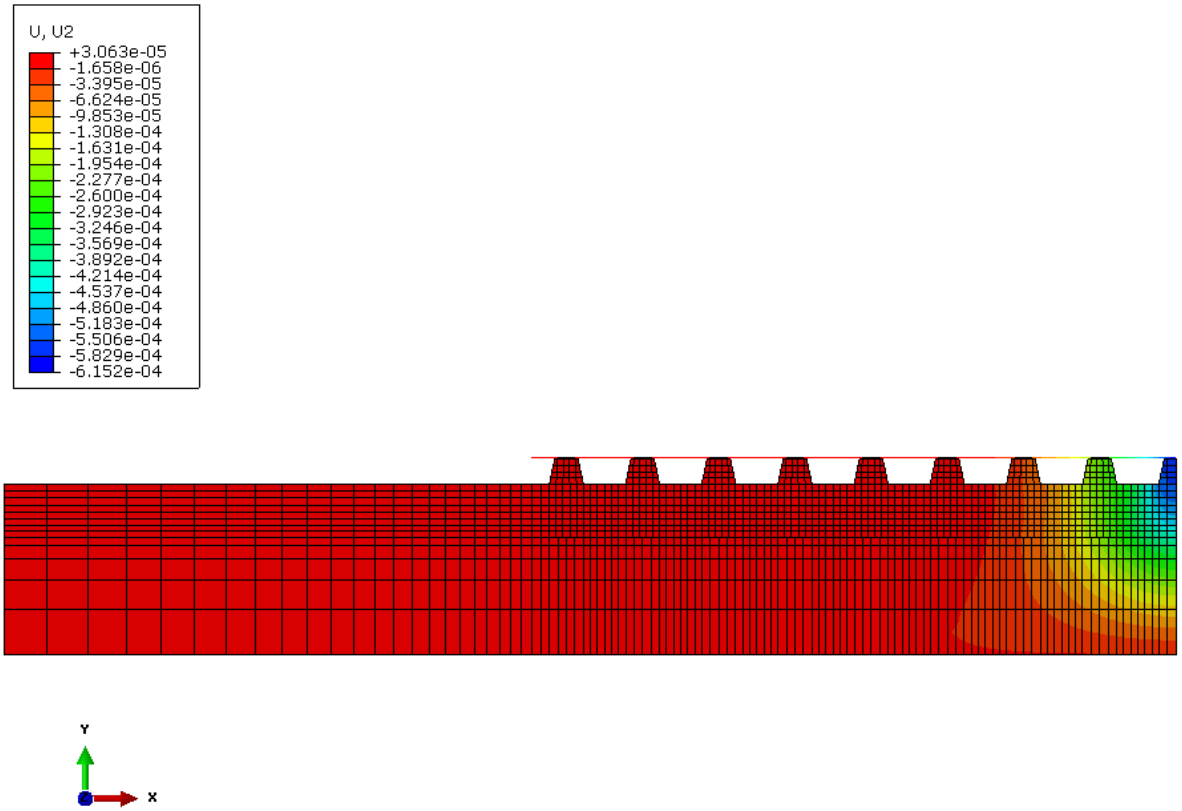



Figure 3.13 Contour plot of vertical displacement distribution

A comparison of the vertical rail displacement changes with distance from the load between the simulation and the theoretical calculation is shown in Figure 3.14. As the track modulus k cannot be calculated from the model directly, two curves with different k values are presented to compare the similarities. Clearly, the curves from the theoretical calculation and simulation match well in most places and the

equivalent track modulus should be within the range of 64 to 69N/mm$^2$. Nevertheless, compared to the curve where k=69N/mm$^2$, the results overlap perfectly with those from the simulation except over the first 0.2m where the simulation result rises to the k=64N/mm$^2$ case. This is mainly due to the difference between continuous support and individual sleepers. In addition, the loading area is extremely small compare to the model length, and this can be seen as a concentrate load and causes stress concentration so that the vertical displacement is becoming higher than expected.

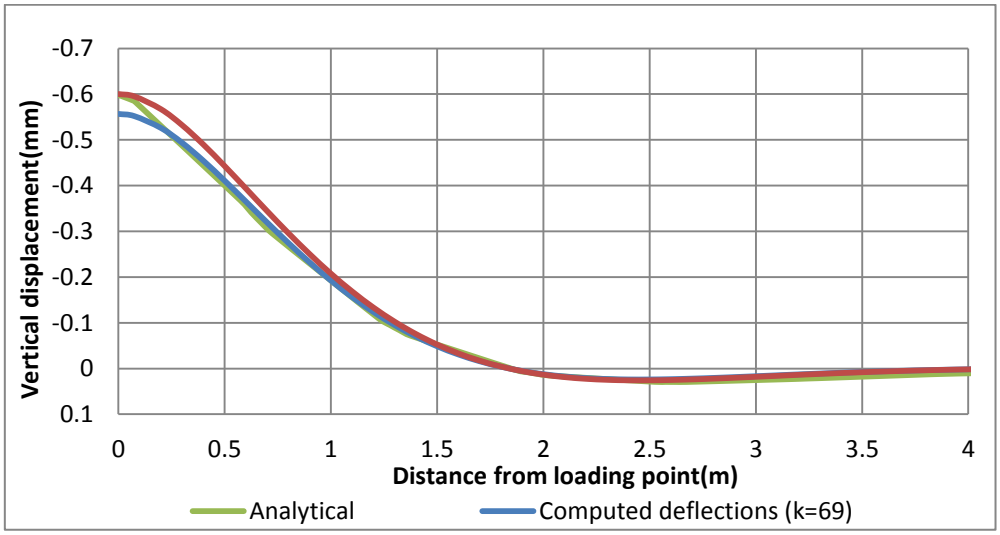



Figure 3.14 Trends of vertical rail displacement

### 3.1.2 Transversal Cross section

#### 3.1.2.1 Model Description

All dimensions of the cross section model are shown in Figure 3.15. Similar to the longitudinal section model, due to the fully symmetric trackbed structure, a half model was adopted. In this model, four components are included, which are sleeper,

ballast, subballast and subgrade. To guarantee a reliable and stable trackbed structure, a slope of 1.5:1 for edges of the ballast and subballast layers was adopted. Furthermore, several assumptions and simplifications have been made and are listed as follows:

- The behaviour for all the components of the model is assumed to be linear elastic.
- For a traditional railway track system, the sleeper is embedded into ballast. In this case, a simplified model is utilised in which the shoulder ballast is omitted, which means only one sleeper surface is in contact with the ballast.
- Both rail and fastening system are ignored in this model and the load is applied directly on the sleeper surface.
- The pressure applied due to the wheel-rail contact should be over an elliptical area. Following the data from Table 3.3 and calculation of an elliptical area, the length over which the pressure acts is assumed to be 3.3mm. Also, it is about 150mm long at the rail-sleeper contact. The pressure is then simplified as a concentrated point load with a magnitude of 60kN.

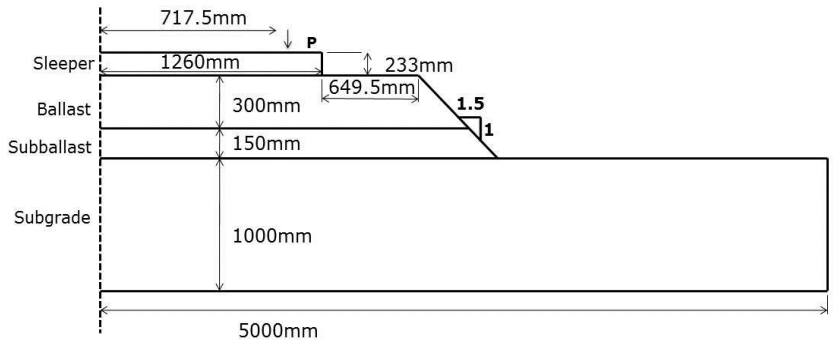



Figure 3.15 Dimensions of the transversal cross section model in 2D

For the boundary condition, a symmetric boundary regarding plane x is applied on the left side of the model where horizontal displacement is restricted. Also, the displacement in x direction is set to zero at right side of the model; a rigid boundary is also set for the bottom of the subgrade. All other surfaces have free boundaries.

The properties of all the materials as well as the units in this model are exactly the same as for the previous model, as given in Table 3.1 and Table 3.2. Mesh density optimisation was carried out initially. Five average mesh sizes with dimensions of 0.1, 0.08, 0.06, 0.04 and 0.02m, comprising 258, 391, 623, 1552 and 5207 elements respectively were investigated. These are called Cases 1 to 5 respectively. A meshed model with CPE8R elements is illustrated in Figure 3.16.

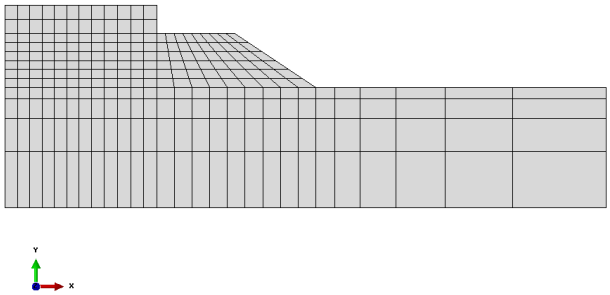


Figure 3.16 Sketch of Case 1 meshed model

For a better understanding of the effects of mesh density, six measuring nodes were chosen and are shown in Figure 3.17.

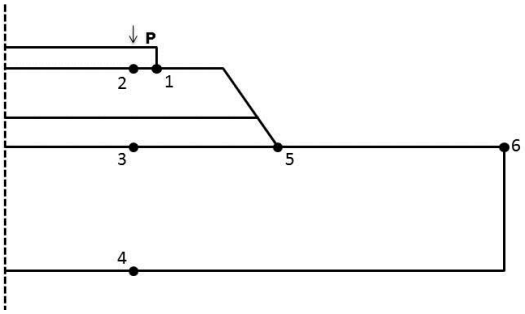



Figure 3.17 Measuring nodes distribution

### 3.1.2.2 Data analysis

In this study, data from all the nodes that were chosen are presented in Appendix A. The 2D model which contains 5207 CPE8R elements is used to illustrate the results. A contour plot of vertical displacement and vertical stress under load are presented in Figure 3.18 and 3.19 respectively. Similar to the longitudinal model, the displacement reduces gradually from load centre to the surrounding area. A maximum positive displacement of about 0.02mm occurred at the right side of ballast.

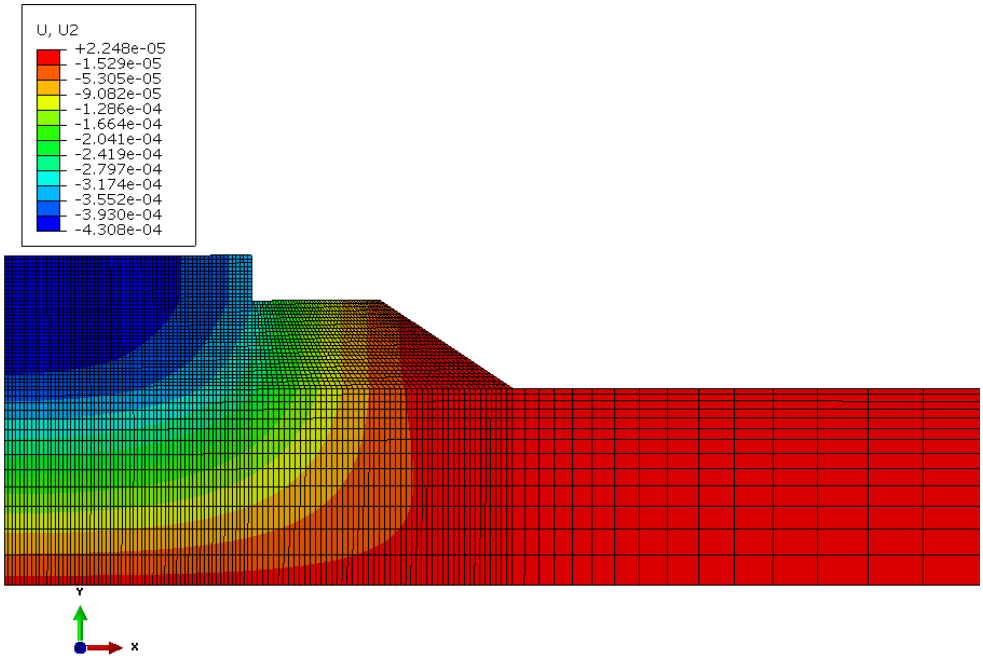



Figure 3.18 Contour plot of vertical displacement distribution for the entire model

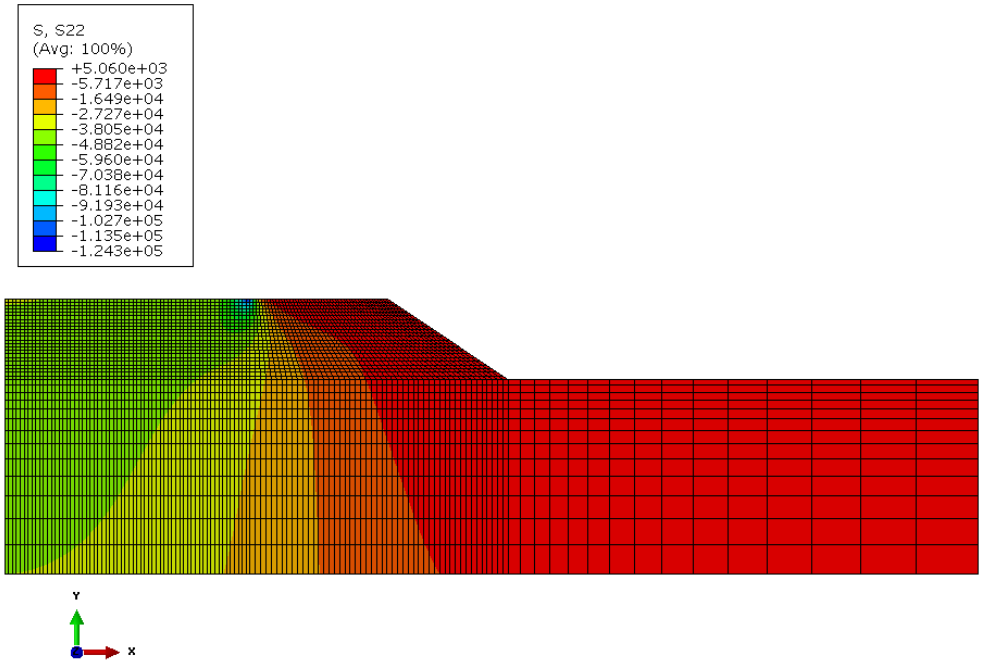



Figure 3.19 Contour plot of vertical stress distribution

The vertical displacements at different locations vary with mesh size as shown in Figure 3.20. It is clear that there is very little change in displacement across all cases. The difference between Case 1 and 5 for all nodes is less than 0.5%. Moreover, the vertical displacements at Nodes 5 and 6 are positive which means the ballast in this area is displaced upwards, whereas this is not true in reality. This is likely to be due to the limitations of FEM, in that ballast is assumed as a continuum whereas the truth is that aggregate consists of separate particles.

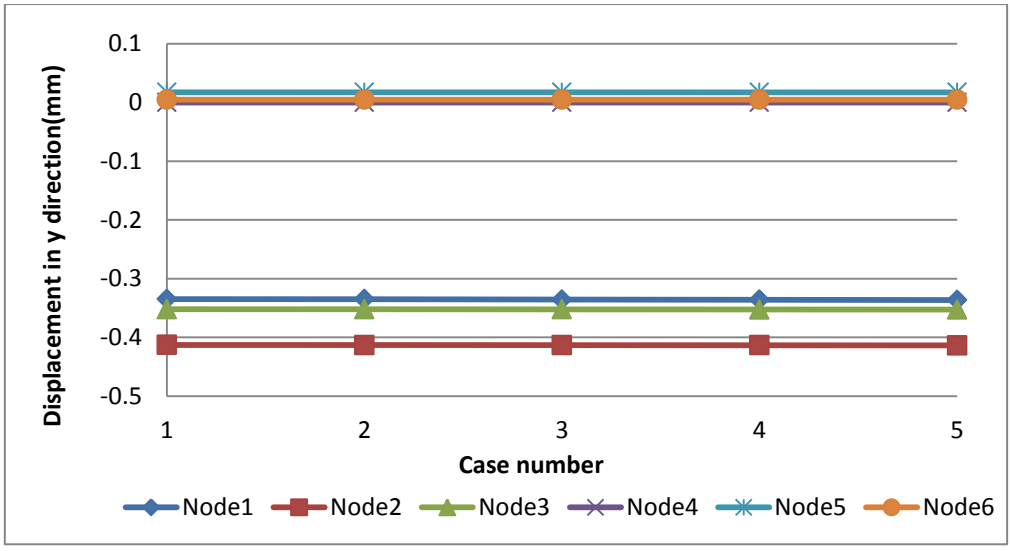
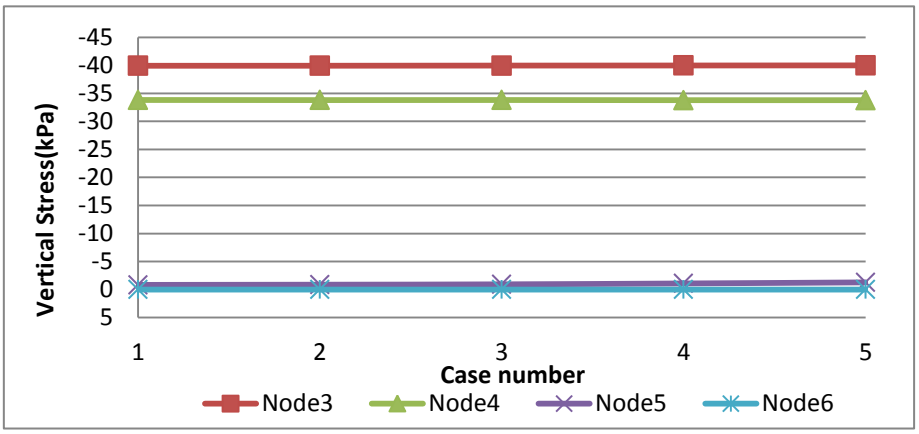



Figure 3.20 Comparison of vertical displacements with different mesh sizes

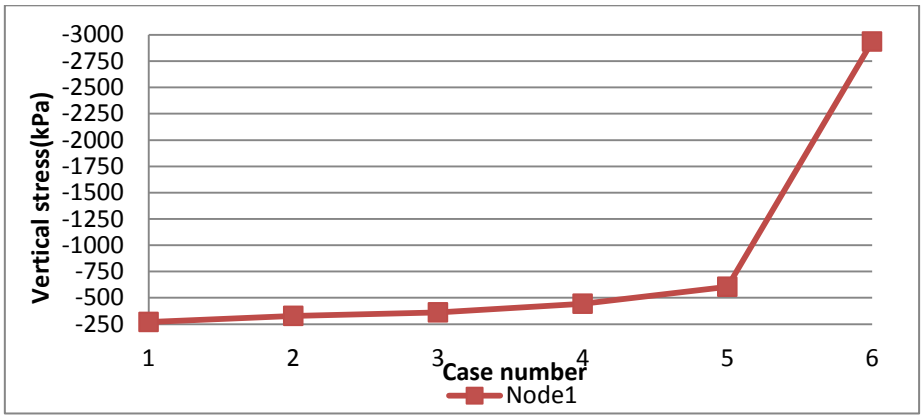
The vertical stress at all six nodes against mesh size is illustrated in Figure 3.21. Similar to variation of vertical displacement, the stress changes at Nodes 3, 4 and 6 are negligible, as presented in Figure 3.21(a). The vertical stress of Node 5 at Case 5 is 1.5 times greater than at Case 1. In contrast, the stress changes much more at Nodes 1 and 2 even when the element quantity at Case 5 becomes twenty times more than Case 1 as shown in Figure 3.21(b) and (c).

A special case study, Case 6, with extremely dense mesh with a minimum element size of 0.001m has therefore been applied to investigate the variations at Nodes 1 and 2. It is worth noting that the gradient of the curve in Figure 3.21(c) for Node 2 reduces and tends to be flat as the mesh density increases. This indicates convergence to a solution when the elements become denser. However, as shown in Figure 3.21(b), the vertical stress at Node 1 never stops increasing no matter how dense the mesh is. This indicates that calculation difficulties may be occurring in the stress concentration area, which will cause inaccuracy in the result. This suggests

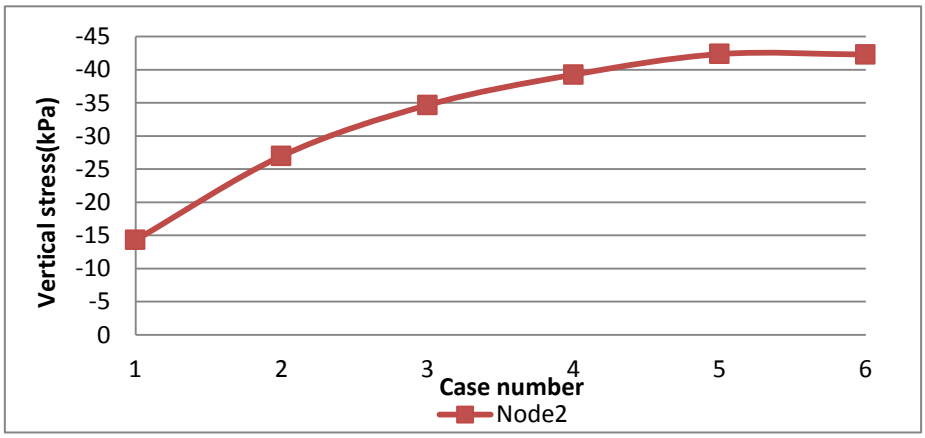
that data collected from points at the bottom corner of a sleeper may not be valid in the 3D analysis either.




(a)




(b)




(c)

Figure 3.21 Vertical stresses vary with mesh sizes at (a) nodes 3-6 (b) node 1 (c) node 2

As shown in Figure 3.22, a comparison of vertical stress at the same position in both longitudinal section and cross section models has been carried out. Ideally, both values should be exactly the same, but the vertical stress in the longitudinal model is around 13% lower than the stress in the cross section model. This is partly because the rail and fastening system are neglected in the cross section model, more stresses directly spread into substructure so that the vertical stress is much higher than the one in longitudinal model. In other words, rail and fastening system play a significant role to decrease the stress spreading to substructure, which means both of these two components can effectively reduce the vertical stress from the static wheel load. Furthermore, these two models are all simulated in two dimensions, the results cannot be ensured accurately enough.

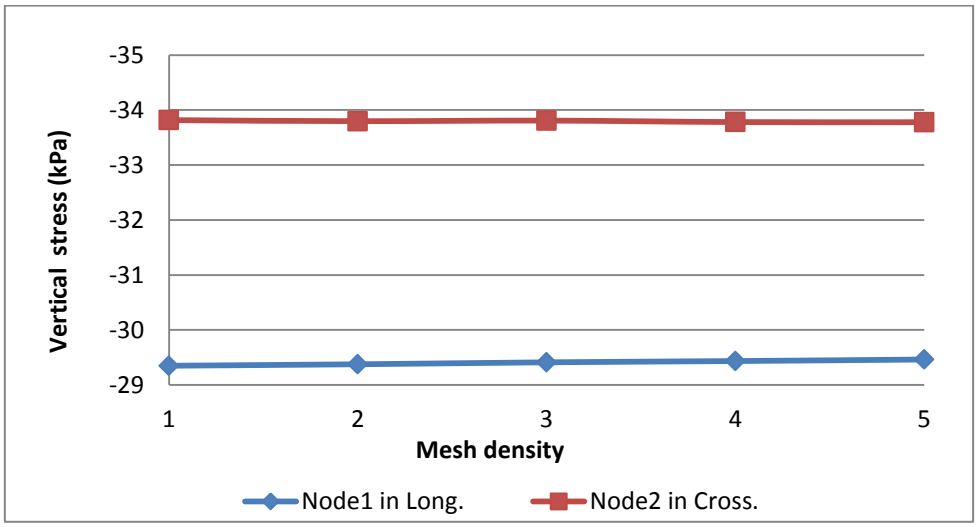



Figure 3.22 Comparison of the results from same position in two different models

## 3.2 Summary

Two different section models for a railway track system have been described and analysed in this chapter. After comparing the two simulated models, a significant issue has to be taken into account: all the stresses calculated at measuring points at the bottom corner of the sleeper change depending on mesh density (Figure 3.10; Figure 3.21(b)). It is hard to achieve an accurate stress value at the bottom corner of the sleeper because of calculation difficulties when a stress concentration occurs. This suggests that data collected from points at the bottom corner of a sleeper may not be valid in the 3D analysis either.

Both the advantages and disadvantages of 2D simulation are briefly presented as well. For a 2D simulation, it is impossible to reproduce traffic loadings in reality. Also, it is not possible to simulate either displacement or stress state in all three axes. Consequently, a 3D model needs to be built up and a full analysis will be presented in the following chapters.

# 4 3D Trackbed Model Design

In order to have a better and detailed understanding of stress states as well as displacements underneath sleepers in different planes, a 3D railway trackbed model has been designed and developed in this research. Several factors including dimension, boundary condition and mesh details need to be taken into account. Therefore, a series of confirmation tests and analyses have been done and are described in this chapter. Furthermore, an assessment of the difference in response between single and dual axles has also been carried out.

## 4.1 3D Model

Before the testing model can be set up, dimensions and material properties for all parts have to be determined. Meanwhile, the steps used in the simulation, load level, boundary conditions and mesh details for this initial model will be introduced in this section.

### 4.1.1 Dimension

As mentioned in the 2D simulation work, because the rail trackbed structure is fully symmetric, it is unnecessary to build the entire trackbed system. In order to save time during simulation, a half model, which is symmetric about YZ plane, has been adopted during the whole research.

The first step in the 3D model study was to simulate the UIC60 type of rail, for which the actual profile of the rail was simplified as an ‘I’ shape with the dimensions shown in Figure 4.1. Between sleeper and rail, a rail pad with dimension of 200*150*10mm is inserted.

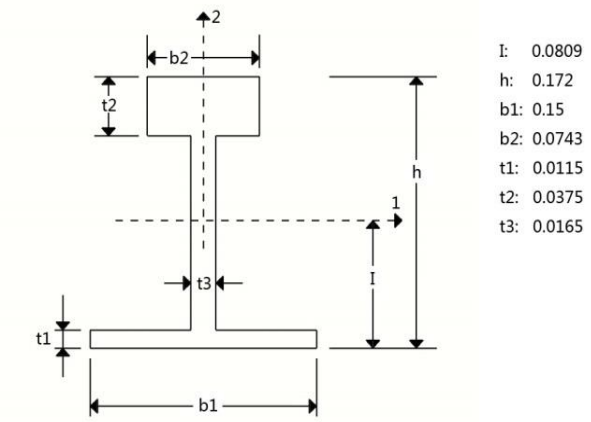



Figure 4.1 Dimensions of the simplified rail UIC60 in m (Esveld, 2001)

Following the International Union of Railways (UIC) Code719R (1994), 300mm of ballast and 150mm of subballast were adopted in the analysis. Next, to guarantee a representative length for data evaluation, and based on the results of the 2D model illustrated in Chapter 3, a longer substructure with 22m length was set up. A set of illustrations with partitions and dimensions is presented in Figure 4.2 (a), (b) and (c) respectively. A layered railway configuration was designed overlying a semi-circular shape with radius R forming the profile of the subgrade. This special design allows fewer elements to be generated in comparison to a traditional rectangular shape.

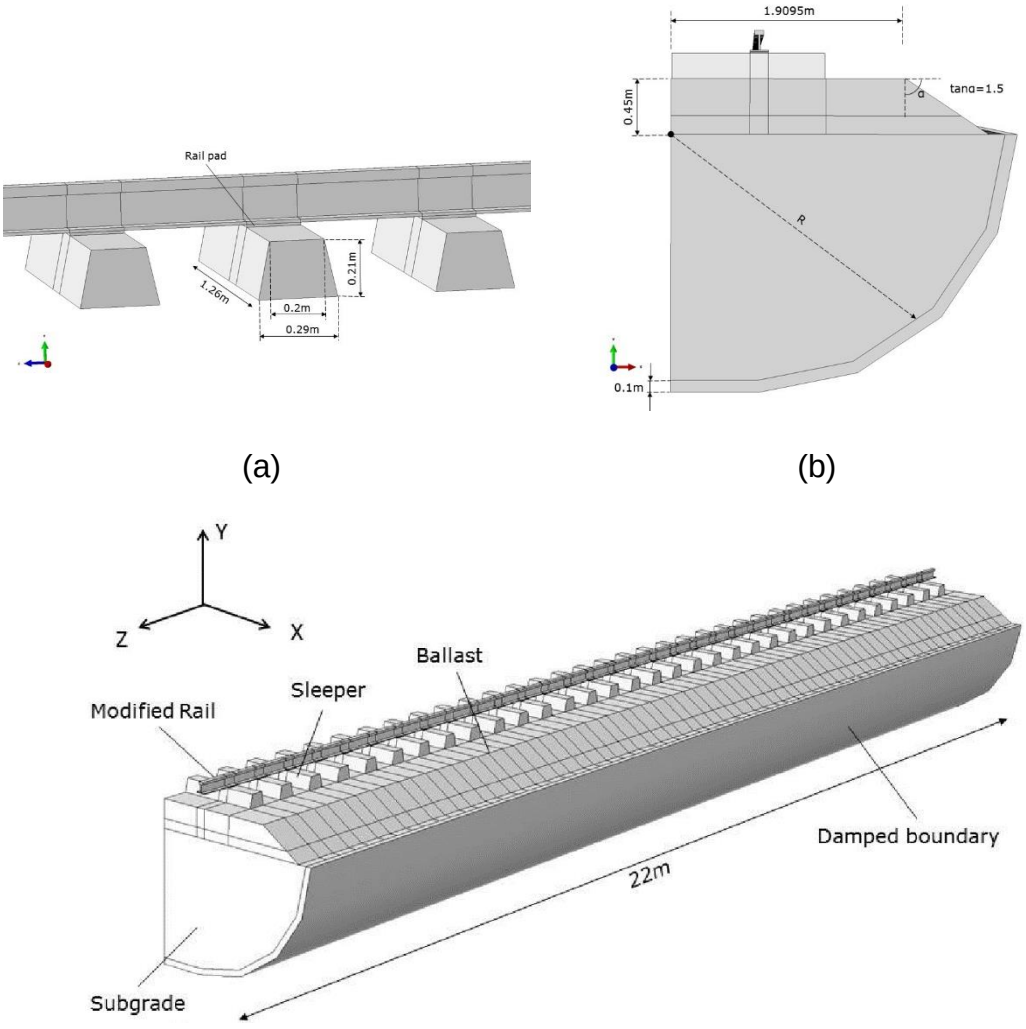



Figure 4.2 (a) Sketch of sleeper and railpad (b) Dimensions of model (c) Overview of 3D model

A key requirement was that any energy wave which is generated by the dynamic moving load must be allowed to dissipate at the boundary of the model and not to get reflected. Based on this consideration, a conventional solution would be to set up a foundation with sufficiently large depth so that there is enough space for wave propagation and no time for reflection. However, this would lead to a very large number of elements and it would be hard to satisfy the computational requirements.

To illustrate the difficulty, the shortest distance required between the load and a rigid boundary in order to avoid reflected wave effects has been calculated to be 151m; this will be shown in detail in Section 4.3. Also, the average volume of each subgrade element which has been used in the ultimate model in Chapter 5 is approximately 0.06m$^3$, which is a relatively coarse mesh for the FE model, but the total element quantity still reached 17621. Also, the time consumed for a run is about 5 hours. If 151m is required, then approximately 356 times more elements than this would be generated. The time consumed for simulation increases exponentially. As a result, it is not realistic to apply a far boundary in this research.

Although the ballast shoulder is vital to retain the railway trackbed and to fix sleepers in a stable position, however, its function is not as significant as the main layer of ballast. Since the simulation applies to a one-off moving load, the long term effect of the ballast shoulder is irrelevant. Consequently, this part has been simplified and the sleepers are assumed to be placed over the ballast layer directly.

### 4.1.2 Material Properties

Rail trackbeds are composed of different materials. As commonly used on UK rail lines, the G44 sleeper which is made of reinforced concrete was chosen as the sleeper within this model (Pen, 2008). All material properties in this model which relate to a normal railway trackbed are listed in Table 4.1 (Yang *et al*., 2009). Since this model is a linear elastic simulation, only Young's modulus and Poisson's ratio with typical values are taken into account.

Due to dynamic effects, density is also used. An additional layer of boundary which is displayed in Figure 4.2(c) has been utilised in the 3D model so that it absorbs the energy wave. Material damping is only used in this layer. A set of alpha values will be determined in Section 4.2.

Table 4.1 Material Properties

| Component description | Young's Modulus E (MPa) | Poisson Ratio v | Density ρ (kg/m$^3$) | Others |
|---|---|---|---|---|
| Rail | 210000 | 0.3 | 7850 | Flexural inertia $I_r$ (m$^4$): 3.055 x 10$^{-5}$ |
| Pad | 6.9357 | 0.49 | 1280 | Natural rubber |
| Sleeper | 30000 | 0.2 | 2400 | Reinforced concrete |
| Ballast | 140 | 0.4 | 1700 | |
| Sub-ballast | 140 | 0.4 | 2300 | |
| Subgrade | 75 | 0.35 | 2300 | |

### 4.1.3 Load

A wheel load is simplified as a uniform pressure and applied on the surface of the rail which is shown in Figure 4.3. A user subroutine named VDLoad is used to control the speed and the area location for the moving load. The original code is shown in Figure 4.4. As mentioned in Chapter 3, the real contact area between rail and wheel is about 155mm$^2$. However, the small area is only needed to calculate stresses in the rail close to the contact and it makes negligible difference to stresses below rail level. As a result, it is not necessary to simulate such a small area in this model, for

which a huge quantity of elements would be required. For example, a single element surface on top of the rail is 1238mm$^2$ which is already small enough for most FEM simulations. In order to satisfy the real contact area, about 8 times more than the current quantity of elements would be needed. To achieve a simpler calculation and save computing time, an equivalent pressure has been used according to the following equation:

$$F = PA = P_{modified}\, A_{modified} \qquad \text{Equation 4.1}$$

Where: F is the constant single wheel load,

P is the pressure in reality, and

A is the contact area in reality.

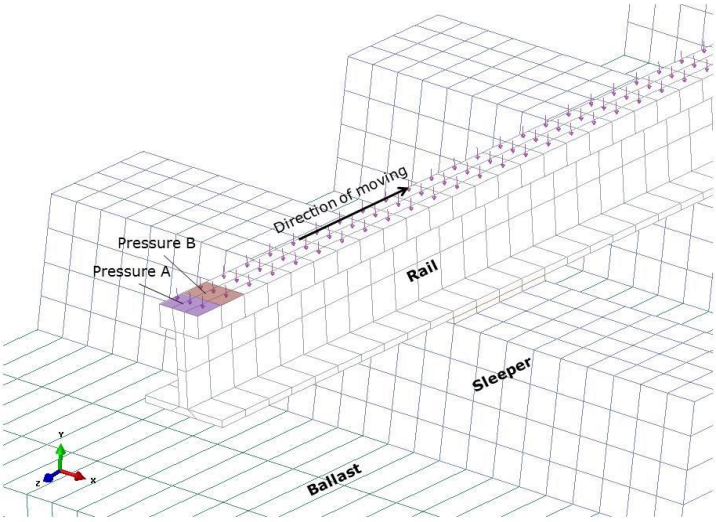



Figure 4.3 Load pressure located on the surface of rail

```
      subroutine vdload (
     C Read only (unmodifiable)variables -
     1 nblock, ndim, stepTime, totalTime,
     2 amplitude, curCoords, velocity, dirCos, jltyp, sname,
     C Write only (modifiable) variable -
     1 value )
     C
      include 'vaba_param.inc'
     C
      dimension curCoords(nblock,ndim), velocity(nblock,ndim),
     1 dirCos(nblock,ndim,ndim), value(nblock)
      character*80 sname
     C
      parameter(vel=84.0d0,dlen=0.05d0,pressure=16150.74024d3)
      integer k
       disp=vel*steptime
              zc=disp
              zmax=zc
              zmin=zmax-dlen

              do k=1, nblock
        if(curCoords(k,3).lt.zmax.and.curCoords(k,3).ge.zmin) then
          value(k)=amplitude * pressure
              else
                value(k)=0.0
              end if
              enddo

      return
      end
```

Figure 4.4 The user subroutine moving load control

Normally, a static wheel load of a passenger coach is around 60kN (Esveld, 2001). Therefore, a constant single wheel load F=60kN is applied in the conformation tests.

### 4.1.4 Step

As the moving load code VDload can only been used under ABAQUS/Explicit, an explicit dynamic load step approach was chosen for these tests. It is an automatic type of incrementation. The maximum increment size is unlimited. All the data output frequency is evenly spaced in 440 time intervals so that enough results from all the nodes located on the rail surface can be collected.

### 4.1.5 Boundary Condition

Referring to Figure 4.2(c), displacement in the z direction has been restricted at both ends of the model whereas the x and y directions are still free to move. For the

symmetric surface, a symmetric boundary in the YZ plane is applied. This means there is no movement in the x direction and no rotation regarding y and z directions. In order to optimise the dimensions as well as reduce element quantities, a 10mm thin layer of damped boundary has been fixed at the outer subgrade edge which will be fully described in Section 4.2 and 4.3. With respect to the interaction properties between two different layers, a simplification has been made that all the nodes at the interfaces are completely tied to ensure the stress and displacements can spread downwards with no interruption.

### 4.1.6 Mesh

Figure 4.5 shows the mesh of a 3D model for initial tests aimed at designing an optimised final model. For a fine meshed element, many requirements such as face corner angle and edge length have to be satisfied in order to achieve the most accurate result. However, this chapter will mainly be concerned with the broad characteristics of the model, and only coarse trends of the data are needed; hence it is not necessary to employ a fine mesh at the very beginning. Consequently, only coarse C3D8R elements (8-node linear brick type with reduced integration) are included in Figure 4.5, which can achieve results more efficiently and sharply reduce the computing time. However, the elements on the rail surface still need to be seeded evenly to permit equal time step intervals.

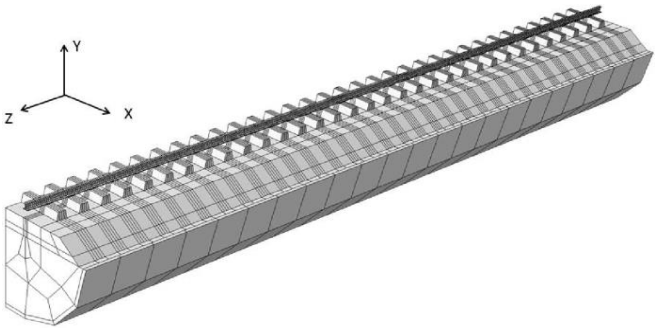



Figure 4.5 The mesh of the 3D model for optimising design

Although most of the elements presented above do not meet the requirements for easy and correct computation in ABAQUS which have been discussed in Chapter 2, the nodes at the interface between two different parts (e.g. rail and rail pad, sleeper and ballast) have to be aligned and connected properly.

## 4.2 Boundary Condition

Before optimising the depth of subgrade, a layer of damped boundary was added to the FE model to prevent wave reflection. Damping was not considered in any other parts of the model, a decision which is justified by the comparative study of results with and without material damping presented in Appendix B.

It is difficult to assign the alpha and beta damping mathematically. As fully described in Chapter 2, only the alpha damping has been chosen for the damped boundary layer. Tao (2010) also indicated that there is no obvious influence on wave absorption if the alpha value is relatively low. Consequently, a comparison of the

effects of alpha damping on vertical displacement has been made, using the following set of alpha damping values: 10, $10^2$, $10^3$, $10^4$, $10^5$ and $10^6$.

Figure 4.6 shows a sketch of the 0.1m thick damped boundary. The radius of this layer is 2m, the layer being immediately adjacent to the outer subgrade. Moreover, all the basic elastic material properties are exactly the same as in the subgrade. It can therefore be expected that less computational difficulties will occur from interaction effects.

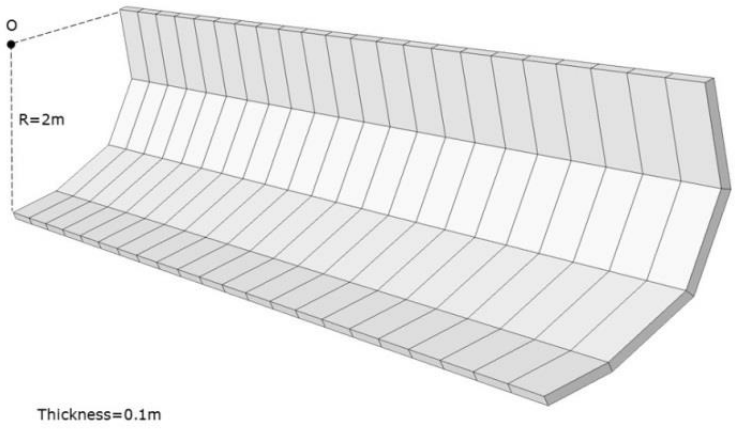



Figure 4.6 Meshed damped boundary for alpha value test

It is worth noting that all the degrees of freedom have been constrained at the outer surface of this layer to prevent any movement or rotation. A single wheel moving load with a magnitude of 60kN and speed of 300km/h is applied in the test.

Figure 4.7 shows the history of vertical displacement retrieved from the 3D model with different alpha damping coefficients. All data relate to a point on the ballast surface under the $13^{th}$ sleeper from the moving load start point of the model. This is expected to avoid the boundary effects and to have a sufficient loading period to

generate the displacement curve. The properties for all cases are exactly the same except the damping value. The vertical deflection decreases with increasing alpha damping up to a value of $10^4$. However, it is noted that the maximum vertical deflection increases again when the alpha damping is larger than $10^4$. It may be because the extremely large alpha damping (i.e. $10^5$ and $10^6$) leads to a vibration whose frequency is similar to the system's natural frequency that causes a larger deflection. The values of $10^3$ and $10^4$ for alpha are evidently the optimum in terms of decreasing amplitude, however, $10^4$ gives marginally quicker amplitude reduction. Ultimately, $10^4$ is confirmed as the alpha damping value of the extra thin boundary layer for all models in this project. However, it is clear that there is still some oscillations with a 2m subgrade depth and so it is now necessary to find the most suitable subgrade depth with this damping value.

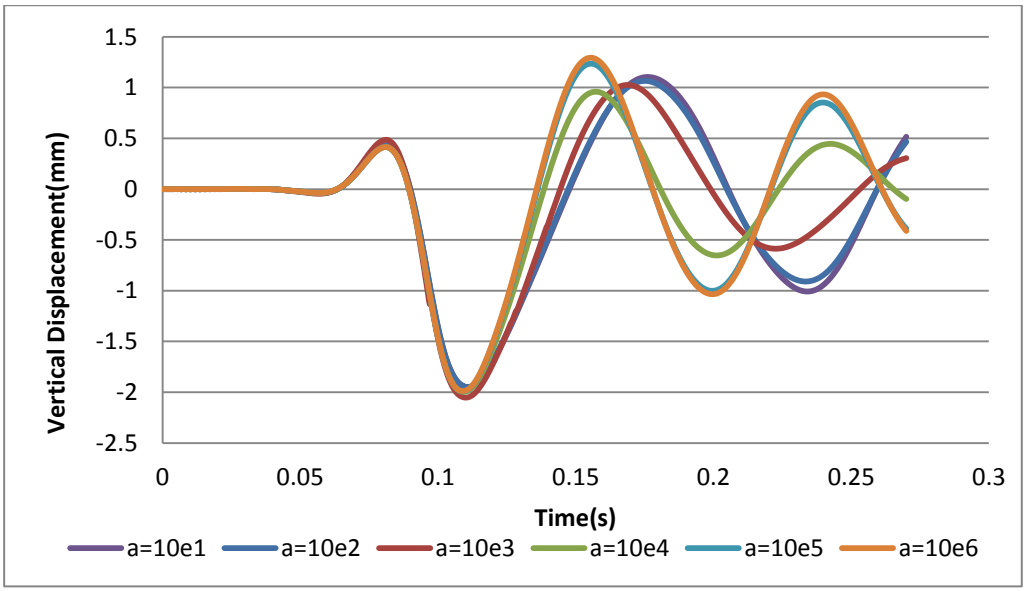



Figure 4.7 Influence of the alpha damping coefficient on vertical displacement

## 4.3 Subgrade Depth

### 4.3.1 Theoretical Depth

After the alpha damping coefficient has been set for the boundary, an exact depth for the subgrade needed to be confirmed. The subgrade is the largest part of the model; minimizing the depth can significantly reduce the element quantity as well as the simulation computing time.

To ensure that the energy wave reflection will not affect the results in the trackbed, a calculation has been made to determine the minimum depth of subgrade required with a rigid boundary.

An incident energy wave (elastic body wave) including primary wave where the movement is parallel to the direction of wave propagation and, secondary wave where the movement is vertical (perpendicular to the direction of wave propagation), act on the boundary. The velocity for the primary wave can be calculated by Equation 4.2.

$$\mathrm{Vp} = \sqrt{\frac{(1-\nu)\mathrm{E}}{(1-2\nu)(1+\nu)\rho}} \qquad \text{Equation 4.2}$$

where: E is the Young's modulus,

v is the Poisson's ratio,

ρ is the density of the propagation medium.

Also, Equation 4.3 gives the velocity of the secondary wave.

$$Vs = \sqrt{\frac{E}{2(1+\nu)\rho}} \qquad \text{Equation 4.3}$$

All the values of parameters are listed in Table 4.2.

Table 4.2 Characteristic for wave velocity calculation

| Component | E (MPa) | v | ρ (kg/m$^3$) |
|---|---|---|---|
| Subgrade | 75 | 0.35 | 2300 |

$V_p$ and $V_s$ can be calculated from these two equations, giving 228.8m/s and 109.9m/s. If it is assumed that the subgrade depth is D, then the return journey for the wave is 2D, and in order to avoid the effect of the wave reflection and minimise the distance between the load path and the bottom of the subgrade, then:

$$T_{wave}=2D/V_p \geq T_{max} \qquad \text{Equation 4.3}$$

where: $T_{wave}$ is the total time for a wave return from the bottom subgrade and,

$T_{max}$ is the time for a moving load to pass by a 22m long model at a speed of 60km/h. This is to ensure the wave reflection cannot reach the subgrade surface at the lowest load speed within the duration of the applied moving load.

From the equations, 151m is found as the minimum depth required for the subgrade.

### 4.3.2 Subgrade Depth Design

Before optimizing the subgrade depth, a group of different depths, namely 2m, 5m, 8m, 10m, 12m and 20m have been evaluated. Models with these subgrade depths have been generated, all with a damped boundary with an alpha coefficient of $10^4$ and applying a wheel speed of 300km/h. A depth of 155m for the subgrade with a fixed end far boundary was also set up, since it can be expected that this depth is sufficient to avoid the influence of energy wave reflection.

Figure 4.8 shows the maximum vertical displacement on the ballast surface right underneath the loading path with different subgrade depths. In order to achieve a good understanding of the variation for all curves, a sufficient number of nodes in the longitudinal direction need to be highlighted. However, because of the large amount of elements generated in the ballast, it is neither necessary nor possible to output the data for every node. Therefore, the nodes that have been used to show the data have been chosen evenly from both the middle bottom and corner of the sleeper and the two far ends of the model.

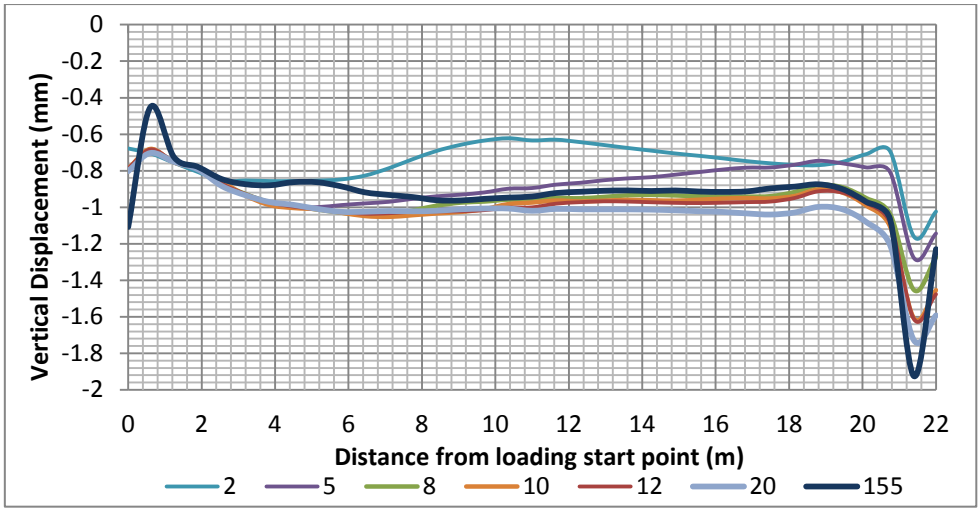



Figure 4.8 Vertical displacement comparisons on different subgrade depths

The vertical displacement for all curves of 8m, 10m, 12m, 20m and 155m subgrade depth increases over the first four metres and tends to be smooth after that. Moreover, all these curves with different subgrade depths with damped boundary are close to the result for 155m and a rigid boundary. However, the 2m and 5m subgrades give relatively irregular variation with distance. In this case it can be seen that the subgrade is either too shallow or the alpha value is not large enough to prevent wave reflection. As a result, an 8m depth subgrade was finally chosen for the optimised 3D model for use in the rest of project.

Furthermore, as presented in Figure 4.9, vertical displacements are quite similar between 8m with damped boundary and 155m with rigid boundary, especially over the distance range of 8.4m-18.15m, with only about 1.6% difference on average. Since this distance range appears to be most suitable for data analysis, a more detailed mesh will be made in this area, as described in section 4.4.

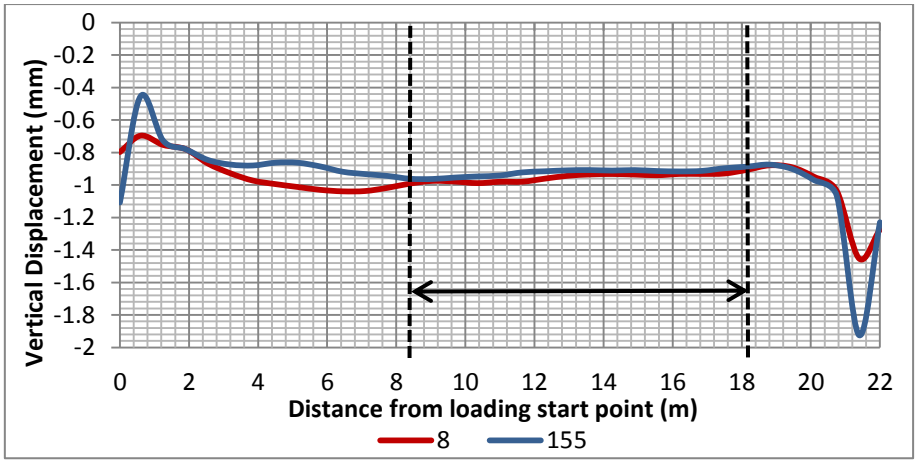



Figure 4.9 Comparison of peak vertical displacement from 8m and 155m depth subgrade models

It is noted that significant deviations occur at both ends for all the curves. This is expected to happen and neither change of boundary conditions nor change to the load application approach (e.g. a static load applied at the start followed by a moving load) will avoid the boundary effects. At the start, the load was applied immediately onto the rail and this may have caused an unrepresentatively large vertical deflection. Meanwhile, the substructure is then lifted slightly after the load has moved a certain distance, and this causes a lower vertical displacement at about 1m away from moving load starting point. With regard to the end zone, the vertical displacement has a sharp increase. However, since the maximum vertical displacement occurred as the loading point passed by the last sleeper of the model, this should not affect the analytical area which is between 8 and 18m as shown in Figure 4.9.

A brief study on the influence of the boundary at both ends was conducted. A partial distance loading was applied to the 3D model, with 8m deep subgrade and damped boundary layer, as shown in Figure 4.10. Both the start and end points for loading were about 3.85m away from the ends of the model. This effectively avoids the

influence of the end boundaries. All the other properties were exactly the same as in previous cases.

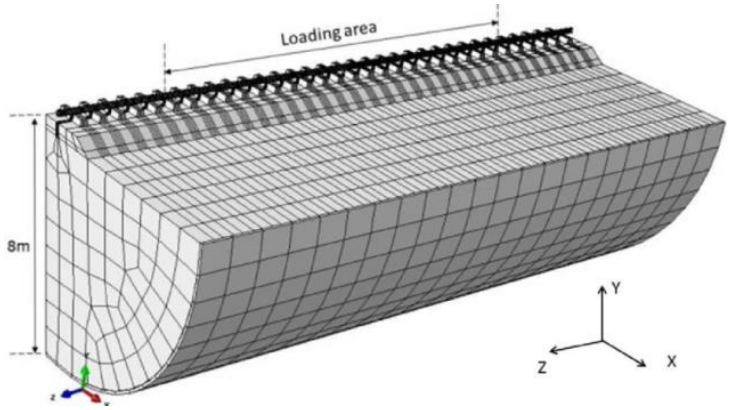



Figure 4.10 Coarse meshed 3D model sketch

Figure 4.11 shows the comparison of the maximum vertical displacement at different nodes on the ballast surface right underneath the loading area shown in Figure 4.9 and Figure 4.10. The maximum vertical displacement increases sharply from about 0.3mm to 0.9mm over the first 4m of the loading path. The curve then tends to be smooth and this lasts to the end. Compared to the curves which were presented in Figure 4.9, there is no sharp change at all when the moving load reached the end of its travel. Clearly, vertical displacement can be affected seriously by the boundary condition. Meanwhile, the average vertical displacement of 0.95mm between 8.4 and 18.15m is exactly the same as for the 8m-deep-subgrade case shown in Figure 4.9. From this study it can be seen that the results over the specified area will not be affected by the boundary condition.

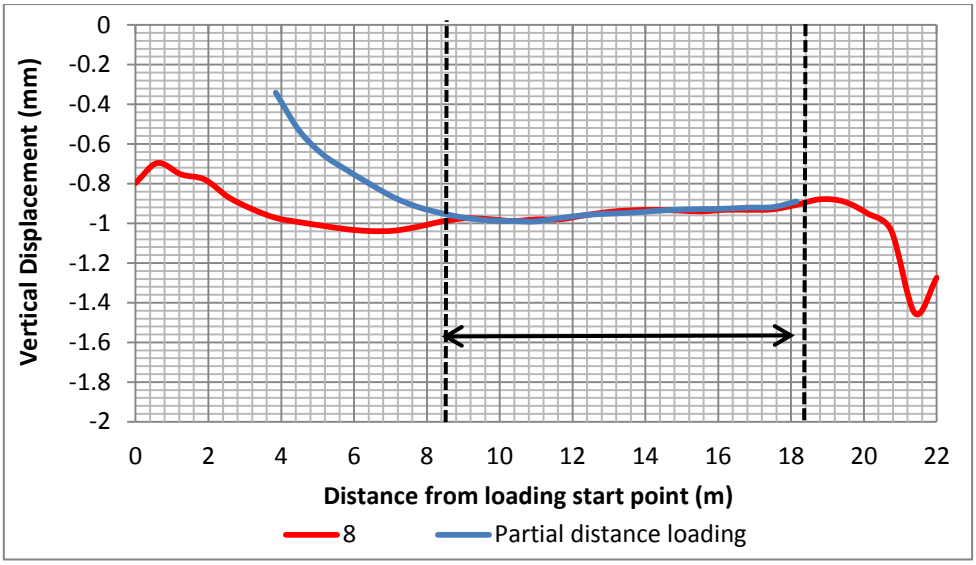



Figure 4.11 Maximum vertical displacements on different nodes

## 4.4 Mesh Density

An optimised fine meshed model then had to be set up. This was optimised not only for the accuracy of analysis, but also to optimise time usage in the simulations. Four different mesh densities were trialled, covering what was considered to be the range of potentially viable and computationally feasible solutions. The element details for those four different meshes, with 12026, 63427, 121403 and 145967 elements respectively, are listed in Table 4.3. Based on the aims of this research, the differences between these meshes are controlled by mesh density at the sleeper-ballast interface. Therefore, the mesh density mainly varies at ballast.

Table 4.3 Mesh quantities for three models

| Case number | A | B | C | D |
|---|---|---|---|---|
| Rail | 3520 | 3520 | 3520 | 3520 |
| Rail pad | 12*33 | 12*33 | 12*33 | 12*33 |
| Sleeper | 24*33 | 336*33 | 400*33 | 400*33 |
| Ballast | 2324 | 33750 | 86130 | 109890 |
| Subgrade | 4690 | 14137 | 17621 | 18425 |
| Boundary layer | 308 | 536 | 536 | 536 |
| Total amount | 12030 | 63427 | 121403 | 145967 |

As can be readily seen in Figure 4.12, all curves are relatively flat at about 9-17m after some settling down at the very beginning. Curves B, C and D are reasonably close to each other during the whole period. The average differences between curves B and C, and C and D, are 2.22% and 2.57% respectively. However, it is worth noting that there is a 4% difference between curves B and C and only 1.06% difference between curves C and D over the area of more detailed mesh mentioned above. Because the analysis will mainly be focussed on this range, and with regard to computing efficiency, case C was chosen for the ultimate optimised model.

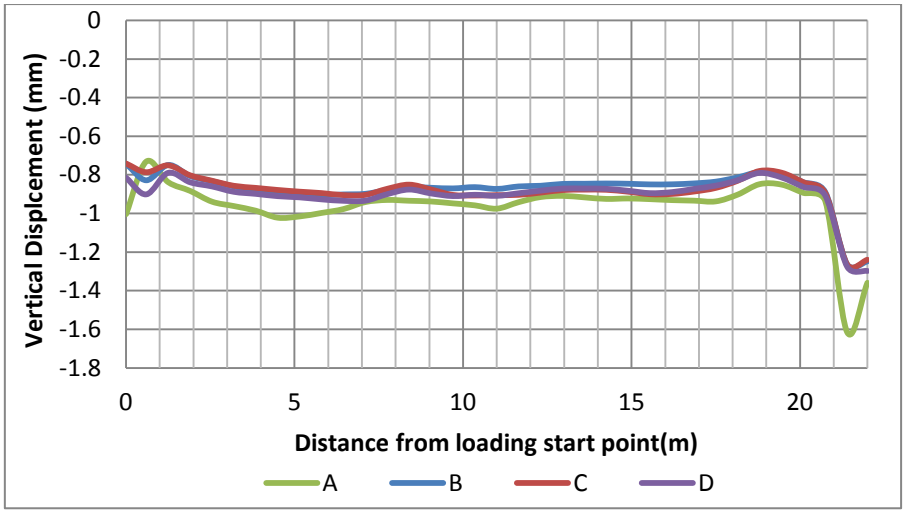



Figure 4.12 Maximum vertical displacement comparisons on different mesh quantities

## 4.5 Loading

A test exploring the differences between a single load and double loads is presented in this section. The test used the same material properties for the model as shown in Table 4.1. A uniform pressure equivalent to a 125kN concentrated load which is the maximum permitted static wheel load in the UK was applied as a moving wheel load. A set of load speeds, namely 60km/h, 120km/h, 200km/h and 300km/h, has also been applied. Conventionally, the bogie wheel separation on a passenger coach is about 2400mm-2700mm and 2700mm was chosen in this test of the influence of multiple loads rather than one. The VDload code for controlling the two-wheel load is displayed in Figure 4.13.

```
      subroutine vdload (
C Read only (unmodifiable)variables -
     1 nblock, ndim, stepTime, totalTime,
     2 amplitude, curCoords, velocity, dirCos, jltyp, sname,
C Write only (modifiable) variable -
     1 value )
C
      include 'vaba_param.inc'
C
      dimension curCoords(nblock,ndim), velocity(nblock,ndim),
     1  dirCos(nblock,ndim,ndim), value(nblock)
      character*80 sname
C
      parameter(vel=84.0d0,dlen=0.05d0,pressure=33647.3755d3)
      integer k
       disp=vel*steptime
              zc=disp
              zmax=zc
              zmin=zmax-dlen
       zmax1=zmin-2.7
       zmin1=zmax1-dlen
              do  k=1, nblock
       if((curCoords(k,3).lt.zmax.and.curCoords(k,3).ge.zmin).or.
     1 (curCoords(k,3).lt.zmax1.and.curCoords(k,3).ge.zmin1)) then
           value(k)=amplitude * pressure
                else
                  value(k)=0.0
                end if
       enddo

             return
      end
```

Figure 4.13 The user subroutine for two moving loads

Based on the results from Figure 3.21, to avoid being deceived by potentially inaccurate results due to stress concentration at the bottom corner of the sleeper, a range of key positions located in different depths of the ballast underneath the rail (away from the sleeper-ballast interface at the sleeper corners where stress concentrations occur) in the detailed meshed area are chosen for 3D simulations and illustrated in Figure 4.14. Points at both the interface of sleeper-ballast and 150mm below the ballast surface have been considered in this sensitivity study.

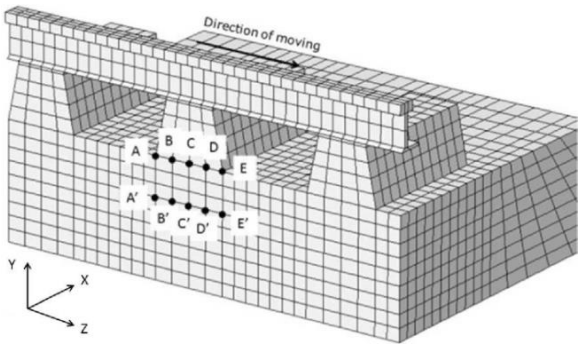
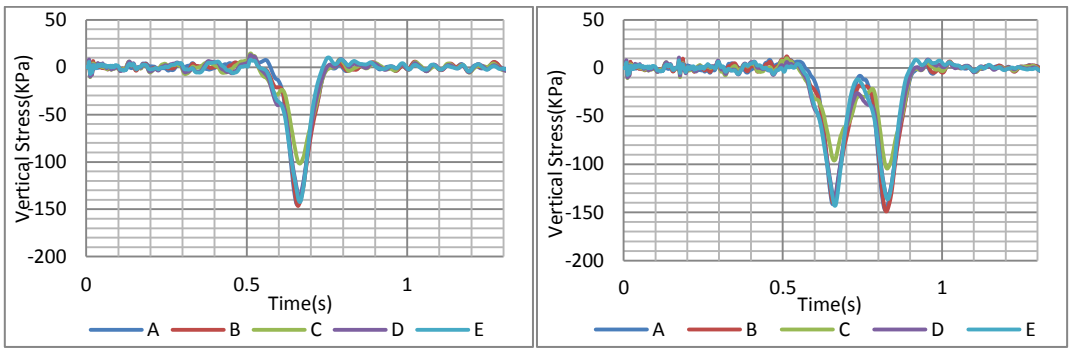
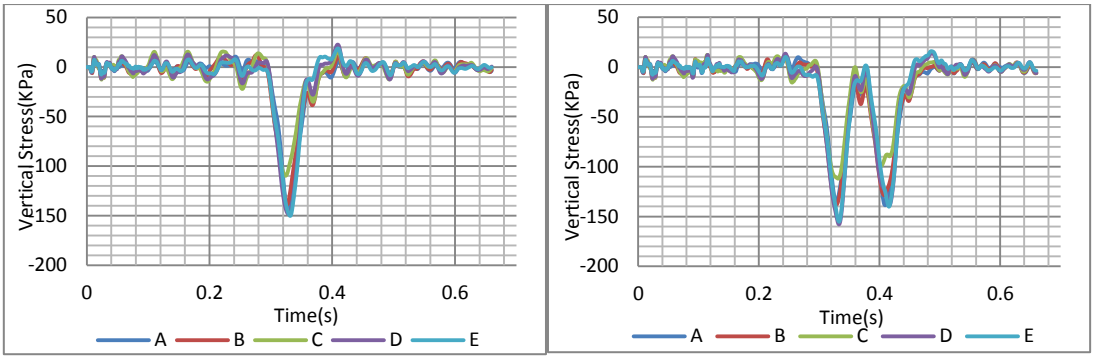



Figure 4.14 Points underneath moving load path

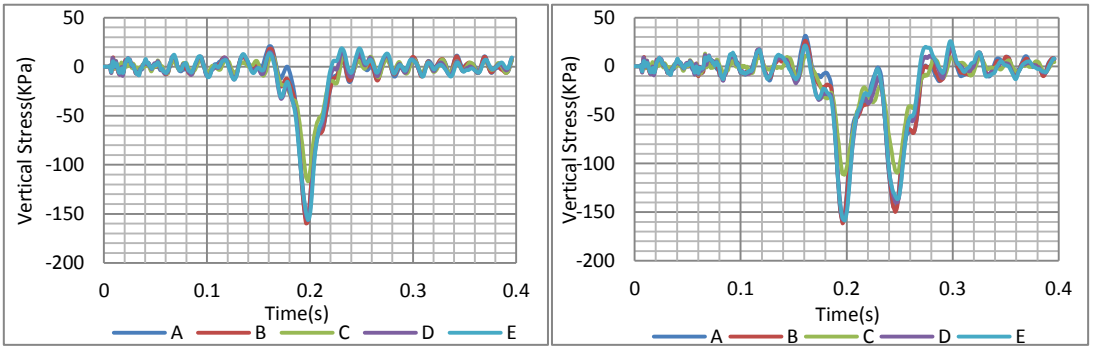
A comparison of the vertical stress changes at the ballast surface under single and double moving loads at different speeds has been made and is displayed in Figure 4.15. Despite the peaks of vertical stresses that occurred when the moving load was in the neighbourhood of the measured points, there was little stress oscillation when the load was away which could be a result of ambient vibration. The maximum vertical stress in both cases occurs at the bottom corner of the sleeper where it would logically cause a stress concentration. Furthermore, the magnitude at all locations under a single load is very similar to those under double loads.



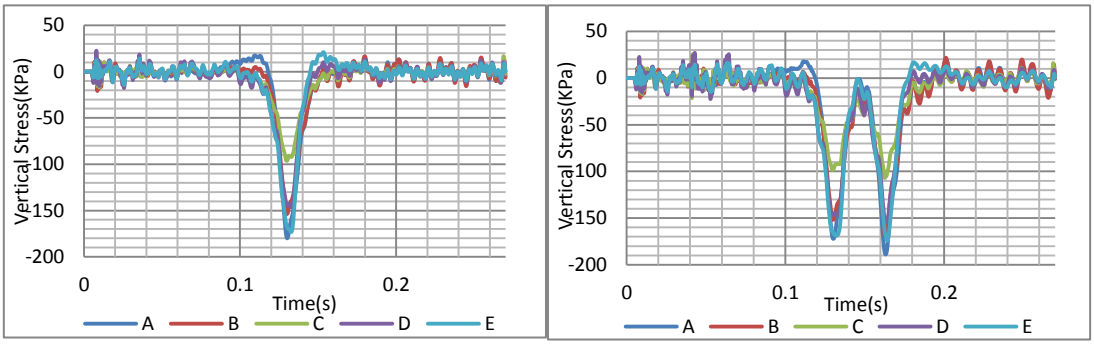

(a)




(b)




(c)

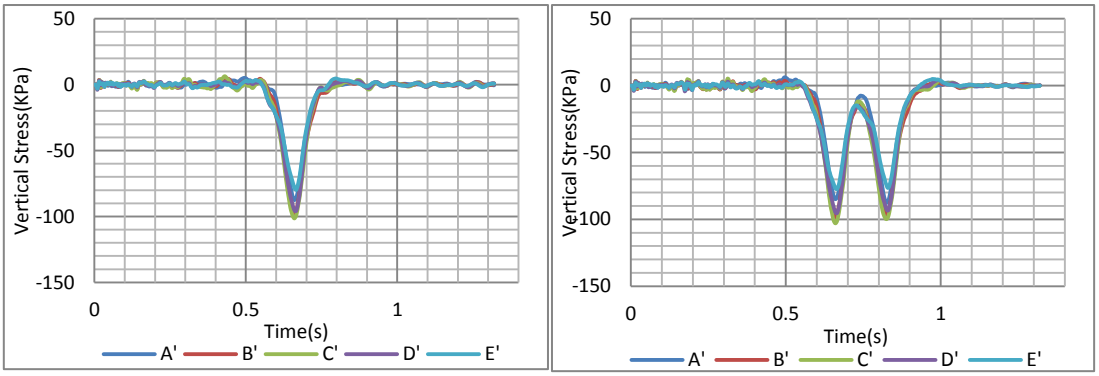



(d)

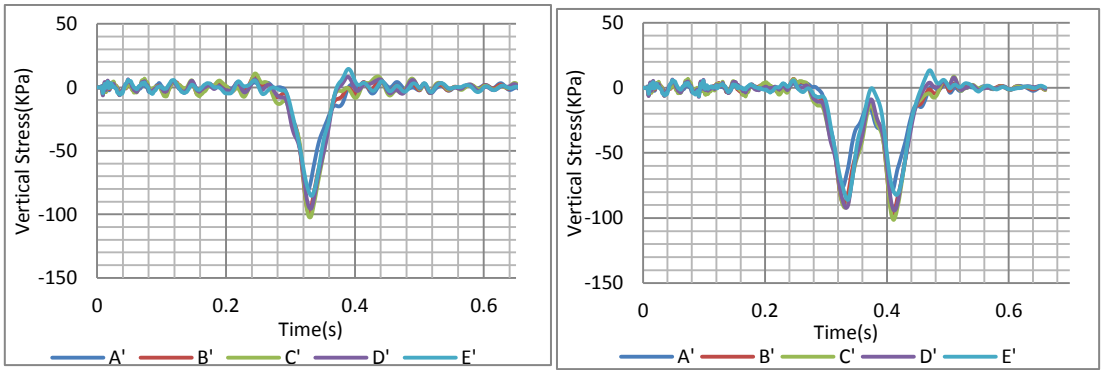
Figure 4.15 Vertical stresses on ballast surface under single load and double loads with a speed of (a) 60km/h (b) 120km/h (c) 200km/h and (d) 300km/h

Figure 4.16 shows the vertical stress 150mm below the ballast surface under single and double moving loads at different speeds. This can be expected to avoid possible computation difficulties at the interface and stress concentrations at the bottom

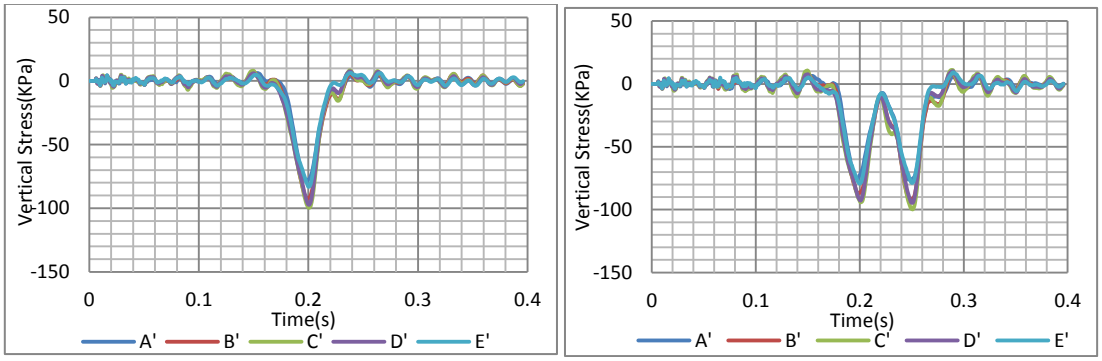
edges of a sleeper. As can be found in Figure 4.15, the maximum vertical stresses at all locations when under a single load are all very close to those under double loads.



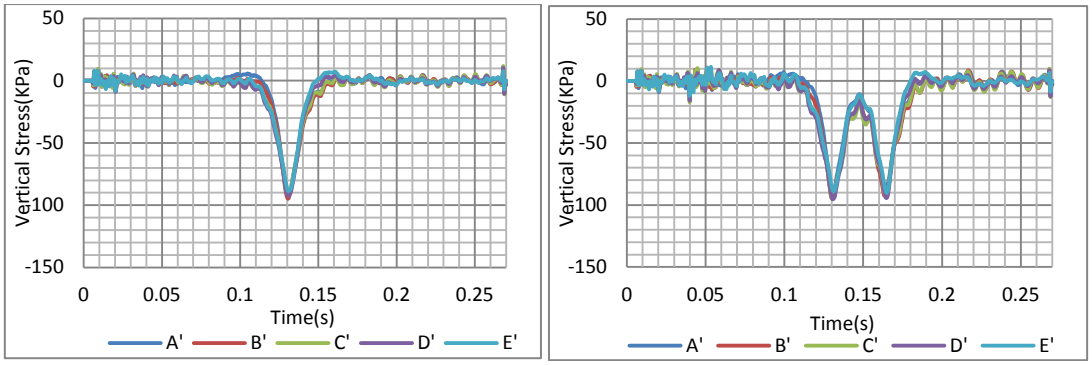

(a)




(b)




(c)




(d)

Figure 4.16 Vertical stresses 150mm beneath ballast surface under single load and double loads with a speed of (a) 60km/h (b) 120km/h (c) 200km/h and (d) 300km/h

All the differences in maximum stress at each node between single and double moving loads shown in Figure 4.15 and 4.16 are listed in Table 4.4. The locations of the nodes can be found in Figure 4.14. It is clear that the differences in maximum vertical stress are generally relatively small. However, it is worth noting that at a speed of 300km/h, the average difference for A-E is higher than those at lower speeds. It can be concluded that at high speeds, there can be a significant difference between the results for the single and double loads, especially at middle points i.e. points B, C and D. These points will not be selected for further study which focuses on the response at point A (i.e. see Figure 6.5).This is logical since a higher loading speed leads to more significant dynamic effects, including interaction between the two wheel effects.

Figure 4.17 presents the difference in maximum vertical displacement between the above two cases at a moving load speed of 300km/h. The trends for both curves are similar. In particular, between the distances of 8.4-18.15m, i.e. the more detailed mesh area, the magnitude of the differences is least. The average difference is about 4.2%, which is considered acceptably small. Consequently, and bearing in mind the

need to minimize computation time, the case with a single moving load will be adopted for the rest of the project as representative of actual vehicle loading.

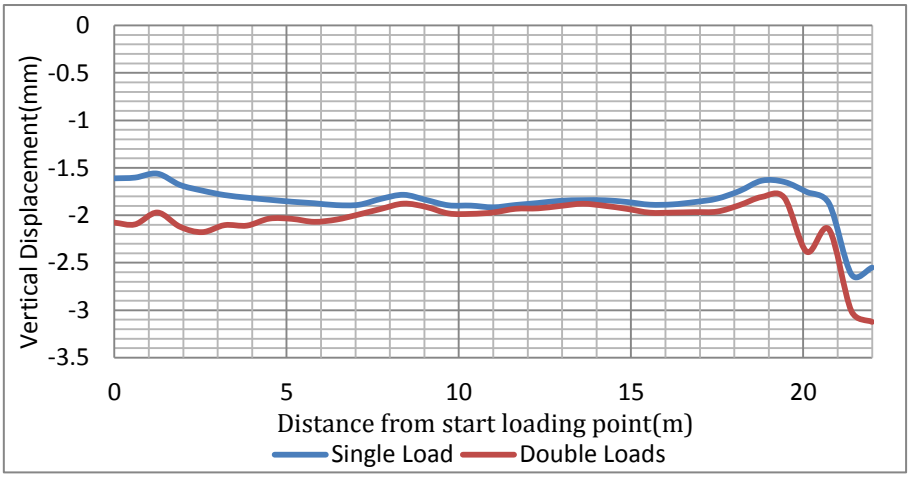



Figure 4.17 Maximum vertical displacement comparisons with single and double wheel loads

Table 4.4 Maximum vertical stress differences

| | 60km/h | | | 120km/h | | |
|---|---|---|---|---|---|---|
| Node No. | Single Load(kPa) | Double Loads(kPa) | % | Single Load(kPa) | Double Loads(kPa) | % |
| A | -145.107 | -147.595 | 2% | -144.653 | -138.742 | 4% |
| B | -146.573 | -149.046 | 2% | -138.758 | -138.317 | 0% |
| C | -101.798 | -104.574 | 3% | -109.745 | -111.993 | 2% |
| D | -137.042 | -136.716 | 0% | -148.183 | -157.994 | 7% |
| E | -142.426 | -143.066 | 0% | -150.300 | -155.275 | 3% |
| Average | | | 1.4% | | | 3.2% |
| A’ | -87.5642 | -87.5764 | 0% | -80.8893 | -794.815 | 2% |
| B’ | -98.2504 | -98.3538 | 0% | -98.6006 | -96.3349 | 2% |
| C’ | -101.491 | -102.980 | 1% | -102.391 | -101.449 | 1% |
| D’ | -95.9399 | -95.4393 | 1% | -95.6865 | -94.2163 | 2% |
| E’ | -78.3781 | -77.4327 | 1% | -85.423 | -86.1499 | 1% |
| Average | | | 0.6% | | | 1.6% |
| | 200km/h | | | 300km/h | | |
| A | -156.852 | -159.781 | 2% | -179.947 | -189.007 | 5.6 |
| B | -159.721 | -161.687 | 1% | -153.817 | -170.24 | 10.5 |
| C | -116.958 | -111.594 | 5% | -96.3523 | -106.929 | 10.9 |
| D | -156.636 | -157.520 | 1% | -144.136 | -155.155 | 7.6 |
| E | -156.211 | -158.771 | 2% | -173.318 | -173.819 | 0.3 |
| Average | | | 2.2% | | | 7.0% |
| A’ | -78.7333 | -76.034 | 3% | -91.7951 | -89.1328 | 2.9 |
| B’ | -92.446 | -91.7772 | 1% | -94.8278 | -95.2587 | 0.5 |
| C’ | -99.6376 | -99.8026 | 0% | -91.6189 | -95.0594 | 3.8 |
| D’ | -97.2606 | -94.5761 | 3% | -92.7138 | -95.4263 | 2.9 |
| E’ | -82.9947 | -79.4064 | 4% | -88.5897 | -90.2211 | 1.8 |
| Average | | | 2.2% | | | 2.4% |

## 4.6 Frequency Response

Track geometry is easily changed and the maintenance costs could be potentially high due to the vibration of railway track. A recent study on power spectrum analysis was carried out by Priest *et al.* (2010). The study related to a 60km section of freight rail track of the COALlink line in South Africa.

A four layered foundation was made between the underlying subgrade and ballast. All the material properties of this section of the rail track were obtained by Shaw (2005) and are presented in Table 4.5.

Table 4.5 Material Properties for the track monitoring site in South Africa

| Component description | Young's Modulus E (MPa) | Poisson Ratio v | Density ρ (kg/m$^3$) | Remarks |
|---|---|---|---|---|
| Rail | 210000 | 0.3 | 7850 | Flexural inertia $I_r$ (m$^4$): 3.055 x 10$^{-5}$ |
| Pad | 6.9357 | 0.49 | 1280 | Natural rubber (Liegner, 2002) |
| Sleeper | 30000 | 0.2 | 2400 | Reinforced concrete |
| Ballast | 100 | 0.3 | 1800 | |
| Foundation 1 | 321 | 0.3 | 2300 | |
| Foundation 2 | 296 | 0.3 | 2200 | |
| Foundation 3 | 143 | 0.3 | 2100 | |
| Foundation 4 | 118 | 0.3 | 2100 | |
| Natural ground | 27000 | 0.25 | 2300 | |

Evidently, the formation of the track system shown above is similar to the model which is used in this project apart from the four layered foundation. Therefore the results from both in situ monitoring and simulations should be comparable.

A list of freight wagon parameters is illustrated in Table 4.6 (Priest *et al.,* 2010). An equivalent static load of 128kN was then derived and applied in the 3D simulation model. Base on the measured train speed from the section of track monitored in South Africa, a matching single moving load at a speed of 13.2m/s has been set for the 3D model.

Table 4.6 Freight wagon parameters (Priest *et al.,* 2010)

| | |
|---|---|
| Mass per vehicle body (kg) | 94400 |
| Mass per bogie (kg) | 2800 |
| Mass per wheel (kg) | 1000 |

The output data of the 3D simulation was collected from the end of the central sleeper (i.e. point A in Figure 5.5). The power spectrum analysis which was calculated from fast Fourier transforms of the velocity data from vertical geophones attached to the sleeper has been compared with the results from simulations and is shown in Figure 4.18. Clearly, the power density spectrum for the vertical geophone velocity data shown in Figure 4.18(b) has two dominant frequencies which are ~1 and ~2Hz respectively. Additional peaks occur between 4 and 8Hz. Generally, the power density spectrum for vertical simulated velocity output shows similar peak frequencies to the geophone data. However, continuous peaks in the range of ~1 to

~3Hz and ~7 to ~9Hz occurred in the simulation. This may be due to the differences between simulations and real world rail trackbed system including loading conditions and substructure configuration.

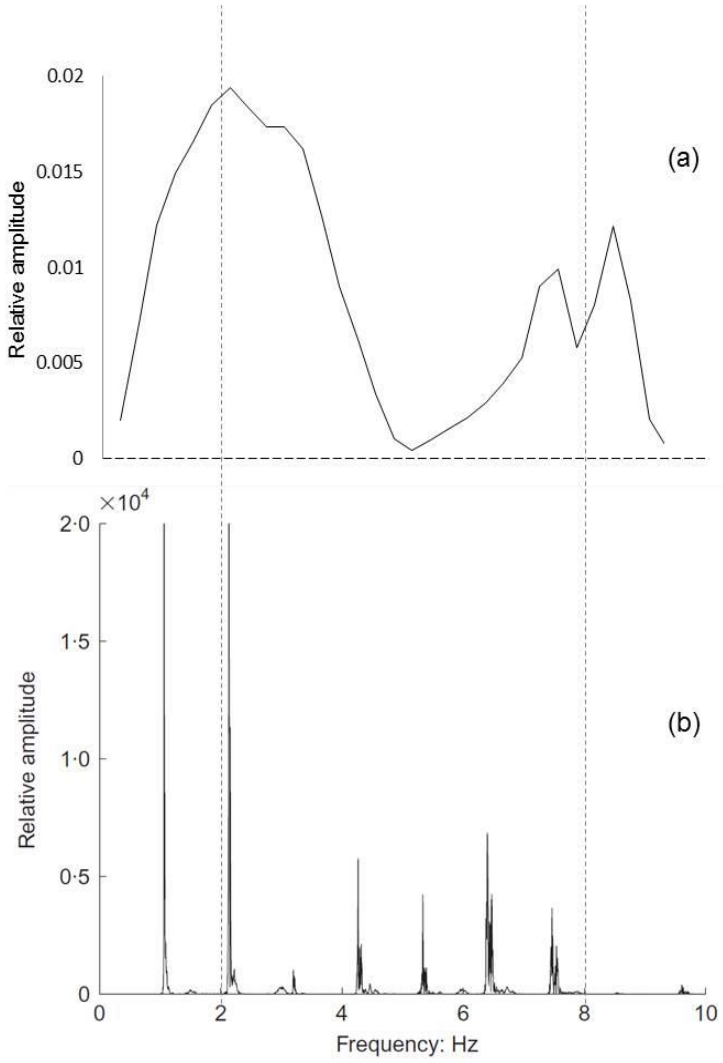



Figure 4.18 Power spectrum analysis obtained from vertical sleeper velocity data of (a) 3D simulation and (b) geophone attached to the sleeper

A similar situation can be found in Figure 4.19, which presents a comparison of the power spectrum analysis of horizontal sleeper velocity data from 3D simulation and in situ geophones. Both the power density spectrums match well and it is obvious

that the dominant frequency for both cases occurs at ~6Hz and the additional peak occurs at ~7-8Hz.

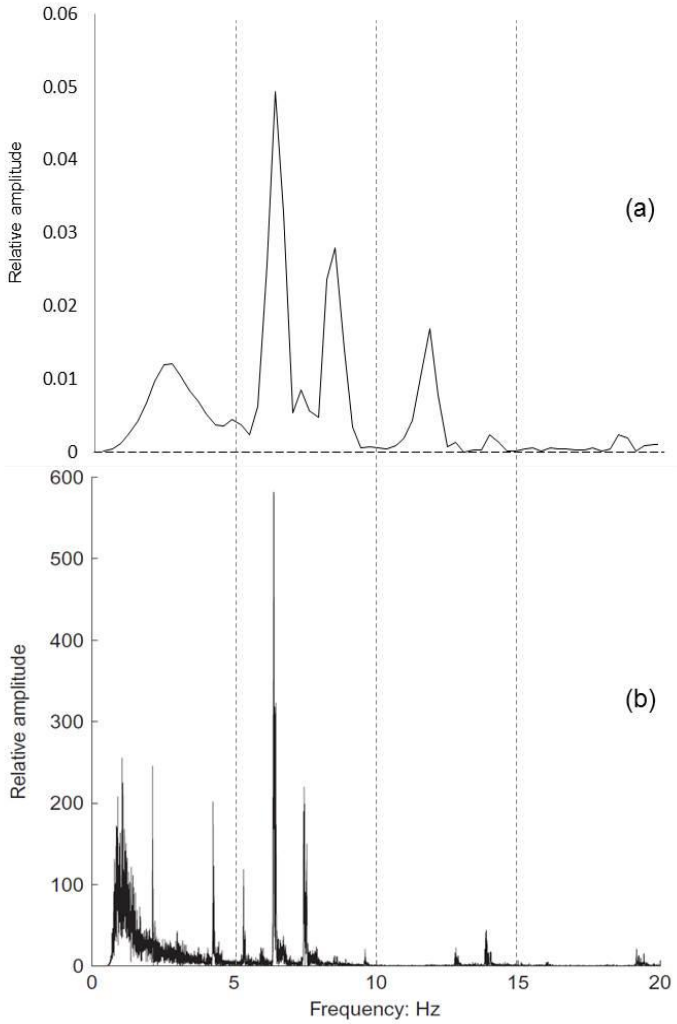



Figure 4.19 Power spectrum analysis for horizontal sleeper velocity data obtained from (a) 3D simulation and (b) geophone attached to the sleeper

In conclusion, the above analysis has clearly demonstrated that the simulation results and the in situ measurements are in fairly good agreement. Therefore, the FE dynamic trackbed model utilised in this project has been considered appropriate for practical applications.

## 4.7 Summary

In this chapter, all parameters of the model including damping boundary coefficient, subgrade depth, mesh density and wheel configurations have been investigated, design values have been chosen and ultimately confirmed by a series of simulation tests. All the results achieved from the sensitivity study are as expected, and the experiment design has been found to be acceptable.

In the damping boundary coefficient validation test, the vertical displacements increase with the increasing alpha damping value. This shows an opposite trend to the results of Lu (2010). Thus, $10^4$ is determined as the alpha damping value to control the energy reflection.

In the subgrade depth investigation, six different subgrade depths with damping boundary layer were compared with a 155m depth subgrade with a fixed boundary, calculated to be adequate to avoid wave reflection effects. After plotting all the maximum displacements against distance, the result from the model with 8m depth subgrade is one of the closest to that with 155m depth subgrade whereas lower subgrade depths show significantly different results. The 8m depth was then selected.

It has been noted that the boundary conditions at both longitudinal ends can affect the results of maximum displacement in the simulation. This has been verified in this chapter. Different approaches were investigated and the boundary effects are to be expected and cannot be totally avoided. To give an acceptably accurate result, a

distance range of 8.4-18.15m has been selected for a more detailed mesh area. Based on a comparison with a special case study in which the load was applied over a partial distance in the middle of the model, it has been confirmed that the detailed mesh area will not be significantly affected by the boundary conditions.

Four cases with different mesh densities, including a coarse mesh case and three fine mesh cases, have been investigated. The results showed that it was not necessary to increase the mesh density to the densest case. Consequently, an optimised meshed model with 121403 elements was finally selected.

A 3D model with single dynamic moving wheel load was confirmed to give an acceptable simulation of real traffic. The results from both single load and double loads models for maximum vertical stress and vertical displacement were very similar, with 1%, 2.4%, 2.2% and 3.2% differences at 60km/h, 120km/h, 200km/h and 300km/h respectively for the maximum vertical stress.

Finally, a frequency response study was conducted and a power spectrum analysis was calculated from fast Fourier transforms of the velocity data from geophones attached to a sleeper from a South African COALlink line; this was compared to the results from simulations. The study clearly showed that simulation and real measurement gave similar peak frequencies and the power density spectrums matched well in the longitudinal and vertical directions.

Thus, a 3D model has now been properly designed; all details made are ready to be used.

# 5 Detailed Dynamic Loading Case Study

There are several disadvantages of simulation work in two dimensions. In a two dimensional simulation, it is impossible to reproduce the actual traffic loadings accurately. Although a lot of computing time may be saved, many assumptions and simplifications will be present. What is more, it cannot simulate and determine quantities such as stress and displacement in the out-of-plane direction of the railway system, whereas a three dimensional model can (Wang *et al*., 2005).

Consequently, a 3D finite element railway track model developed in the previous chapter was used in the dynamic analysis performed in this chapter. A set of analyses comparing the effects of different variables on stress and deflection within ballast based on this model will be reported later; however, the details of a reference case study will firstly be illustrated in this chapter.

## 5.1 Model Description

### 5.1.1 Step

An explicit dynamic load step approach has been chosen for all the 3D simulations in this project. All the details including type of increment and maximum increment size etc. are exactly the same as in the confirmation tests which were fully described in Chapter 4. The time step will vary because of the different train speeds simulated.

### 5.1.2 Load

An element surface based uniform pressure corresponding to a static wheel load of 60kN with a moving speed of 200km/h has been chosen. These values represent a high speed passenger line. The subroutine of VDLoad has been applied to control the moving load speed, area of loading and load magnitude as has been shown in Figure 4.3 & 4.4.

### 5.1.3 Mesh

Following the confirmation tests on boundary conditions and dimensions of the model carried out as illustrated in Chapter 4, a well-designed fine meshed 3D rail trackbed model is now presented in Figure 5.1. A total of 121403 C3D8R elements, 8-node linear brick type with reduced integration, has been generated in this model.

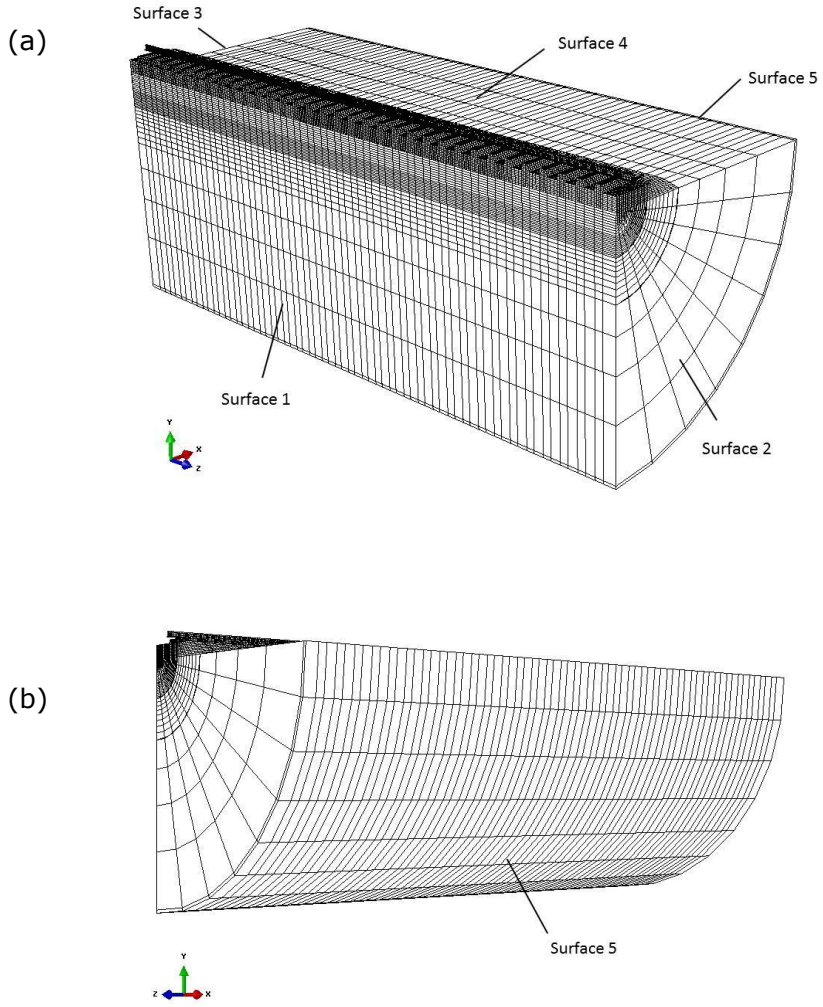



Figure 5.1 An overview of the fine meshed rail trackbed model

In order to achieve relatively accurate simulation results and to allow more details to be found at/near the interface between sleepers and ballast, following on from what was discussed in section 4.3, a detailed mesh area with 9.75m length has been defined in the ballast as shown in Figure 5.2. In this area, the volume of element is only 40% of the elements found elsewhere. More mesh details for the rail trackbed model can be found in Figure 5.3.

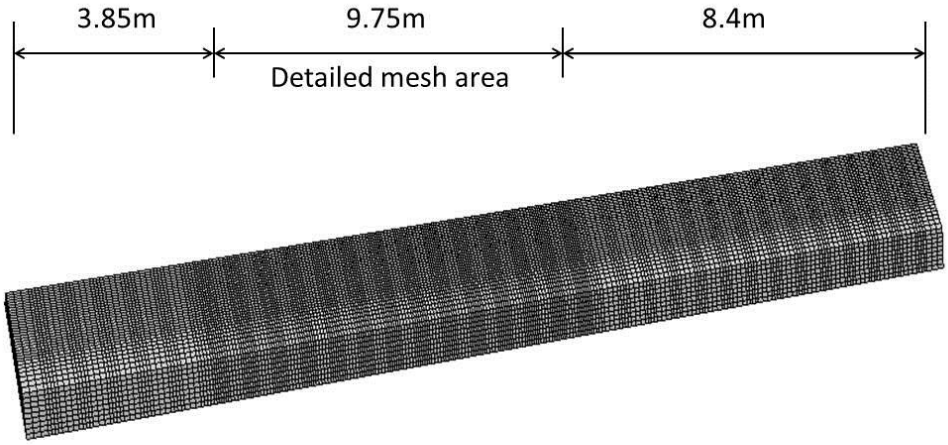
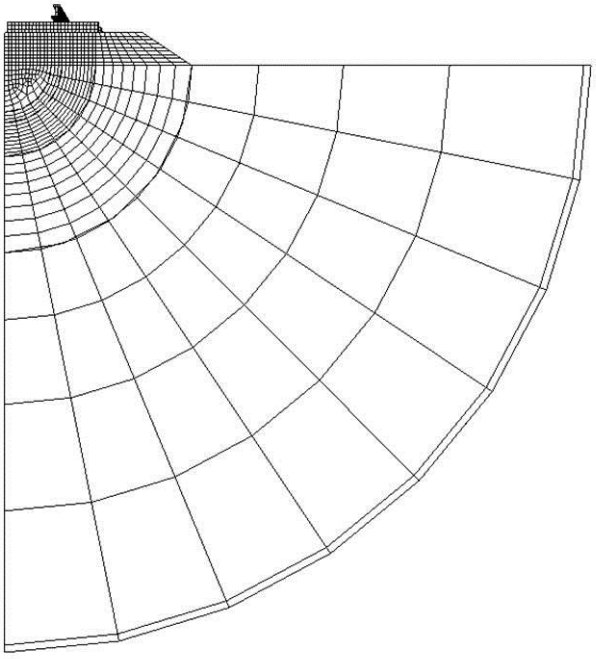
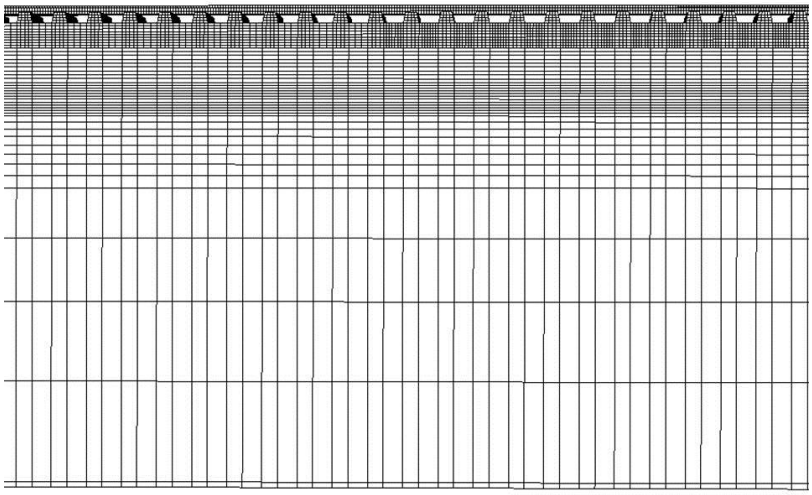



Figure 5.2 Mesh for ballast



(a)



(b)

Figure 5.3 (a) Mesh on Surface 2 & 3 (b) Mesh on Surface 1

Mesh verification has been applied to check the quality of elements which are used in this model. The failure criteria list is as follows:

- Face corner angle less than 10°
- Face corner angle greater than 160°
- Aspect ratio greater than 10
- Edge shorter than 0.01
- Edge longer than 1
- Stable time increment less than 0.0001
- Errors

It is hard to satisfy all the criteria because of the large quantity of elements being used in this model. However, it is fortunate that no error element was found during

this verification. Consequently, it can be assumed that this model is likely to be accurate enough for the purpose of this research.

### 5.1.4 Boundary Conditions

A description of boundary conditions at all five surfaces of the model as shown in Figure 5.1 is given in Table 5.1.

Table 5.1 Boundary conditions for all surfaces as illustrated in Figure 5.1

| Area | Boundary Condition |
|---|---|
| Surface 1 | A symmetry boundary. |
| Surface 2 & 3 | No displacement in z direction, but free in both x and y directions. |
| Surface 4 | Free surface. |
| Surface 5 | Encastre, all degrees of freedom are restrained. |

As shown in Figure 5.4, a thin layer of damping boundary, which has been introduced and justified in chapter 4, has been added as an ‘outer subgrade’.

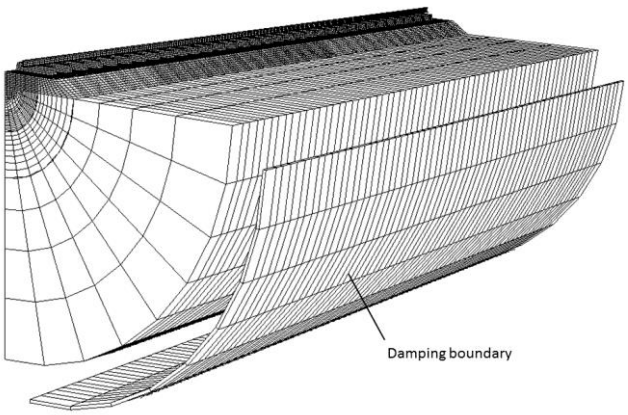



Figure 5.4 A meshed damping layer serves as an absorbing boundary

## 5.2 Reference Model

The various factors which may affect the stress distribution and displacements underneath a sleeper are explored in Chapter 6. However, in order to make comparisons of the effects of these variables accurately and logically, a reference model has first been applied, using the material properties presented in Table 4.1.

A generalised analysis of the stresses and displacements in all three directions, varying with depth, has been carried out. Ten representative paths underneath both the bottom corner and centre line of the middle sleeper of the model have been chosen, illustrated in Figure 5.5. The step time for data plotting is 0.1989s which means the moving load is right above the centre of the sleeper.

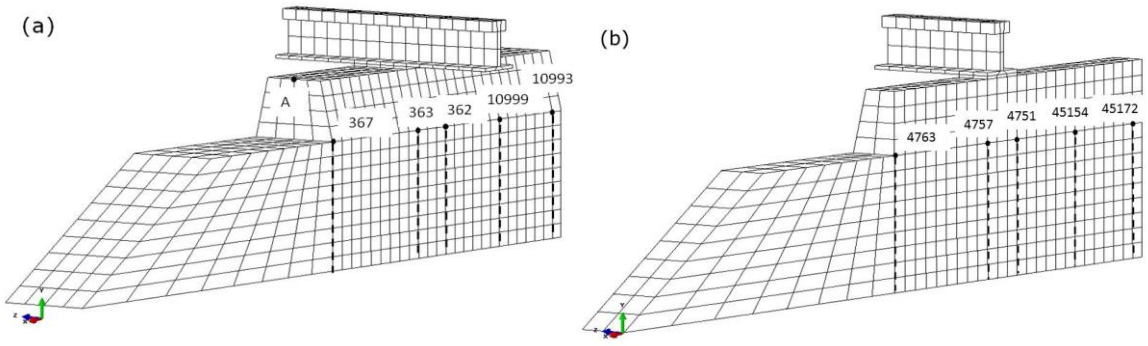



Figure 5.5 Paths at (a) the bottom corner of the sleeper (b) the centre line of the sleeper

### 5.2.1 Stress

Figure 5.6 shows as an example a vertical stress (excluding self-weight stresses) contour plot on the ballast surface underneath the chosen sleeper. All other normal and shear stress and displacement contour plots are attached in Appendix C. It can

be seen that the maximum vertical stress occurred at the interface between the ballast and the bottom corner of the sleeper but not right under the loading rail; it is due to the stress concentration.

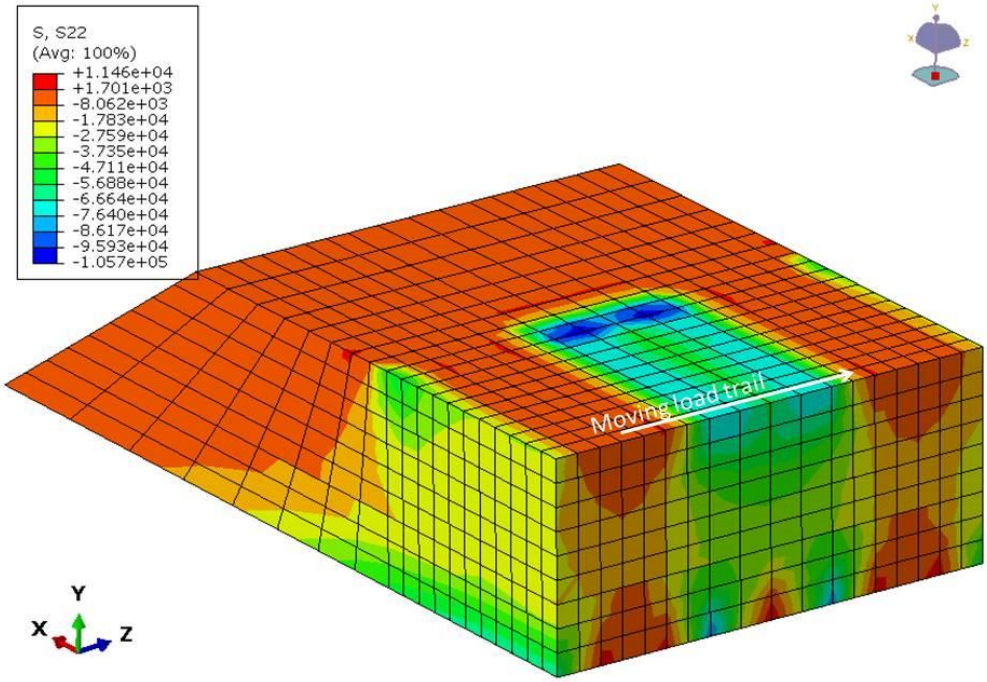



Figure 5.6 Contour plot of vertical stress in ballast

To carry out a detailed exploration of vertical stress distribution under the sleeper, stresses varying with depth on path 367 are presented in Figure 5.7. Stresses varying with depth on all other paths underneath the sleeper shown in Figure 5.5 can be found in Appendix D. It is worth mentioning that 1, 2 & 3 represent the x (lateral), y (vertical) & z (longitudinal) axes respectively in ABAQUS. For example, $s_{ij}$ is a stress acting on a plane normal to i axis and pointing towards j axis. All the maximum stresses occur at the surface of the ballast, at which point the normal stresses from the three axes are very close. As expected, the stresses reduce with increased depth in ballast. There is a total reduction of 68% in vertical stress from top to bottom

of the ballast. Even more significantly, 92% of lateral stress (s11) and 95% of longitudinal stress (s33) have been lost. However, in contrast, normal stresses show a sharp increase against increasing depth in the subballast. This may be due to linear elastic assumption. In addition, the average values of the shear stresses in all three planes are less than 40% of the normal stresses.

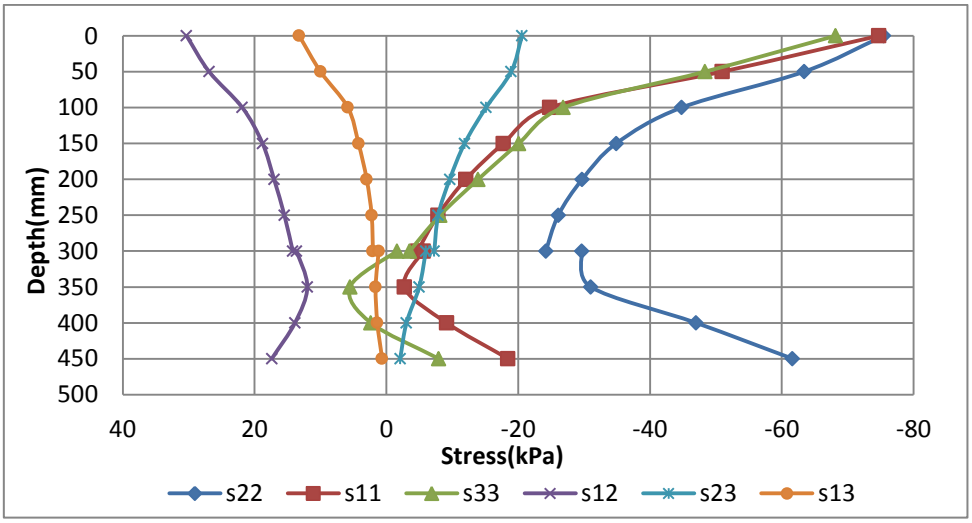



Figure 5.7 Stresses varying with depth at path 367

Figure 5.8 shows a vertical stress contour plot in the ballast under a sleeper. As this project is based on the finite element method, aggregates of discrete particles are simulated as a single continuum. Consequently, in a sense, the results may not totally reflect conditions in real rail trackbed as accurately as would be desirable. In particular, as can be seen from the curves in Figure 5.7, the data show a discontinuity at a depth of 300mm. The discontinuity is expected in horizontal stress and vertical stress. This is because of the tied constraint between the nodes of the ballast and subballast. From Figure 5.8, each node on the dashed line actually consists of two separate nodes from ballast and subballast respectively, so that the results shown from those nodes are different.

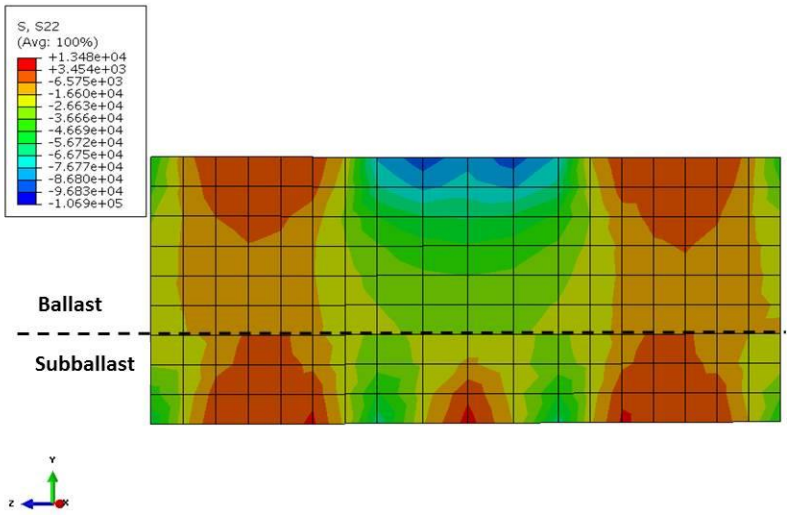



Figure 5.8 Vertical stress contour plot of YZ plane underneath bottom sleeper

At the interface between ballast and sleeper, normal stresses change against time at different locations. As shown in Figure 5.9, five key nodes at the interface between sleeper and ballast underneath the rail have been chosen to illustrate this. These specific nodes can also be seen to effectively avoid the stress concentration generated at the bottom corner of sleepers, which has been shown in Figure 3.21 and can also be seen in Figure 5.6 where high vertical stress is again apparent at the bottom corner of the sleeper.

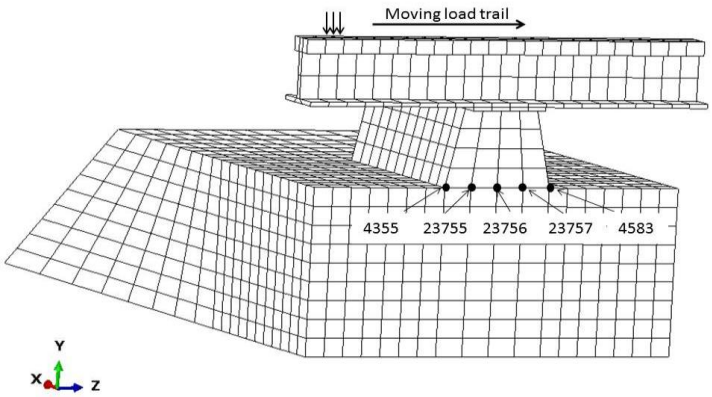



Figure 5.9 Locations at the interface underneath moving load

Figure 5.10 shows the variation in normal stress with depth beneath the loading point. Similar to the variations happening at other locations, because only vertical load has been applied, vertical stress always has the greatest value. Furthermore, as stress concentration happens at the corners of the sleeper, stresses on all three axes are less on the ballast surface for path 23756 compared with the stresses at the bottom corner of the sleeper which were given in Figure 5.7.

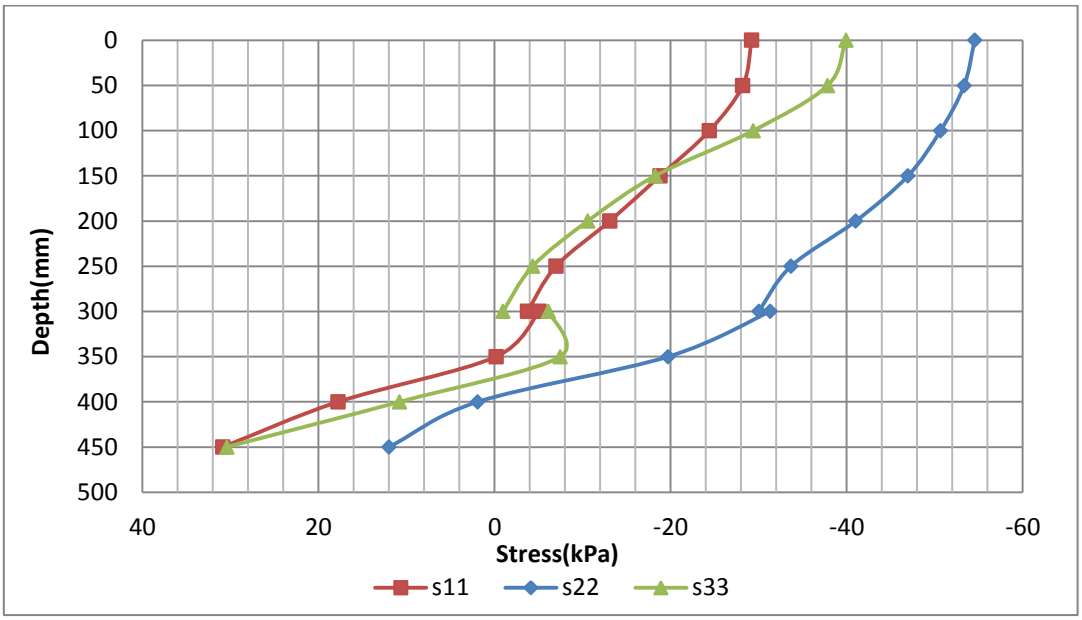



Figure 5.10 Variation in stress at path 23756 (middle of sleeper)

Other than that, it is worth noting that both horizontal and lateral stresses go tensile at the bottom of the subballast which is possibly due to the subballast being much stiffer than the subgrade, then effectively it has a plate in bending, which tensile stresses happen at its base. A deformed partial model under applied load is shown in Figure 5.11. Subballast elements at the interface penetrate into the subgrade. This causes seriously inaccurate results in this area. Since the subgrade is extensive and less critical to this research, a coarse mesh has been applied to reduce the total amount of elements and save computing time. For this reason, nodes at the interface

could not be connected fully because the average length of element in the subballast is 72mm which is only about 22% of the length of a subgrade element. The number of subgrade elements is 17621, and the number of elements for the entire model is 121403. To match the size of the subballast elements, approximately 4.5 times the number of subgrade elements would have to be used which is equal to 79295. This would have led to unacceptably long computing times.

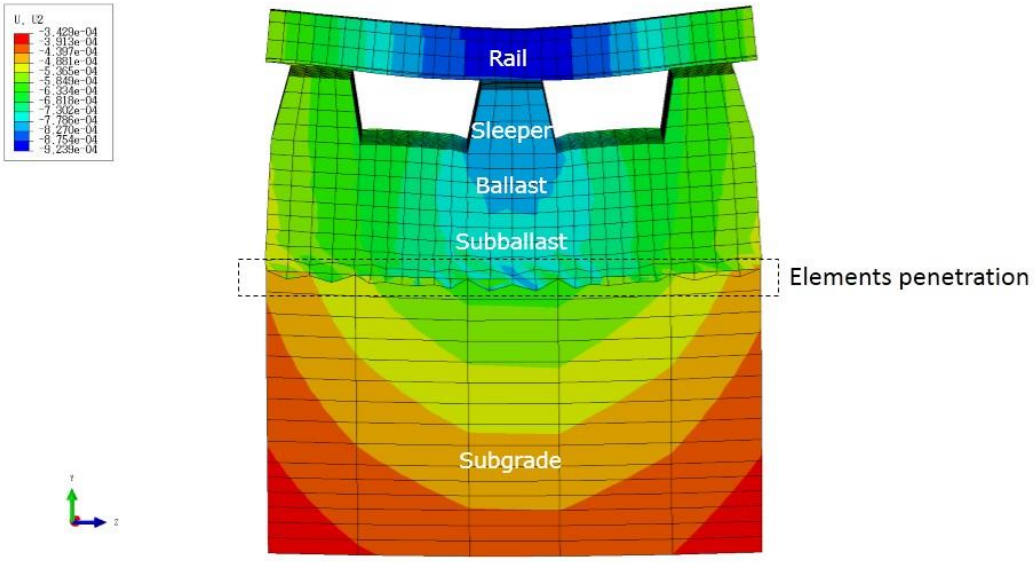
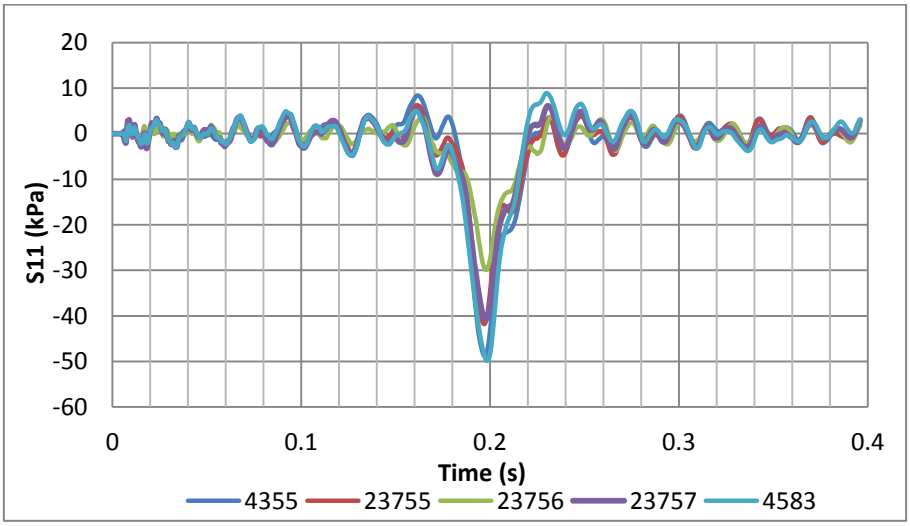


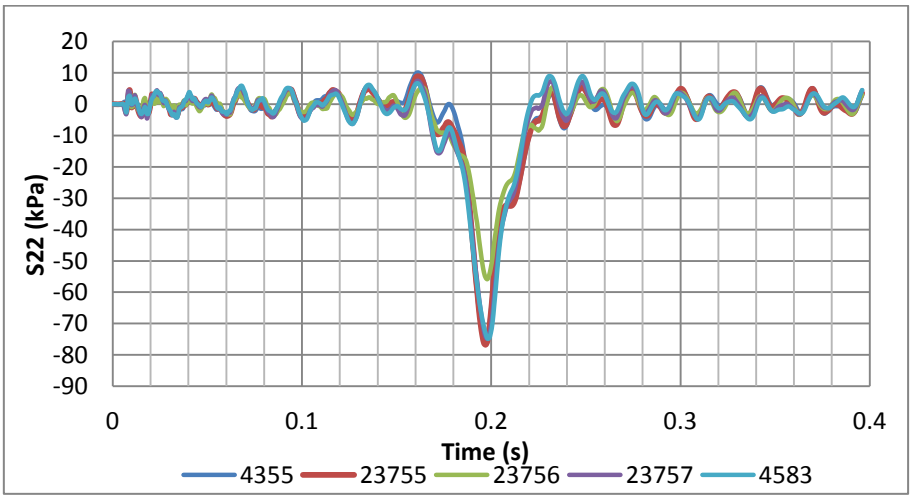

Figure 5.11 Element penetration occurs at the interface between subballast and subgrade

Figure 5.12 plots three stresses against time at the positions shown in Figure 5.9 in the X, Y and Z directions individually. Irregular ambient vibration is apparent in all three graphs, which has been discussed in the previous chapter. With reference to the positions shown in Figure 5.9, both $S_{11}$ and $S_{33}$ reduce gradually from the bottom corner to the centre line of sleeper. However, for the vertical stress, the only obvious

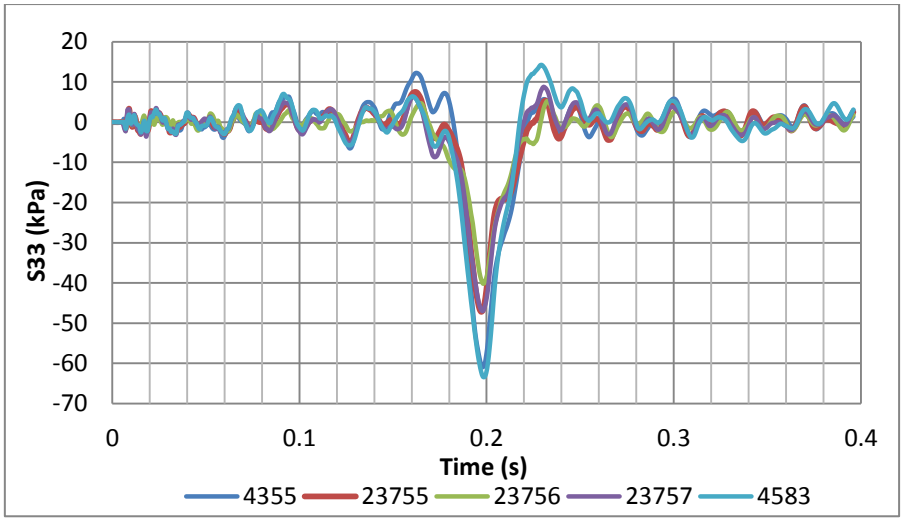
variation is a sharp reduction at the centre. In fact the central point consistently has the least normal stress which is generally only 60-70% of the maximum values at bottom corners.




(a)



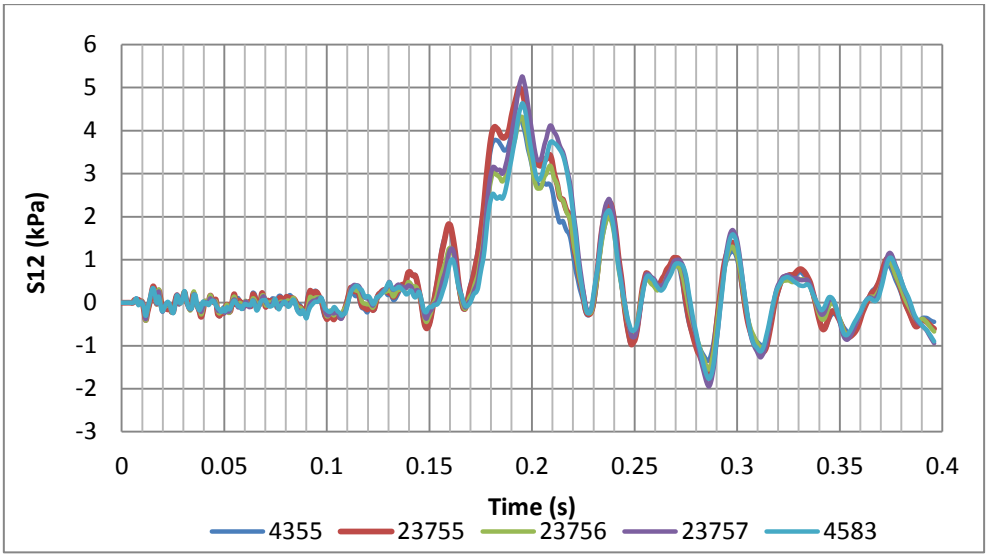

(b)



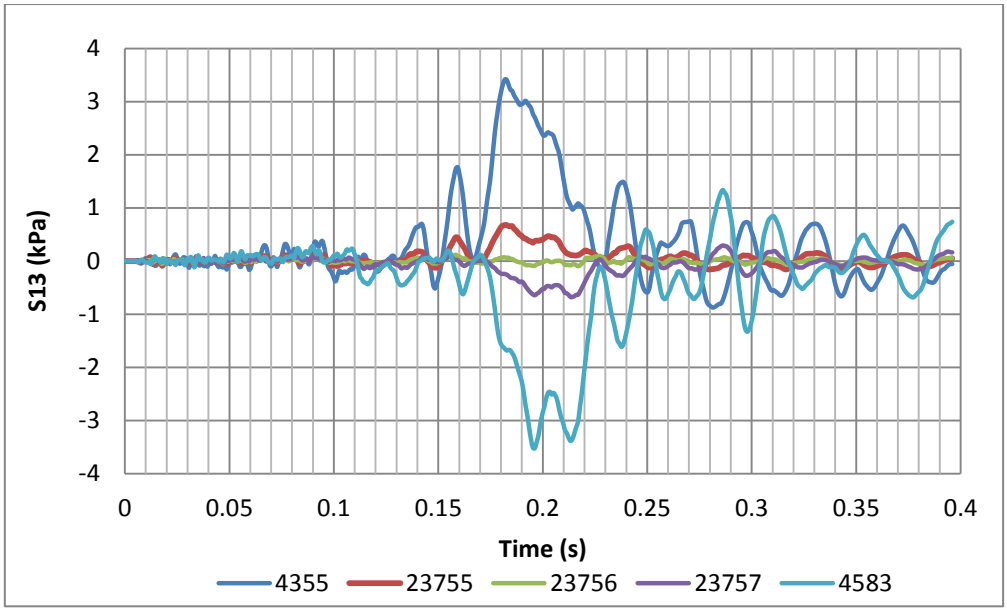

(c)

Figure 5.12 (a) Lateral stress (b) Vertical stress (c) Horizontal stress versus time at different nodes

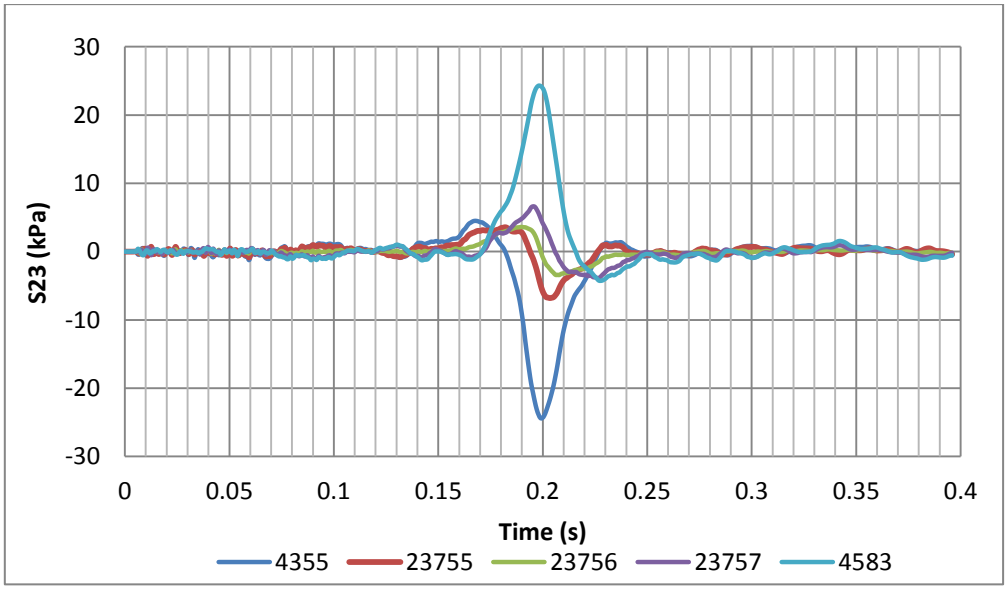
Figure 5.13 shows the shear stress changes on three different planes. Compared to the peak values of shear stress of 5 and 3kPa in XY and XZ planes respectively, the peak stress in the YZ plane has the greatest value which is approximately 23kPa. Furthermore, the peak in-plane shear stresses at the central point at the bottom of the sleeper are always the lowest. In particularly, the XZ in-plane shear stress at point 23756 is nearly zero during the entire loading period.




(a)




(b)




(c)

Figure 5.13 Shear stresses changes against time at different nodes

### 5.2.2 Sleeper Rotation

For design and analysis purposes, sleepers are generally assumed to lie horizontally on the ballast layer with assumed full contact between ballast and sleepers. However, the sleeper cannot be always fully supported in reality. Voids form at the contact interface of ballast and sleepers and sleeper rotation cannot be neglected. This

would cause stability problems especially with a completely unsupported sleeper or if cracking of concrete sleepers occurs and it would increase the trackbed deterioration rate.

Lundqvist and Dahlberg (2005) investigated the influence of one or several unsupported sleepers on track dynamics using a simulated 3D FE model. A conclusion had been made that for the single hanging sleeper, the sleeper/ballast contact force and the displacement at the adjacent sleeper can increase up to 70% and 40% respectively. Meanwhile, the increasing train speed will cause a larger contact force and displacement. The uneven load may eventually lead to an irregular ballast settlement. Kaewunruen and Remennikow (2007) also emphasised the effects of ballast voids on the free vibration response of concrete sleepers using a dynamic FE model. Different mode shapes of a sleeper in its longitudinal direction that resulted in different contact patterns with ballast were analysed. It is found that the support stiffness reduces with the larger size of voids between sleeper and ballast. Bogacz et al. (2014) looked at the influence of single and double fastening systems on horizontal sleeper rotation as presented in Figure 5.14. Loss of the periodicity of sleeper space can lead to a mistuning of wave propagation and irregular contact forces whilst an advantage of double fasteners is obtained.

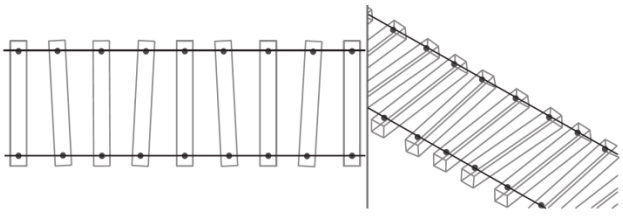


Figure 5.14 Sketch of sleeper rotation under the moving train (Bogacz et al., 2014)

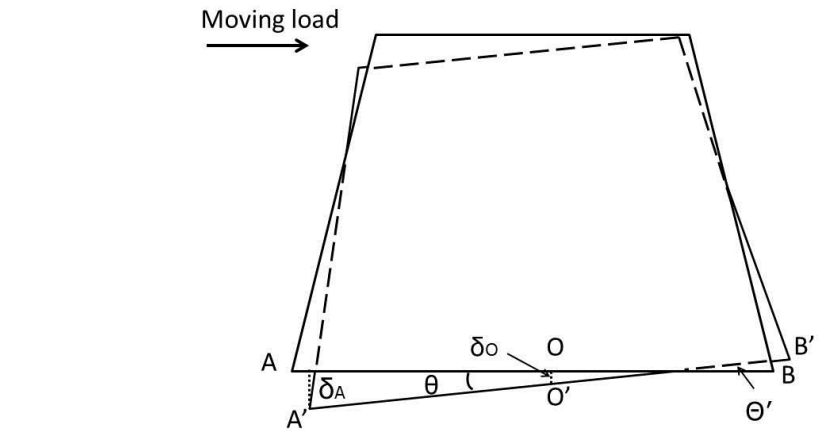
Nevertheless, there is lack of understanding of sleeper rotation around the horizontal axis perpendicular to the moving load direction. In this project, effects of different variables of trackbed including Young's modulus of rail pad, ballast and subgrade on sleeper rotation have been assessed.

A sketch of sleeper rotation about a horizontal axis is displayed in Figure 5.15(a). The calculation of rotation can be expressed as follows:

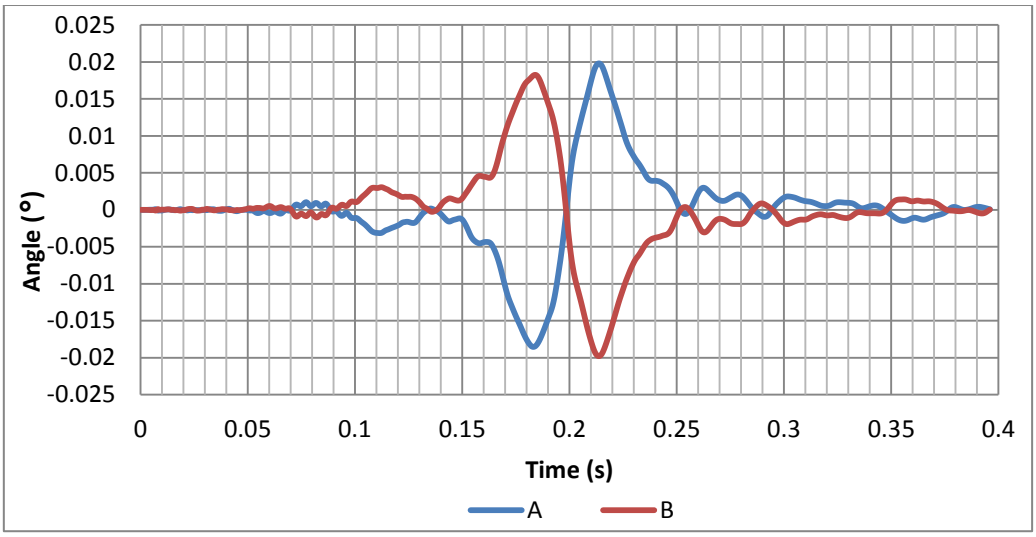
$$\sin\theta = \frac{\delta A - \delta O}{OA} \qquad \text{Equation 5.1}$$

where δA, δO: vertical displacements at points A, O.

Similarly, the rotation angle θ' at point B can be calculated in the same way. The angles of rotation θ and θ' at both bottom corners during a wheel passage are presented in Figure 5.15(b), where a negative angle means rotating anticlockwise. The angle reaches to a maximum value of approximately 0.018 degrees when the moving load passes over the sleeper. It is worth noting that the maximum angle of rotation is slightly larger after the moving load has passed than before it arrives. The angle of rotation increase 6.9% at point A and 8.8% at point B respectively. Ideally, the absolute angle of rotation at both points should be exactly the same wherever the loading area moving to. During the train passage, especially when the loading area is moving around the specific sleeper, there is only an average difference of 3% between θ and θ' which is negligible. However, a huge difference of approximately 29% occurred when the loading area is moving above the sleeper.




(a)




(b)

Figure 5.15 Rotation of the sleeper during the train passage

### 5.2.3 Initial Stresses

In reality, permanent strain is not only caused by the wheel load and material properties, but also depends on the self-weight stresses. For a comprehensive prediction of permanent strain in ballast in reality, gravity effects have to be taken into consideration. Figure 5.16 shows a rough sketch of crib ballast. In order to work out the initial stresses caused by gravity in the ballast, crib ballast which is not included in simulations has been added to the calculation.

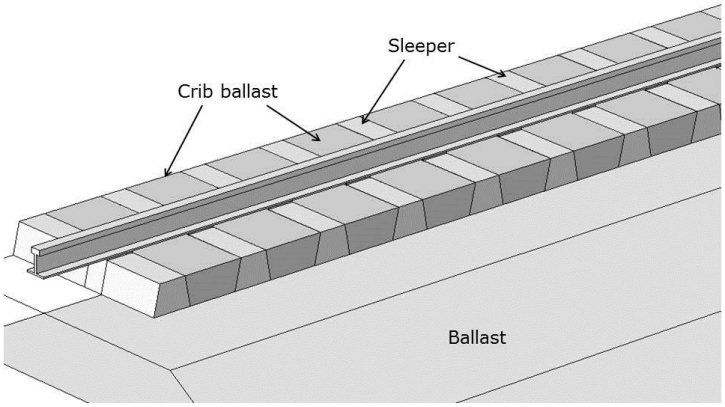



Figure 5.16 Sketch of crib ballast

To allow calculation to proceed, all the superstructure including rail, sleeper, rail pad and crib ballast is simplified as a continuous uniformly distributed load above the ballast. The average density can be derived by the following equation:

$$\rho_{rail}V_{rail}+ \rho_{pad}V_{pad}+\rho_{sleeper}V_{sleeper}+ \rho_{crib}V_{crib}=\rho_{ave}V_{tot} \qquad \text{Equation 5.2}$$

where,

$\rho_{rail}$, $\rho_{pad}$, $\rho_{sleeper}$, $\rho_{crib}$, $\rho_{ave}$ are the density of rail, rail pad, sleeper, crib ballast and the average density of the entire superstructure respectively and,

$V_{rail}$, $V_{pad}$, $V_{sleeper}$, $V_{crib}$ and $V_{tot}$ are the volume of rail, rail pad, sleeper, crib ballast and the entire superstructure respectively.

A sketch of the simplified structure is presented in Figure 5.17. An equivalent height $h_1$ can be calculated using:

$$h_{1=} V_{tot}/S_{tot} \qquad \text{Equation 5.3}$$

where $S_{tot}$ is the entire cross section area of the superstructure.

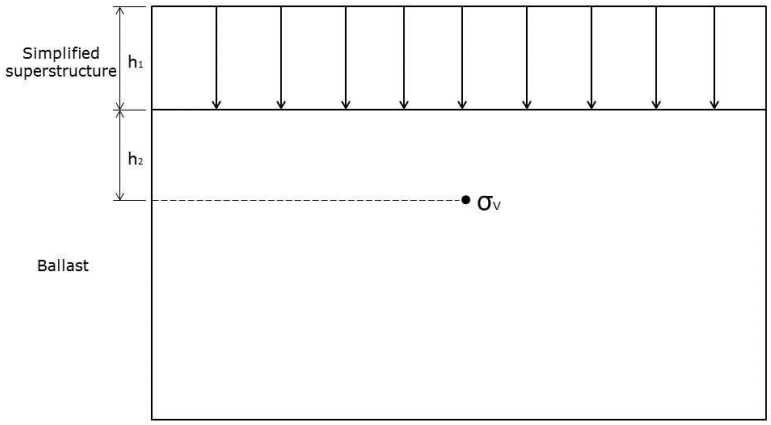



Figure 5.17 Sketch of the simplified structure

Hence, the vertical overburden stress at any point in the ballast can be expressed as:

$$\sigma_{V=}\rho_{ave}gh_1+\rho_{ballast}gh_2 \qquad \text{Equation 5.4}$$

where $\rho_{ballast}$ is the density of ballast.

In addition, the horizontal stress can be expressed as:

$$\sigma_H=K_0\,\sigma_V \qquad \text{Equation 5.5}$$

where $K_0$ is the earth pressure coefficient, which normally varies a lot with different type of granular material and is difficult to define for ballast. In this research, $K_0$=1-sinΦ is chosen where Φ is 46.6°, the friction angle of ballast (Jaky, 1948).

Both vertical and horizontal stresses caused by gravity will be considered in addition to the stresses from dynamic simulation analysis in the following sections.

### 5.2.4 Principal Stress Rotation

In contrast to stress calculation on an essentially static basis, the stress changes in a ballast element are complicated and these can lead to a rotation of principal stress under a train passage. Many researchers have discussed the influence of this effect on the build-up of permanent vertical strain. Shi (2009) stated that the ballast and subgrade in a railway test suffer continuous change in the direction of principal stress, which increases the accumulation of permanent strain. Ishikawa et al. (2007) stated that with an increase in major principal stress rotation, the stability of ballast decreases so that the axial permanent strain increases. Figure 5.18 presents data comparison of plastic deformation under cyclic loading with or without principal stress rotation from repeated loading tests using a multi-ring shear apparatus from Inam et al. (2012). Clearly, under the same experimental conditions, the permanent axial strain is higher under repeated loading with principal stress rotation than without. What is more, larger principal stress rotation may lead to a more serious permanent axial strain. Consequently, it is necessary to explore the details of the stress field at different depths in the ballast under a moving load.

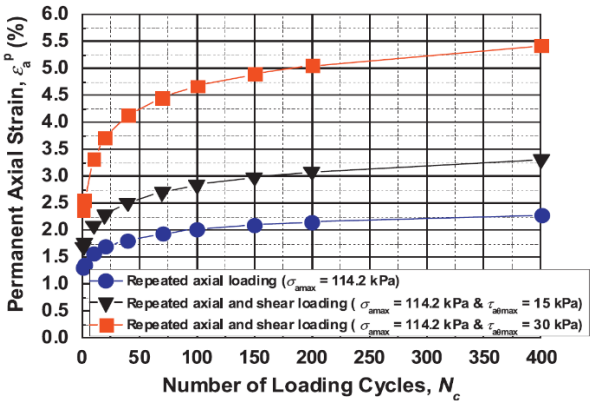
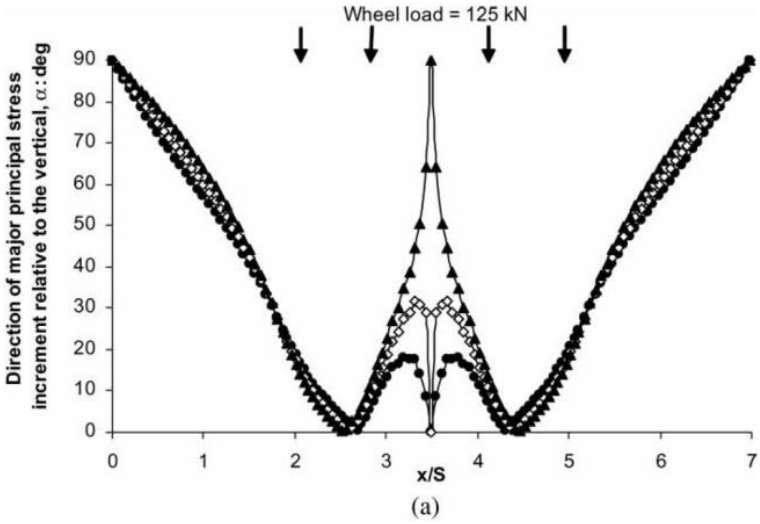



Figure 5.18 Permanent deformation under repeated loading (Inam et al., 2012)

A Finite Element study on the effect of variable parameters on principal stress rotations in a soil element below ballasted railway track was presented by Powrie *et al.* (2007). In their research, a 3D linear elastic model under a pair of adjoining wagons comprising four wheel loads of 125kN each was constructed, and a series of parameters including soil Young's modulus, heterogeneity (stiffness increasing linearly with depth) and Poisson's ratio were taken into consideration. All the lengths presented in this analysis were normalised against sleeper length S = 2420mm. The effects of Young's modulus and Poisson's ratio on the rotation of principal stress are shown in Figure 5.19 and 5.20 respectively.

In Figure 5.19, the direction of principal stress is at or near vertical under the wheel loads at the surface of natural ground. Between the wagons, the principal stress remains near vertical when E=30MPa and 60MPa, but it becomes horizontal when the soil Young's modulus reaches 120MPa. However, the results are almost independent of the Young's modulus at a depth of 0.49S below the natural ground surface.



(a)

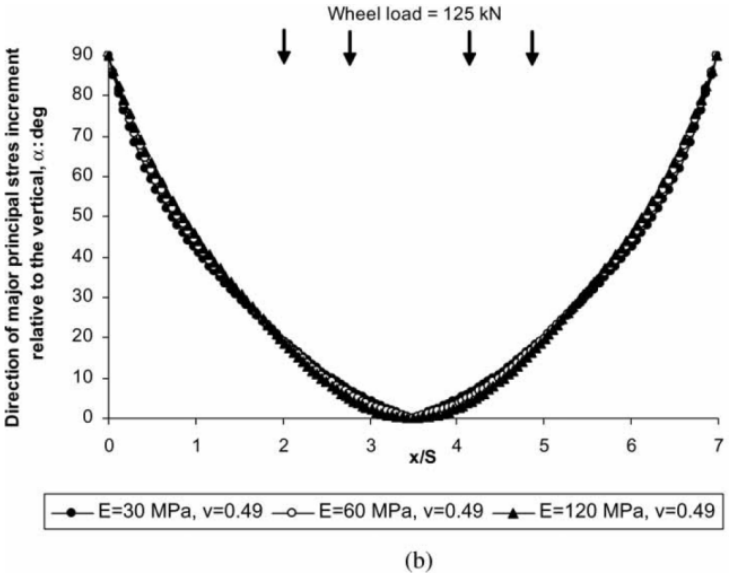



Figure 5.19 Effect of Young's modulus on principal stress rotation at (a) surface of natural ground (b) 0.49S below the natural ground surface at the centreline of two rails (Powrie *et al.* 2007)

Figure 5.20 shows the principal stress rotation analyses for a soil with E=30+10.89(z/S) MPa and Poisson's ratios of 0.49, 0.3 and 0.1. Apparently, principal stresses tend to be horizontal when under the centre of the wagons. They only remain vertical when the Poisson's ratio v=0.1 at a depth of 0.49S in the soil. In addition, the effect of the changes of Poisson's ratio is reduced at a depth of 0.49S than the ground surface between the wagons.

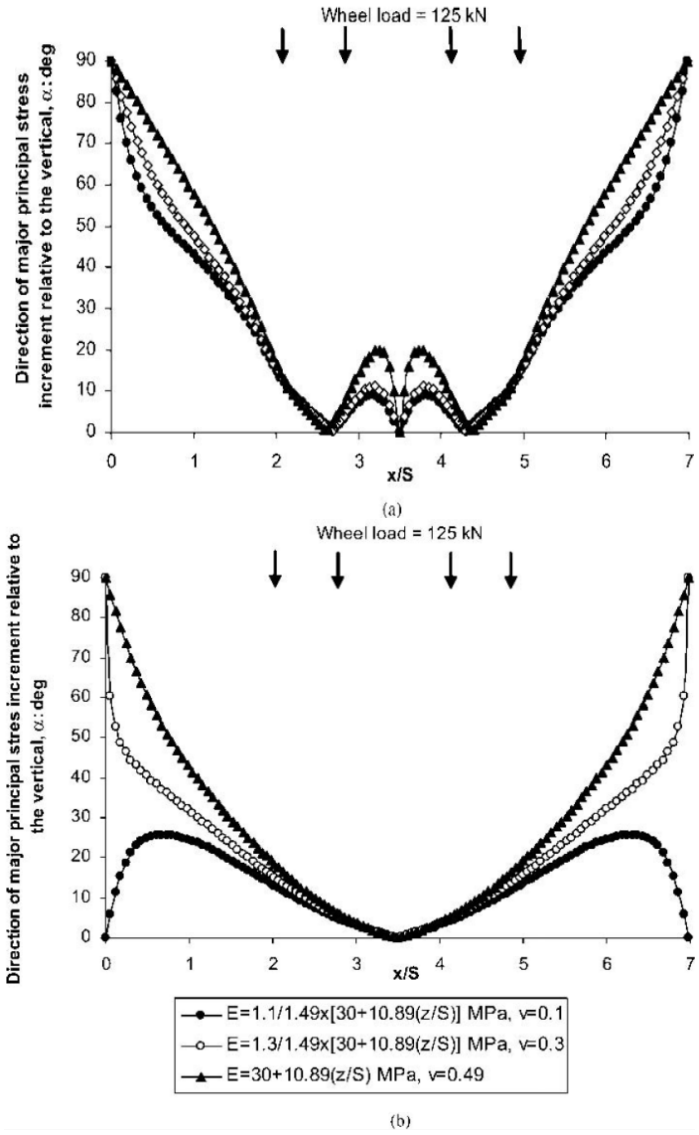



Figure 5.20 Effect of Poisson's ratio on principal stress rotation at (a) surface of natural ground (b) 0.49S below the natural ground surface at the centreline of two rails (Powrie *et al.* 2007)

An in-depth study of the effect of different factors involving Young's modulus, load speed and Poisson's ratio on principal stress rotation in ballast will be presented in Chapter 6 based on the theory of previous analyses of principal stress rotation in natural ground. A basic investigation is firstly presented in this section.

As presented in Figure 5.21, under the passing load, 15 positions which are located at the bottom corner, sleeper centre or mid-way between two adjacent sleepers have

been chosen to investigate the effect of different loading positions on principal stress rotation. 8 stress analysis points at different depths in the ballast are also shown. To avoid inaccuracy of calculation, the two top points are chosen located one element underneath the ballast surface. The maximum principal stress rotation, vertical stress and shear stress have been analysed in this section.

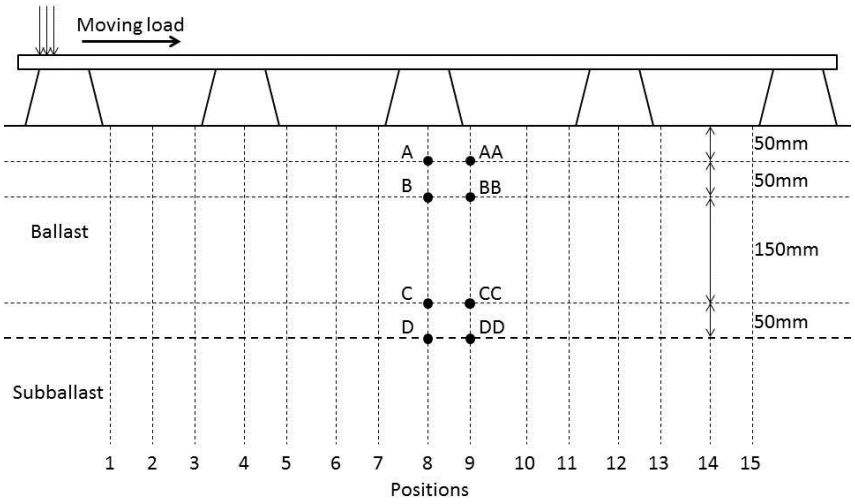



Figure 5.21 Calculation points for principal stress rotation

Figure 5.22 shows the YZ in-plane maximum principal stress rotation development at various points underneath the sleeper centre line when the moving load is passing by different positions. The angle shown on the graph is the absolute value of the angle between the horizontal axis and the plane on which a principal stress acts. As illustrated in Figure 5.22, it is evident that the principal stress is at 90° at all depths when the moving load is locating right above the points. The results also demonstrate that the rotation of the principal stress axes varies. Furthermore, there are normally two stages of principal stress rotation at all points in ballast. Initial rotations happen on both sides of the model, which are positions 1 to 5 and 11 to 15. The rotations are relatively large in these stages. Secondary rotations happen at positions 6 to 10 where the rotations are relatively small when the moving load is

close by. However, it is worth noting that the angle changes at point A and B are relatively small and that a sharp increase in rotation occurs after 250mm depth and the minimum angle decreases to less than 50 degrees at point D, which means that approximately a total rotation of 90 degrees has occurred.

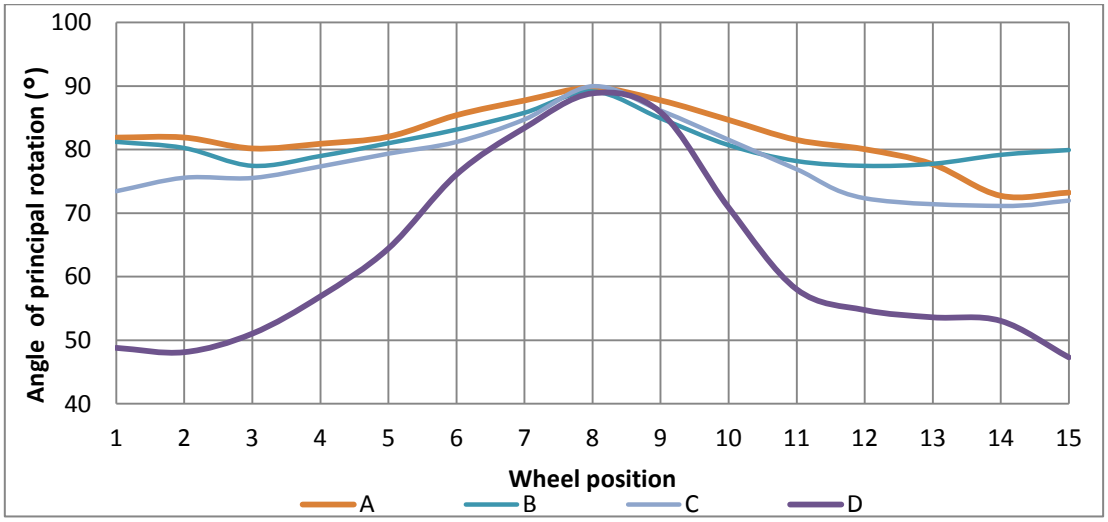



Figure 5.22 Principal stress rotations at the points under middle sleeper

Similarly, Figure 5.23 shows the rotation development at various points underneath the bottom corner of the sleeper. In contrast to the angle developments shown in Figure 5.22, the peak angle at all points has an apparent phase lag depending on depth. As the stress concentration occurs at the bottom corner of the sleeper, stresses at the points nearby suffer more stresses and maximum sleeper rotation presumably occurs when the load is in position 13. Meanwhile, the peak angle increases as the depth decreases.

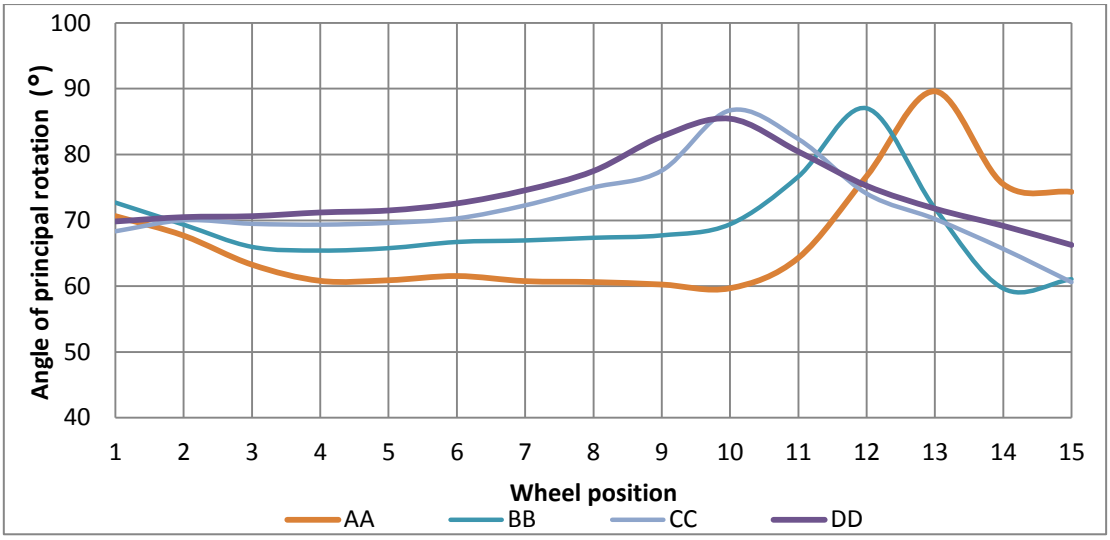
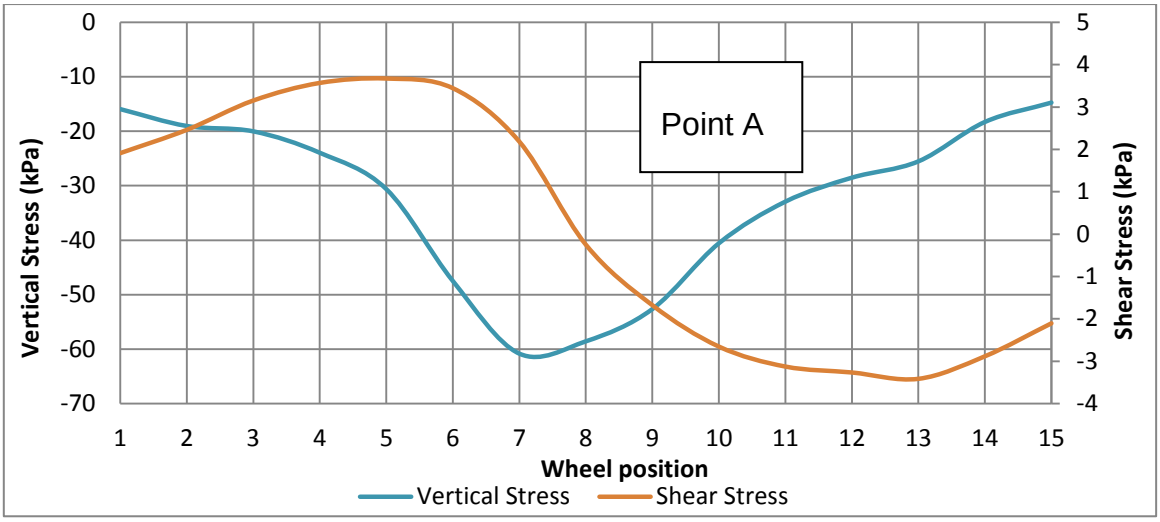
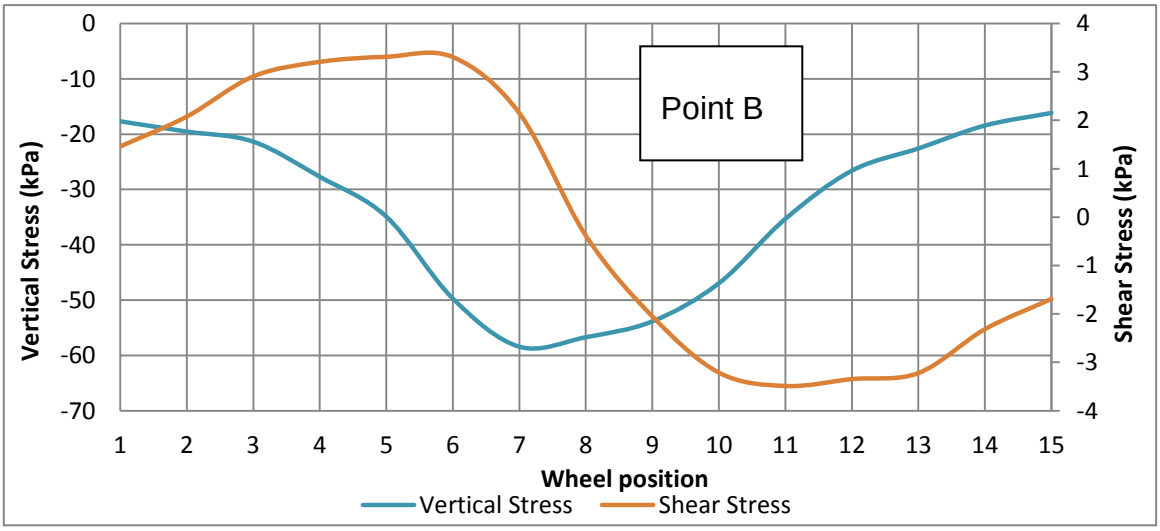



Figure 5.23 Principal stress rotations at different points under the bottom corner of the sleeper

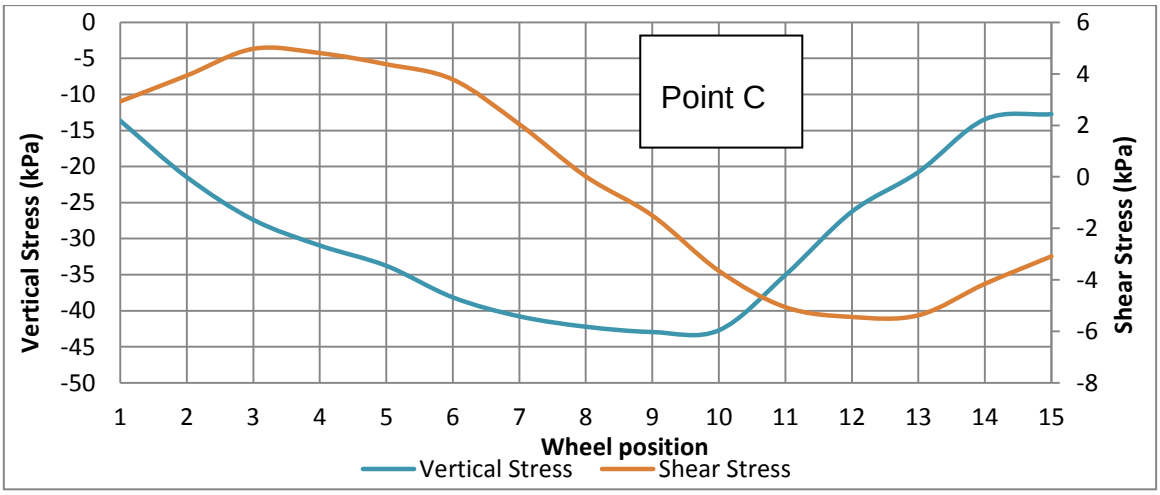
Figure 5.24 illustrates both the YZ in-plane vertical and shear stresses at different analysis points under different moving load positions. Because of the calculation difficulties and inaccuracy at the interface of ballast and subballast, the stress states at point D and DD are not included. It can clearly be seen that vertical stress remains negative during the entire loading period which means the elements are always compressed. However, shear stress changes its direction according to the different moving load positions. Consequently, principal stress rotation occurs during the train passage.


Point A
Vertical Stress (kPa)
Shear Stress (kPa)
Wheel position
Vertical Stress
Shear Stress

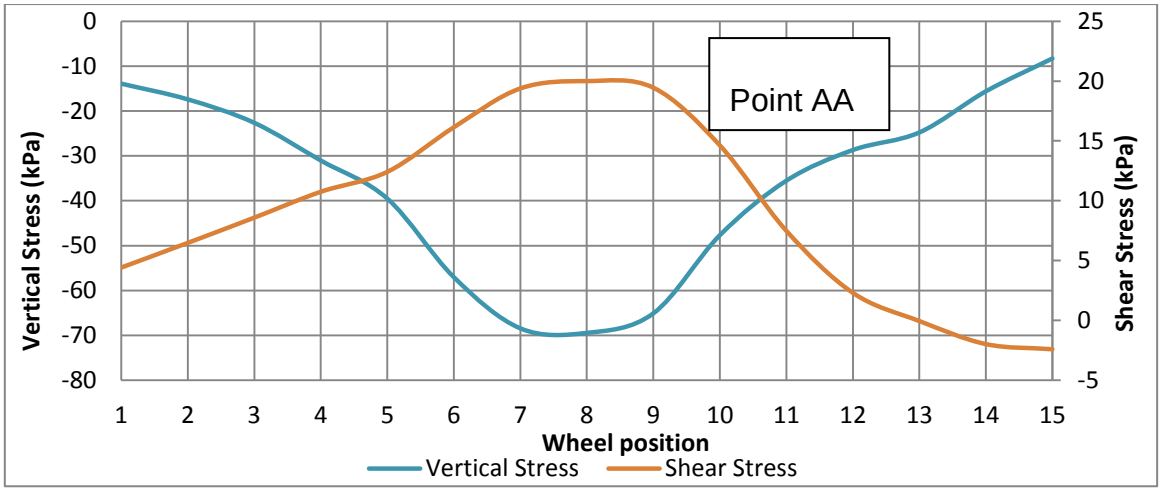
(a)


Point B
Vertical Stress (kPa)
Shear Stress (kPa)
Wheel position
Vertical Stress
Shear Stress

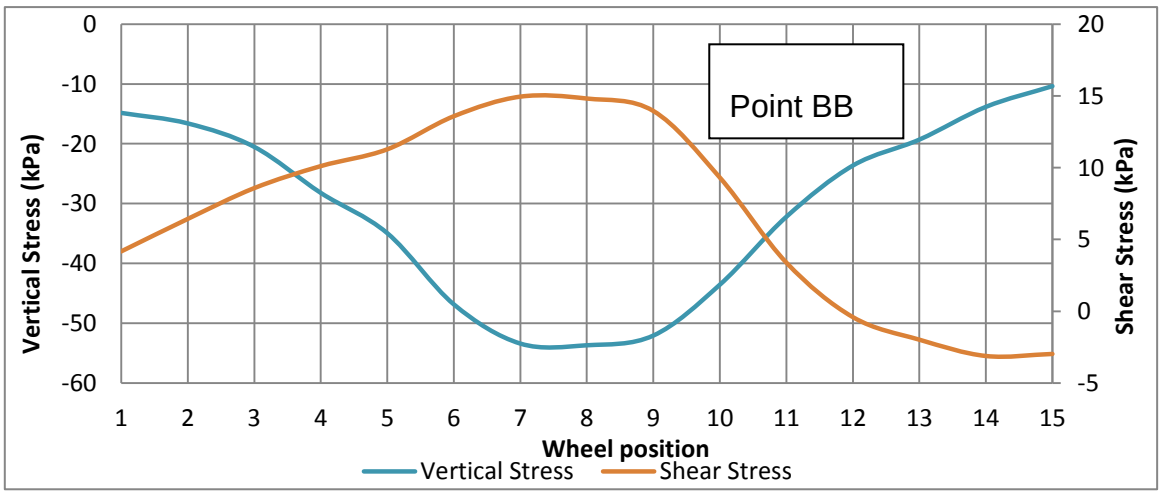
(b)


Point C
Vertical Stress (kPa)
Shear Stress (kPa)
Wheel position
Vertical Stress
Shear Stress

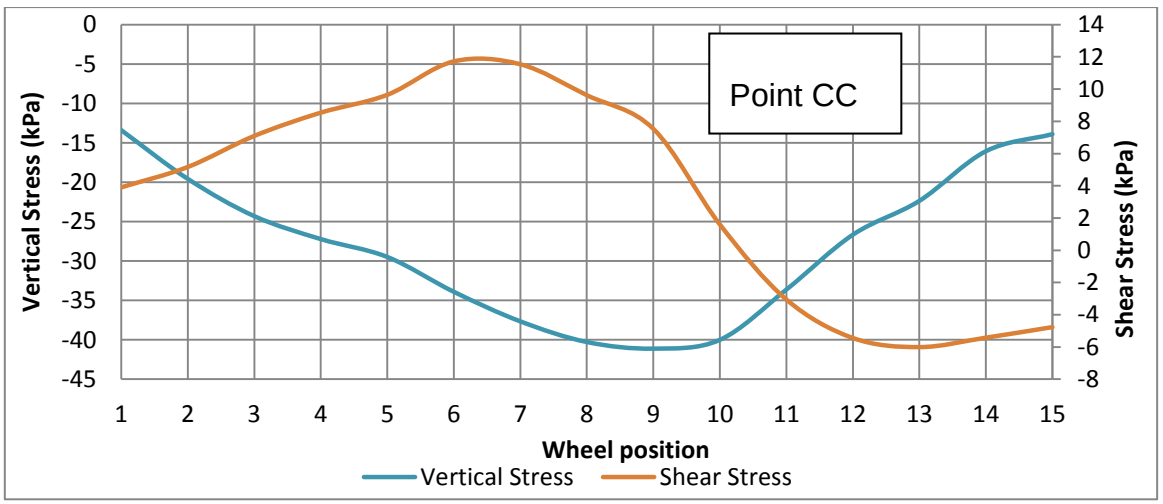
(c)




(d)



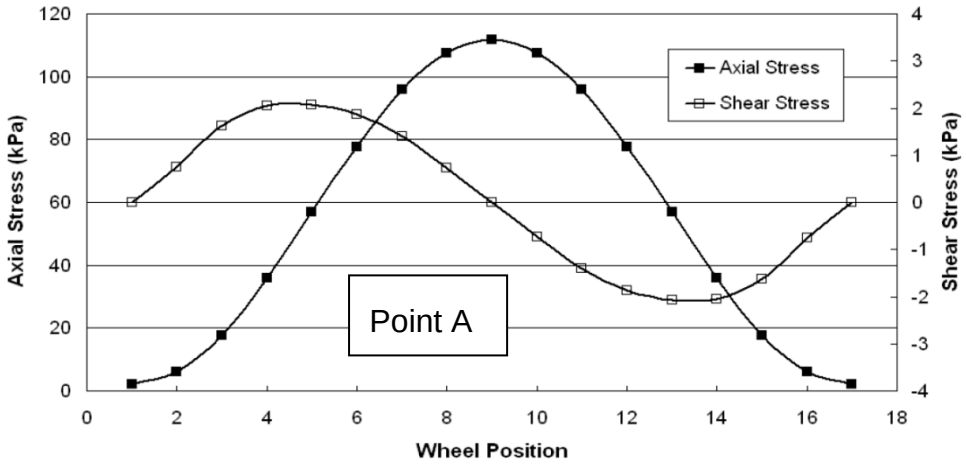

(e)



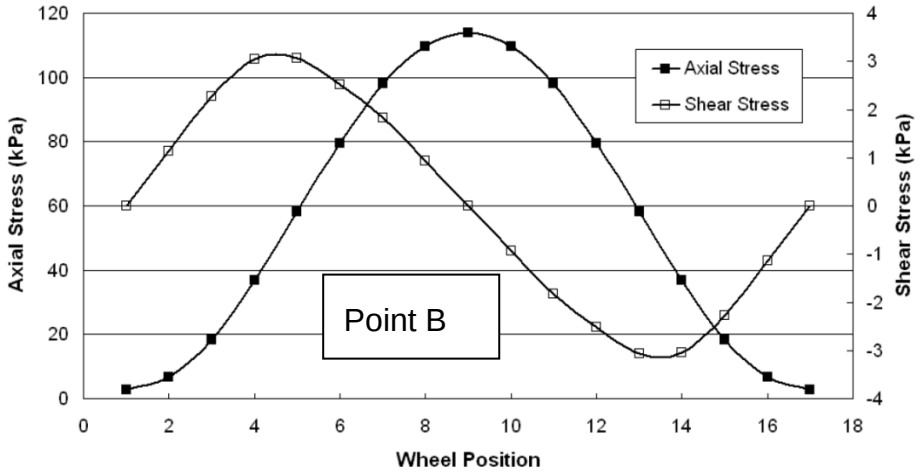

(f)

Figure 5.24 Vertical and shear stress at different points under the moving load

Figure 5.25 illustrates the stress results at points A and B respectively from tests by Shi (2009) carried out in a full-scale railway test facility but at low travel speed. Compared to the results plotted from the FE simulations as presented above in Figure 5.24(a) and (b), although the loading magnitudes as well as the material properties of the trackbed are not the same, both vertical and shear stresses show similar characteristics.




(a)




(b)

Figure 5.25 Axial and shear stresses at different points under a moving load (Shi, 2009)

## 5.3 Summary

Permanent deformation in ballast is complex in reality and it accumulates under cyclic moving wheel load. As the simulation based on this research is linear elastic, it is not possible to calculate this directly. However, ballast deformation can be predicted in terms of stress distribution under the dynamic moving load. In this chapter, a 3D railway track model developed in previous chapter was utilised in dynamic analysis and a reference case study on stress and deflection within ballast as well as sleeper rotation has been fully described.

A number of stress analyses have been presented in this chapter. Both normal and shear stresses on all three planes at different nodes directly beneath a sleeper have been plotted. There was little stress oscillation when the load was away which could be a result of ambient vibration. A sharp reduction of vertical stress from the outer edge of the sleeper to the centre occurred and this may lead to a larger deformation at the bottom corner of the sleeper than in other places.

Self-weight stress has been included for a more accurate result when analysing principal stress rotation. The gravity effect from crib ballast is taken into consideration. Maximum principal stress rotations at different calculation points in the ballast have then been calculated. It is worth noting that a sharp rotation may happen at a depth 250mm or deeper in the ballast. Meanwhile, rotations at the points underneath the bottom corner of the sleeper show an apparent phase lag along with the decreasing depth in ballast.

Finally, vertical and shear stresses at different calculation points have been plotted. Since the shear stress keeps changing its direction according to different loading positions, principal stress rotation may occur during the passing of a train. The effect of principal stress rotation on permanent deformation has also been noted. The stress results from tests by Shi (2009) have been compared to the results plotted from the FE simulations. Both vertical and shear stresses show similar characteristics although the loading magnitudes as well as the material properties of the trackbed are not exactly the same.

# 6 Parametric Analysis of Trackbed Properties

A purpose-designed 3D dynamic railway track model using finite element analysis and a reference case study have been presented in previous chapters. A set of analyses comparing the effects of different variables including moving load magnitude, loading speed and stiffness of materials on stress and deflection within ballast as well as sleeper rotation based on this model will be reported in this chapter. All the details regarding model dimensions, boundary conditions, material properties and mesh etc. have been fully described in previous chapters.

## 6.1 Solution controls

To compare the effects of velocity, load level and material properties, a range of variable parameters which can be found in Table 6.1 have been applied in the simulations. Other material properties for all models in this chapter are as shown in Table 4.1. Only one variable will be changed at a time during each of the following simulation series and compared to the results of the reference model.

Table 6.1 Variable parameters used in simulations

| Variable | Values | Reference |
|---|---|---|
| Vertical Load (kN) | 60, 90, 110, 125 | 60 |
| Speed (km/h) | 60, 120, 200, 300 | 200 |
| Stiffness of ballast (MPa) | 100, 140, 200, 280 | 140 |
| Stiffness of rail pad (MPa) | 6.9, 20, 60 | 6.9 |
| Stiffness of subgrade (MPa) | 35, 75, 100, 150 | 75 |

To set this in context, an example railway project has been studied to confirm the validity of the above parameters. Madshus and Kaynia (2000) described the line between Göteborg and Malmö, operating by the Swedish National Rail Administration. This line was built with UIC60 rail on concrete sleepers and traversed on area with an extremely soft clay subgrade. Also, the X-2000 passenger train operated at a running speed up to 202km/h, with wheel loads ranging from 60 to 90kN.

In general, the stiffness values used in this research represent the cases of loose, intermediate and firm ballast; soft, intermediate and hard pads; poor, medium, good and excellent level of subgrade.

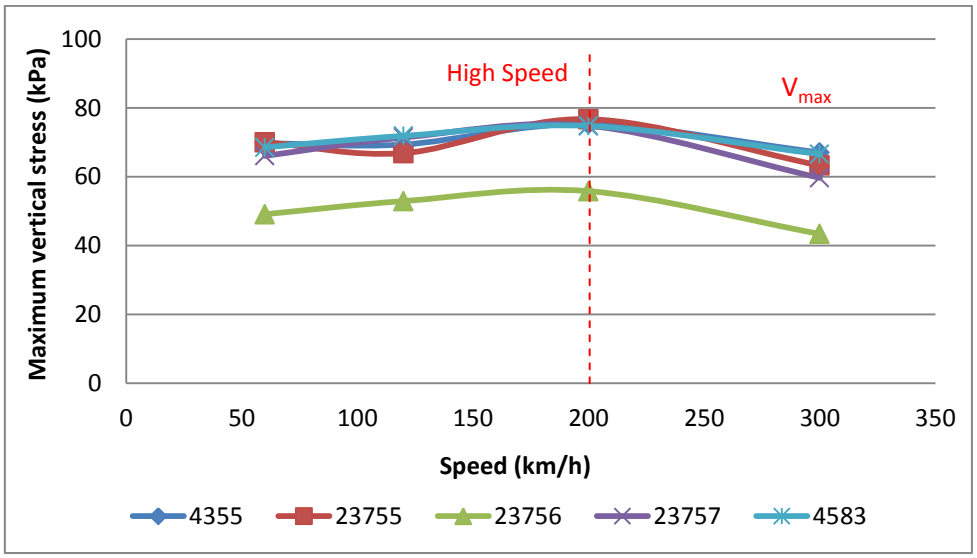
Thus, most of the values of the variables in various combinations used in the simulations (shown Table 6.1) reflect real-world practice, although it is acknowledged that a train speed of 200km/h with 125kN wheel load which is equivalent to a freight train is unlikely. Nevertheless, according to the aim of the research, it is essential to have a full understanding of the effect of different variables on stress and deflection in ballast in order to predict railway trackbed condition. Thus, although some of the combinations of variables are beyond their practical ranges, they allow a broader view of the problem to be obtained.

## 6.2 Load speeds

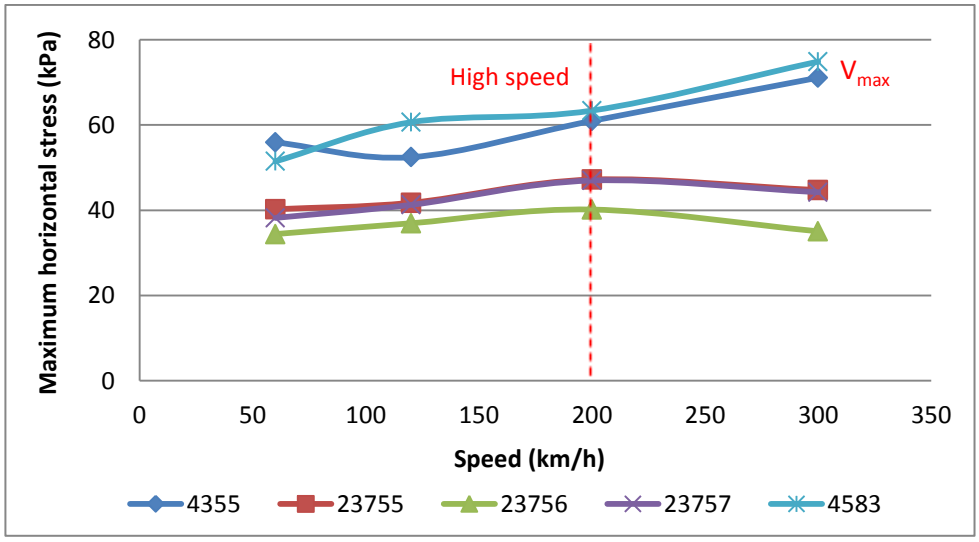
For dynamic analysis of a railway system, dynamic effects cannot be ignored when the train speed is higher than 240km/h on a firm subgrade (Grabe and Clayton, 2009). On the other hand, different subgrades will lead to different results. As rail trackbed consists of many parts, it is hard to foresee which part will be affected the most by dynamic effects. Consequently, a range of speeds needs to be taken into account. In general, train speed can be classified as maximum running speed ($V_{max}$=300km/h), high speed ($V_{high}$≥200km/h), average speed ($V_{ave}$=120km/h) for passenger trains, and low speed ($V_{low}$=60km/h) for heavy freight lines (Pyrgidis, 2016). Thus, bearing in mind the average speed of freight trains and passenger trains around the world, these four typical moving load speeds, namely 60km/h, 120km/h, 200km/h and 300km/h, have been utilised in the dynamic analysis.

The effects of moving wheel load speed on the changes in maximum YZ in-plane stresses are presented in Figure 6.1. Five representative points from the middle sleeper of the model shown in Figure 5.9 have been analysed. Generally, the middle point (23756) always has the lowest maximum stress at all speeds. However, differences for all stresses as a function of speed are relatively modest with the except of the horizontal and shear stresses at both bottom corners of the sleeper (points 4355 and 4583) and this relates to stress concentrations around these areas. As illustrated in Figure 6.1(c), for example, the maximum shear stress at point 4355 is about 24kPa at 200km/h, which is approximately 4 times larger than at point 23757 and 7 times larger than at the middle point.

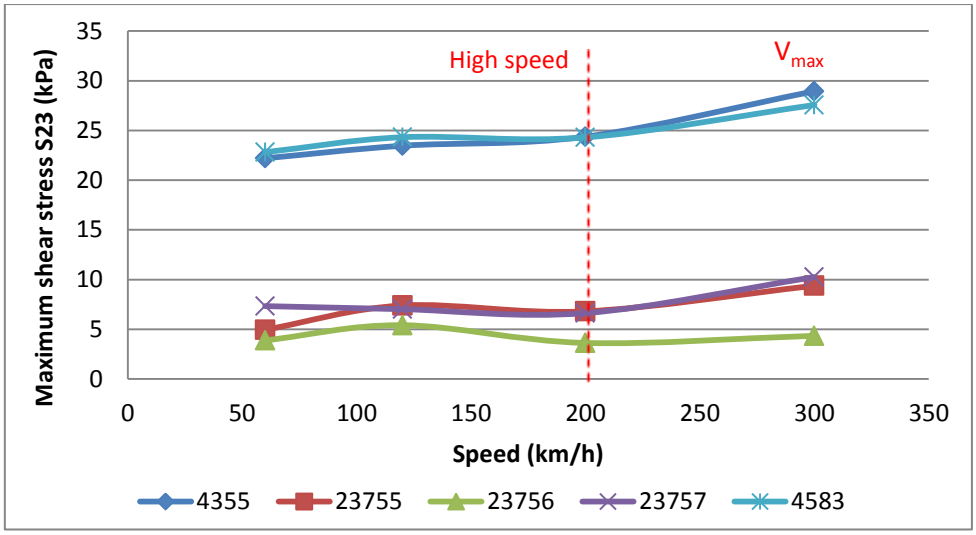
With regard to the vertical and horizontal stress changes at points 23755, 23756 and 23757, which can be found in Figure 6.1 (a) and (b), it is noticed that stresses increase slightly up to a speed of 200km/h and then reduce with higher speeds. Meanwhile, there is no significant change in shear stress when loading speed is under 200km/h but it increases slightly thereafter.




(a)




(b)




(c)

Figure 6.1 Maximum in-plane (a) Vertical stress (b) Horizontal stress (c) Shear stress with different speeds

Figure 6.2 shows the maximum vertical displacement at the interface of the middle sleeper of the model and the ballast (point 4355) at different moving load speeds. As the moving load speed increases from 60km/h to 200km/h, there is little change in the maximum vertical displacement, suggesting that dynamic effects may be negligible, whereas a sharp increase occurs when the speed becomes higher than 200km/h.

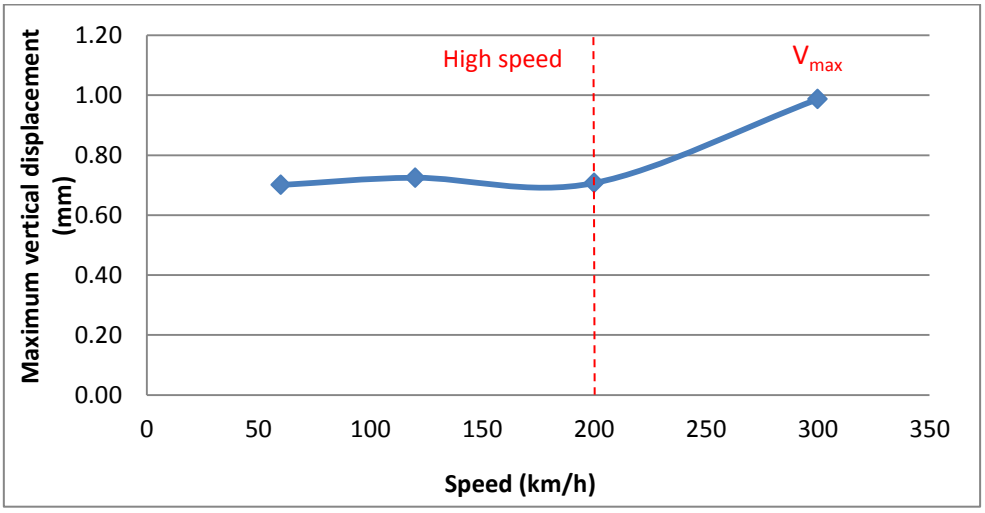



Figure 6.2 Maximum vertical displacement on the bottom corner of the sleeper (4355 in Figure 5.9) at different speeds

Figure 6.3 presents the calculated maximum rotation (from the horizontal) of the middle sleeper of the rail trackbed model at different speeds. Both sides of the sleeper as shown in Figure 5.15(a) and denoted as A (approach side) and B (departure side) are analysed respectively. Nevertheless, the maximum rotation attains a similar angle in each case. It may be noted that rotations during both approach and departure phases increase gradually when the speed is under 200km/h. However, a sharp increase of approximately 45% occurs between 200 and 300km/h. The maximum rotation is about 0.026 degree, representing a difference in level of a little over 0.1mm across the base of a G44 sleeper.

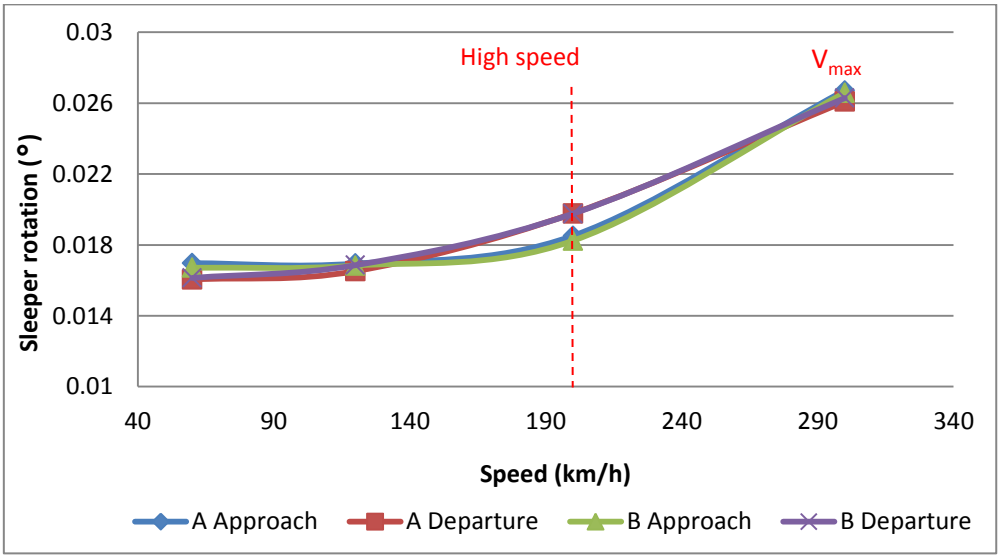
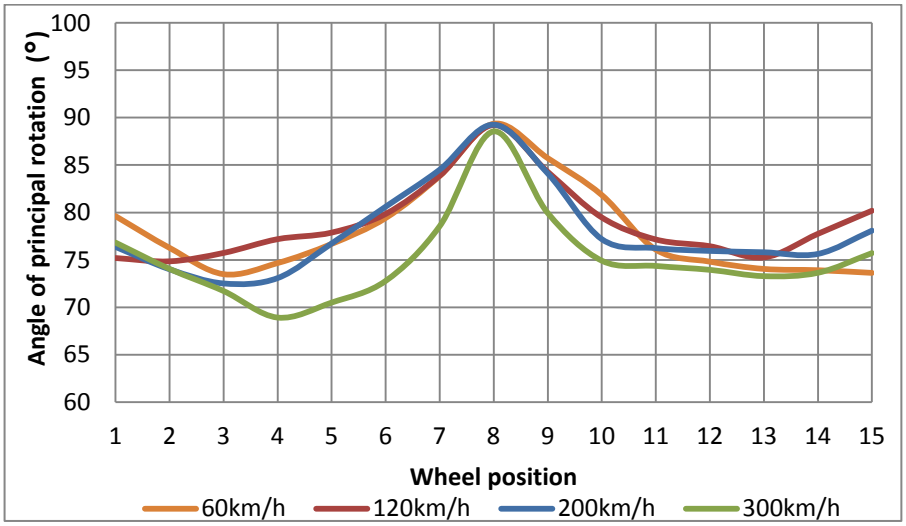


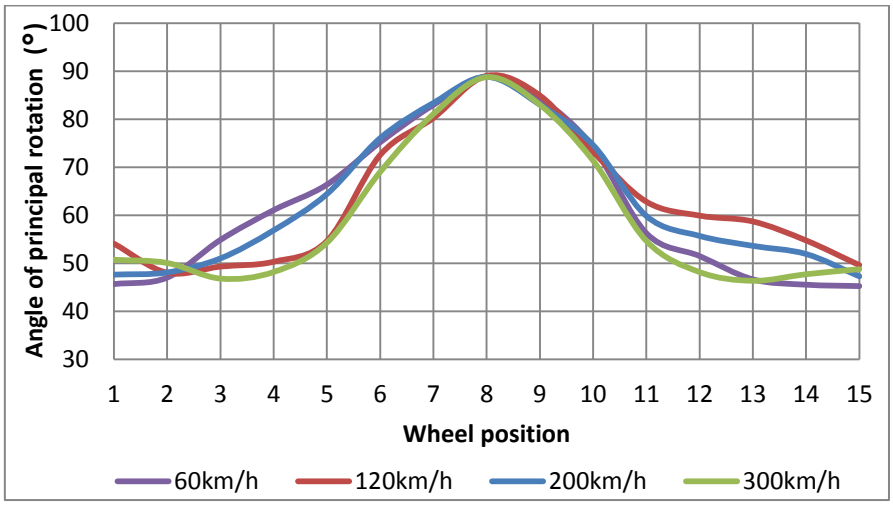

Figure 6.3 Rotations of sleeper at different speeds

Effects of load speed on direction of principal stress at two different locations in ballast are shown in Figure 6.4. The stress remains nearly vertical at both locations under the wheel load. The angle changes at point A, which is near to the ballast surface, are much smaller than at point D, which is at the interface of ballast and subballast. Apparently, there is little effect of load speed on direction of principal

stress, as seen from the similar trend of angle changes at both of locations. However, it is worth noting that at a speed of 300km/h, the principal stress rotates more heavily at point A when the wheel load passes between positions 2 and 14.




(a)




(b)

Figure 6.4 Effect of load speed on principal stress rotation at (a) A (b) D (see Figure 5.21)

Figure 6.5 shows the stress paths for a point in the ballast between the interface of the ballast and the bottom corner of the middle sleeper at different speeds during the passage of a moving load where $t=½(\sigma_1-\sigma_3)$ and $s=½(\sigma_1+\sigma_3)$ stand for a measure of

shear stress and confinement respectively. $\sigma_1$ and $\sigma_3$, which are the principal stresses, can be derived from following equations:

$$\sigma_1 = \frac{I_1}{3} + \frac{2}{3}\left(\sqrt{{I_1}^2 - 3I_2}\right)\cos\emptyset$$

Equation 6.1

$$\sigma_3 = \frac{I_1}{3} + \frac{2}{3}\left(\sqrt{{I_1}^2 - 3I_2}\right)\cos(\emptyset + \frac{4}{3}\pi)$$

where $\emptyset$, $I_1$, $I_2$ and $I_3$ can be calculated as follows:

$$\emptyset = \frac{1}{3}cos^{-1}\left(\frac{2{I_1}^3 - 9I_1I_2 + 27I_3}{2\left({I_1}^2 - 3I_2\right)^{\frac{3}{2}}}\right)$$

$$I_1 = \sigma_{11} + \sigma_{22} + \sigma_{33}$$

$$I_2 = \sigma_{11}\sigma_{22} + \sigma_{22}\sigma_{33} + \sigma_{33}\sigma_{11} - {\sigma_{12}}^2 - {\sigma_{23}}^2 - {\sigma_{13}}^2$$

$$I_3 = \sigma_{11}\sigma_{22}\sigma_{33} - \sigma_{11}{\sigma_{23}}^2 - \sigma_{22}{\sigma_{13}}^2 - \sigma_{33}{\sigma_{12}}^2 + 2\sigma_{12}\sigma_{23}\sigma_{13}$$

where 1,2& 3 stand for x, y, z directions.

The initial stress states under gravity have been fully described in Chapter 5, and an earth pressure coefficient $K_0$ of 1 has been applied, resulting in an initial stress of 4.37kPa both horizontally and vertically. This represents the start point for all the stress paths and is plotted in Figure 6.5(a). A Mohr-Coulomb failure line as well as

the stress path experienced by point 4355 (which can effectively avoid the significant difference between results achieved by single and double loads as shown in Chapter 4) have also been plotted, assuming a frictional angle of 46.6° and a cohesion value of 0 for dry clean ballast (Light *et al*., 2014).

As can be seen on the graphs, arrows shown towards point A mean the load approach paths, and away from A means departure paths. The initial stress under dead weight is relatively low since the analysis point is located immediately beneath the sleeper. As a result, all stress paths start and end close to zero. Clearly, both t and s generally increase as the load moves faster. However, there is no clear pattern to changes in maximum stress ratio (t/s).

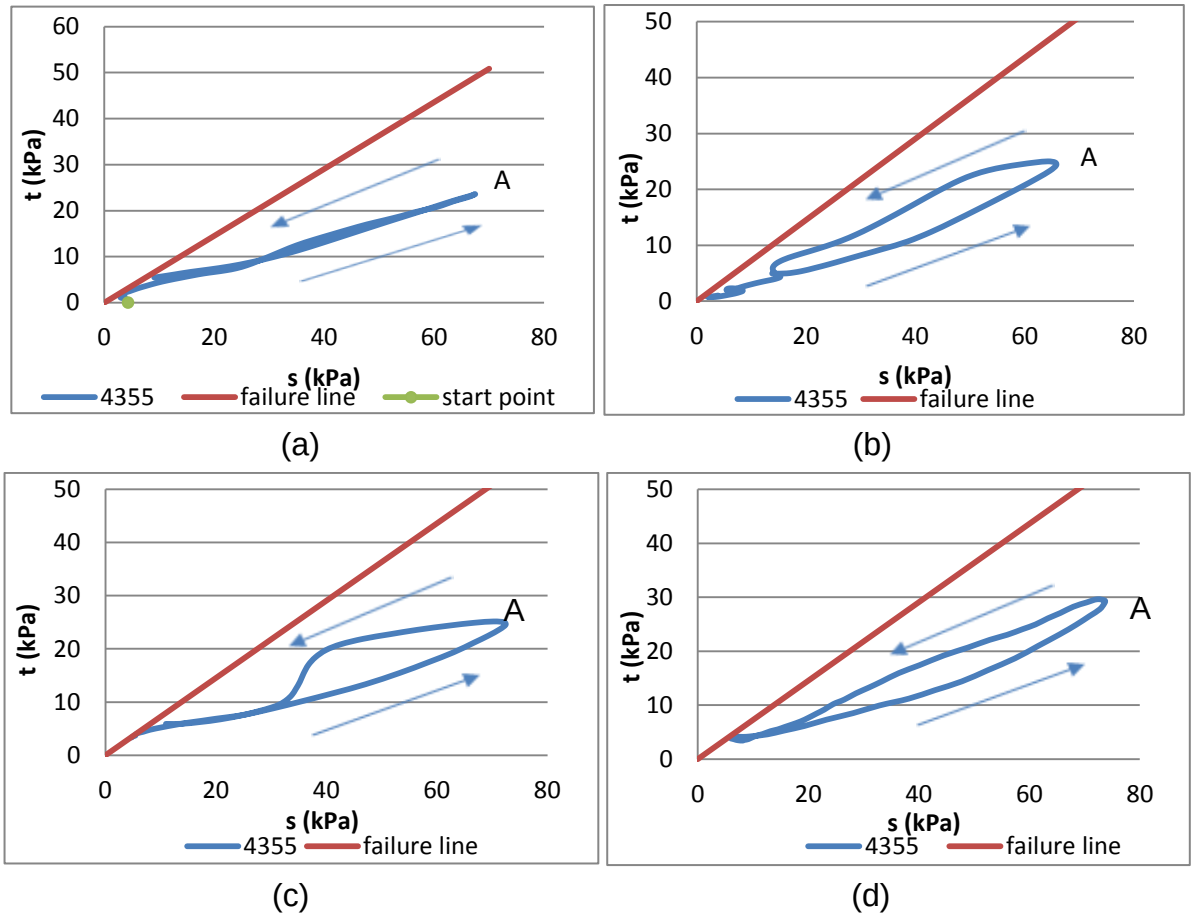
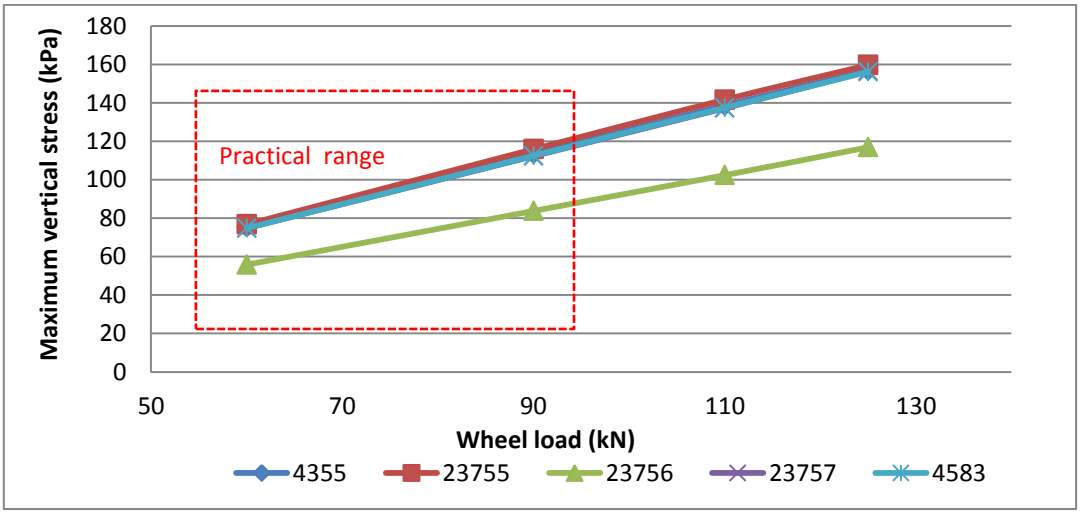



Figure 6.5 Stress path for ballast at sleeper bottom corner at different speeds: (a) 60km/h (b) 120km/h (c) 200km/h (d) 300km/h

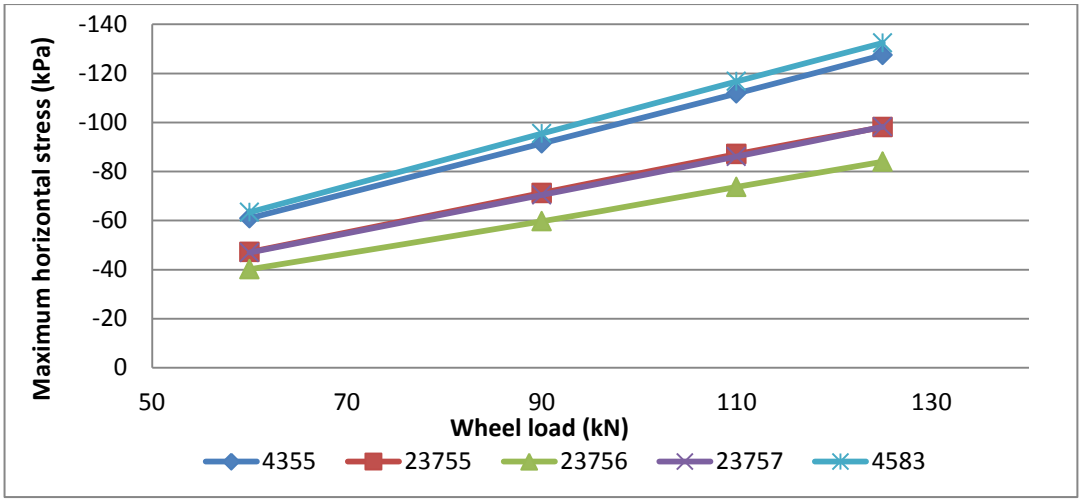
## 6.3 Loading magnitudes

Typically, a maximum permitted static wheel load is around 125kN, while a normal static wheel load of a passenger coach is around 60kN (Esveld, 2001). Consequently, to investigate the effects of loading magnitude on stress states and sleeper rotations, four load levels have been combined covering the range from 60 to 125kN.

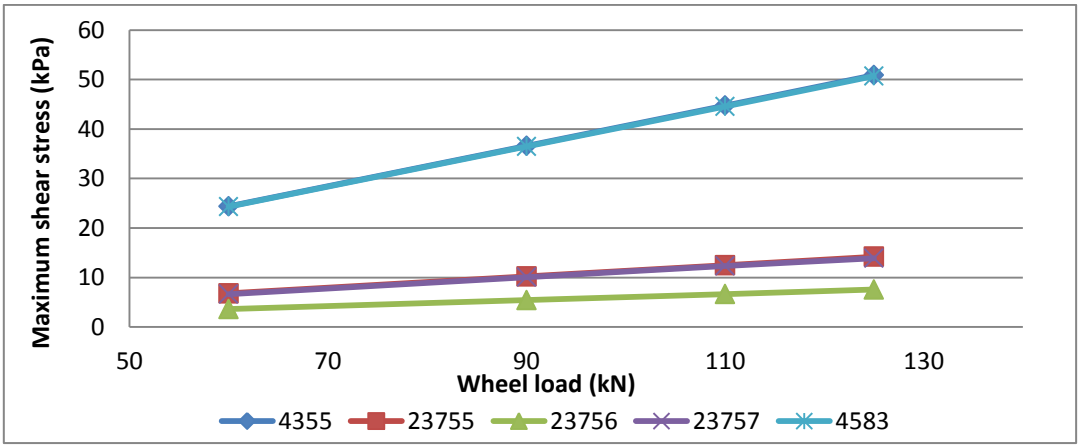
The maximum YZ in-plane stresses varying with different load values are presented in Figure 6.6. All stresses at all five analysis points at the bottom of the middle sleeper increase approximately linearly with loading magnitude. As previously, the middle point at the bottom sleeper always has the lowest stresses. The area shown in Figure 6.6(a) represents the practical range of wheel load at a speed of 200km/h. Furthermore, as illustrated in Figure 6.6(c), the average shear stress at points 4355 and 4583 is about 6.6 times higher than at the central point.




(a)




(b)




(c)

Figure 6.6 Maximum in-plane (a) Vertical stress (b) Horizontal stress (c) Shear stress with different loading magnitudes

As shown in Figure 6.7, sleeper rotation also increases approximately linearly at both point A and B. However, the angle during departure phase is always larger than that during the approach phase. There is an average difference of 0.0022 degrees between approach and departure. This is logically due to the inertia effects such that the sleeper continues rotating after the moving load has gone.

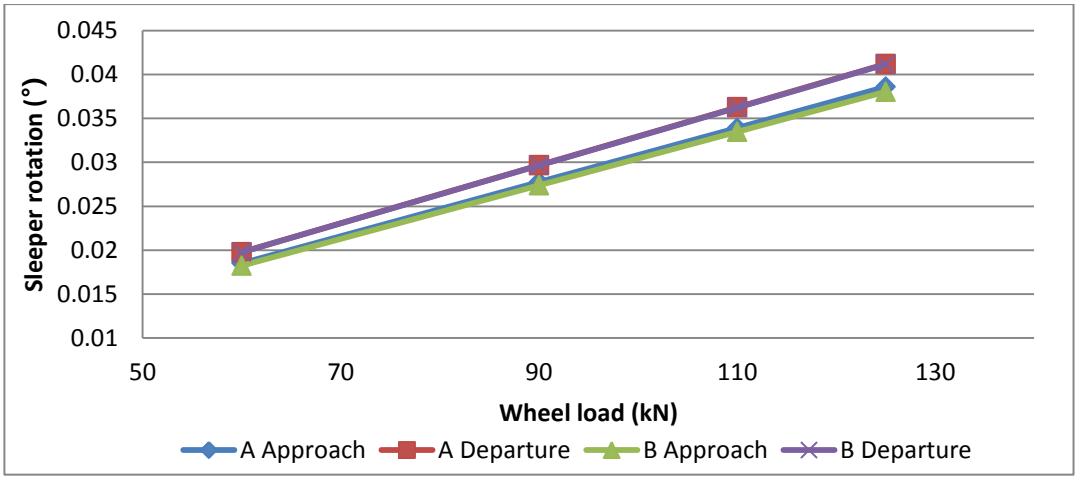


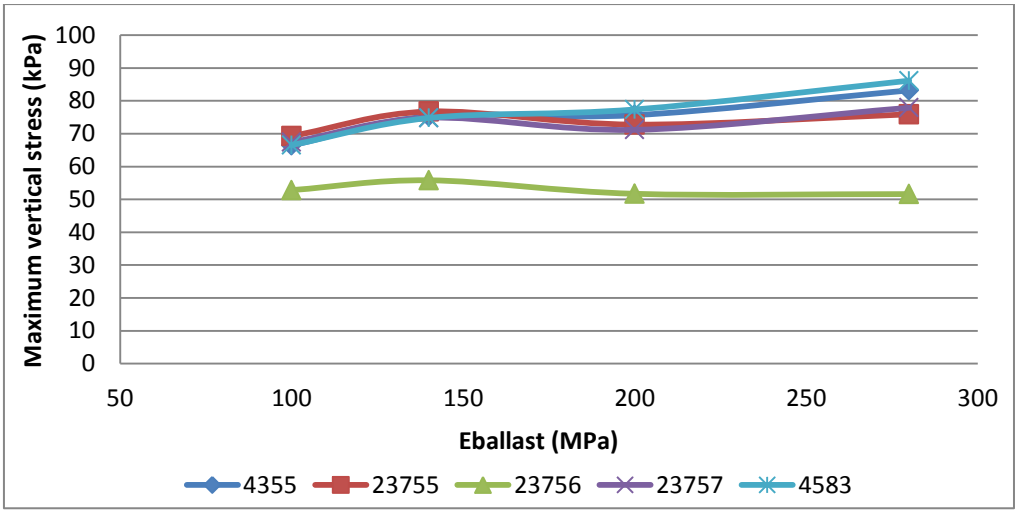

Figure 6.7 Rotations of sleeper at different loading magnitudes

## 6.4 Material properties

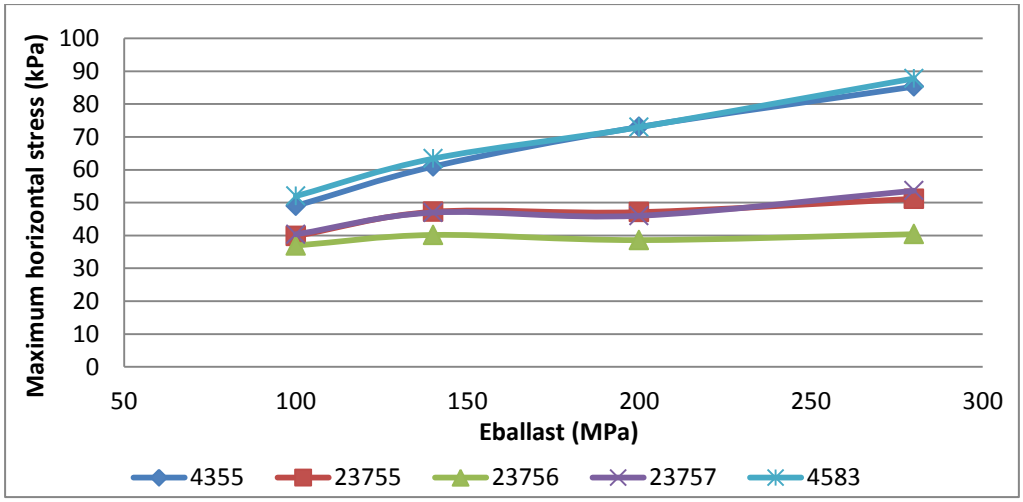
To evaluate the effects of material properties on stress conditions and sleeper rotation, Young's modulus of rail pad, ballast and subgrade have all been varied. All the variables can be found in Table 6.1 and the influences of different materials are analysed individually.

### 6.4.1 Young's modulus of ballast

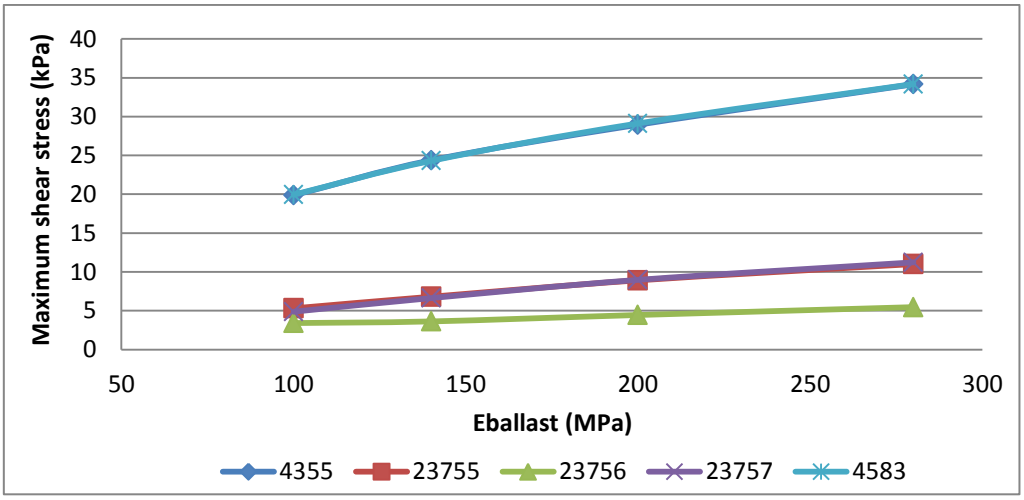
The effects of Young's modulus of ballast on stress states are presented next. Four $E_{ballast}$ values, 100, 140, 200 and 280MPa, have been analysed in this section. The maximum YZ in-plane stresses varying with $E_{ballast}$ are shown in Figure 6.8. While there is very little change at sleeper centre (point 23756) for in-plane normal and shear stresses, the stresses at all other points tend to increase gradually as $E_{ballast}$ increases. In particular, the horizontal and shear stresses at the bottom corners of the sleeper increase relatively sharply, by 69% and 72% respectively, when $E_{ballast}$ increases from 100MPa to 280MPa.




(a)




(b)




(c)

Figure 6.8 Maximum in-plane (a) Vertical stress (b) Horizontal stress (c) Shear stress with different $E_{ballast}$

As presented in Figure 6.9, there is only slight change in the sleeper rotation for both load approach and departure phases as $E_{ballast}$ increases. As in Figure 6.7, the sleeper rotates more during the departure than the approach phase because of inertia effects.

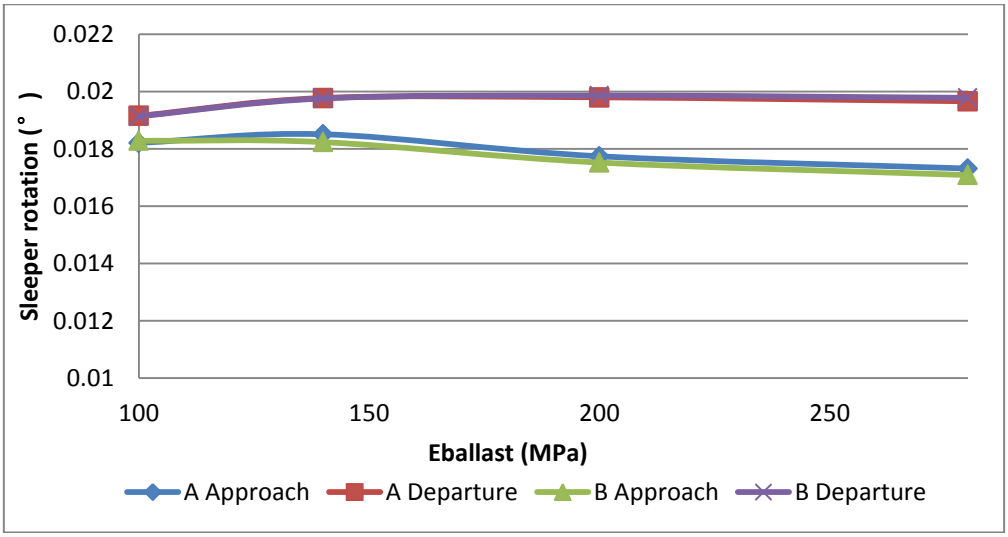
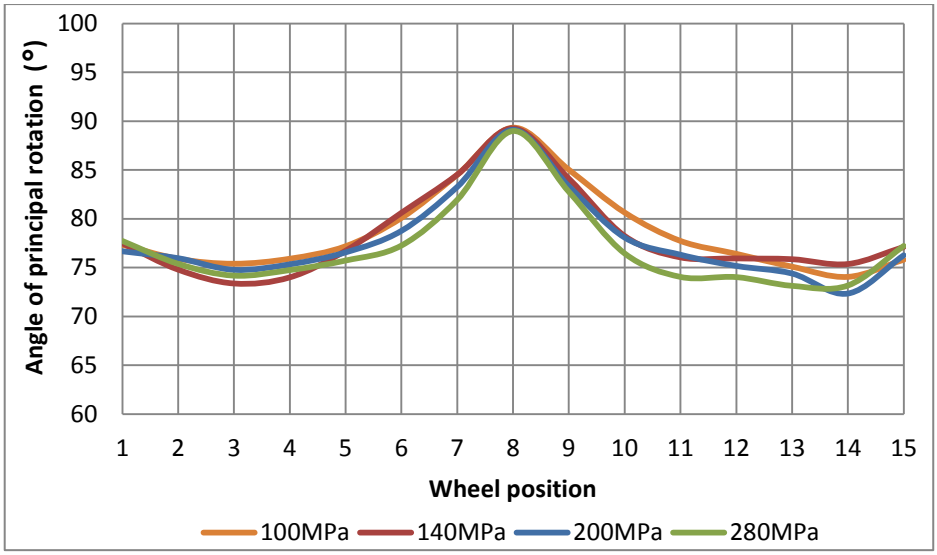
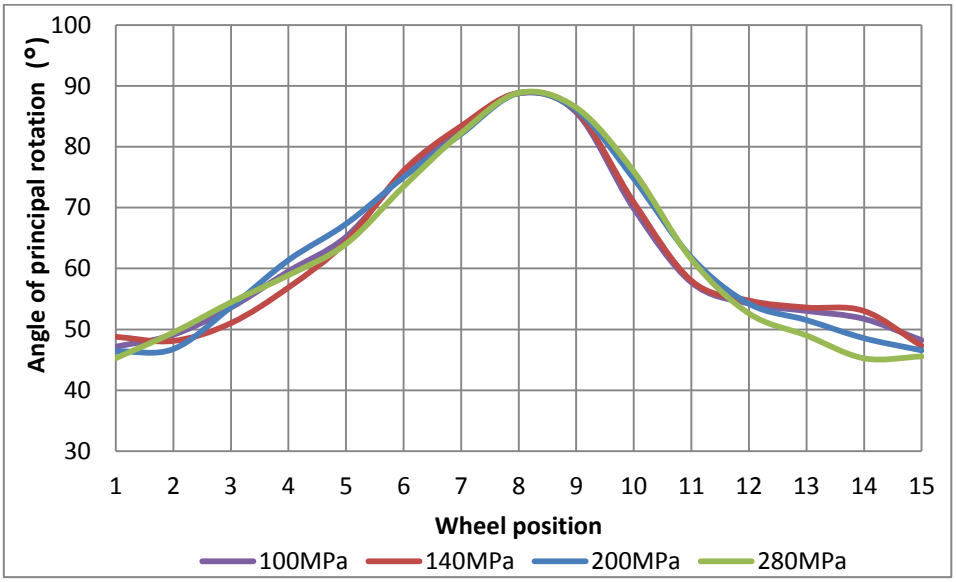



Figure 6.9 Rotations of sleeper at different $E_{ballast}$

A comparison of principal stress rotation with different $E_{ballast}$ values is shown in Figure 6.10. Results are similar with all variables at both locations in the ballast. However, in Figure 6.10(a), principal stress rotates less with decreasing $E_{ballast}$ when the load passes between position 5 and 12.




(a)




(b)

Figure 6.10 Effect of $E_{ballast}$ on principal stress rotation at (a) A (b) D (see Figure 5.21)

As presented in Figure 6.11, comparing the stress paths at different $E_{ballast}$ values, the maximum values of both t and s increase with increasing $E_{ballast}$. As stated above, the analysis point is located immediately adjacent to the sleeper corner; the initial dead weight stress is relatively low. As a result, the path at the start and end zones where the moving load is located far from the sleeper is close to zero and may even break the theoretical failure line. However, there is no obvious trend for the distance

between the stress path and the failure line, which means that the possibility of failure will not be greatly affected by $E_{ballast}$.

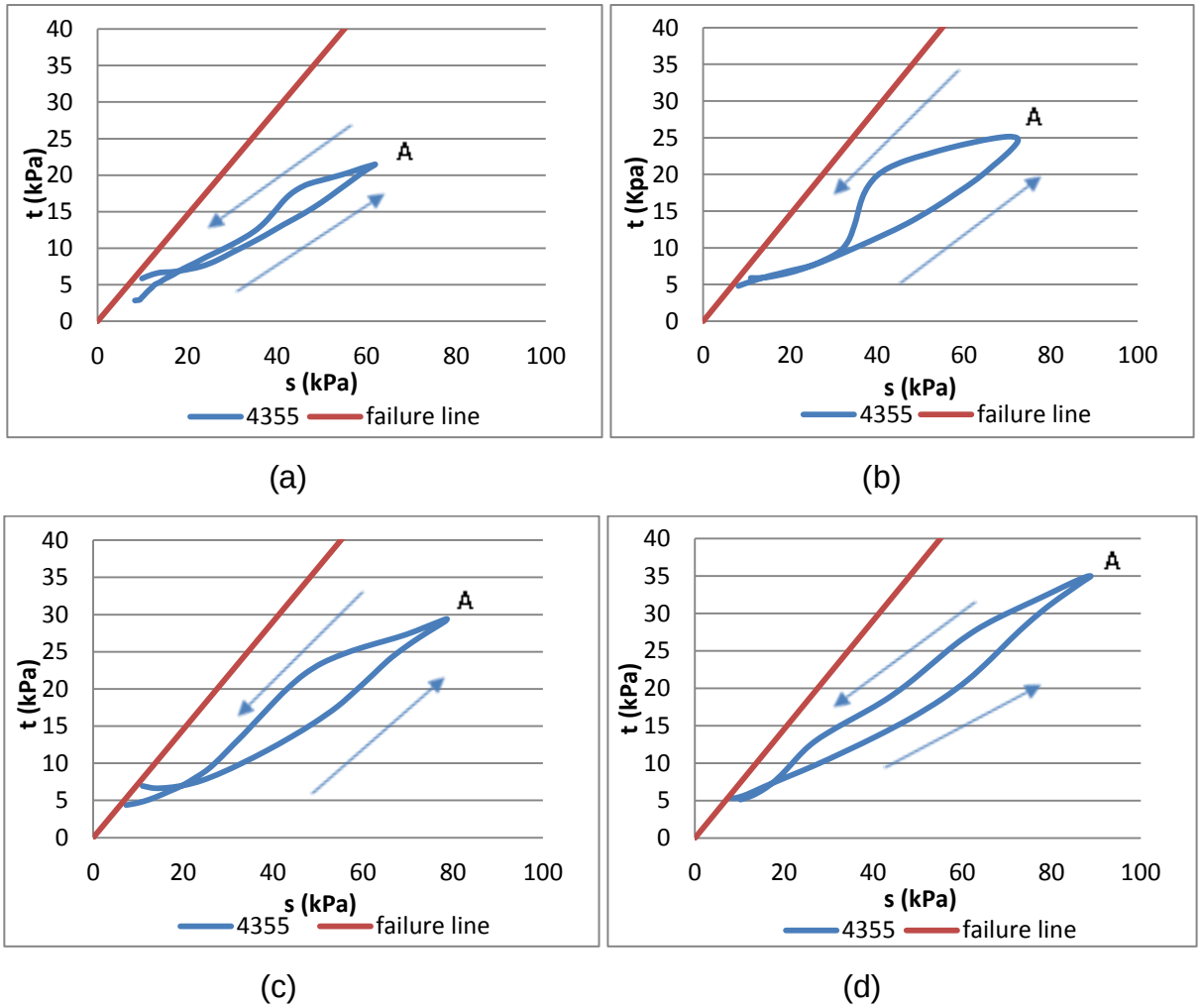



Figure 6.11 Stress path in ballast at sleeper bottom corner at different $E_{ballast}$: (a) 100MPa (b) 140MPa (c) 200MPa (d) 280MPa

Further to the study in Section 4.5, effects of single and dual load on stress path were investigated and are presented in Figure 6.12. Clearly, stress paths at all $E_{ballast}$ values overlap fairly closely and the effects of dual load are insignificantly different compared to the one under a single load. This suggests that simulations under single load are sufficient to fulfil the aims of this research.

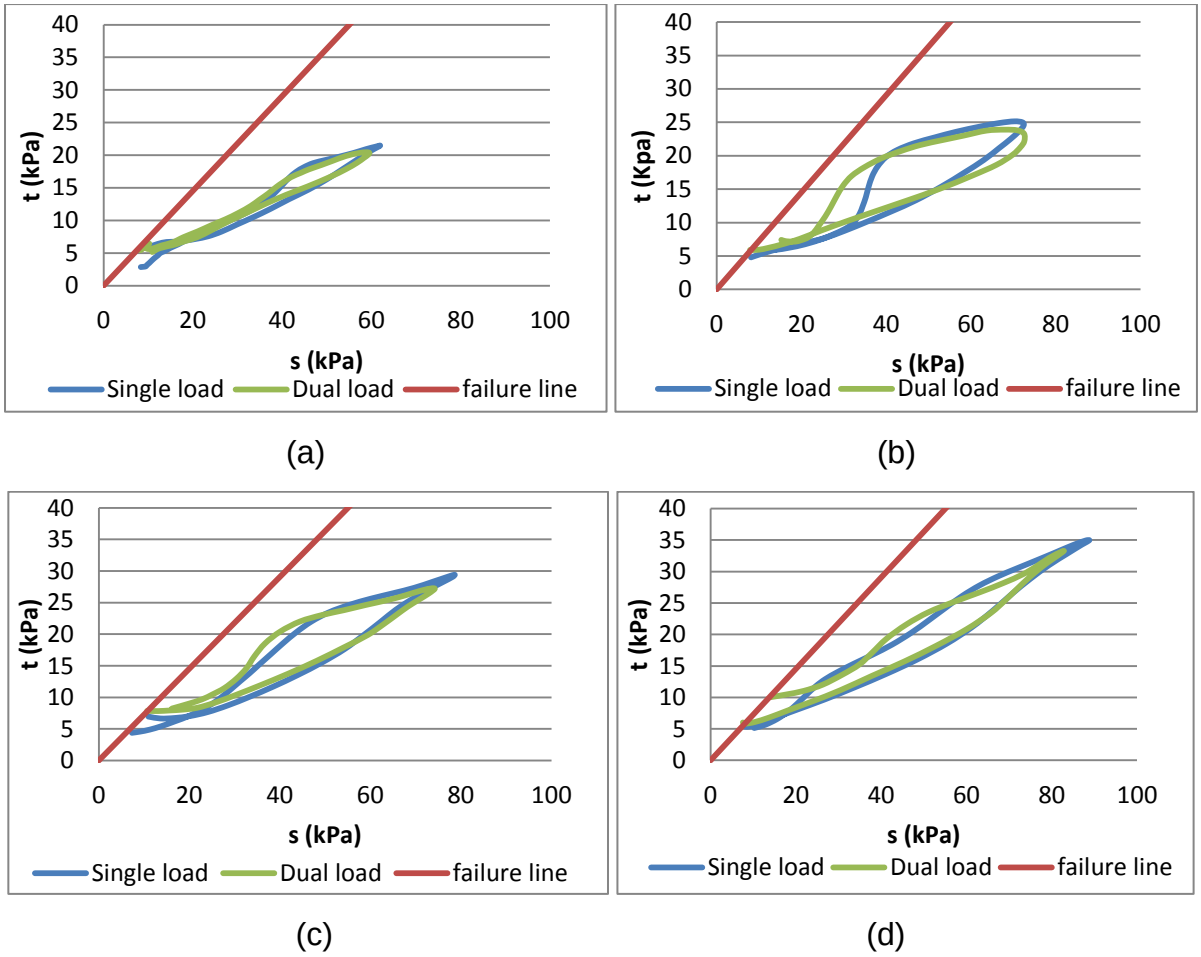
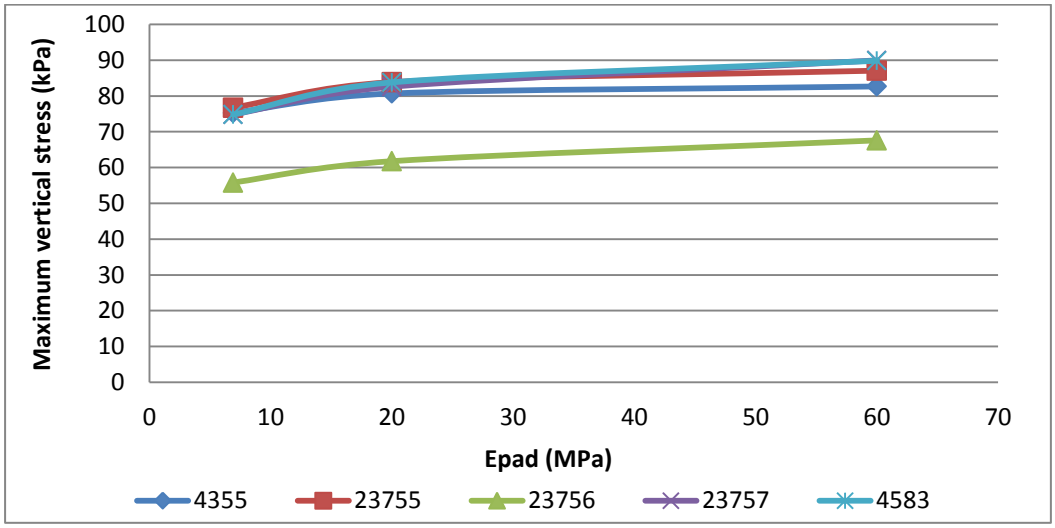



Figure 6.12 Stress path under single and duel load in ballast at sleeper bottom corner at different $E_{ballast}$: (a) 100MPa (b) 140MPa (c) 200MPa (d) 280MPa

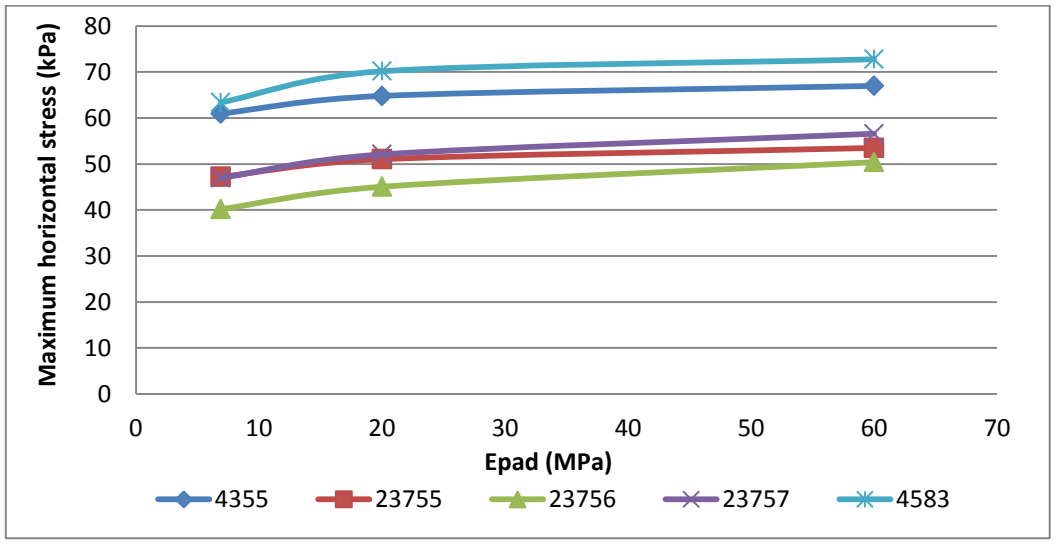
### 6.4.2 Young's modulus of rail pad

With regard to the stiffness of the rail pad, three typical values of rubber stiffness ($k_{pad}$), 20, 60, and 180kN/mm corresponding to soft, intermediate and hard pads respectively, have been chosen. Equivalent the Young's modulus of the assumed 10mm thick rail pad ($E_{pad}$), 6.9, 20, and 60MPa, can then be derived from $K_{pad}$ values. Figure 6.13 illustrates the maximum stress changes with different $E_{pad}$ values. It is evident that all stresses increase as the pad becomes harder. Moreover, as discussed in previous sections, stresses at the middle point of the sleeper always show the lowest value whereas the largest stress always occurs at the two bottom

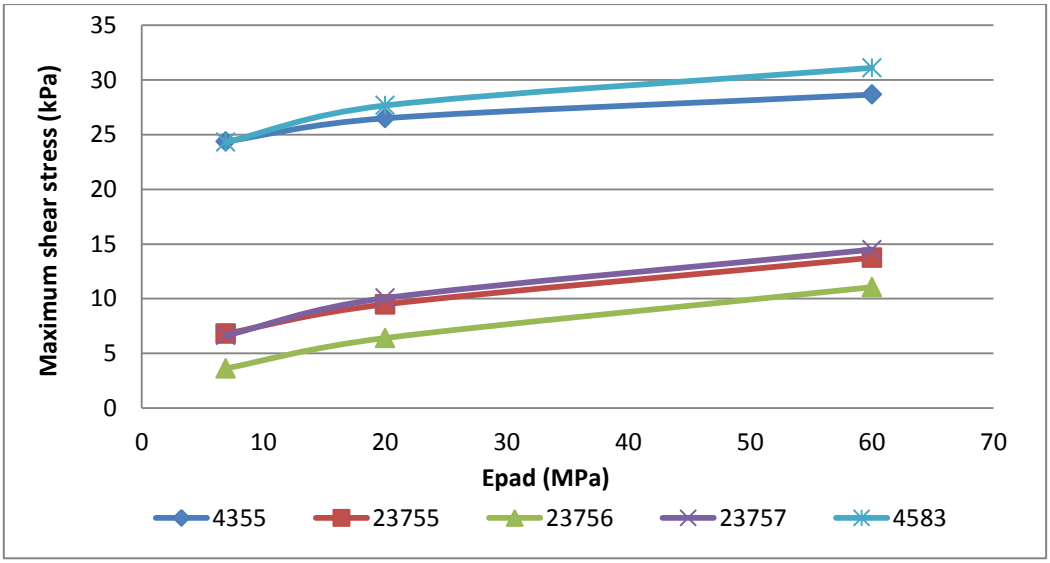
corners. In particular, for the shear stress, values at corner points can reach a maximum of about 30kPa while the maximum value at the other three analysis points is only 13kPa on average.




(a)




(b)




(c)

Figure 6.13 Maximum in-plane (a) Vertical stress (b) Horizontal stress (c) Shear stress with different $E_{pad}$

The calculated maximum rotation of the middle sleeper at different $E_{pad}$ values is presented in Figure 6.14. The angles at points A and B both reduce with increasing $E_{pad}$, while the gradient of the approach and departure curves which are shown in the graph decreases when the rail pad becomes harder. This may indicate that $E_{pad}$ tends to have less effect on sleeper rotation when it is higher than 20MPa. Again, the maximum angle of rotation during departure is always larger than during approach because of the inertia effects.

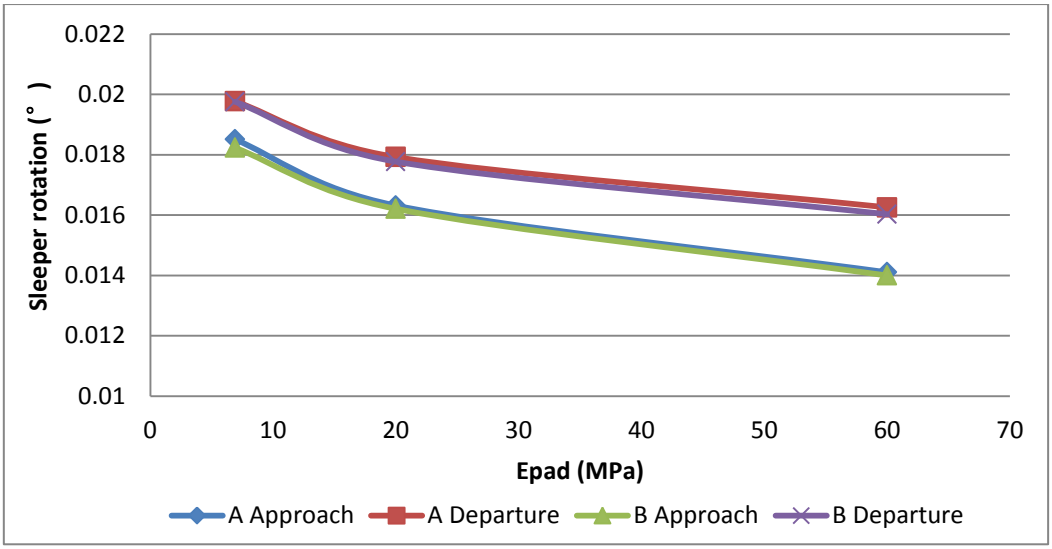
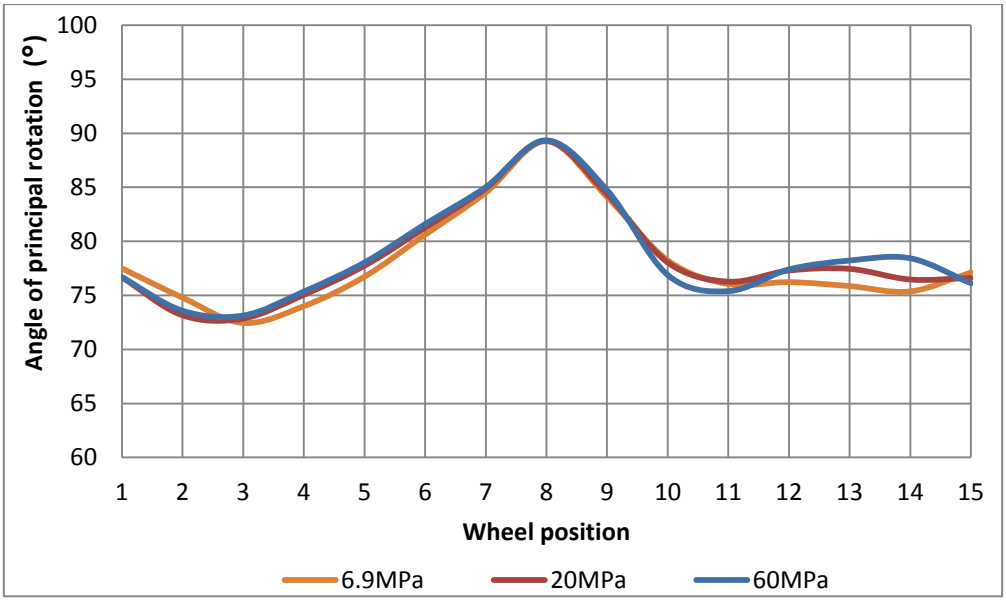


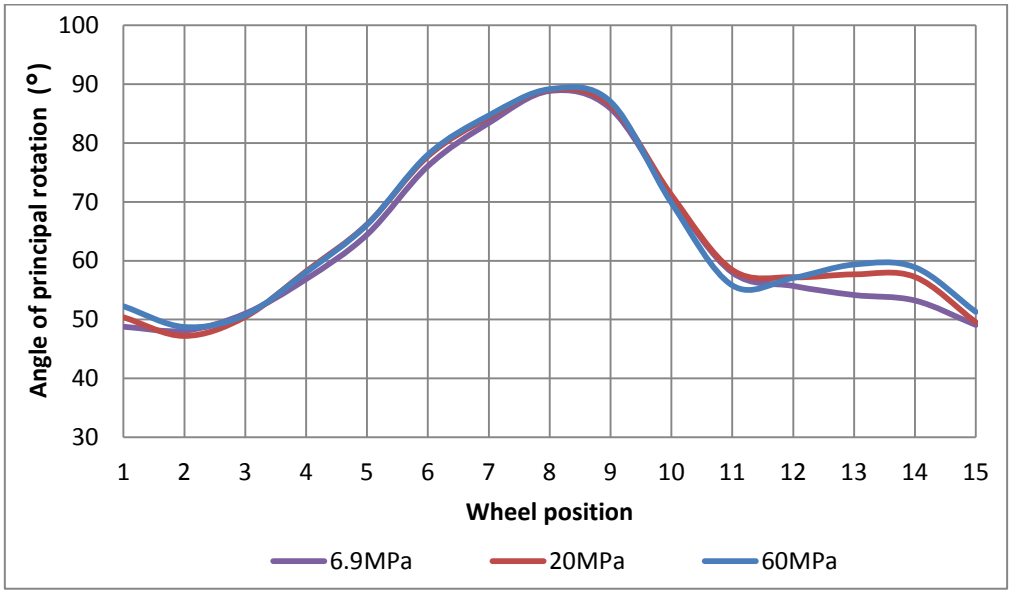

Figure 6.14 Rotations of sleeper at different $E_{pad}$

Figure 6.15 shows the effects of $E_{pad}$ on direction of principal stress at different locations in the ballast. Similar to the results presented in previous sections, there is little difference between the curves corresponding to various $E_{pad}$ values, which means that the effects of $E_{pad}$ are insignificant in this respect.

The stress paths adjacent to the bottom corner of the sleeper are shown in Figure 6.16. It is clear that the stress path moves closer to the failure line when $E_{pad}$ increases, which means the ballast element located near the bottom corner of the sleeper could be deformed more easily as $E_{pad}$ increases. Additionally, the maximum values of both t and s increase with increasing $E_{pad}$. Nevertheless, there is little increase in maximum value of t and s at point A when $E_{pad}$ is higher than 20MPa.




(a)




(b)

Figure 6.15 Effect of $E_{pad}$ on principal stress rotation at (a) A (b) D (see Figure 5.21)

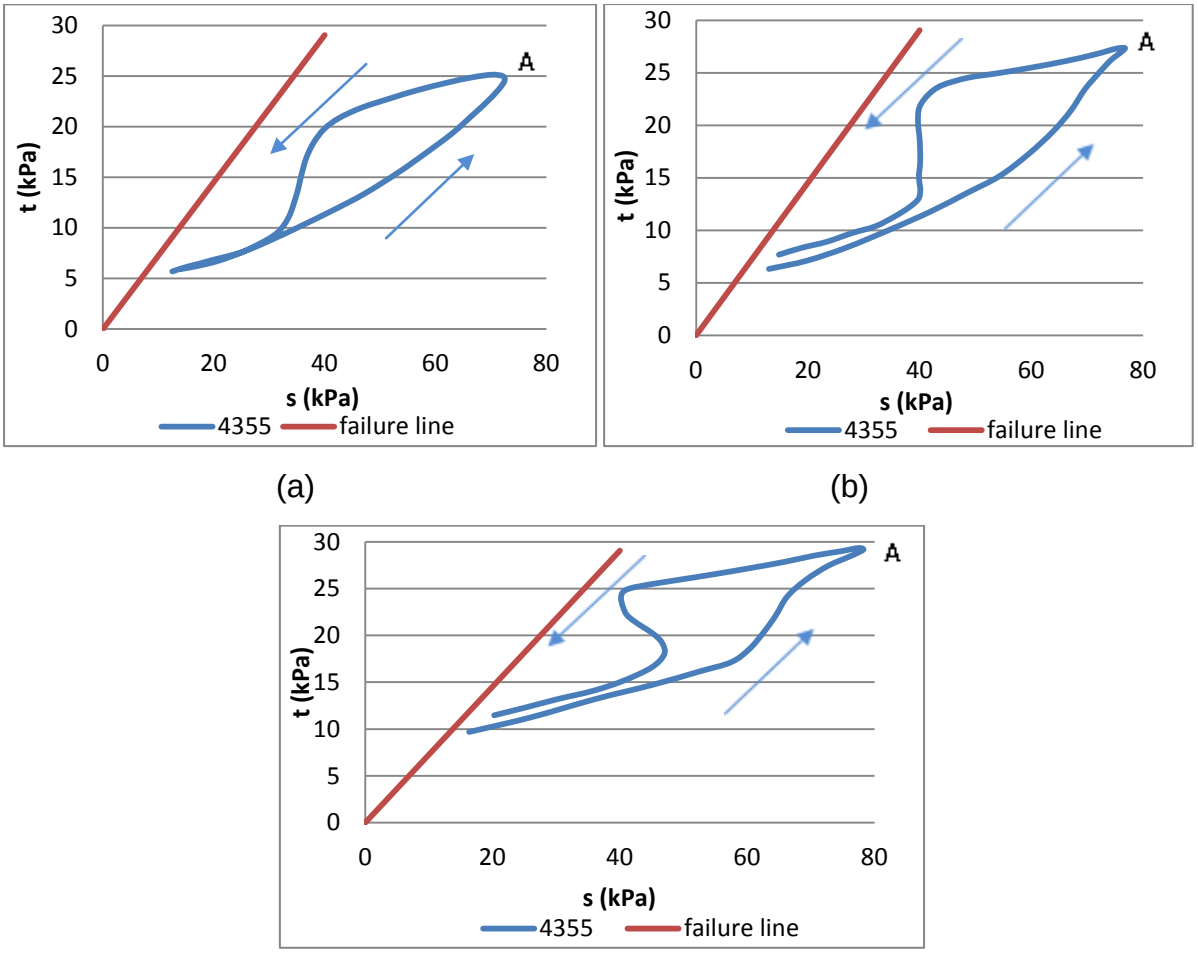
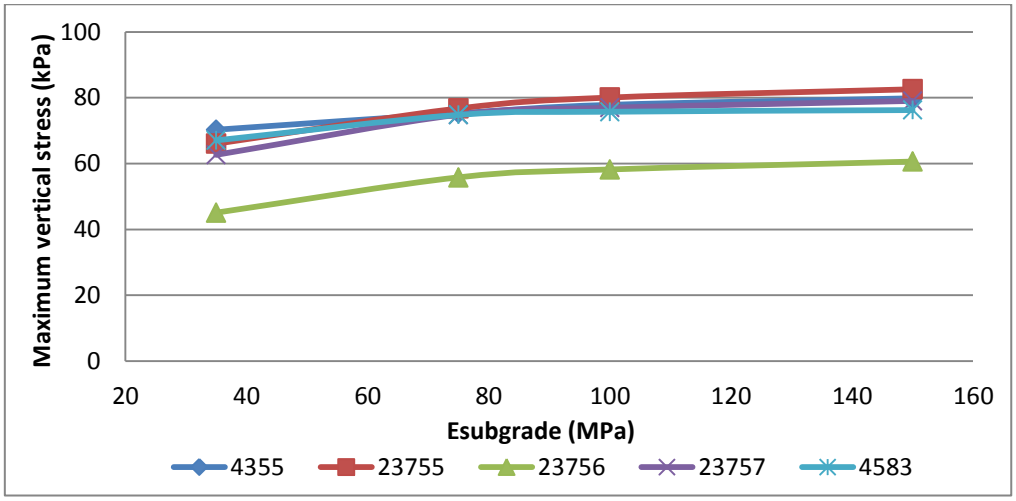



Figure 6.16 Stress path for ballast at sleeper bottom corner at different $E_{pad}$: (a) 6.9MPa (b) 20MPa (c) 60MPa

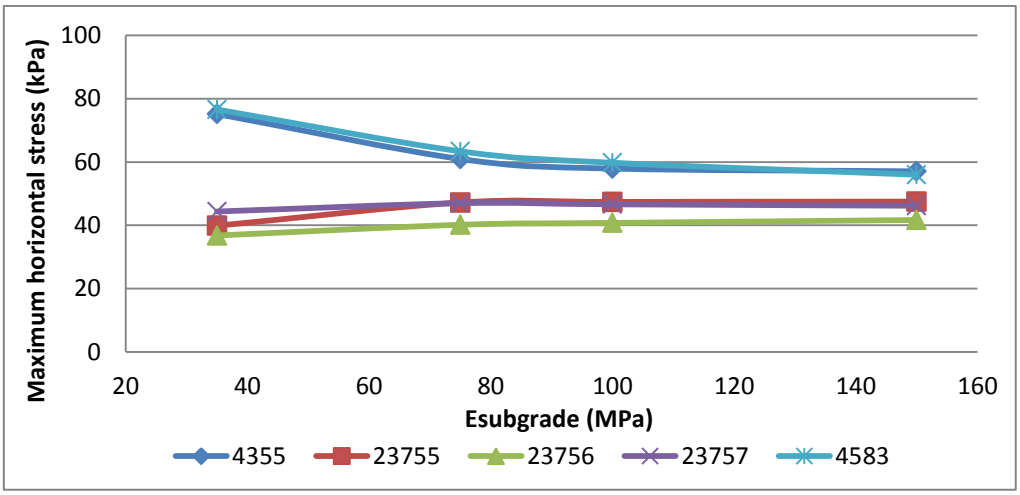
### 6.4.3 Young's modulus of subgrade

Four $E_{subgrade}$ values, 35, 75, 100 and 150MPa, which represent poor, medium, good, and excellent level based on the classification for subgrade suggested by Profillidis (2000), have been investigated. As shown in Figure 6.17(a), the maximum vertical stress at all points increases with increasing $E_{subgrade}$ but tends to level out from 75MPa to 150MPa. Regarding the horizontal stress presented in Figure 6.17(b), there is a clear change due to varying $E_{subgrade}$ at the bottom corners of the sleeper. The stress reduces from 76.6 to 63.3kPa when $E_{subgrade}$ increases from 35 to 75MPa

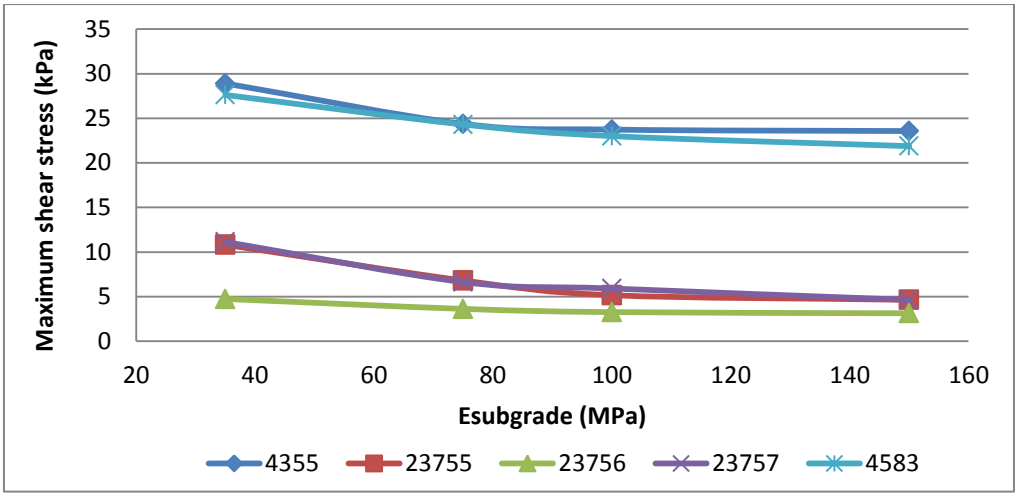
and tends to be approximately constant thereafter. Similarly, as can be seen in Figure 6.17(c), shear stress reduces gradually when $E_{subgrade}$ increases from 35 to 75MPa with little change thereafter. In conclusion, there is little effect of $E_{subgrade}$ on in-plane stresses once the subgrade becomes stiffer than 75MPa.




(a)




(b)




(c)

Figure 6.17 Maximum in-plane (a) Vertical stress (b) Horizontal stress (c) Shear stress with different $E_{subgrade}$

The maximum rotation of the sleeper recorded at both bottom corners is displayed in Figure 6.18. The sleeper has the largest rotation of 0.033 degrees when the load passes over the softest subgrade. A sharp decrease of angle occurs when $E_{subgrade}$ increases from 35MPa to 75MPa, but changes in the angle of rotation are less as the subgrade becomes stiffer.

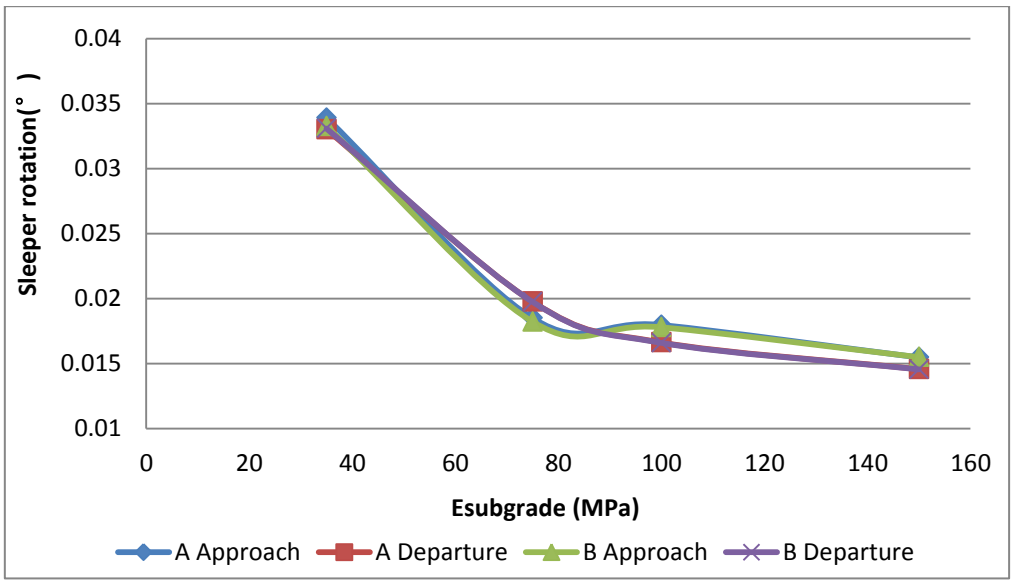
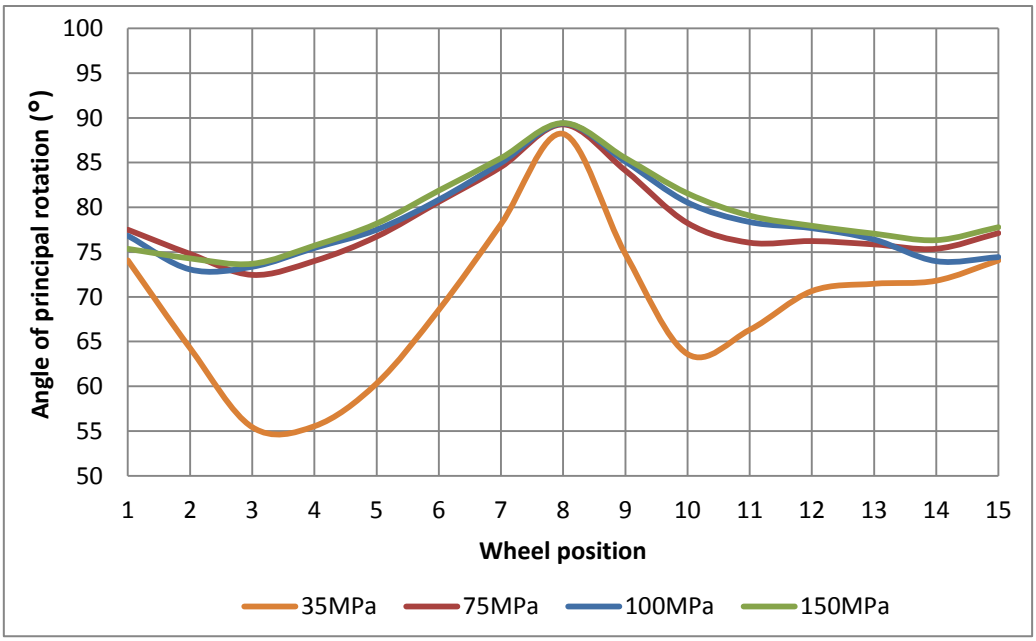
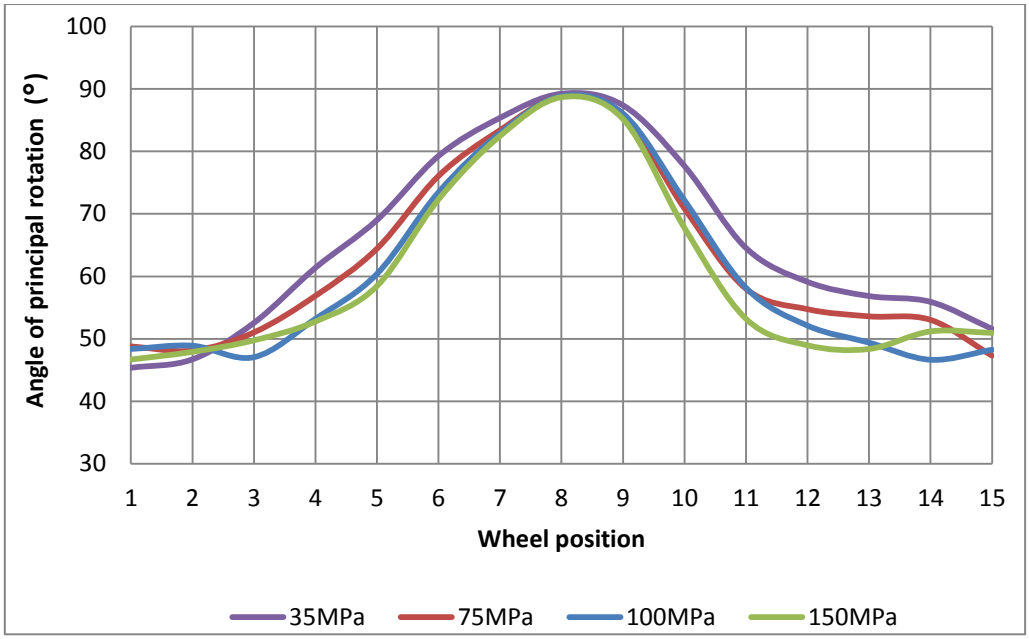



Figure 6.18 Rotations of sleeper at different $E_{subgrade}$

As presented in Figure 6.19(a), principal stresses rotate similarly when $E_{subgrade}$ is higher than 75MPa. However, the principal stress in the ballast experiences significant rotation over soft subgrade ($E_{subgrade}$=35MPa). The rotation of principal stress at point A can be divided into 4 distinct phases. In phase 1, it rotates away from the vertical position while the wheel load is passing through position 1 to 3. The direction of principal stress gradually reverses back to vertical when the load moves from position 3 (56°) to 8 (90°) in phase 2. With the wheel load departing, it continuously rotates until the position 10, and reduces after that. Moreover, as presented in Figure 6.19(b), principal stress at the bottom of the ballast experiences a greater rotation with increasing $E_{subgrade}$ values.




(a)




(b)

Figure 6.19 Effect of $E_{subgrade}$ on principal stress rotation at (a) A (b) D (see Figure 5.21)

Figure 6.20 shows the stress paths with different value of $E_{subgrade}$. Both t and s at point A reduce as $E_{subgrade}$ increases from 35MPa to 75MPa, while changes in maximum t and s in Figure 6.20 (b)-(d) are slight. Meanwhile, the stress paths in all graphs are approximately at similar distances from the failure line.

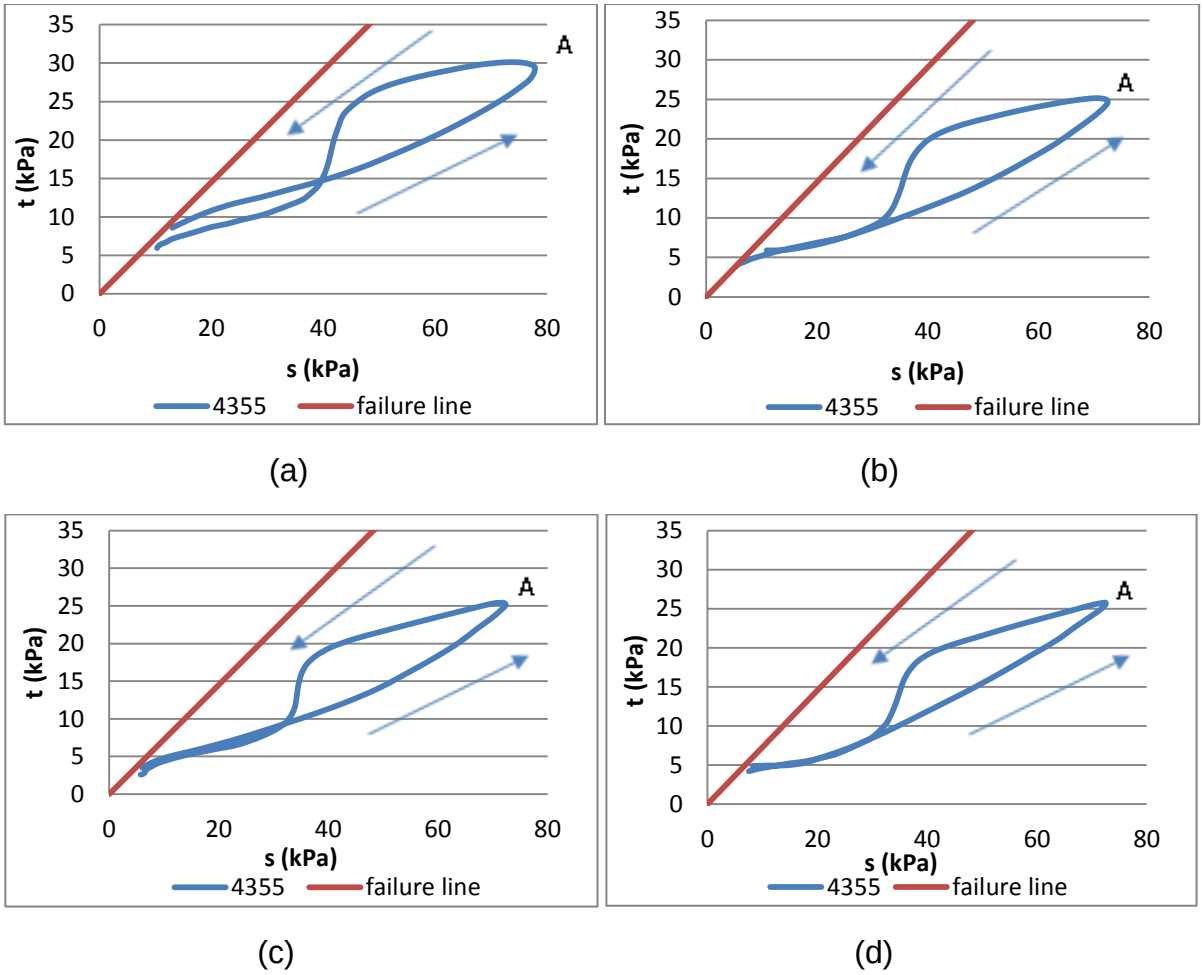



Figure 6.20 Stress path in ballast at sleeper bottom corner at different $E_{subgrade}$: (a) 35MPa (b) 75MPa (c) 100MPa (d) 150MPa

## 6.5 Summary

Using the Finite Element model developed in the previous chapter, a set of variables has been investigated and the effects of load magnitude, speed and the stiffness of materials on stress, deflection and sleeper rotation have been computed.

Generally, no matter which parameter of the model changes, the maximum in-plane stresses at the middle point of the bottom sleeper are always the lowest among the five analysis points selected. Also, points at both bottom corners of the sleeper always show the largest normal and shear stresses, i.e. they present stress concentrations, in which then cause larger strain. Furthermore, there is only slight change in maximum in-plane stresses at the other three points as loading speed and Young's modulus of materials increases.

With regard to sleeper rotation, the angle increases sharply when the loading speed is higher than 120km/h. Also, the angle reduces with increasing $E_{pad}$ and $E_{subgrade}$. In particular, $E_{subgrade}$ affects the sleeper rotation most when it is lower than 75MPa, whereas the change is slight when it increases beyond 75MPa. However, there is no appreciable change in the maximum sleeper angle as $E_{ballast}$ increases.

There is little effect of using different values of load speed, $E_{ballast}$ and $E_{pad}$ on rotation of principal stress. However, at a speed of 300km/h, the principal stress just under the sleeper rotates more heavily than at lower speeds; it also rotates less prominently with decreasing $E_{ballast}$. But, principal stress under the sleeper experiences significant rotation over soft subgrade ($E_{subgrade}$=35MPa), while at the

interface of ballast and subballast it has a greater rotation with increasing $E_{subgrade}$ values.

Both shear and confining stresses increase with increasing load speed, $E_{pad}$ and $E_{ballast}$ but decrease when $E_{subgrade}$ increases from 35MPa to 75MPa, although there is little effect of $E_{subgrade}$ on stress states when $E_{subgrade}$ is higher than 75MPa. It is worth noting that the stress path moves closer to the failure line when $E_{pad}$ increases, which means the ballast surrounding the bottom corner of the sleeper will deform more easily as the rail pad becomes harder.

Stress paths under dual wheel loads were very similar to those under a single wheel load at all values of $E_{ballast}$. This suggests that simulations under a single load are sufficient to meet the aims of this research.

# 7 Conclusions and Recommendations

The key results and the main findings from the research are summarised in this Chapter. All the aims and objectives of this project have been achieved. The limitations of this project will also be identified. Lastly, final conclusions and several recommendations for further studies are presented.

## 7.1 Conclusions

The aim of this research was to develop an understanding of the performance of railway trackbed under realistic traffic loading through a simulation model using the Finite Element Method (FEM). The goal of the research was to investigate the stress and displacement characteristics within ballast which may be further used for predicting the long term behaviour of railway trackbed system so as to minimise maintenance costs due to ballast settlement and particle degradation and in improving the long term performance of a railway trackbed system. The specific objectives of this project are listed below:

- To develop 2D and 3D finite element models of the entire trackbed system. This includes optimisation of mesh type and density in order to reduce calculation time effectively, as well as to make the results more accurate in simulating engineering reality.
- To identify the stress and deformation behaviour of rail trackbed, especially in the ballast, in a three-dimensional simulation model under dynamic moving load.

- To evaluate the effects of different variables including moving load magnitude, loading speed and stiffness of materials on stresses and deflections within ballast based on the 3D railway trackbed model through a comprehensive parametric analysis.
- To identify the impact of the analyses during the research on the prediction of the long-term performance of railway track.

A list of key findings and conclusions is as follows:

- After comparing the two 2D simulation models, a key issue was identified, namely that all the stresses calculated at measuring points at the bottom corner of the sleeper change depending on mesh density (Figure 3.10; Figure 3.21(b)). It is therefore hard to achieve an accurate stress value at the bottom corner of the sleeper because of calculation difficulties when a stress concentration occurs.
- Based on the results of the 2D model, both vertical stress and displacement are relatively low at the far end boundary from the loading point. A longer substructure with 22m length for the 3D model was then set up and this was shown to be of sufficient length to avoid wave reflection and resulting inaccuracy due to boundary conditions.
- In the damping boundary coefficient validation test, the vertical displacements increased with increasing alpha damping value. Also, the curves rebounded more heavily with increasing alpha damping after the loading period. On that basis, $10^4$ was determined as the alpha damping value to control energy reflection.

- In the subgrade depth investigation, six different subgrade depths with damping boundary layer were compared with a 155m depth subgrade with a fixed boundary, calculated to be adequate to avoid wave reflection effects. The result from the model was that an 8m depth subgrade with damping boundary was found to be one of the closest to that with the 155m depth subgrade, whereas lower subgrade depths show significantly different results. The 8m depth was therefore selected.
- Four cases with different mesh densities, including a coarse mesh case and three fine mesh cases, were investigated in a 3D model. All three fine mesh models showed similar results. The results showed that it was not necessary to increase the mesh density to the densest case. Consequently, an optimised mesh with 121403 elements was finally selected.
- A 3D model with single dynamic moving wheel load was confirmed to give an acceptable simulation of real traffic. The results from both single load and double load models for maximum vertical stress and vertical displacement were found to be very similar.
- Stress paths under dual load were very similar to those under a single load. Thus results from single load analyses are considered valid.
- A frequency response comparison of the results from simulations to those from a real rail line showed that simulation and real measurement gave similar peak frequencies and the power density spectra matched well in the longitudinal and vertical directions.
- Based on the results of the 3D reference case, because of ambient vibration, noise was found to occur in all cases.

- A sharp reduction in the vertical stress from the outer edge of the sleeper to the centre was observed and this may logically lead to more damaging stress conditions at the bottom corner of the sleeper than in other places.
- Maximum principal stress rotations at different calculation points in the ballast have been computed and a sharp rotation was found at depths of 250mm or more in the ballast, which may lead to axial permanent strain increases.
- Generally, no matter which combination of model parameters in the 3D dynamic loading simulations, the maximum in-plane stresses at the middle point of the base of the sleeper are always lower than those nearer the bottom edge. Both bottom corners of the sleeper always show the largest normal and shear stresses and this would logically cause larger strain.
- The sleeper rotation in YZ plane increases sharply when the loading speed is higher than 120km/h. This can result in a higher vertical displacement underneath. Also, the rotation angle reduces along with increasing modulus of either pad or subgrade. In particular, subgrade modulus affects the sleeper rotation most when it is lower than 75MPa. No obvious change of the maximum rotation angle was observed with changes in ballast modulus.
- With regard to the stress paths occurring with different input variables, both shear stress t and confining stress s increase with increasing load speed, pad stiffness and ballast stiffness but decrease with increasing subgrade stiffness. However, there is relatively little change in the stress ratio across all cases and a significant effect of subgrade stiffness on stress paths can only be found when subgrade modulus is at a low level.
- There is little effect from using different values of load speed, ballast stiffness and pad stiffness on the direction of principal stress. In particular, principal

stress experiences significant rotation within soft subgrade ($E_{subgrade}$=35MPa). Principal stress at the interface of ballast and subballast has a greater rotation with increasing subgrade stiffness values.

- The stress path can be seen to move closer to the failure line as the stiffness of the pad increases which means that the ballast element located around the bottom corner of the sleeper will deform more easily as the rail pad becomes harder.

## 7.2 Recommendations

Since the model simulates purely linear elastic materials, and several other assumptions have also been made, the results cannot be considered as a true simulation of reality. Thus, several suggestions for future work are listed as follows:

- A 3D non-linear model could be made to simulate stress distribution as well as dynamic effects more accurately.
- The influence of a greater range of variables, including sleeper shape and rail pad dimensions, on stress condition and sleeper rotation could be incorporated into the study.
- To reduce computing time and avoid convergence difficulties, all the surfaces between two adjacent parts of the trackbed were tied, which may lead to inaccurate results at the interface. Thus, studies of the detailed interaction properties would be useful, allowing frictional slip at the sleeper-ballast interfaces.

- The detailed stress predictions arising from this research and any subsequent added work should be incorporated into a detailed prediction of ballast permanent deformation, exploring a range of potentially appropriate behavioural models.

# References

*ABAQUS User's Manual 6.10* (2010). Pawtucket

Aikawa, A. (2015). *Dynamic characterisation of a ballast layer subject to traffic impact loads using three-dimensional sensing stones and a special sensing sleeper.* Construction and Building Materials, 92, 23-30.

Alva-Hurtado, J. E. (1980). *A methodology to predict the elastic and inelastic behaviour of railroad ballast.* Ph.D. dissertation, Univertisy of Massachusetts, Amherst, Massachusetts.

Banimahd, M. and Woodward, P.K., (2007). *3-Dimensional Finite Element Modelling of Railway Transitions*, Proceedings of 9th International Conference on Railway Engineering London, June 2007.

Bian, X., Cheng, C., Jiang, J., Chen, R., & Chen, Y. (2016). *Numerical analysis of soil vibrations due to trains moving at critical speed*. Acta Geotechnica, 11(2), 281-294.

Blanco-Lorenzo, J., Santamaria, J., Vadillo, E. G., & Oyarzabal, O. (2011). *Dynamic comparison of different types of slab track and ballasted track using a flexible track model*. Proceedings of the Institution of Mechanical Engineers, Part F: Journal of Rail and Rapid Transit, 225(6), 574-592.

Bodin, V. (2001). *Comportement du ballast des voies ferrées soumises à un chargement vertical et latéral* (PhD dissertation, Ecole Nationale des Ponts et Chaussées)

Bogacz, R., Czyczuła, W., & Konowrocki, R. (2014). *Influence of sleepers shape and configuration on track-train dynamics*. Shock and Vibration, 2014.

British Standard: BS EN 13450 (2002). Aggregates for railway ballast.

Brown, S.F., (1996). *Soil mechanics in pavement engineering*. Geotechnique, 1996, 46(3), 384-426.

Cheng, Y.P., Bolton, M.D. and Nakata, Y., (2004). *Crushing and Plastic Deformation of Soils Simulated Using DEM*. Géotechnique, 54, 131-141.

Eason, G. (1965). *The stresses produced in a semi-infinite solid by a moving surface force.* International Journal of Engineering Science, 2(6), 581-609.

Eisenmann, J., Leykauf, G. and Mattner, L., (1994). *Recent Developments in German Railway Track Design.* Proceedings of the Institution of Civil Engineers, Transportation, 105, pp. 91-96.

Esveld, C., (1989). *Modern Railway Track.* MRT-Productions, the Netherlands.

Esveld, C., (2001). *Modern Railway Track (Second Edition).* MRT-Productions, the Netherlands.

Fryba, L. *Vibration of solids and structures under moving loads*, 1999.Academia Prague.

Gaskin, P.N. and Raymond, G., (1976). *Contribution to Selection of Railroad Ballast.* Transportation Engineering Journal, ASCE, 102 (TE2), pp. 377-394.

Grabe, P. J. (2002). *Resilient and permanent deformation of railway foundations under principal stress rotation* (PhD dissertation, University of Southampton).

Grabe, P.J., and Clayton, C.R.I., (2009). *The Effects of Principal Stress Rotation on Permanent Deformations in Rail Track Formations*. J. Geotech. Geoenviron. Eng., 135(4), 555-565.

Han, X & Selig, T. (1997). *Effects of fouling on ballast settlement*. 6th International Heavy Haul Conference. St Louis; Int. Heavy Haul Association; Spoornet Vol. 1, pp. 257-268.

Hicks, R. G. & Monismith, C. L. (1971). *Factors influencing the resilient response of granular materials.* Highway Research Record 345, Highway Research Board, Washington, DC, pp. 15-31.

Housain, Z, Indraratna, B, Darve, F and Thakur, P, (2007). *DEM Analysis of Angular Ballast Breakage under Cyclic Loading*. Geomechanics and Geoengineering: International Journal, 2(3), 175-182.

Huang, H., & Chrismer, S. (2013). Discrete element modeling of ballast settlement under trains moving at “Critical Speeds”. *Construction and Building Materials*, *38*, 994-1000.

Indraratna, B., Ionescu, D. and Christie, H.D., (1998). *Shear Behaviour of Railway Ballast Based on Large-scale Triaxial Tests*. Journal of Geotechnical and Geoenvironmental Engineering 124, No. 5, pp. 439-449.

International Union of Railway (UIC), (1994). *UIC Code 719: Earthworks and trackbed layers for railway lines*. UIC, Paris, France.

Ionescu, D., Indraratna, B. and Christie, H.D. (1998). *Behaviour of Railway Ballast under Dynamic Loads*. Proc. 13th Southeast Asian Geotechnical Conference, Taipei, pp. 69-74.

Ishida, M., Namura, A., & Suzuki, T. (2002). *Track dynamic analysis for track settlement & irregularity growth*. In PROCEEDINGS OF THE INTERNATIONAL CONFERENCE RAILWAY ENGINEERING 2002, HELD LONDON, UK, JULY 2002-CD ROM.

Ishikawa, T., Miura, S., Sekine, E., (2007). *Development and Performance Evaluation of Multi-ring Shear Apparatus*. In: Proceedings of the International Workshop on Geotechnical Aspects and Processed Material. 13th September 2005, Osaka, pp. 53-64

Inamn, A. Ishikawa, T., and Miura, S., (2012). *Effect of Principal Stress Axis Rotation on Cyclic Plastic Deformation Characteristics of Unsaturated Base Course Material*. Soils and Foundations 2012; 52(3): 465-480

Jaky, J., (1948). *Pressure in Soils.* Second International Conference Mechanics and Foundation Engineering. Rotterdam.

Jeffs, T. and Tew, G.P., (1991). *A Review of Track Design Procedures, Vol. 2, Sleepers and Ballast,* Railways of Australia.

Jiang, T., & Zhang, X, (2004). *Dynamic Analysis of Elastic Half Space Problems by Using FEM with Viscous Boundary Element*. 25(4), 535-540.

Kaewunruen, S., & Remennikov, A. M. (2007). *Investigation of free vibrations of voided concrete sleepers in railway track system.* Proceedings of the Institution of Mechanical Engineers, Part F: Journal of Rail and Rapid Transit, 221(4), 495-507.

Kempfert, H.G. and Hu, Y., (1999). *Measured dynamic loading of railway underground.* Proc. 1the Pan-American Conf. on Soil Mech. And Geotech. Engg., Brazil, pp. 843-847

Knothe, K. L., & Grassie, S. L. (1993). *Modelling of railway track and vehicle/track interaction at high frequencies*. Vehicle system dynamics,22(3-4), 209-262.

Knutson, R. M. (1976). *Factors influencing the repeated load behaviour of railway ballast.* PhD Dissertation, University of Illinois at Urbana-Champaign.

Krylov, V. V. (1995). *Generation of ground vibrations by superfast trains*. Applied Acoustics, 44(2), 149-164.

Lei, W., & Wei, D., (2005). *Spring-viscous Boundary in Finite Element Analyses for Infinite Media*. Earthquake Engineering and Engineering Vibration, 25(3), 110-114.

Lei, X., & Noda, N. A. (2002). *Analyses of dynamic response of vehicle and track coupling system with random irregularity of track vertical profile*. Journal of Sound and Vibration, 258(1), 147-165.

Lekarp, F. and Dawson, A., (1998). *Modelling Permanent Deformation Behavior of Unbound Granular Materials*. Construction and Building Materials 12, No. 1, 9-18.

Lekarp, F., Isacsson, U., & Dawson, A. (2000a). *State of the art. I: Resilient response of unbound aggregates*. J. Transp. Engrg., ASCE. Vol 126, No. 1, pp. 66-75.

Lekarp, F., Isacsson, U., & Dawson, A. (2000b). *State of the art. II: Permanent strain response of unbound aggregates.* J. Transp. Engrg., ASCE. Vol 126, No. 1, pp. 76-83.

Liao, C., Chang, T. and Young, D., (1995). *Elasto-Plastic Constitutive Modelling of Granular Assembly,* International Journal of Solids and Structures, 32 (8-9), pp. 1121-1133.

Light, T.J., Ho, C.L., and Lambert, R.S., (2013). *Effect of Moisture on Engineering Characteristics of Fouled Ballast*. TRB 2014 Annual Meeting.

Lim, W.L., (2004). *Mechanics of Railway Ballast Behaviour*, PhD Dissertation, School of Civil Engineering, the University of Nottingham, UK.

Lim, W.L. and McDowell, G.R., (2005). *Discrete Element Modeling of Railway Ballast*. 375 Granular Matter, 7, 19--29.

Lu, T, (2010), *The Influence of Pavement Stiffness on Vehicle Fuel Consumption.* PhD Dissertation, School of Civil Engineering, the University Of Nottingham.

Lundqvist, A. and Dahlberg, T., (2005). *Load Impact on Railway Track Due to Unsupported Sleepers.* Proceedings of the Institution of Mechanical Engineers, Part F: Journal of Rail and Rapid Transit March 1, 2005 vol. 219 no. 2 67-77.

Madshus, C., & Kaynia, A. M. (2000). *High-speed railway lines on soft ground: dynamic behaviour at critical train speed*. Journal of Sound and Vibration, 231(3), 689-701.

McDowell, G.R., Bolton, M.D. and Robertson, D., (1996). *The Fractal Crushing of Granular Materials*. J. Mech. Phys. Solids 44, No. 12, 2079-2102.

Network Rail (2015), *Annual Report and Accounts 2011*. Network Rail, London.

Network Rail (2013), *Strategic Business Plan for England and Wales*. Network Rail, London.

Nguyen, K., Goicolea, J. M., & Galbadon, F. (2012). *Comparison of dynamic effects of high-speed traffic load on ballasted track using a simplified two-dimensional and full three-dimensional model.* Proceedings of the Institution of Mechanical Engineers, Part F: Journal of Rail and Rapid Transit, 0954409712465710.

Office of Rail and Road (2015), *Freight Rail Usage 2014-2015 Quarter 4 Statistical Release*. Office of Rail and Road, London

Office of Rail and Road (2015), *Passenger Rail Usage 2014-2015 Quarter 4 Statistical Release*. Office of Rail and Road, London

Pen, L.L., (2008). Track Behaviour: The Importance of the Sleeper to Ballast Interface. PhD Dissertation, University of Southampton.

Popp, K., Kaiser, I., & Kruse, H. (2003). *System dynamics of railway vehicles and track*. Archive of Applied Mechanics, 72(11-12), 949-961.

Powrie, W., Yang, L.A and Clayton, C.R.I. (2007). *Stress changes in the ground below ballasted railway track during train passage. Proceedings of the Institution of Mechanical Engineers, Part F: Journal of Rail and Rapid Transit,* 221, (2), pp. 247-262.

Prakash, S. (1981). *Soil dynamics*. McGraw-Hill Companies.

Priest, J. A., Powrie, W., Yang, L., Grabe, P. J., & Clayton, C. R. I. (2010). *Measurements of transient ground movements below a ballasted railway line*. Géotechnique, 60(9), 667-677.

Profillidis, V. A. (2000). *Railway engineering*.

Railtrack Line Specification (2000). *RT/CE/S/006 Issue 3*. Track Ballast.

Raymond, G. P. & Bathurst, R. J. (1987). *Performance of large-scale model single tie-ballast systems.* Transportation Research Record 1131, pp. 7-14.

Ross, M. (2004). *Modelling Methods for Silent Boundaries in Infinite Media*. Fluid-Structure Interaction. ASEN 5519-006.

Salim, M.W., (2004). *Deformation and Degradation Aspect of Ballast and Constitutive Modelling Under Cyclic Loading*. PhD Dissertation, the University of Wollongong.

Sato, Y. (1995). *Japanese studies on deterioration of ballasted track*.Vehicle system dynamics, 24(sup1), 197-208.

Seed, H.B., Chan, C.K. and Lee, C.E., (1962). *Resilience Characteristics Subgrade Soils and Their Relation to Fatigue Failures.* Proc. Int. Conf. Structural Design of Asphalt Pavements, Ann Abor, Michigan, pp. 611-636.

Selig, E.T., (1984). *Ballast for Heavy Duty Track*. Track Geotechnology, Proc. of a Conf. organized by the Inst. of Civil Engineers and held at University of Nottingham, pp. 245-252.

Selig, E.T and Waters, J.M., (1994). *Track Geotechnology and Substructure Management.* Thomas Telford, London.

Shenton, M.J., (1975). *Deformation of Railway Ballast under Repeat Loading Conditions.* Railroad Track Mechanics and Technology (Kerr ed.), Proc. of a Symposium held at Princeton Univ., pp. 387-404

Shenton, M.J., (1984). *Ballast deformation and trrack deterioration*. In proceedings of a Conference on Track Technology, University of Nottingham:253–265, 11-13 July 1984.

Shi, X.Y., (2009), Prediction *of Permanent Deformation in Railway Track*. PhD Dissertation, School of Civil Engineering, the University of Nottingham, UK.

Skoglund, K.A., (2002). *A study of some factors in mechanics railway track design,* PhD Dissertation, Norwegian University of Science and Technology.

Suiker, A. S. J., Selig, E. T., and Frenkel, R. (2005). *Static and cyclic triaxial testing of ballast and subballast* Journal of geotechnical and geoenvironmental engineering, ASCE. Vol. 131, No. 6, pp. 771-782.

Sun, Y. Q., Dhanasekar, M., & Roach, D. (2003). *A three-dimensional model for the lateral and vertical dynamics of wagon-track systems*. Proceedings of the Institution of Mechanical Engineers, Part F: Journal of Rail and Rapid Transit, 217(1), 31-45.

Thom, N.H., (2009). *Railway Engineering*. Lecture Notes from Railway Engineering Course, School of Civil Engineering, the University of Nottingham, UK

Thom, N.H. and Brown, S.F., (1988). *The Effect of Grading and Density on the Mechanical Properties of a Crushed Dolomitic Limestone*. Proceedings of the 14th Australian Road Research Board Conference, Part 7, pp. 94-100.

Wang, J.C., Zeng, X.W., and Mullen, R.L., (2005). *Three-Dimensional Finite Element Simulations of Ground Vibration Generated by High-Speed Trains and Engineering Countermeasures*, Journal of vibration and control, Vol. 18, No.12, pp. 1437-1453.

Woodward, P., Laghrouche, O., & El-Kacimi, A. (2013). *The development and mitigation of ground mach cones for high speed railways*. In *ICOVP 2013-International Conference on Vibration Problems*.

Wright, S. E. (1983). *Damage caused to ballast by mechanical maintenance techniques*. British Rail Research Technical Memorandum TM TD 15, May 1983.

Yang, S. C. (2009). *Enhancement of the finite-element method for the analysis of vertical train—track interactions*. Proceedings of the Institution of Mechanical Engineers, Part F: Journal of Rail and Rapid Transit, 223(6), 609-620.

Yang, L.A., Powrie, W., and Priest, J.A., (2009), *Dynamic Stress Analysis of a Ballasted Railway Track Bed during Train Passage*. Journal of Geotechnical and Geoenvironmental Engineering 135, (5), pp.680-689.

Zaman, M., Chen, D.H., and Laguros, J., (1994). *Resilient Moduli of Granular Materials*. Journal of Transportation Engineering, 120 (6), pp. 967-988.

Zhai, W., & Cai, Z. (1997). *Dynamic interaction between a lumped mass vehicle and a discretely supported continuous rail track*. Computers & structures, 63(5), 987-997.

Zhai, W., Wang, K., & Cai, C. (2009). *Fundamentals of vehicle–track coupled dynamics.* Vehicle System Dynamics, 47(11), 1349-1376.

# Appendix A

**SIMULATION DATA**

Table A1 Longitudinal Section

| Mesh | | Stress (Pa) | | Displacement (m) | |
|---|---|---|---|---|---|
| Amount | Details | Node1 | Node2 | Node1 | Node2 |
| 897(0.1) | 56+61+390+390 | -105827 | -584509 | -0.000547771 | -0.00054558 |
| 1185(0.08) | 70+119+546+450 | -114676 | -590459 | -0.000549304 | -0.000547054 |
| 1741(0.06) | 93+193+920+535 | -107474 | -588844 | -0.000550827 | -0.000548567 |
| 2999(0.04) | 138+294+1812+755 | -101802 | -791214 | -0.000553033 | -0.000550804 |
| 9210(0.02) | 276+1206+6348+1380 | -104109 | -966093 | -0.000554592 | -0.000552343 |
| | | | | | |
| Amount | Details | Node3 | Node10 | Node3 | Node10 |
| 897(0.1) | 56+61+390+390 | -74454.1 | 2019.16 | -0.00017543 | 1.4442E-06 |
| 1185(0.08) | 70+119+546+450 | -92075.7 | 2493.4 | -0.000177196 | 1.46683E-06 |
| 1741(0.06) | 93+193+920+535 | -106508 | 2900.01 | -0.000177803 | 1.47326E-06 |
| 2999(0.04) | 138+294+1812+755 | -115381 | 3163.35 | -0.000178262 | 1.48175E-06 |
| 9210(0.02) | 276+1206+6348+1380 | -167404 | 4651.75 | -0.000178988 | 1.49169E-06 |
| | | | | | |
| Amount | Details | Node11 | Node12 | Node11 | Node12 |
| 897(0.1) | 56+61+390+390 | -29349.6 | -2.11777 | 0 | 4.94977E-08 |
| 1185(0.08) | 70+119+546+450 | -29376.2 | -2.15524 | 0 | 5.01729E-08 |
| 1741(0.06) | 93+193+920+535 | -29411.7 | -2.16503 | 0 | 5.03141E-08 |
| 2999(0.04) | 138+294+1812+755 | -29434.8 | -2.17499 | 0 | 5.04808E-08 |
| 9210(0.02) | 276+1206+6348+1380 | -29462.8 | -2.18801 | 0 | 5.07065E-08 |

Table A2 Cross Section

| Mesh | | Stress (Pa) | | Displacement (m) | |
|---|---|---|---|---|---|
| Amount | Details | Node1 | Node2 | Node1 | Node2 |
| 258(0.1) | 24+126+108 | -269233 | -14302.9 | -0.000334857 | -0.000412943 |
| 391(0.08) | 48+168+175 | -326582 | -26983.1 | -0.000334953 | -0.000412996 |
| 623(0.06) | 84+304+235 | -360672 | -34669.5 | -0.000335532 | -0.000413156 |
| 1552(0.04) | 221+728+603 | -441846 | -39255.9 | -0.000335943 | -0.000413414 |
| 5207(0.02) | 756+2800+1651 | -603164 | -42358.3 | -0.000336385 | -0.000413598 |
| | | | | | |
| Amount | Details | Node3 | Node4 | Node3 | Node4 |
| 258(0.1) | 24+126+108 | -39921.8 | -33817.2 | -0.000351963 | -1.45469E-34 |
| 391(0.08) | 48+168+175 | -39926.7 | -33798.5 | -0.000352047 | -5.65194E-35 |
| 623(0.06) | 84+304+235 | -39952.9 | -33808.6 | -0.000352276 | -4.06249E-35 |
| 1552(0.04) | 221+728+603 | -39968.3 | -33781.8 | -0.000352435 | -2.7217E-37 |
| 5207(0.02) | 756+2800+1651 | -39988.6 | -33779.7 | -0.000352613 | -3.93387E-35 |
| | | | | | |
| Amount | Details | Node5 | Node6 | Node5 | Node6 |
| 258(0.1) | 24+126+108 | -839.345 | 0.165859 | 1.74492E-05 | 4.89957E-06 |
| 391(0.08) | 48+168+175 | -875.301 | 0.857572 | 1.73968E-05 | 4.90112E-06 |
| 623(0.06) | 84+304+235 | -935.513 | 0.617792 | 1.74434E-05 | 4.90261E-06 |
| 1552(0.04) | 221+728+603 | -1092.79 | 0.22666 | 1.73286E-05 | 4.89713E-06 |
| 5207(0.02) | 756+2800+1651 | -1283.4 | 0.102734 | 1.73182E-05 | 4.89272E-06 |

# Appendix B

**A STUDY OF THE INFLUENCE OF MATERAIL DAMPING**

In this study Rayleigh damping was used in rail pads, ballast, subballast and sleepers of the trackbed model. Based on the dominant frequencies of 2Hz and 10Hz generated from the simulations, the frequencies of $\omega_1$=12.6 rad/s and $\omega_2$=62.8 rad/s were utilised. The alpha and beta damping coefficients can be found from:

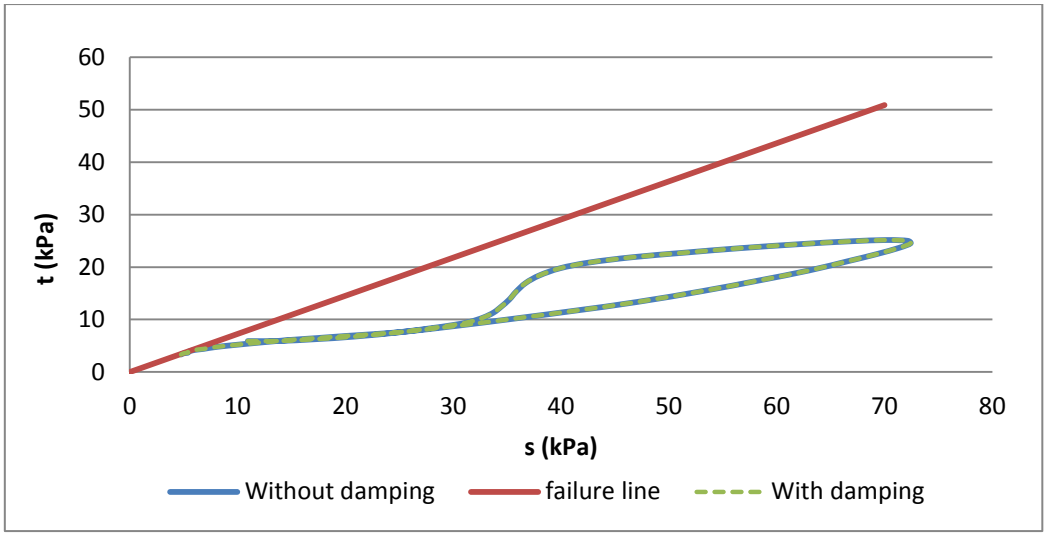
$$\alpha = \frac{2\omega_1\omega_2\xi}{100(\omega_1+\omega_2)} \qquad \text{Equation B1}$$

$$\beta = \frac{2\xi}{100(\omega_1+\omega_2)} \qquad \text{Equation B2}$$

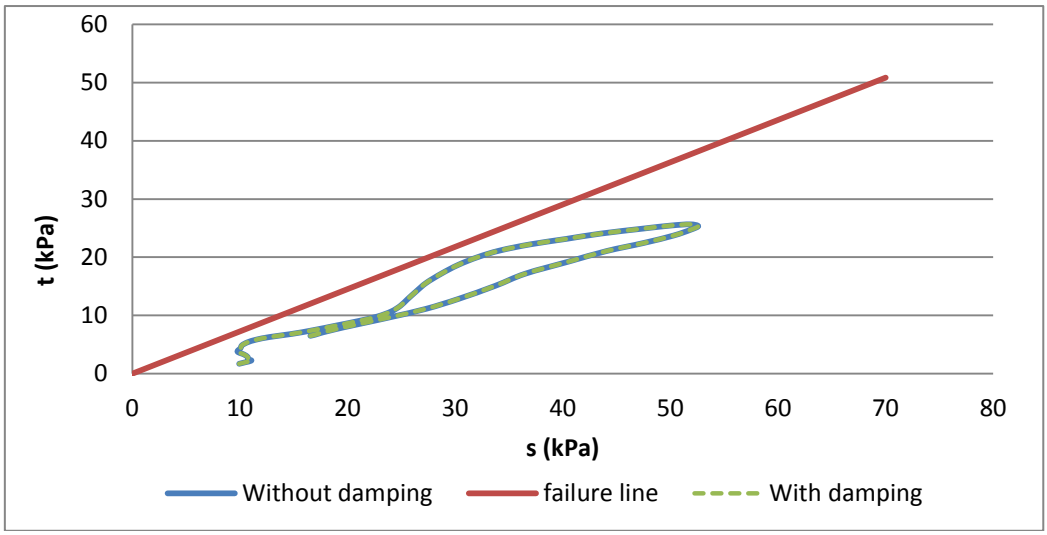
where,

$\xi$: target damping ratio at 5% for linear railway trackbed model (Woodward et al., 2013)

Effects of the damped model on stress paths at nodes 4355 and 23756 in the ballast have been computed and are presented in Figure B1. Here it may be seen that there is almost no difference between the models with and without damping. It is therefore concluded that the omission of material damping effects does not invalidate the results of the research and the model without damping was finally used in the research.



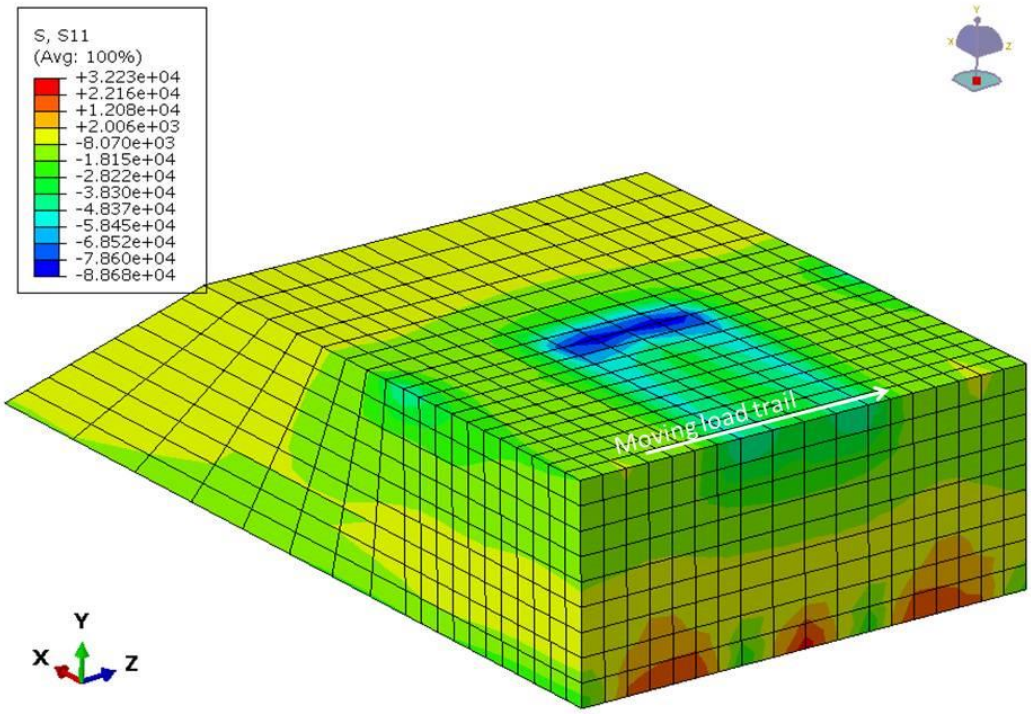

(a)



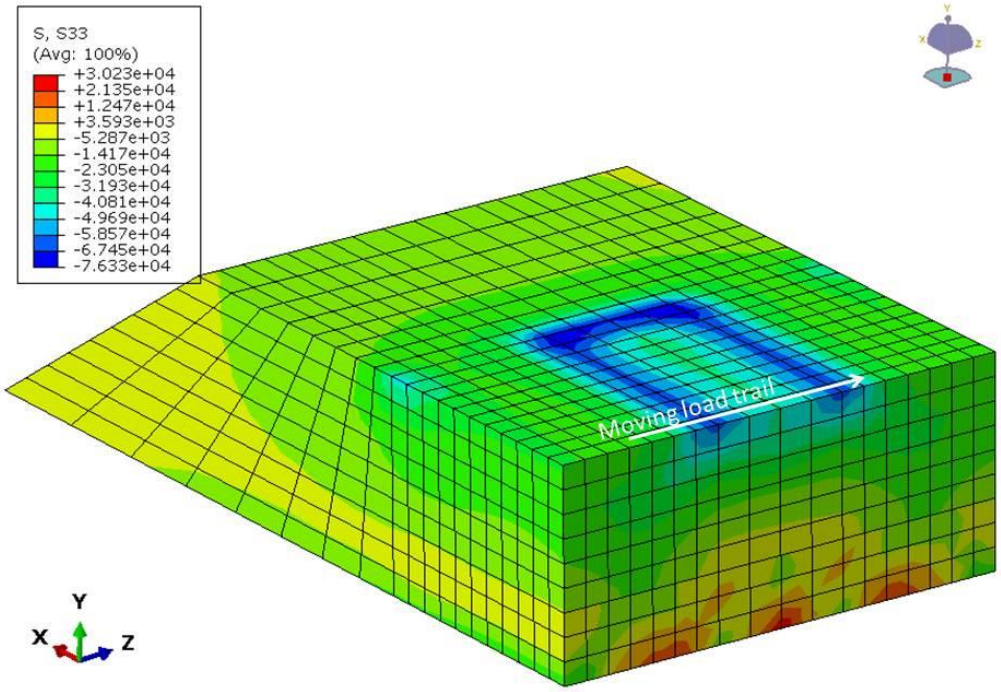

(b)

Figure B1 Stress path under model with and without damping at nodes (a) 4355 and (b) 23756

# Appendix C

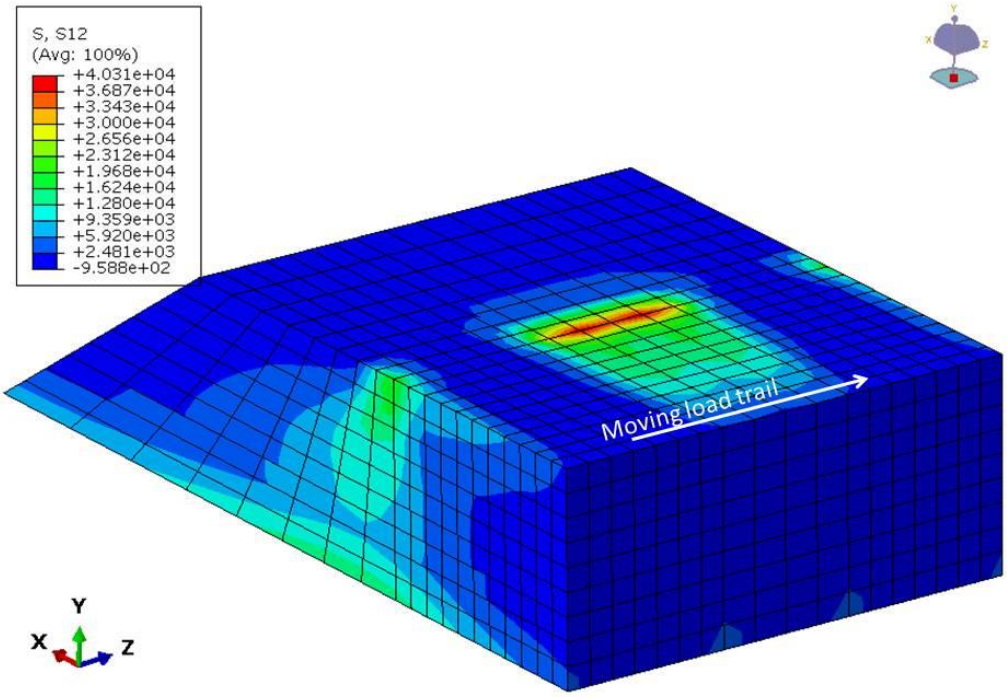



(a)

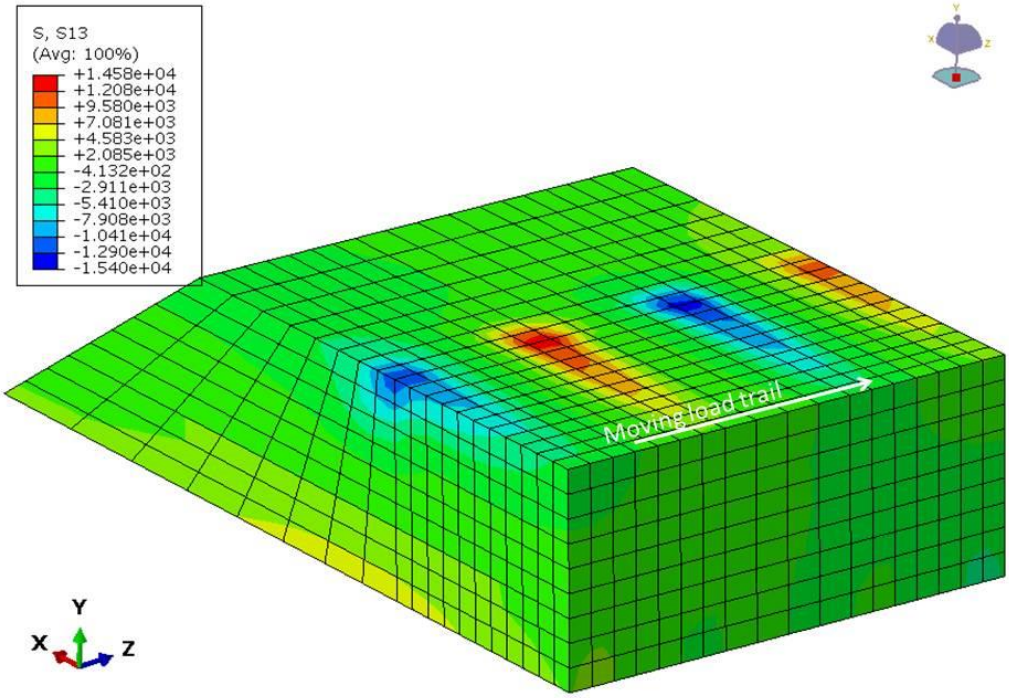



(b)

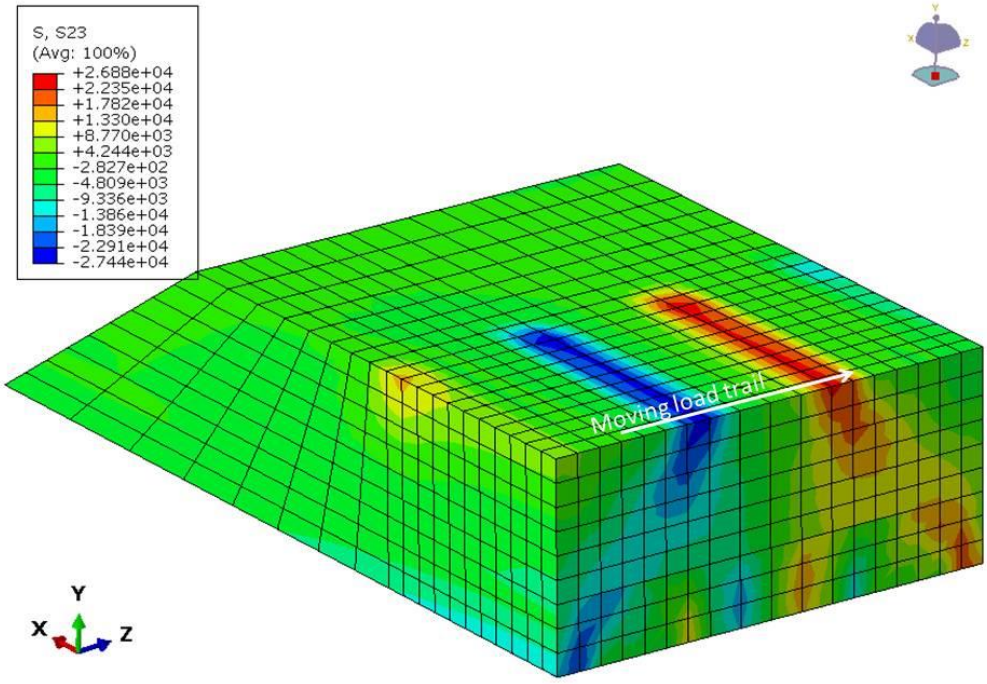
Figure C1 Contour plot of (a) x axis (b) z axis normal stress


S, S12
(Avg: 100%)
+4.031e+04
+3.687e+04
+3.343e+04
+3.000e+04
+2.656e+04
+2.312e+04
+1.968e+04
+1.624e+04
+1.280e+04
+9.359e+03
+5.920e+03
+2.481e+03
-9.588e+02
Moving load trail
Y
X
Z

(a)

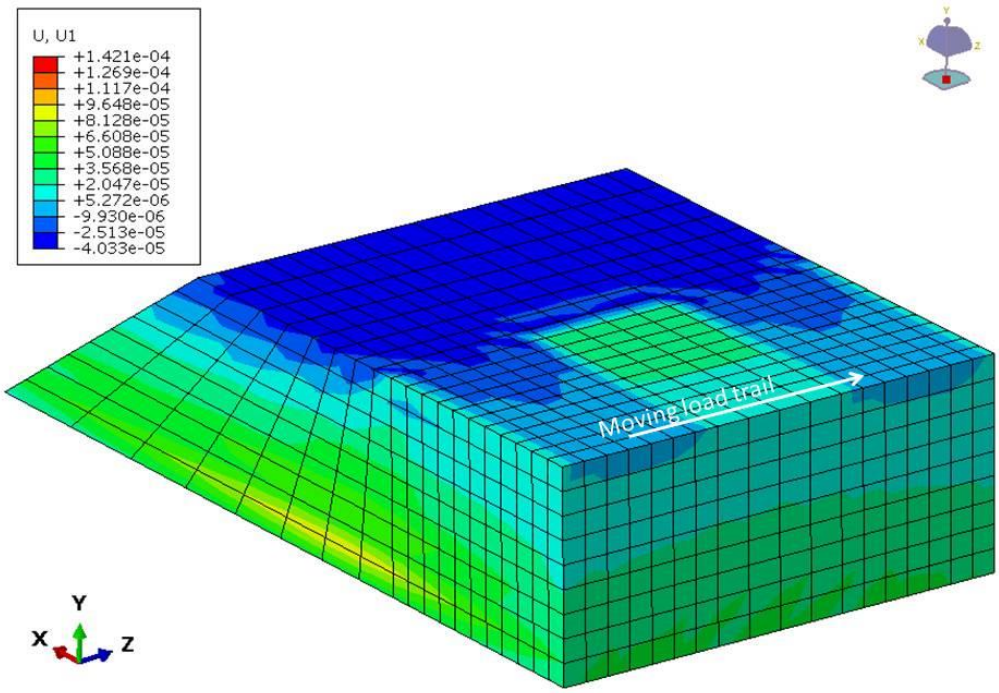

S, S13
(Avg: 100%)
+1.458e+04
+1.208e+04
+9.580e+03
+7.081e+03
+4.583e+03
+2.085e+03
-4.132e+02
-2.911e+03
-5.410e+03
-7.908e+03
-1.041e+04
-1.290e+04
-1.540e+04
Moving load trail
Y
X
Z

(b)

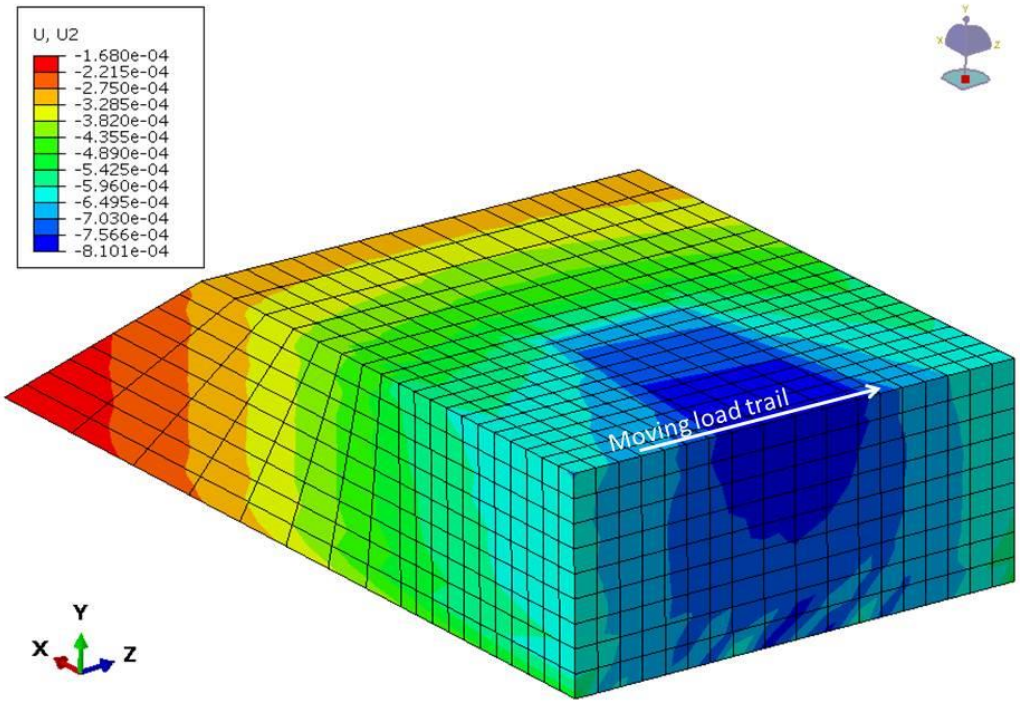



(c)

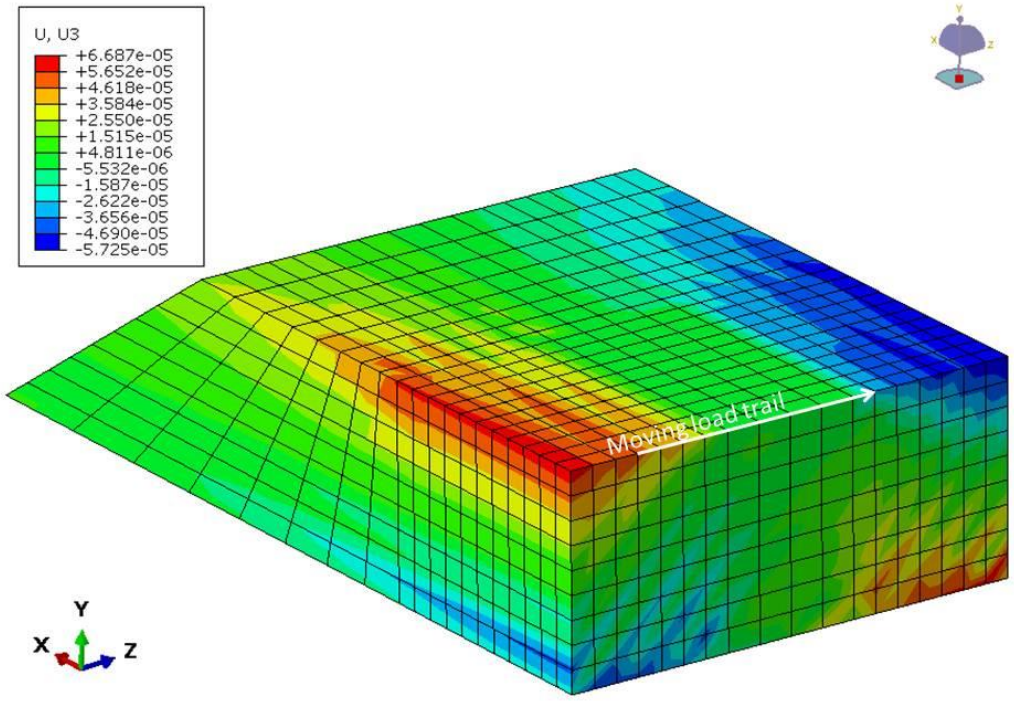
Figure C2 Contour plot of shear stress on (a) XY (b) XZ (c) YZ plane




(a)



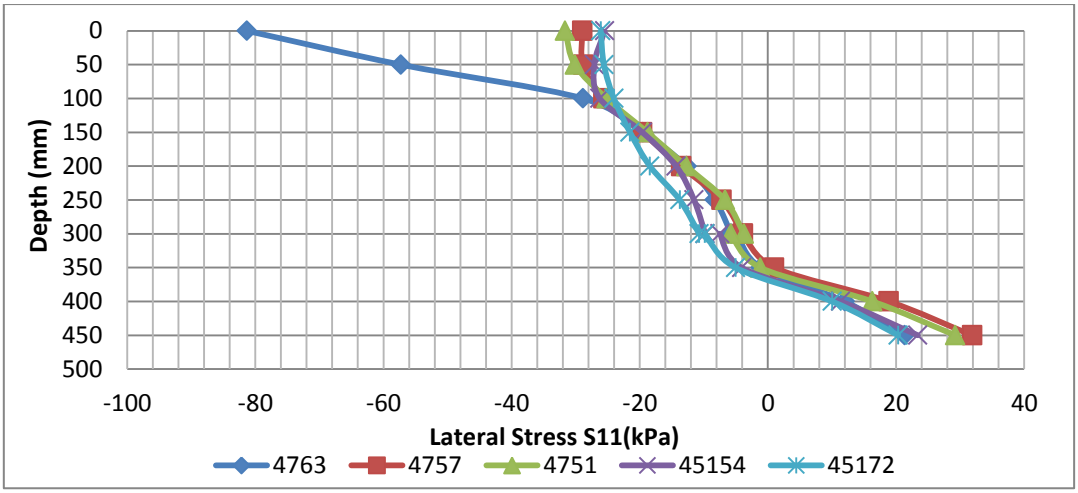

(b)



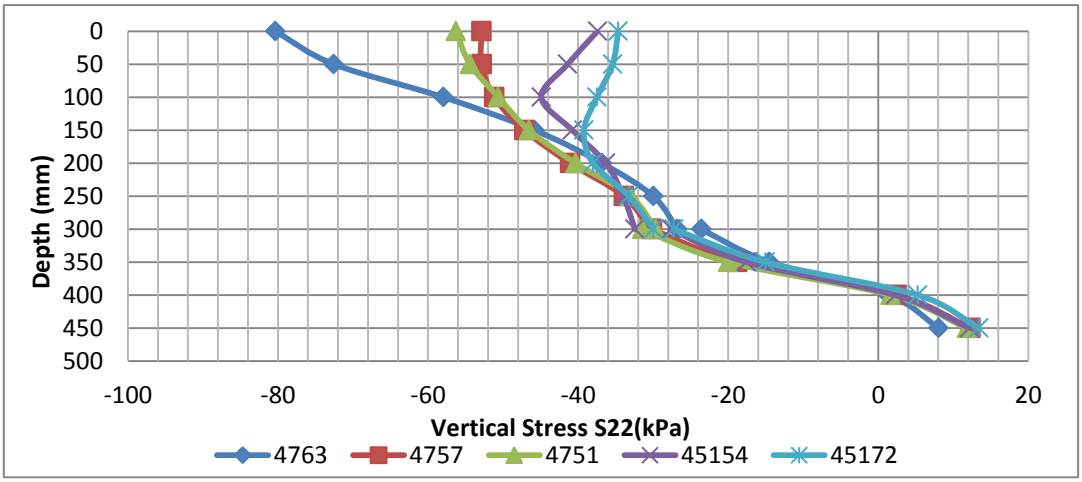

(c)

Figure C3 Contour plot of longitudinal displacement towards (a) X (b) Y (c) Z axis

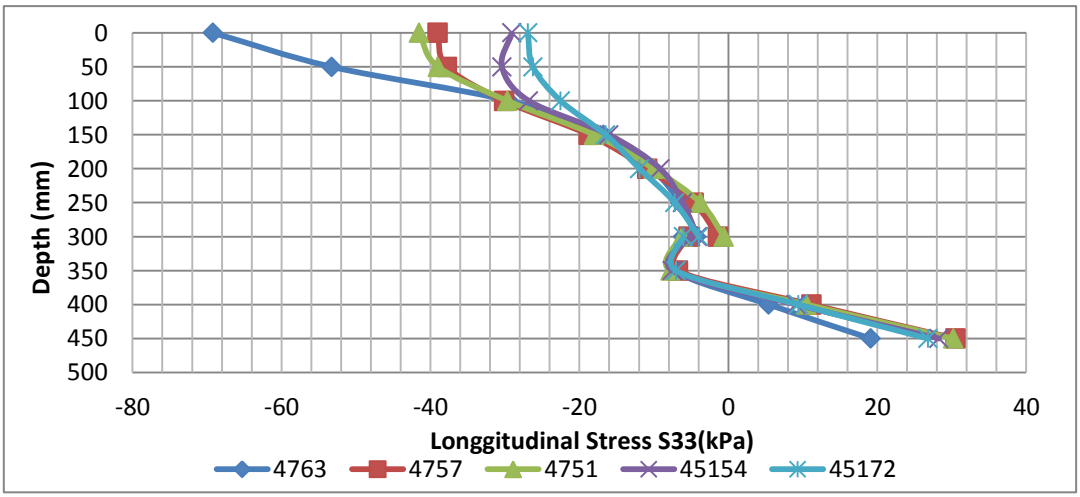
# Appendix D




(a)

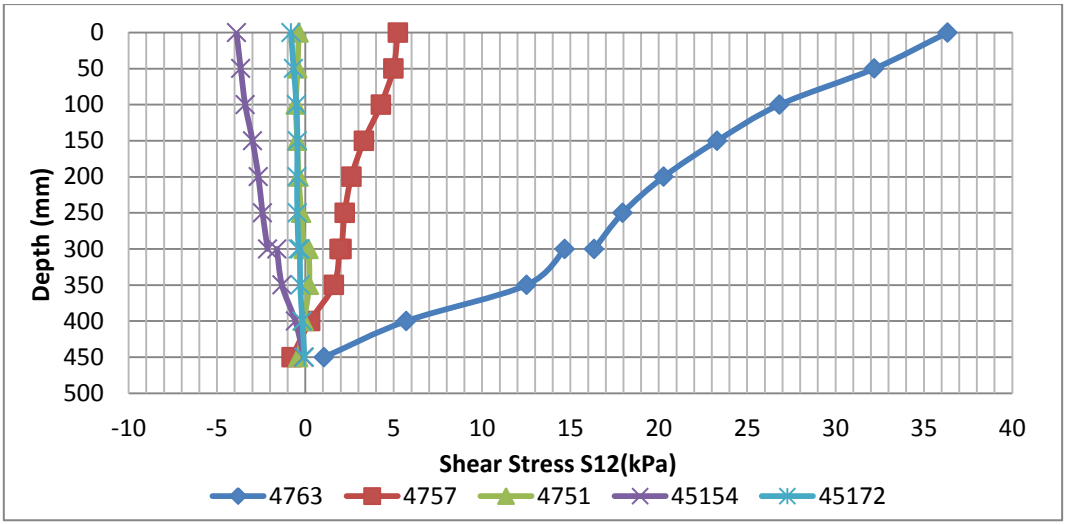



(b)

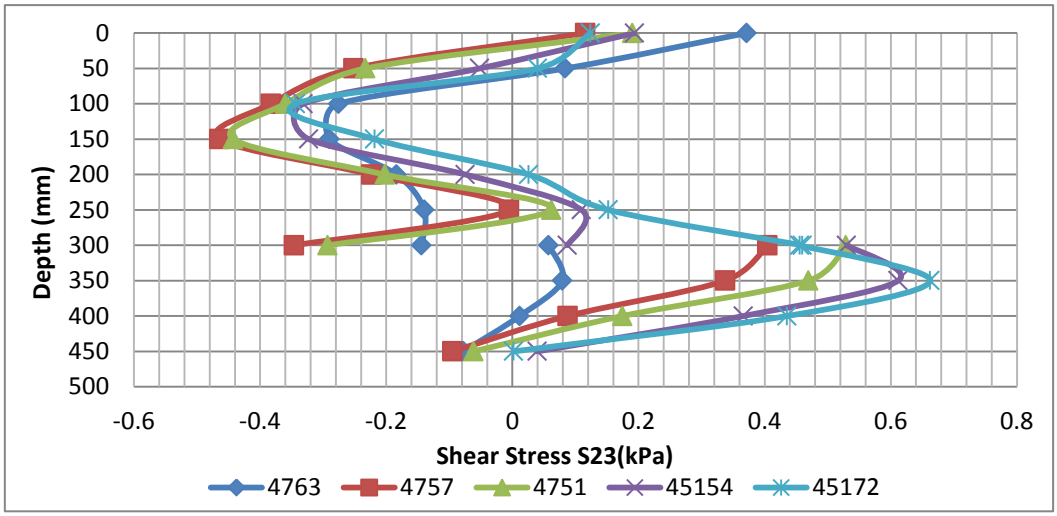



(c)

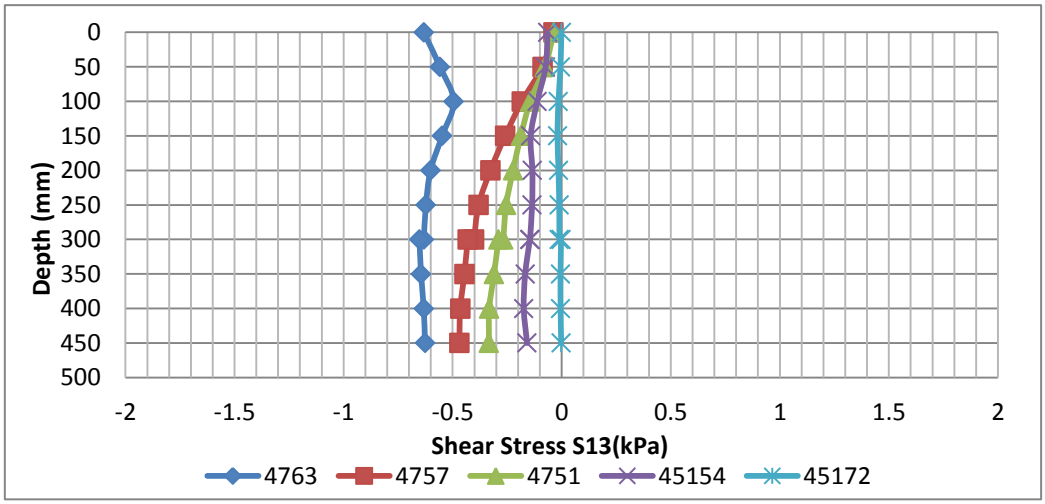
Figure D1 (a)Lateral (b) Vertical (c) Longitudinal stress paths at middle bottom of the sleeper




(a)

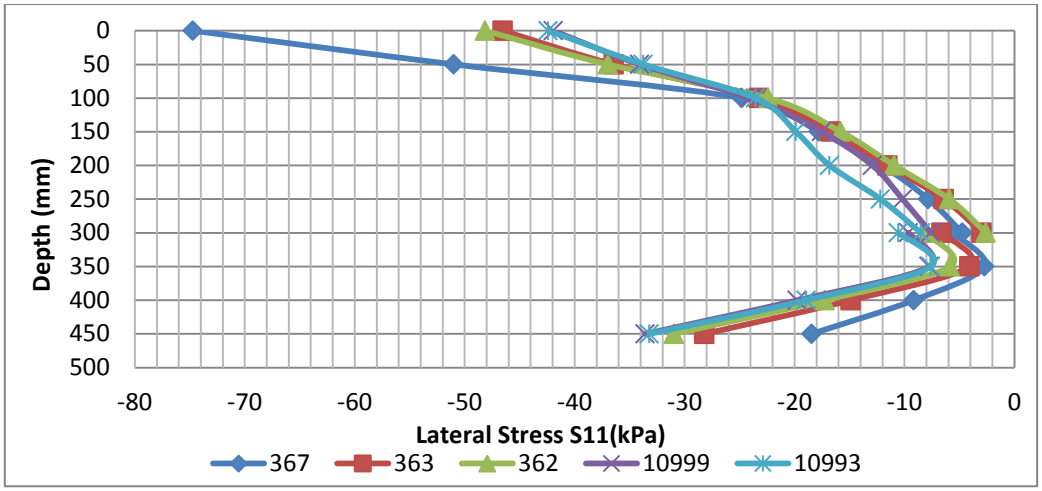



(b)

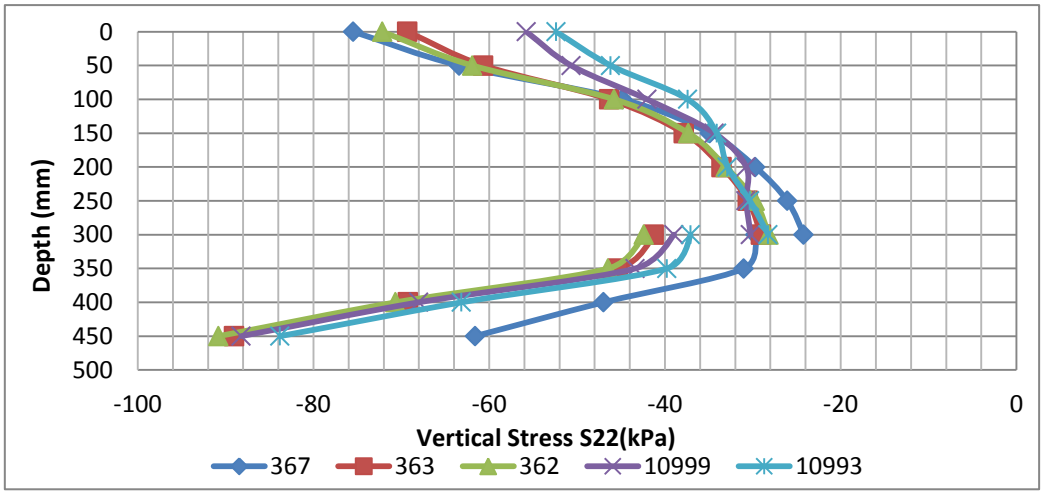



(c)

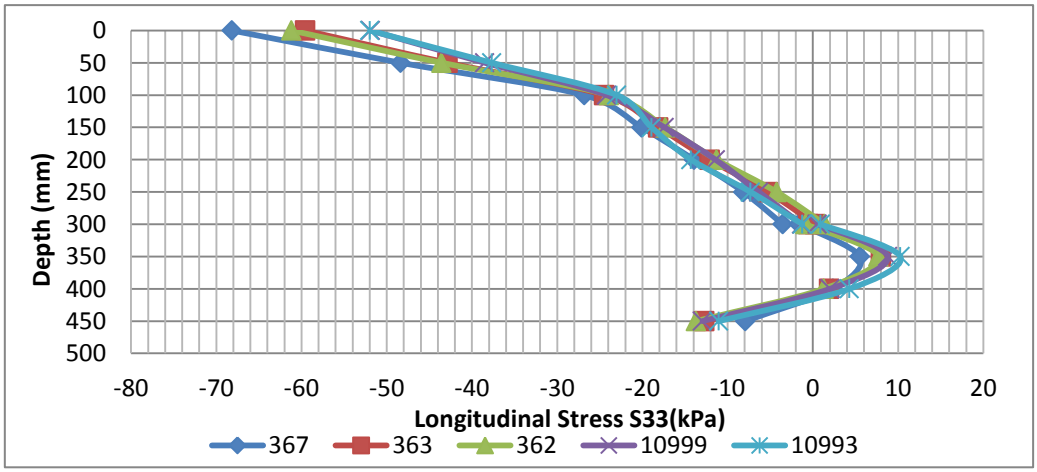
Figure D2 Shear stress paths at middle bottom of the sleeper




(a)

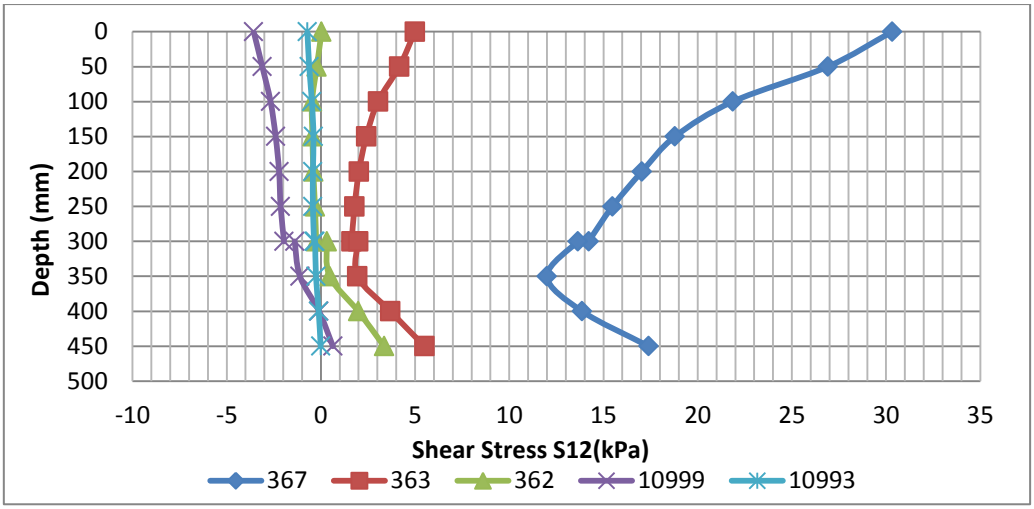



(b)

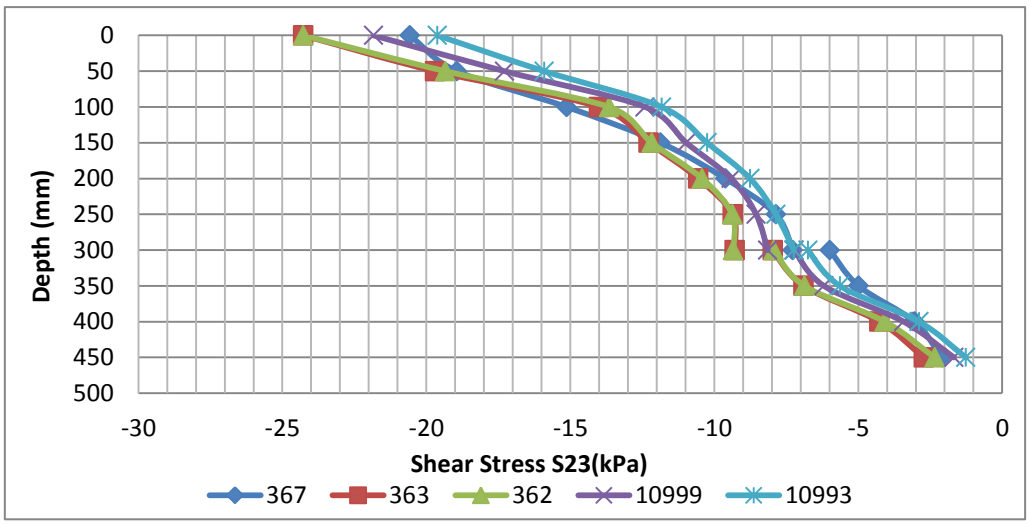



(c)

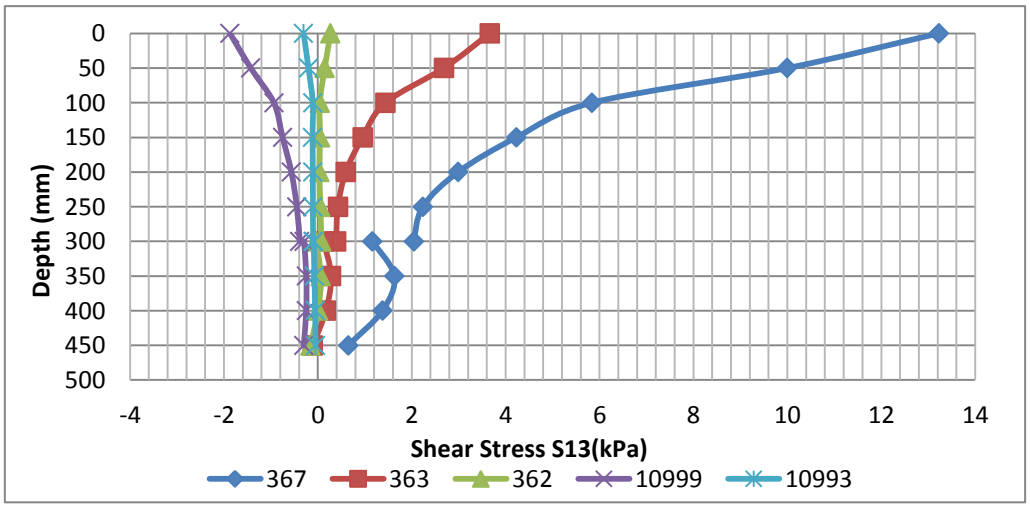
Figure D3 (a) Lateral (b) Vertical (c) Longitudinal stress paths at bottom corner of the sleeper




(a)




(b)




(c)

Figure D4 Shear stress paths at bottom corner of the sleeper